TRANSONIC SEPARATED FLOW AROUND A CAVITY

By

JOHN MARTEL

A DISSERTATION PRESENTED TO THE GRADUATE SCHOOL OF THE UNIVERSITY OF FLORIDA IN PARTIAL FULFILLMENT OF THE REQUIREMENTS FOR THE DEGREE OF DOCTOR OF PHILOSOPHY

UNIVERSITY OF FLORIDA

2001

ACKNOWLEDGEMENTS

The author would like to thank his committee, Dr. Pasquele Sforza, Dr. Chris Anderson, Dr. Wei Shyy, Dr. David Mikolaitis, Dr. Ulrich Kurzweg, and Dr. Henry Zumada, for their invaluable guidance during this effort. An expression of sincere gratitude is owed to Dr. Chris Anderson for the many helpful discussions and insights provided. Dr. Anderson's support and guidance contributed substantially to this dissertation.

I especially want to thank my parents, Dominique and Lucette Martel, for their love and support. Each one has had a tremendous impact in my life and I am truly thankful they raised me.

Special thanks go to my wife, Debbie, whose support and understanding are deeply appreciated. Without her support and encouragement I would never even have begun this endeavor.

I am immensely indebted to Cheryl Mack and Dawn Jackson of the Air Force Research Laboratory Munitions Directorate's Technical Library. Their help in locating references was a lifesaver.

I am extremely grateful for the support I received from William Clements. Without his assistance and occasional direction, the wind tunnel could not have been built.

TABLE OF CONTENTS

ACKNOWLEDGEMENTS ii

TABLE OF CONTENTS iii

LIST OF FIGURES vi

ABSTRACT xi

CHAPTERS

1 INTRODUCTION AND LITERATURE REVIEW 1

1.1 Background 1

1.2 Literature Review 3
1.2.1 Experimental Investigations 3
1.2.2 Computational Investigations 16

1.3 Summary 23

1.4 Scope of Present Research 25

1.5 Contribution of Present Research 27

2 WIND TUNNEL 29

2-1 Design Objective 29

2.2 Design Options 30
2.2.1 Shock Tube 30
2.2.2 Choked Flow with Friction 45

2-3 Wind Tunnel Design 48

2-4 Tunnel Performance 51

3 FLOW MEASUREMENT SYSTEM 53

3.1 Objective 53

3.2 Measurement Options 54
3.2.1 Shadowgraph 55
3.2.2 Schlieren 56

3.2.3 Dark Central Ground (DCG) 57
3.2.4 Interferometry 65
3.2.5 Shack Hartman Sensor 67
3.2.5.1 Single exposure 69
3.2.5.2 Multiple exposure 71

3.3 Shack Hartman Sensor Performance 77
3.3.1 Density Distribution, Constant Area Duct 77
3.3.2 Theoretical Density Compared to Measured Results 83

4 EXPERIMENTAL DATA 85

4.1 Laser Timing options 85
4.1.1 Laser Pulse Spacing. 85
4.1.2 Laser Pulse Integration 87

4.2 Shack Hartman Sensor Data 87
4.2.1 Shack Hartman Density Measurement 88
4.2.2 Two-Dimensional Assumption 90

4.3 Direct Results 96
4.3.1 Density Gradient in y Direction 96
4.3.2 Density Gradient in x Direction 97
4.3.3 Local Time Derivative of Density 99
4.3.4 Digital Dark Central Ground (DCG) 100

4.4 Derived Results 102
4.4.1 Pressure Coefficient (Cp) Distribution 102
4.4.2 Ensemble Average ($\overline{\rho}$) 106
4.4.3 Density Deviation (ρ') 107
4.4.4 Pressure Distribution (P(x,y)) 109

4.5 Flow Structure Position and Velocity 115
4.5.1 Shear/Mixing Layer 116
4.5.2 Shear Layer Large-Scale Structures 116
4.5.3 Cavity Large-Scale Structures 116
4.5.4 Data Presentation Example 116

4.6 Comparison with Past Experimental Work 119

4.7 Summary 122

5 RESULTS AND DISCUSSIONS 124

5.1 Cavity Flow Model 125

5.2 L/D = 4 Cavity 131
5.2.1 Individual Results, L/D = 4 132
5.2.1.1 Test6-9feb 132
5.2.1.2 Test7-9feb 134
5.2.1.3 Test2-6feb 136
5.2.1.4 Test8-9feb 138
5.2.1.5 Test9-9feb 140
5.2.1.6 Test1-10feb 142
5.2.2 Cavity Cycle, L/D = 4 144
5.2.3 Flow Structure Position and Movement, L/D = 4 149

5.3 L/D = 8 Cavity 153
5.3.1 Individual Results, L/D = 8 153
5.3.1.1 Test11-10feb 153
5.3.1.2 Test10-10feb 155
5.3.1.3 Test3-11feb 157
5.3.1.4 Test4-11feb 159
5.3.1.5 Test5-11feb 161
5.3.2 Cavity Cycle, L/D = 8 163
5.3.3 Flow Structure Position and Movement, L/D = 8 170

5.4 Summary 174
5.4.1 Mass Injection/Ejection 174
5.4.2 Shear Layer Movement 175
5.4.3 Floor Cp Distribution 177
5.4.4 Pressure Disturbance Sources 178

5.5 Conclusions 179

5.6 Future Work 180

REFERENCES 184

BIOGRAPHICAL SKETCH 189

LIST OF FIGURES

Figure Page

1-1 Cavity Flow 2

1-2 Representative Cavity Pressure Distributions 8

1-3 Effect of geometry and Mach on cavity classification 12

1-4 Schlieren View Ports 14

1-5 Absolute and Differential Interferograms 15

2-1 Shock Tube and In-draft Tunnel Configuration 31

2-2 Notional x-t Diagram 32

2-3 Shock Tube Mach Number 41

2-4 Shock Tube Reynolds Number 42

2-5 Region II Useable Time 43

2-6 Region III Useable Time 43

2-7 Region II x-t Diagram 44

2-8 Region III x-t Diagram 44

2-9 Mach Number Choked Flow 46

2-10 Reynolds Number Choked Flow 47

2-11 In-draft Tunnel 48

2-12 Cavity Models 49

2-13 In-draft Tunnel Pressure Time History 50

3-1 Optical Flow Visualization 54

Figure Page

3-2 Diagram of Operation of a Basic Shadowgraph System 56

3-3 Schematic of Schlieren System with Knife Edge Filter 57

3-4 Schematic of Dark Central Ground with Circular Spot 58

3-5 Schematic of DCG Test Set Up 59

3-6 Laboratory DCG Test Set Up 60

3-7 DCG Choked Flow 62

3-8 DCG Unchoked Flow 63

3-9 Schematic of an Interferogram System 66

3-10 Shack Hartman Sensor 67

3-11 Shack Hartman Sensor Choked Flow, Single Exposure 70

3-12 Shack Hartman Sensor Unchoked Flow, Single Exposure 71

3-13 Four-Laser Point Source 72

3-14 Multiple Expose CCD Array 73

3-15 9X9 4 Spot Cluster 74

3-16 Cavity Geometry 75

3-17 Density Distribution 76

3-18 Incompressible and Compressible Velocity Profile Comparison 80

3-19 Temperature and Density Distribution, Preliminary Tunnel 82

3-20 Shack Hartman Density, Preliminary Tunnel 84

3-21 Shack Hartman Density, In-draft Tunnel 84

4-1 In-Draft Tunnel Test Section Optical Coverage 88

Figure Page

4-2 Shack Hartman Density Distributions 90

4-3 Three Dimensional Effect Test Configuration 92

4-4 Oil Flow Visualization at Mach 1.5 for L/D = 3 93

4-5 Schlieren Plan Views of Flow Over Cavities 94

4-6 Density Gradient in Y direction 97

4-7 Density Gradient in X direction 98

4-8 Local Time Derivative of Density 100

4-9 Gradient of Density (Digital Dark Central Ground) 102

4-10 Mean Pressure Coefficient Distribution, L/D = 4 104

4-11 Mean Pressure Coefficient Distribution, L/D = 8 105

4-12 Density Ensemble Average, L/D = 4 106

4-13 Density Ensemble Average, L/D = 8 107

4-14 Density Deviation 108

4-15 Comparison of Density Deviation, X Gradient, Time Derivative 109

4-16 Shear Layer Thickness 110

4-17 Theoretical Shear Layer Temperature Profile 111

4-18 Estimated Shear Layer Temperature Profile 113

4-19 Pressure Distribution, L/D = 4 114

4-20 Pressure Distribution, L/D = 8 115

4-21 Temporal Environment, L/D = 4, test9-9feb 118

4-22 Strouhal Number $\Phi_d = 0.57$ 121

Figure Page

4-23 Strouhal Number $\Phi_d = 0.40$ 122

5-1 Cavity Flow Model 127

5-2 Shear Layer Peaks & Valleys, L/D = 4 128

5-3 Shear Layer Peaks & Valleys, L/D = 8 130

5-4 Test6-9feb, L/D = 4 134

5-5 Test7-9feb, L/D = 4 136

5-6 Test2-6feb, L/D = 4 138

5-7 Test8-9feb, L/D = 4 139

5-8 Test9-9feb, L/D = 4 141

5-9 Density Distribution, test9-9feb, L/D = 4 142

5-10 Test1-10feb, L/D = 4 144

5-11 Test1-9feb, L/D = 4 145

5-12 Test1-6feb, L/D = 4 146

5-13 Test2-9feb, L/D = 4 147

5-14 Test2-10feb, L/D = 4 148

5-15 Test3-6feb, L/D = 4 149

5-16 Flow Structure Position (y/L) 150

5-17 Transverse Velocity, L/D = 4 151

5-18 Non-dimensional Flow Structure Statistics, L/D = 4 152

5-19 Test11-10feb, L/D = 8 155

5-20 Test10-10feb, L/D = 8 156

Figure Page

5-21 Test3-11feb, L/D = 8 159

5-22 Test4-11feb, L/D = 8 160

5-23 Test5-11feb, L/D = 8 163

5-24 Test4-10feb, L/D = 8 164

5-25 Test5-10feb, L/D = 8 165

5-26 Test6-10feb, L/D = 8 166

5-27 Test7-10feb, L/D = 8 167

5-28 Test8-10feb, L/D = 8 168

5-29 Test1-11feb, L/D = 8 169

5-30 Flow Structure Position (y/L) (L/D = 8) 171

5-31 Transverse Velocity, L/D = 8 172

5-32 Non-dimensional Flow Structure Statistics, L/D = 8 173

ABSTRACT

Abstract of Dissertation Presented to the Graduate School
of the University of Florida in Partial Fulfillment of the
Requirements for the Degree of Doctor of Philosophy

TRANSONIC SEPARATED FLOW AROUND A CAVITY

By

John Martel

December 2001

Chair: Dr. Pasquale M. Sforza
Major Department: Aerospace Engineering, Mechanics, and Engineering Science

Unsteady flow over shallow cavities (L/D = 4 and L/D = 8) at Mach = 0.8 is investigated experimentally. Data acquisition in and above two-dimensional rectangular cavities is accomplished optically via a multiple exposed Shack Hartman sensor. This technique provides a time-accurate picture of the density behavior in and above the cavity without the need to insert any type of recording device into the flow. The Shack Hartman sensor measures the change in slope of an optical wave front passing through the test area. The change in phase angle may be calculated from this change in slope of the optical wave front. The density distribution is then found from the change in phase angle distribution.

An in-draft tunnel was designed and built to produce the desired Mach number at a Reynolds number of 11.0 x10^6 per meter. Pressure and temperature in the tunnel, supply reservoir and receiving reservoir are measured using traditional pressure and

temperature sensors. The temporal behavior of the shear/mixing layer and temporal behavior of the flow structures in the cavity (position and velocity) is analyzed. The impact of the interaction of the shear layer and the cavity structures on the pressure coefficient distribution on the surface of the cavity is also analyzed.

CHAPTER 1
INTRODUCTION AND LITERATURE REVIEW

The cavity is a basic fluid dynamic configuration. It occurs in many aerodynamic vehicles such as wheel wells, bomb bays and missile bays. The requirement for reduced radar cross-section and improved aerodynamic performance has necessitated the internal carriage of weapons. While internal carriage of weapons provides reduced radar cross section and improved aerodynamic performance, difficulties such as large nose up pitching moments or structural vibration can arise when a store is required to separate from a cavity or when exposed to an external flow. This external flow does not follow the cavity surface but instead develops regions of separated flows in, above and behind the cavity. This separated flow is often characterized by a strong oscillation inside the cavity. It is necessary to study the flow disturbances generated when a rectangular cavity is subjected to a uniform flow.

1.1 Background

Flow in, above and behind a cavity does not follow the cavity surface but instead develops regions of separated flow as shown in Figure 1-1. When the flow passes over the cavity, it separates and forms vortices within the shear layer and within the cavity. If the free stream flow is supersonic, additional flow structures such as expansion and shock waves are also present. The shear layer moves up and down and interacts with the vortices formed in the cavity. This interaction of the shear layer and vortices causes pressure fluctuations on the surface of the cavity. The shear layer eventually spans the

cavity and reattaches downstream of the aft wall of the cavity. This research is concerned with the flow in and above the cavity. The focus is to investigate experimentally transonic flow over cavities. Specifically, the structures in the shear/mixing layer, the structures in the cavity, and the impact of the interaction of these structures on the surface pressure coefficient distribution are investigated.

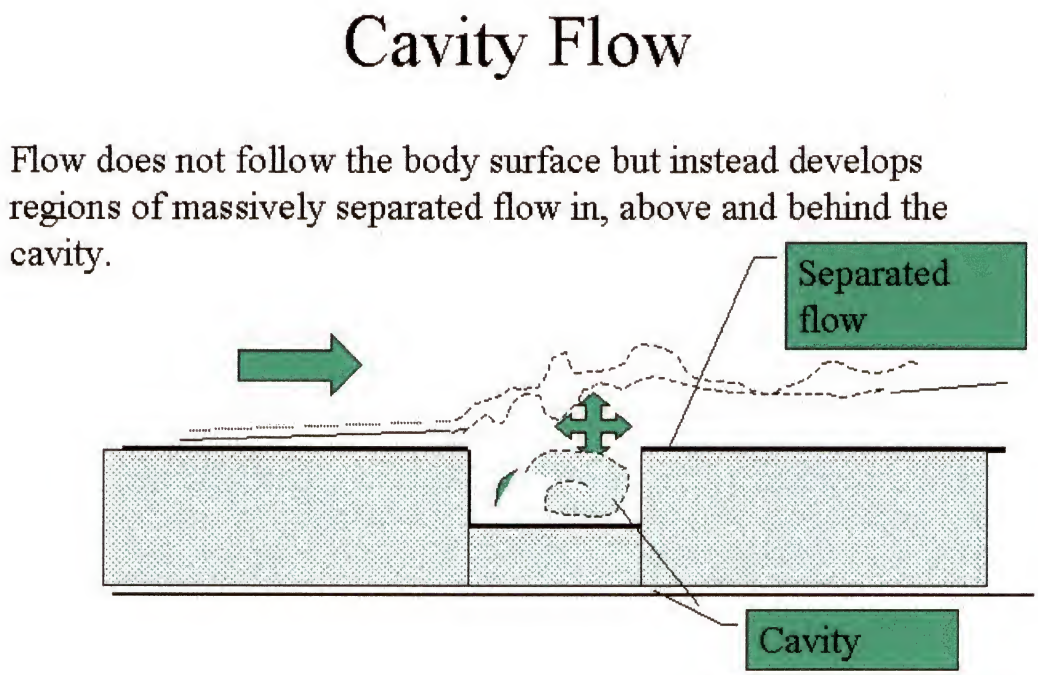

Figure 1-1 Cavity Flow

This experimental research will concentrate on measuring and analyzing the flow inside and above the cavity as opposed to the surface of the cavity. A unique mean pressure distribution exists on the surface of the cavity for a given geometry and free stream conditions, which allows the cavity to be classified as open, closed or transitional. By measuring the flow in and above the cavity, the flow structures and their interaction in and above the cavity that cause a unique mean pressure distribution can be identified and

analyzed. With a known set of flow structures and knowledge of how they interact, methods to control the flow in and above the cavity can be more easily developed and analyzed. It is important to know how the flow field behaves and how to control this flow field especially when jettisoning or releasing bodies of revolution through this flow field.

1.2 Literature Review

Numerous experimental and computational investigations have been undertaken in the past to try to understand the flow in and above cavities. Experimental investigations have concentrated on the cavity acoustic problem as well as cavity classification by means of the mean pressure coefficient distribution on the floor of the cavity. Cavities are classified as open, closed or transitional based on the mean pressure distribution on the centerline of the floor of the cavity. Computational investigations have been mainly concerned with validating various two and three-dimensional codes against known experimental investigations so these codes can be used to study other aspects of the cavity flow problem. The problem with comparison of the results of computations is that it is restricted to comparing only the mean and fluctuating surface pressure coefficient distribution. There exist no measured quantitative results of the flow in and above the cavity against which computational results can be compared.

1.2.1 Experimental Investigations

There have been many investigations into unsteady flow in, above, and behind cavities. Emphases of past experimental investigations were focused on the acoustic problem and on classifying the cavity as open, closed or transitional based on the surface pressure coefficient distribution. Experimental investigation was restricted by the flow

measurement technology. Since flow in and above cavities is highly unsteady, insertion of any type of probe would alter the flow of interest. Therefore, measurements were restricted to surface pressure measurements or sound/acoustic far field measurements.

Krishnamurty (1955) determined that a cavity oscillates under a broad band of flow situations. Flow oscillations might occur predominantly in the span wise (width W), longitudinal (length L) or transverse (depth D) directions. When the length to depth ratio of the cavity is equal to or larger than one, the longitudinal oscillation is likely to become a dominant feature of the cavity flow.

Plumblee et al. (1962) concluded that the turbulent shear layer spanning the free boundary of the cavity provides it with a broadband noise source from which the cavity picks up certain frequencies to amplify. While this may be true for the transverse modes when the cavity length to depth ratio is equal to or less than one, it is has not been justified for the longitudinal oscillatory modes of the cavity. Strong oscillations have been observed when the shear layer of a cavity flow is laminar.

Rossiter (1964) theorized that the driving mechanism of the cavity flow oscillation is a property of the flow over the cavity rather than of the oncoming boundary layer. He proposed a mechanism based on acoustic feedback. Noticing that there are discrete vortices shedding from the leading edge of the cavity, he assumed that the vortices interact with the trailing edge of the cavity, generating acoustic pulses, which then propagate upstream inside the cavity. These acoustic pulses deflect the oncoming boundary layer at the leading edge of the cavity and produce vortices that are shed downstream. The longitudinal oscillation of the cavity then occurs when the vortices and the acoustic pulse form closed loops.

Heller et al. (1970) conducted wind tunnel tests on cavities of L/D ratio of 4 to 7 over a Mach number range from 0.8 to 3, obtaining spectra of pressure fluctuations inside the cavity and under the approach boundary layer. They observed stronger spectral peaks when the boundary layer was laminar. They showed that the cavity temperature was related to the free stream temperature with recovery factors from 0.8 to 0.95. Pressure fluctuations were seen to be highest near the trailing edge of the floor of the cavity, falling off inversely with distance towards the leading edge.

Heller and Bliss (1975) determined that cavity oscillations are caused by the interaction of the free shear layer and the cavity internal medium, which involves both acoustic and hydrodynamic mechanism. The unsteady motion of the external shear layer leads to a periodic mass addition and removal at the cavity trailing edge. In a shallow cavity ($L/D > 1$), this generates forward traveling waves in the cavity that reflect from the front bulkhead and become rearward traveling waves. The resulting wave structure in the cavity forces the shear layer in an unsteady manner over the entire length of the cavity.

Komerath et al. (1987) summarized previous investigations into the acoustic problem. The incoming boundary layer separates at the cavity lip, a free shear layer containing span wise instabilities begins to develop, and the shear layer then reattaches either downstream or on the back wall of the cavity. Under certain conditions, disturbance waves are aerodynamically and/or acoustically fed back to the original disturbance source, the leading edge flow separation area. This feedback loop subsequently builds up the disturbance wave at certain frequencies, creating large oscillating pressure waves and noise. Most flows over cavities are susceptible to

oscillations. Oscillating flows can be classified according to the fluid resonant interactions or fluid dynamic interactions.

Fluid resonant interactions usually occur in cavities with large depths normal to the flow or large volumes with small openings to the flow. In this class of cavities (L/D < 2) flow induced oscillations are influenced by the resonant "wave" effects (Zhang and Edwards 1992). The characteristic of flow-induced oscillations in a resonator is that the shear layer at the orifice produces eddies that grow as they are convected across the cavity gap. If the growth rate and the convection velocity take the proper values, the eddy grows to fill the gap. In this manner, the eddy that has developed creates compression in the cavity. The compressed fluid then ejects the eddy into the mainstream flow and a new eddy develops in the gap. The oscillation, if it occurs, is therefore dominated by transverse modes, and the levels of the pressure fluctuations are relatively small.

Fluid dynamic interactions involve coupling between oscillations of the shear layer over the cavity with the flow inside the cavity. The mechanisms involved are believed to arise from the shear layer instability and vortex shedding. Large-scale coherent structures present in the shear layer are known to play the major role in such interactions. Cavities with L/D greater than 2 oscillate with a mechanism that is attributed to the feedback of small disturbances on the downstream face of the cavity. The disturbances propagate upstream to form a closed loop by influencing the shedding of the vortices (Rockwell and Naudascher 1978).

Fluid dynamic interactions dominate flow in and above shallow cavities. These types of cavities are commonly referred to as open cavities and they can have L/D ratios

as high as 8. Open cavity flow is typically encountered in weapon bay applications. In this flow, the longitudinal pressure and flow oscillations have been associated with the shear layer interactions within the cavity (Vakili and Gauthier 1991). As explained by a self-exiting feedback mechanism, perturbations are produced when the shear layer interacts with the cavity trailing edge. These perturbations travel upstream within the cavity and eventually excite the shear layer at the cavity leading edge. As a result of these excitations, the shear layer development along the cavity is altered, and consequently, the subsequent interactions at the trailing edge are also affected. The whole feedback process is therefore continuously altered. Whenever proper timing exists between these events, the feedback process can lead to resonance (self-excite) and result in a large amplification of the cavity oscillations at certain frequencies.

Flow in and above a cavity is highly unsteady. The frequency and amplitude at which the pressure will fluctuate is a function of the cavity geometry and free stream flow conditions. The approaching boundary layer has been shown to impact the frequency and amplitude of the pressure fluctuation but the boundary layer is itself a function of the geometry ahead of the cavity along with the free stream flow conditions. The predominant variables that impact the pressure fluctuation are the L/D ratio and the free stream Mach and Reynolds number. Past experimental studies attempting to classify cavities have also reached the same conclusion that the important parameters are the geometry (L/D ratio) and free stream conditions (Mach and Reynolds number).

Cavities are classified as open, closed, or transitional. This classification is based on the mean pressure coefficient distribution on the centerline of the floor of the cavity.

Plentovich et al. (1993) summarized these classifications as follows and is shown in Figure 1-2.

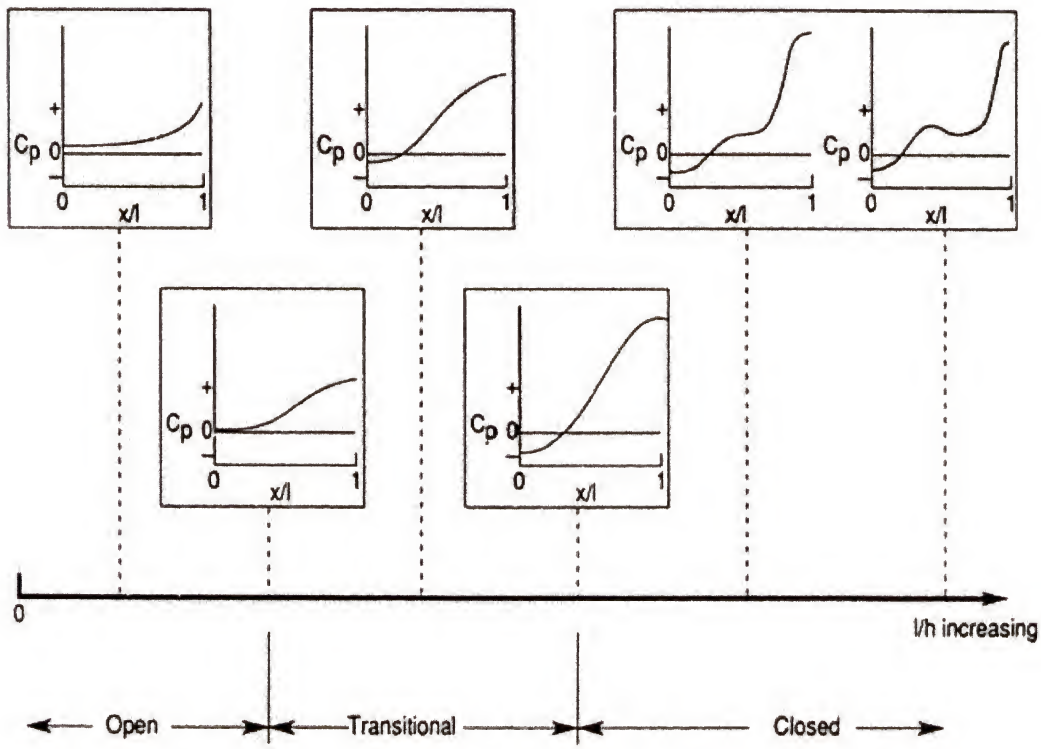

Figure 1-2 Representative Cavity Pressure Distributions

Open Flow

- The value of the pressure coefficient (Cp) is approximately 0.0 in the front half of the cavity.
- The aft cavity pressure coefficient increases the further aft along the cavity floor and the distribution has concave-up shape.

Open/Transitional Flow Boundary

- The Cp distribution over the rear portion of the cavity floor changes from concave-up to a concave-down shape.
- The Cp distribution over the forward portion of the cavity is close to 0.0.

Transitional Flow

- Cp distribution over the rear portion of the cavity floor has a concave-down shape.
- As L/D increases, the Cp distribution along the cavity floor gradually varies from the shape of the distribution shown at the open/transitional flow boundary to that shown at the transitional/closed flow boundary.

Transitional/Closed Flow Boundary

- Cp increases uniformly from negative values in the vicinity of the front face to large positive values ahead of the rear face. The minimum values in the vicinity of the front face and maximum values ahead of the rear face are approximately of the same magnitudes measured for closed cavity flow.

Closed Flow

- The flow becomes closed when an inflection occurs in the Cp distribution midway along the length as a result of increasing L/D.
- A further increase in L/D causes the inflection point to become a plateau region in the Cp distribution.
- A still further increase in L/D causes a decrease in Cp downstream of the plateau region followed by an increase in Cp to the maximum value ahead of the rear face.
- The maximum Cp ahead of the rear face remains at approximately the same value measured at the boundary with transition flow.

Rossiter (1964) investigated the pressure distribution on the centerline of the floor of the cavity. His investigation covered Mach numbers from 0.5 to 1.2 at a constant Reynolds number per meter of $7.2 * 10^6$. L/D and W/D were varied from 2 to 10 and .25 to 2.5 respectively. Although his main area of interest was to investigate the pressure oscillation within the cavity, the pressure distribution shape as a function of L/D shown in his report follows the description provided by Plentovich et al. (1993). Rossiter concluded that when the L/D ratio of the cavity was decreased, the attachment and separation point on the floor moved closer together until a reverse flow developed between the high-pressure region ahead of the rear wall and the low-pressure region

behind the front wall. The flow was no longer attached to the floor of the cavity. A further reduction in L/D eventually produced a large captive eddy.

Stallings and Wilcox (1987) investigated the mean pressure coefficient distribution for supersonic Mach numbers 1.5 to 2.86. L/D and W/D were varied from 1 to 24 and 1 to 5 respectively. The free stream Reynolds number was held constant at 6.6 * 10^6 per meter and the approaching boundary layer was artificially set to 5.08 mm. It was concluded that over the range of variables tested, cavities may be classified as open for L/D less than 10 and closed for L/D greater than 13. Cavities are considered transitional when L/D is in the range of 10 to 13. An analysis of the pressure distribution provided in the report agrees with the description given by Plentovich et al. (1993). Zhang and Edwards's (1990) investigations for a Mach of 1.5 and 2.5 over an L/D range of 1 to 9 at a constant width also agrees with this classification description.

Plentovich (1990) performed an experimental investigation for the subsonic and transonic Mach numbers 0.3 to 0.95 for an L/D of 4.4 and 11.7 and a W/D of 1 and 2.67. An investigation on the effect of Reynolds number and approaching boundary layer was also accomplished. Varying the free stream Reynolds number while holding all other variables constant had no effect on the mean Cp distribution. However, larger pressure fluctuations for open cavities were observed for Re > 9.84 * 10^6 per meter. Approaching boundary layer thickness also showed no effect on the classification of the cavity, as the shape of the pressure distribution remained the same. However, it was found that the thinner the approach boundary layer thickness for a given L/D, the higher the mean pressure on the aft floor of the cavity. By decreasing the boundary layer thickness, the ratio of the depth to the boundary layer thickness (D/δ) was increased. Chung (2000)

showed the same trend by increasing the depth of the cavity keeping the ratio L/D constant. He showed that with increasing D/δ, the pressure distribution remained the same but the mean pressure on the floor of the cavity at the aft end increased. Plentovich et al. (1991) reached the same conclusions.

Plentovich et al. (1993) investigated the mean pressure distribution as a means of classifying cavities in the subsonic and transonic range. Mach number was varied from 0.2 to 0.95. L/D and W/D were varied from 1 to 17.5 and from 1 to 10 respectively. They established the criteria shown in Figure 1-2. They concluded that a cavity might be classified as open when the L/D ratio is less than 6 to 8, transitional for L/D 7 to 14, and close when L/D is greater than 9 to 14. This range includes the conclusions of Stallings and Wilcox (1987). The reason for the wide range in L/D ratio for the different classifications is due to other factors that affect the mean Cp distribution. These factors are the width of the cavity as well as the free stream Mach number. Figure 1-3 shows the effect of varying the width or varying the Mach number. Increasing the width of the cavity or increasing the Mach number of the free stream widens the range of L/D where the cavity is defined as transitional. Increasing Mach number may cause a cavity classified as closed or open for a given width to become transitional as the Mach number is increased. Increasing the width may cause a cavity classified as transitional or closed to become open or transitional as the width is increased. Stallings et al. (1995) reported similar results for increasing Mach. Chung (2000) reported similar results for increasing cavity width.

Dix and Dobson (1990) conducted an investigation to record the pressure, force, and trajectory data for several contemporary missile configurations in the presence of a

simple flat plate and cavity model. As part of their investigations, the centerline mean Cp distribution was recorded when no stores were present in the cavity. They proposed the classification of the cavity as open when the L/D ratio was less than 9, closed when L/D is greater than 13 and transitional when between 9 and 13. The experiment was completed in two tunnels located at Arnold Engineering Development Center. Tunnel 4T was used for Mach 0.6 to 2.0. Tunnel A was used for Mach 2.0 to 5.0. L/D was 4.5, 9.0, and 14.4. W/D was 1, 2, and 3.3. These ratios were investigated in both tunnels.

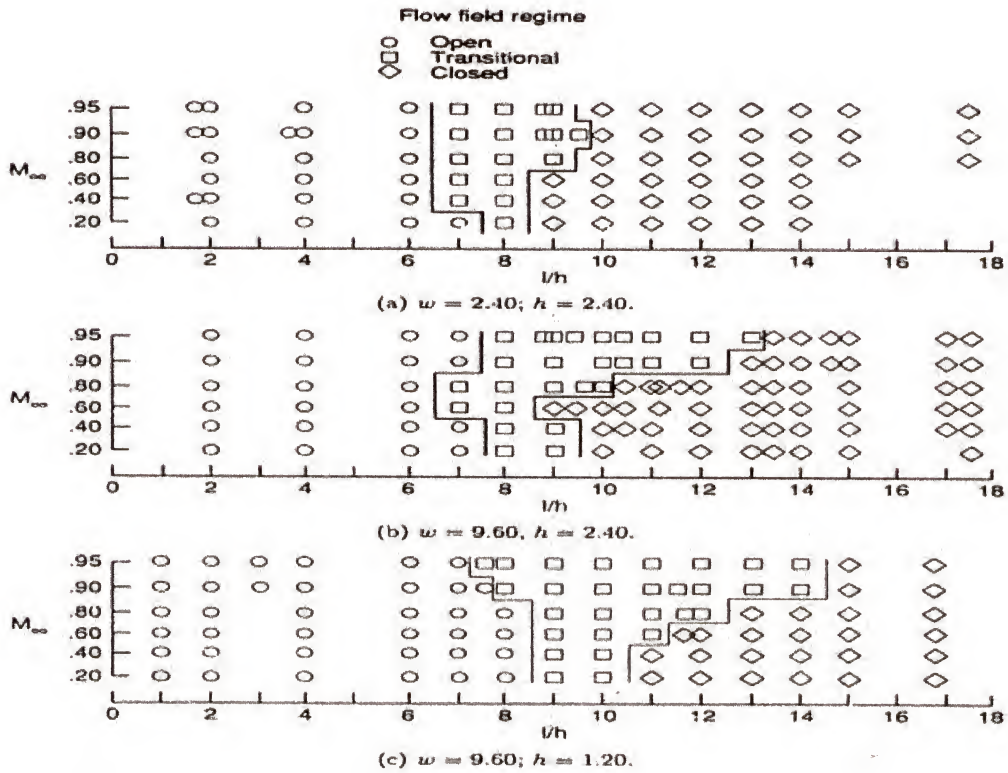

Figure 1-3 Effect of geometry and Mach on cavity classification

Chung (2000) studied the effects of L/D, L/W and D/δ_o on a rectangular cavity at a Mach number of 1.28 and Reynolds number base on the incoming boundary layer thickness of 2.1×10^5. The boundary layer was allowed to develop naturally over a flat plate ahead of a rectangular cavity and was measured at 7.0 mm just ahead of the cavity.

His plots of mean pressure coefficient on the floor of the cavity at the various L/D tested agree with the classification criteria shown in Figure 1-2.

These investigations were restricted to measuring the surface pressure. In order to understand what was going on in the cavity, various forms of flow visualization were used. An experiment not previously mentioned was done by Shchukin et al. (1980). The original intent was to investigate the influence of the depth of the cavity and Reynolds number on heat transfer in cavities in compressible gas flow. The Mach was 4.5 with a L/D and W/D range of 1 to 5 for each. A specially prepared composition was spotted on the surface of the cavity. The tunnel was activated and observations of the spreading of the droplets were made through the viewing window. As soon as the spreading terminated, the tunnel was turned off and prints were taken. A symmetrical vortex at L/D of 1 was found. As L/D was increased to 2, the vortex became unsymmetrical. Further increase in L/D split the single vortex into two vortices with the aft vortex stronger and center above mid section of cavity. The aft vortex was found to decrease in intensity as L/D approached 5. Steady state prints were the only flow visualization results available.

Rossiter (1964) took Shadowgraph at random time intervals. He then put the photographs in what he thought to be a correctly timed sequence and reconstructed the flow pattern. His conclusion was that these Shadowgraph did not show what was happening inside the cavity.

Schlieren photographs were able to identify the existence of exit and impingement shocks (Stallings and Wilcox, 1987). The Schlieren photographs were used in conjunction with the mean pressure distribution to classify the cavities. Other flow

structures were not identified nor were any conclusions about the unsteadiness of these flow structures made.

Schlieren and vapor screen methods were also used in the subsonic investigations (Plentovich 1990, Plentovich et al. 1991, Plentovich et al. 1993). These methods did not reveal any useful information on the type of flow field for the Mach number range of the subsonic and transonic test. These visualization methods were primarily used to identify the presence of shocks and to determine if the shocks reflected off the tunnel walls into the cavity therefore invalidating the data. For the range of Mach number, it was found that no shock waves from the model leading edge were reflected from the tunnel wall into the cavity region at any Mach number tested.

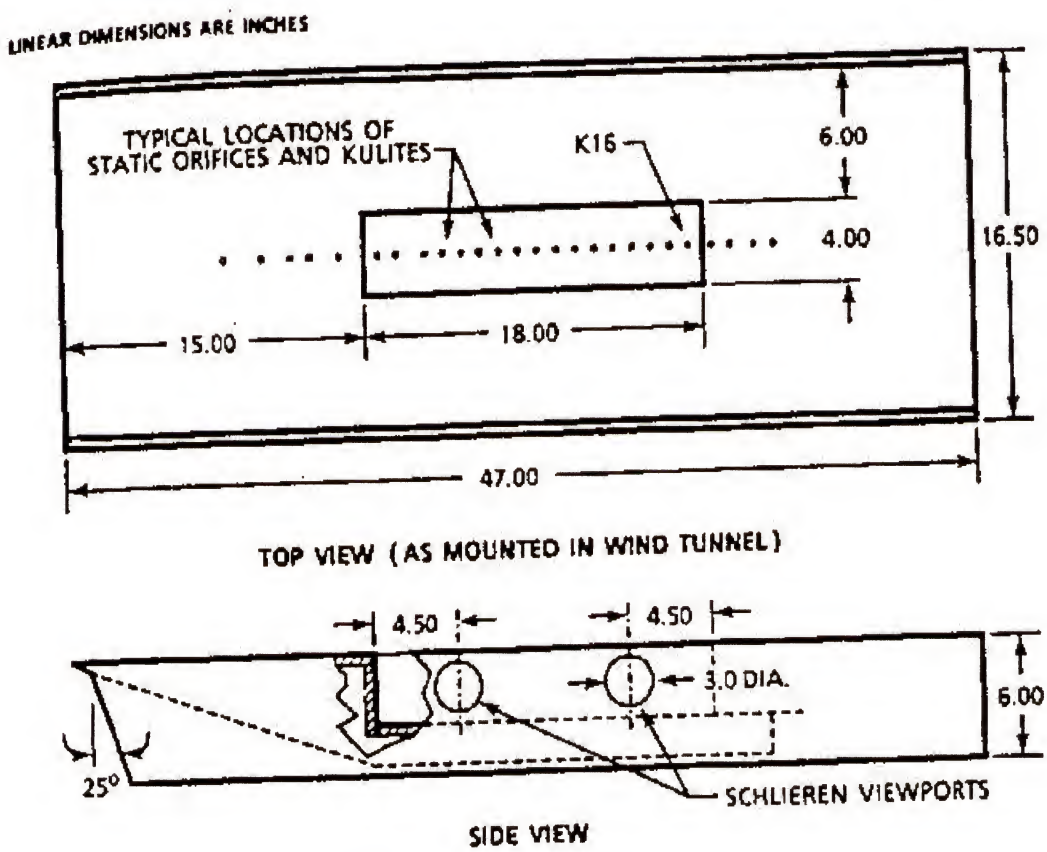

Figure 1-4 Schlieren View Ports

Dix and Dobson (1990) used the Schlieren technique in Tunnel A and recorded at 4000 frames/sec for selected test conditions. No statement in the report was made as to the use of the recordings. The tapes were made available by AEDC and were reviewed. Figure 1-4 shows where the Schlieren view ports were located with respect to the cavity. The flow as seen through the view ports was the only high speed Schlieren for the experiment. Identifiable structures (vortices, shock and expansion waves, shear layers etc.) were not visible on the high-speed recordings. The flow ahead and above the cavity was also recorded using Schlieren but at normal camera speed. No unsteadiness in shocks or expansion waves was observed. Schlieren were not available in the 4T tunnel. No other form of flow visualization was used.

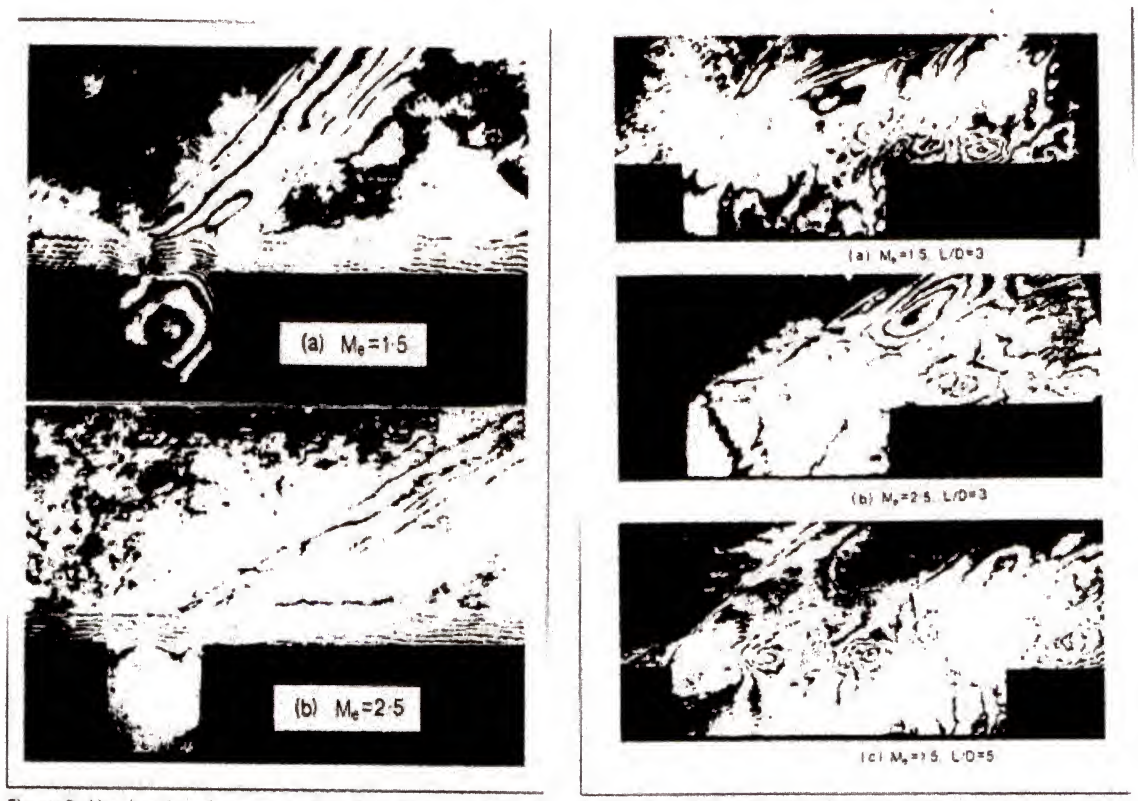

Figure 3. Absolute interferograms of the flow field with L/D = 1

Figure 11. Differential interferograms demonstrating the shea layer deflection due to the convection of large vortical structure (a) ΔT = 10 μs, (b) ΔT = 50 μs, (c) ΔT = 200 μs.

Figure 1-5 Absolute and Differential Interferograms

Zhang and Edwards (1990) used holographic interferometry to observe the flow field and to make density measurements. Both absolute and differential holographic interferograms were taken. Figure 1-5 shows some of the results published in 1990. Absolute interferograms were able to show shocks, vortices and shear layer. The absolute interferograms demonstrate that the flow is unsteady indicated by the different position of the flow structures at different times during the test for constant free stream conditions. However, they did not present a time history of the flow structures. Zhang and Edwards (1990) claim that the differential interferograms demonstrate the oscillation of the flow field as well as the motion of the vortical structures. It is unclear how this was done from the data shown in the report. Zhang and Edwards (1992) used the same method when investigating the flow over cavities in tandem. The same types of results were reported.

1.2.2 Computational Investigations

Numerous studies have been undertaken to computationally analyze the flow in rectangular cavities. The process was first to set up the computation, run a test case and compare the results to a previous experimental investigation, and then use the "validated" computational code to perform the analysis. The majority of the papers found concentrated on trying to find a code that would duplicate a past experimental result when comparing the calculated mean and fluctuating pressure with past experimental results. Only two of the papers actually used the codes after comparison to analyze the effects of cavity geometry (Zhang et al., 1998a, and Zhang et al., 1999).

Hankey and Shang (1979) obtained numerical solutions of the Navier-Stokes equations for an open cavity. They argued that sufficient experience from extensive

measurements exists so that a qualitative description of the flow process can be obtained. However, a quantitative prediction method did not exist which was the motivation for their investigation. The test conditions of Heller and Bliss (1975) were selected to compare the numerical results. Comparison was restricted to the velocity profile immediately upstream and downstream of the cavity. However, this comparison was good.

Baysal and Stallings (1987) investigated unsteady flow over the same set of cavity geometry and free stream conditions from the experimental investigation of Stallings and Wilcox (1987). Comparison of computational results was restricted to the mean surface pressure coefficient on the forward and aft wall as well as the floor of the cavity. Based on the computational results, they were able to plot streamlines, Mach number contours, and density contours for flow in and above the cavity. These results were not compared to experimental results.

Rizzetta (1988) investigated unsteady flow over a three dimensional cavity at a free stream Mach number of 1.5 and Reynolds number of $9.0 * 10^6$ /m. Quantitative comparison with experimental data (Rossiter 1964) was made in terms of mean static pressure, overall acoustic sound pressure levels, and acoustic frequency spectra within the cavity. While most of the comparison is favorable, the numerical solution appeared to over predict the amplitude of the harmonic frequencies.

The purpose of a study by Fuglsang and Cain (1992) was to investigate the basic mechanisms of the shear layer-cavity acoustic interaction and to examine how shear layer forcing affects the cavity acoustic environment. Computation was restricted to two dimensions. Test case was from Rossiter (1964) and consisted of Mach 0.85 flow over a

L/D = 4 cavity at a Reynolds number of 7.55 * 10^6 /m. Comparison of results was restricted to mean surface pressure coefficient and predicted acoustic frequency. Plots of vorticity in and above the cavity were provided. No comparison of these plots to experiment was provided.

Zhang (1995) focused on trying to duplicate the wind tunnel test case from Zhang and Edwards (1990). The focus of the study was to investigate a turbulent flow over an open cavity at supersonic speeds. Attention was focused on a time averaged surface pressure for better cavity drag estimation, narrow band tones, and shock wave and expansion wave interaction for noise radiation predictions. Comparisons of computational results were restricted to mean and fluctuating surface pressure measurements.

Zhang et al. (1995) used computational methods to study the far field noise radiation from an unsteady supersonic cavity flow. It was found in a previous experimental investigation (Zhang and Edwards 1990) that the flow was influenced by unsteady modes at 2645 Hz, 5900 Hz (dominant mode), and 9153 Hz for Mach = 1.5. At Mach = 2.5, the values were 3467 Hz, 6787 Hz, and 10450 Hz (dominant mode) respectively. These compared with the predicted values of 2651 Hz, 5459 Hz and 10450 Hz at Mach = 1.5 and 3408 Hz, 6667 Hz, and 9927 Hz at Mach = 2.5. Numerical instantaneous interferograms were shown in the report. A statement that the interferograms were similar to those obtained experimentally was made but was not elaborated on. Comparison to surface mean and fluctuating pressure was not presented.

Zhang and Edwards (1996) studied the effect of length scale, computational grid and time scale of supersonic flow over a cavity. Results were compared to Zhang and

Edwards (1990). Comparison consisted of the mean pressure distribution on the surface of the cavity. They plotted density contours and streamlines of the flow in and above the cavity. No comparison of the flow solution in and above the cavity was made.

Takahura et al. (1996) investigated supersonic internal flows with a cavity by solving the two-dimensional Navier-Stokes equations and large eddy simulation (LES). The main purpose of the study was to clarify by means of numerical simulation the physical mechanics of supersonic flow field about a two-dimensional rectangular cavity including behavior of the vortex, the oscillations of the shear layer, and shock motion. This was a combined computational and experimental investigation. Comparison of the results of computation was to a Schlieren flow visualization of the shock structures. No comments as to how well the computational results agreed with experiment. They did plot streamlines and density contours for flow in and above the cavity. No comparison of these internal flow variables was provided.

Sinha et al. (1997) attempted to identify the most appropriate parts necessary for accurate simulation of cavity flow, which takes cognizance of the coupling between cavity acoustics and vortical turbulent structures. An assessment of which turbulent model was best to use (VLES, RNS-based two equation $k\varepsilon$ and $k\omega$ turbulence models, and RNS-based algebraic Baldwin-Lomax turbulence model) along with unstructured grid methodology completed their objectives. Test cases were taken from the AEDC Weapons Internal Carriage and Separation (WICS) database (Dix and Dobson 1990). Free stream conditions consisted of Mach 2.0 flow at a Reynolds number of $9.84 * 10^6$ /m and three cavity geometry defined by L/D ratios of 4.5, 9.0, and 14.4. Comparison to experiment was the mean pressure coefficient along the surface of the cavity.

Zhang et al. (1998a) studied the effect of modifying the trailing edge (face) of a baseline rectangular cavity using wedge and ramp shapes to investigate means for the suppression and attenuation of the self-sustained oscillation. Zhang et al. (1999) studied the effect of modifying the leading edge by using compression ramps, expansion surfaces, and mass injection. Baseline case for model comparison was taken from Zhang and Edwards (1990) and consisted of Mach 1.5 flow over a cavity with L/D = 3. Reynolds number was $30.0 * 10^6$ /m. Comparison to experiment was mean surface pressure coefficient and frequency of the first mode of the cavity. These comparisons were good. Plots of the density in and above the cavity were also provided but were not compared to any experimental results.

Zhang et al. (1998b) investigated supersonic flow over a shallow cavity at Mach 1.5 and 2.5. L/D of the cavity was 3 and free stream Reynolds number was $30.0 * 10^6$/m. Objective of the investigation was to identify the types of shock/pressure waves around the cavity. Computational Schlierens were produced from the computations. This was compared to experimental Schlierens taken during the experiment. Five types of waves were identified: a leading edge shock-expansion wave caused by the shear layer deflection; upstream propagating pressure wave inside the cavity; the shock wave associated with the rolling-up of large vortex in the shear layer and convected downstream; the shock wave generated by the periodic interaction between the shear layer and trailing edge; and the quasi-stationary waves immediately downstream of the trailing edge. Qualitatively, there was good agreement.

Zhang and Edwards (1999) investigated computationally the flow over a dual-cavity cascade at supersonic speeds. Mach was set at 1.5 and 2.5. Leading cavity had an

L/D of 3 and 1. The trailing cavity was set at L/D of 1. Reynolds number of the flow was 30 $*10^6$ /m. Comparison was to previous experimental investigation of supersonic flow over two cavities in tandem (Zhang and Edwards, 1992). Comparison of the computational results consisted of comparing the mean pressure distribution on the surface of the cavities to those measured in the experiment. Pressure fluctuations were plotted in eh frequency domain but were not compared to experiment. Instantaneous plots of density were also shown but no comparisons were made

Lillberg and Fureby (2000) compared the use of LES and Smagorinsky (SMG) turbulence models over a three dimensional cavity embedded in an arc-shaped body at Mach of 1.5. L/D ratio was 2 and Reynolds number was 30.0 * 10^6 /m. No comparison to any experiment was provided. Only a comparison between the results using the two different turbulence models was provided. Mach contours in and above the cavity were plotted.

Rona and Dieudonne (2000) investigated two-dimensional Mach 1.5 flow over L/D = 3 cavity. Reynolds number was set to 30.0 * 10^6 /m. These conditions are similar to the conditions investigated by Zhang and Edwards (1990). However, the approaching boundary layer thickness was not identical. No comparison of the computational results to experiment was provided. The objective was to investigate the effect of grid size on the aerodynamic resonance, which is observed in the wall pressure and numerical Schlieren predictions. Only comparison of results at different grid size was presented. Computational Schlieren was produced similar to that produced by Zhang et al. (1998b).

Ashcroft and Zhang (2001) using computational methods investigated far field noise radiated by low speed unsteady flows over plain cavities. Test cases of Mach 0.26

to 0.53 over cavities with L/D ratios of between 1.5 and 3.75 with a Reynolds number lying between 115591 and 587528 based on cavity length. These correspond to cavities investigated by Ahuja and Mendoza (1995). However, comparison was accomplished using data from Rossiter (1964). Comparison was for the Mach 0.53 over L/D = 3.75 test case versus the Rossiter data of Mach 0.50 over a cavity of L/D = 4. Other comparisons to experiment consisted of the Strouhal Number with that reported by Ahuja and Mendoza (1995). Instantaneous density contours were shown for Mach 0.53 over L/D = 3.75 test case. No comparison of density contours with experimental results was presented.

Shieh and Morris (2001) studied the near field unsteady hydrodynamics and acoustics of two and three-dimensional cavity flows using computational aero acoustics and unsteady Reynolds Average Navier-Stokes (RANS) simulations. Test cases consisted of L/D = 4.4 and free stream Mach of 0.6. This test case was similar to that reported by Plentovich (1990). However, the Reynolds number was reduced to a sixth of that reported. Computational results were compared to the mean surface pressure coefficient found in Plentovich (1990). Comparison was fairly good with the exception at the aft end of the cavity. Here, neither the two or three-dimensional results agreed very well with the experimental results. Density contours were plotted but no comparison was provided.

Numerous studies have been undertaken to computationally analyze the flow in rectangular cavities. All solved some form of the averaged Navier Stokes equations. Use of turbulence modeling varied from single equation Baldwin Lomax to two equations k-ε and k-ω models to Large Eddie Simulation (LES). Varying degrees of success were

shown when compared to experimental data. This comparison was limited to the mean surface pressure distribution on the centerline of the floor of the cavity or the pressure fluctuations after a transformation to the frequency domain was made. Experimental data for comparison was obtained from previous experimental investigations or the computational studies included a separate experiment to obtain data for the comparison such as Takahura et al. (1996). The mean pressure distribution and pressure oscillations on the surface of the cavity are the only experimental data available for comparison with computational results.

All the computational studies were able to plot the flow variables in and above the cavities that were calculated by the various models. Typical plots were of the density, pressure, Mach, and the streamlines. These plots were able to show that the flow is unsteady but there was no mention of the validity of the plots. In addition, there was no data with which to compare the results. In doing the literature review, a comparison of computed flow variables in and above the cavity with experimental data was not found.

1.3 Summary

Flow structures such as shock and expansion waves, shear/mixing layers, and vortices are generated as a result of flow over cavities. When the free stream conditions are in the transonic range (Mach $\approx$ 0.8) only shear/mixing layers and vortices are present. The results of past experimental and computational studies have resulted in identifying the existence of these flow structures in and above the cavity. Flow structures have been identified for discrete times and do show the unsteadiness of the flow as the position of the flow structures varies for the different discrete times with the free stream conditions and cavity geometry remaining constant.

Experimental investigations have measured the pressure distribution on the surface of the cavity. They have been able to calculate a mean pressure distribution as well as the pressure fluctuation. Classification of the cavity as open, closed or transitional is based on the mean pressure distribution. Experimental investigations have also shown that this mean pressure distribution and therefore the classification of the cavity are a function of the geometry (L/D and W/D) and the free stream (Mach and Reynolds number). Flow visualization provided some insight into the location and movement of compression and expansion waves for supersonic free stream conditions since the density gradients in and above the cavity were large enough to be recorded. When free stream conditions were of the subsonic and transonic type, flow visualization provided no additional information on the flow in and above the cavity. This short fall was addressed via computational methods.

Computational investigations have been able to obtain and plot a solution of not only the mean pressure distribution and pressure fluctuations but also a plot of the internal flow in terms of the traditional flow variables of density, pressure, Mach, and streamlines. However, the internal flow computations can not be validated since no experimental data exists for the comparison. The problem is further compounded by the fact that the traditional methods of inserting a probe or wire to measure density, pressure or temperature disrupt the flow that you are trying to measure. Inserting an intrusive device into a cavity alters the flow in and above the cavity. Therefore, what is measured is not the flow over the geometry of interest but a different geometry.

The relationship of the flow structures and their position in the cavity with the surface pressure distribution and hence the classification is unknown. The temporal

environment in and above the cavity is unknown and there currently exists no way to measure the flow in a time accurate manner other than to insert probes and/or wires. Insertion of probes and wires in and above the cavity alters the flow that needs to be measured. There is a lack of quantitative data in and above a cavity. This prevents interpretation of the flow behavior in and above the cavity and the influence this flow behavior has on the mean and fluctuating surface pressure.

1.4 Scope of Present Research

Flow in and above cavities generates different flow structures. The position and movement at any one time of these structures in and above the cavity influences the pressure distribution on the surface of the cavity. In order to interpret the flow behavior in and above the cavity and the influence this flow structure behavior has on the surface and internal pressure, certain capabilities in the area of flow measurement are required. First is needed a capability to identify the structures and track them both spatially and in time. Second, one needs to be able to measure or derive from the flow measurement the pressure not only of the surface but also in and above the cavity. This measurement should have the same spatial and time coordinates as the flow structures. And third, the flow velocity distribution needs to be measured. Armed with this required capability, the influence of the structures on the surface and internal pressure can be analyzed as well as the upstream and downstream effects of the flow structures.

The objective of this research is to use a non-intrusive measurement technique to measure a property of the flow or a property of the environment from which a property of the flow can be derived. With an experimentally measured flow property, the research will identify the flow structures in and above the cavity, determine their movement and

interactions, and the impact of these interactions on the surface pressure distribution in the cavity. This research attempts to bridge the gap between past experimental and computational investigation. Table 1-1 summarizes past experimental and computational studies. Computational studies have concentrated on supersonic flows. Two subsonic studies were completed at small Reynolds number. Of the experimental work, all of them measured mean and fluctuating surface pressure. For subsonic flow, not much insight was provided into the cause of the mean and fluctuating pressure due to the limitation of flow visualization techniques.

For this research, transonic flow over open/open transitional cavities will be investigated. The proposed work will investigate cavities with L/D ratios of 4 and 8. The free stream condition will be set at Mach 0.8 and Reynolds number of $11.0 * 10^6$ /m. This investigation attempts to bridge past experimental and computational investigations. This bridge is shown in Table 1-1. At the top of the table is summarized the past experimental studies. Various free stream conditions and cavity geometries have been experimentally investigated. From the table, only two experiments were able to measure a flow property in and above the cavity, the instantaneous density distribution using Holographic Interferometry. At the bottom of the table is summarized the past computational studies. A great emphasis has been place on supersonic flow over cavities In between is the proposed research.

Table 1-1 Experimental and Computational Summary

EXPERIMENTAL							
	Mach	Re(/m)*106	L/D	W/D	Surface Measurement	Internal Flow Measure	Flow Viz
1. Rossiter (1964)	.5 - 1.2	7.2	2 to 10	.25 to 2.5	Mean & Fluct. Cp		Shadow Graph
2. Heller et al. (1970)	0.8 - 3.0	1.77 - 9.5	4 to 7	2.86	Mean & Fluct. Cp		Schlieren
3. Heller and Bliss (1975)	0.8 - 2.0	13.1 - 16.4	2.3, 4.0, 5.5		Mean/Fluct. Cp, BL velocity		N/A
4. Shchukin et al. (1980)	4.5	7.0 - 34.7	1 to 5	1 to 5	Mean & Fluct. Cp		Oil Droplets
5. Stallings and Wilcox (1987)	1.5-2.86	6.6	1 to 24	1 to 5	Mean & Fluct. Cp		Schlieren
6. Plentovich (1990)	.3-.95	3.3 - 13.1	4.4, 11.7	1, 2.67	Mean & Fluct. Cp		N/A
7. Dix and Dobson (1990)	.6-5.0	6.2 - 9.8	4.5, 9, 14.4	1, 2, 3.33	Mean & Fluct. Cp		Schlieren
8. Zhang and Edwards (1990)	1.5,2.5	30	1 to 9	7.6	Mean & Fluct. Cp	Instantaneous Density	Holographic Interferometry
9. Plentovich et al. (1991)	.2 - .9	6.6 - 32.8	4.4 to 20	.98 to 4.46	Mean & Fluct. Cp		N/A
10. Zhang and Edwards (1992)	1.5,2.5	30	1 to 9	7.6	Mean & Fluct. Cp	Instantaneous Density	Holographic Interferometry
11. Plentovich et al. (1993)	.2-.95	7.2 - 15.4	1 to 17.5	1 to 10	Mean & Fluct. Cp		Schlieren, Vapor Screen
12. Stallings et al. (1995)	.2 - .95	6.6 - 15.4	5.4 - 12.5	2, 4	Mean & Fluct. Cp		N/A
13. Chung (2000)	1.28	29.5	2.43 to 43	.5, 1.0, 2.0	Mean & Fluct. Cp		N/A
PROPOSED WORK	0.8	11	4, 8	8, 16		Instant. & Fluct. Density	Shack Hartman
COMPUTATIONAL							
	Mach	Re(/m)*106	L/D	Exp.	Surface Measurement	Internal Measure	Variable Comparison
1. Hankey and Shang (1979)	1.5	13.8	2.25	3	Velocity in BLs	vel., density	Velocity in BLs
2. Rizzetta (1987)	1.5	9.1	5.07	1	Mean & Fluct. Cp	vel., pressure	Mean & Fluct. Cp
3. Baysal and Stallings (1987)	1.5-2.86	6.6	1 to 24	5	Mean & Fluct. Cp	Mach, density, streamline	Mean & Fluct. Cp
4. Fugisang and Cain (1992)	0.85	7.5	4.5	1	Mean & Fluct. Cp	vor., density	Mean & Fluct. Cp
5. Zhang 1995	1.5, 2.5	30	3	8	Mean & Fluct. Cp	Mach, density, streamline	Mean & Fluct. Cp
6. Zhang et al 1995	1.5, 2.5	30	3	8	Fluct. Cp	-	Comp. Interferogram
7. Takahura et al. (1996)	1.83	-	1, 2, 3	Theirs	Mean & Fluct. Cp	vel., density, streamline	Comp. Schlieren
8. Zhang and Edwards 1996	1.5, 2.5	30	3	8	Mean & Fluct. Cp	density, streamline	Comp. Schlieren
9. Sinha et al. (1997)	2	9.8	4.5, 9, 14.4	7	Mean & Fluct. Cp	Mach, density, pressure	Mean & Fluct. Cp
10. Zhang et al. 1998a	1.5	30	3	8	Mean & Fluct. Cp	density	Mean & Fluct. Cp
11. Zhang et al. 1998b	1.5, 2.5	30	3	8	-	-	Comp. Schlieren
12. Zhang and Edwards (1999)	1.5, 2.5	30	1, 3	10	Mean & Fluct. Cp	vel.	Mean & Fluct. Cp
13. Zhang et al. 1999	1.5	30	3	8	Mean & Fluct. Cp	density	Mean & Fluct. Cp
14. Lillberg and Fureby 2000	1.5	30	2	none	N/A	Mach, vel.	N/A
15. Rona and Dieudonne 2000	1.5	30	3	8	Fluct. Cp		Comp. Schlieren
16. Ashcroft and Zhang 2001	0.26 - 0.53	.115 - .587	1.5 - 3.75	1	Mean & Fluct. Cp	density	Mean & Fluct. Cp
17. Shieh and Morris 2001	0.6	1.2	4.4	6	Mean & Fluct. Cp	vor., pressure, streamlines	Mean & Fluct. Cp

1.5 Contribution of Present Research

Successful completion of the present research will make the following contributions.

Demonstration that a flow property can be measured experimentally allowing the identification of flow structures in and above cavities. Using an existing flow measurement technique (Shack Hartman sensor), the density distribution in and above a cavity is measured with a spatial resolution of less than 0.5 mm and a time resolution of less than 10 microseconds. At a free stream Mach number of 0.8, four frames of data spaced 10 microseconds apart provide identification of the position and movement of the shear/mixing layer, the position and movement of large scale structures in the

shear/mixing layer, and the position and movement of the large scale structures in the cavity.

A pressure distribution is found by making some simplifying assumptions concerning the temperature distribution. Along with the assumed temperature distribution and the measured density distribution, the pressure distribution near the floor of a cavity and in and above the cavity can be found. While the pressure on the surface will not be known exactly, the spatial resolution of less than 0.5 mm will provide insight into the distribution near the surface and the impact the flow structures have on this distribution. Now that the location and movement of the flow structures and an estimate of the pressure on the surface of the cavity are known, an analysis of the impact of the position, movement, and interaction of these flow structures has on the surface pressure is accomplished. The position and movement of individual flow structures in a time accurate manner is known. An ability to estimate the surface pressure distribution from the density distribution is made by estimating the surface temperature based on the known free stream temperature. With this assumption and a known density very near the surface (< 0.5 mm), an estimate of the surface pressure coefficient distribution can be made. The position and movement of the flow structures is compared to the pressure coefficient on the surface. The impact the flow structure position, movement and interaction on the pressure in and above the cavity is also accomplished.

The same technique used to analyze the behavior in and above the cavity can also be used to analyze the behavior upstream and downstream of the cavity as well as in and above.

CHAPTER 2
WIND TUNNEL

This chapter presents the two design options that were analyzed for providing Mach = 0.8 flow over a rectangular cavity. The first option was a shock tube using a diaphragm to start the flow of air. The second option was an in-draft tunnel using a quick opening butterfly valve to start the flow of air. Analyses are accomplished for both options. Results are compared to a set of selection criteria and a final tunnel configuration is presented along with the free stream flow properties obtained for the design.

2-1 Design Objective

The primary requirement is a time accurate recording of the flow in and above a cavity. It is anticipated that the use of optical diagnostic tools (to be covered in the next chapter) will be the primary method of recording the flow. The optical method is non-obtrusive and it can be coupled with a high-speed camera, which provides the necessary spacing between frames to get a time accurate evolution of the flow. Therefore, the test section needs to be able to accommodate the use of optical diagnostics. This implies that the test section and hence the tube must have a rectangular cross section. A cylindrical tube could be used but would make the use of optical diagnostics much more difficult.

A free stream Mach number of 0.8 at a Reynolds number of $10.0 * 10^6$ /m is required. The Mach number of 0.8 must be achievable in the test section for a period of

time large enough to accommodate the capability of the data recording/flow diagnostics equipment. A tunnel length of no more than 3.048 meters can be used. This is a physical restriction of the room where the shock tube/in-draft tunnel will be located.

2.2 Design Options

In order to cause air to flow, a pressure gradient needs to exist causing a fluid to move from the high-pressure side to the low-pressure side. There are a multitude of wind tunnel designs that can be used to cause this airflow such as continuous run, blow down/in-draft or shock tube. The shock tube and in-draft options were selected as potential candidates as the means to provide airflow over the cavity. The reason for this selection was the availability of a 5.66 m^3 tank that could be used as a low-pressure reservoir. A shock tube with a diaphragm system or an in-draft tunnel with a butterfly valve can be attached to this available tank. Figure 2-1 shows the two potential configurations. The remainder of this chapter describes the capabilities and characteristics of a shock tube and in-draft tunnel to provide airflow over a cavity.

2.2.1 Shock Tube

The shock tube envisioned is as depicted in Figure 2-1. Both ends of the tube are considered open to infinite reservoirs. The low-pressure reservoir is a 5.66-m^3 tank and the high-pressure reservoir is the room at atmospheric conditions. The initial pressure ratio (P4/P1, high to low, atmospheric to tank) and the location of the diaphragm determine the performance of the shock tube. By performance of the shock tube is meant the steady flow conditions available, the location of the steady flow conditions along the length of the tube, and the length of time these steady flow conditions are available. To use a shock tube, a diaphragm is placed somewhere along the length of the tube to isolate

Shock Tube Configuration

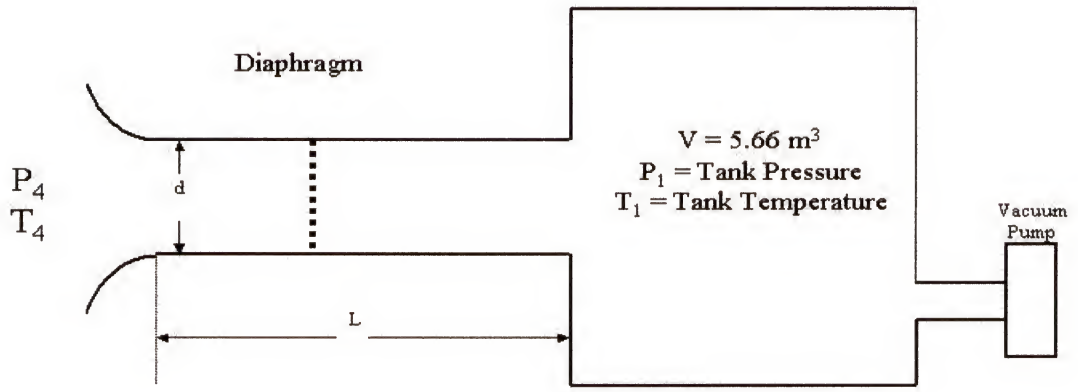

d = 0.0508 m

L = 3.048 m

In-Draft Configuration

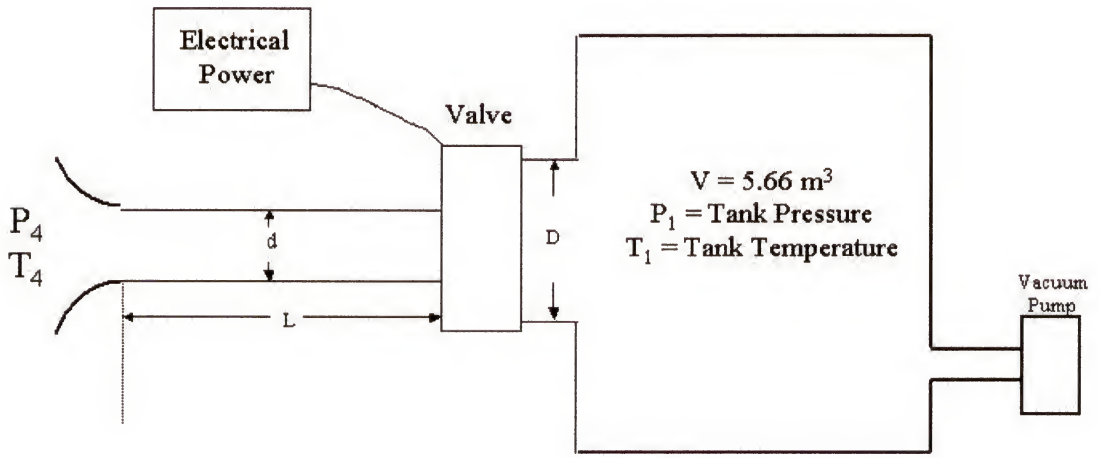

d = 0.0508 m
D = 0.2032 m
L = 3.048 m

Figure 2-1 Shock Tube and In-draft Tunnel Configuration

a high-pressure area from a low-pressure area. For this application, the low-pressure area is located on the tank side of the diaphragm. The pressure in the tank is reduced to a predetermined pressure that provides an initial pressure ratio P4/P1 that will provide the desired free stream conditions in the test section. The initial pressure ratio along with the initial temperatures is used to determine the performance of the shock tube.

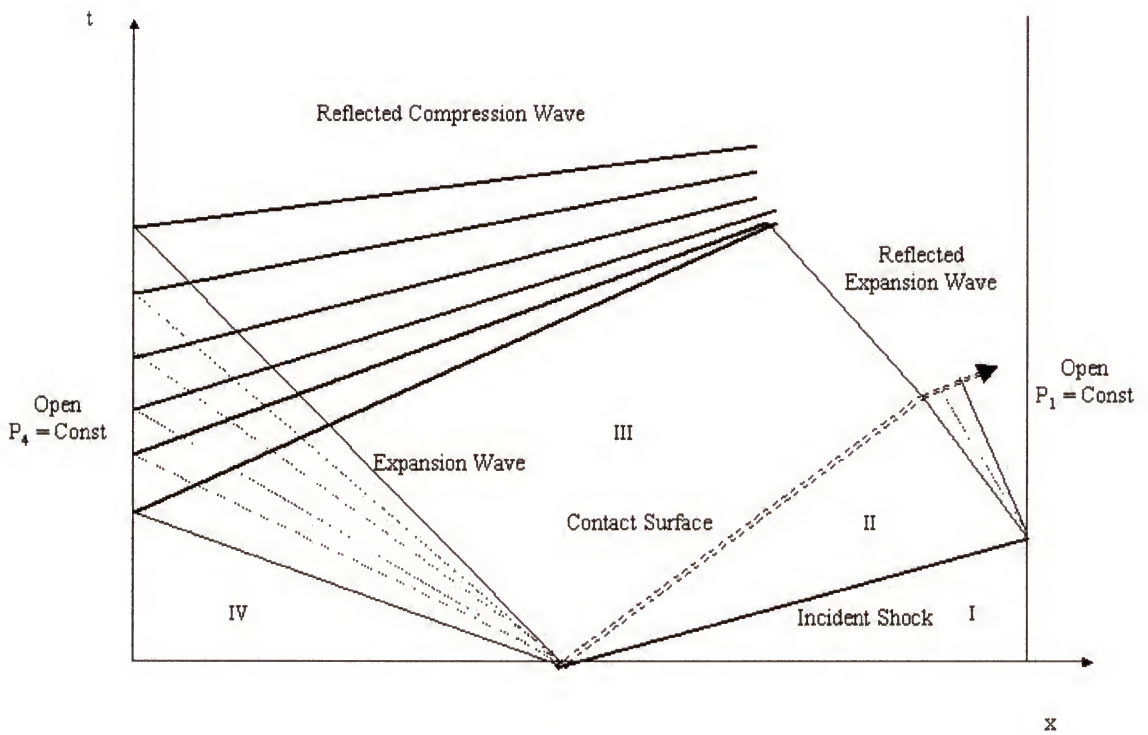

Figure 2-2 Notional x-t Diagram

To start the airflow, the diaphragm is ruptured. Figure 2-2 is a notional x-t diagram illustrating what happens in the shock tube when the diaphragm is ruptured. A normal shock wave moves into the low-pressure side with a series of expansion waves propagating into the high-pressure side. Following the initial normal shock wave down the tube is a contact surface, a temperature discontinuity separating the gases compressed by the shock from those cooled by the expansion. The gases in regions II and III move

with the same velocity and are at the same pressure, yet there is a density and temperature difference distinguishing these regions. The shock strength and gas velocities are dependent on the initial pressure ratio across the diaphragm, the properties of the gas and the initial temperatures. When the expansion wave reaches the open end of the tube, it reflects as a series of compression waves that eventually coalesces into a shock wave. The initial shock wave created by the rupture of the diaphragm arrives at the open end and reflects as an expansion wave. These reflected waves (compression wave from the high-pressure side and expansion wave from the low-pressure side) eventually meet again in the shock tube establishing the boundary for region II and region III.

The steps to calculate the flow properties for a shock tube and display the results on an x-t diagram are:

1. Calculate steady flow properties for region I, II, III, and IV.
2. Establish the upper left boundary for region III. This boundary is the original leading expansion wave that has reflected from the high-pressure open end and is returning as a compression wave. This reflected compression wave interacts with the remaining trailing expansion wave prior to forming one of the boundaries for region III.
3. Establish the upper right boundary for region II. This boundary is the original shock wave that has reflected from the low-pressure open end and is returning as an expansion wave. This reflected expansion wave forms the upper right boundary of region II. If the Mach in region II is greater than 1, there will be no reflection and the remaining boundary of region II will be the end of the tube on the low-pressure side.

4. If there is reflection from the low-pressure side, it will be an expansion wave. This leading expansion wave will interact with the contact surface and continue towards the high-pressure side meeting the reflected compression wave from the high-pressure side. This will form the upper right boundary for region III.

Steps 1 through 4 establish the steady flow properties (pressure, temperature, Mach, and speed of sound) in each region, the location of the steady flow properties along the length of the tube, when steady flow properties exist after the diaphragm has been ruptured, and the boundaries of regions II and III.

5. The last step is to determine the useable time when steady flow is present in the test section. Useable time is defined as when steady flow exists in the test section and no waves of any kind are present. This useable time must be large enough to allow the optical flow diagnostics equipment to record the required information.

The flow properties in region IV and I are either given as the initial conditions or can easily be calculated. For region I, the velocity V_1 is 0.0, the pressure P_1 can be found from the pressure ratio and the known value for P_4, the temperature T_1 is given and the speed of sound a can easily be calculated. Similarly, the properties in region IV are easily determined. The pressure and temperature are given, the velocity is 0.0, and the speed of sound is easily calculated.

$$\begin{aligned} V_1 &= 0.0 \\ P_1 &= P_4 \frac{P_1}{P_4} \\ T_1 &= Given \\ a_1 &= \sqrt{\gamma R T_1} \end{aligned} \qquad \begin{aligned} V_4 &= 0.0 \\ P_4 &= Given \\ T_4 &= Given \\ a_4 &= \sqrt{\gamma R T_4} \end{aligned} \qquad \text{2-1}$$

The flow properties in region II are determined by first calculating the pressure ratio between region II and region I. The pressure ratio, P2/P1, can be found by iteratively solving the following equation. (Owczarek, 1964 and John, 1984)

$$\frac{P_1}{P_4} = \frac{P_1}{P_2}\left[1 - \frac{\gamma-1}{2\gamma}\frac{a_1}{a_4}\frac{\left(\frac{P_2}{P_1}-1\right)}{\sqrt{1+\frac{\gamma+1}{2\gamma}\frac{P_2}{P_1}-1}}\right]^{\frac{2\gamma}{\gamma-1}} \qquad 2\text{-}2$$

Once the pressure ratio between region II and region I is known, the normal shock relationships can be used to find the Mach (M_s) and velocity (V_s) of the shock. (Anderson, 1991)

$$M_s = \left[\left(\frac{P_2}{P_1}-1\right)\frac{\gamma+1}{2\gamma}+1\right]^{\frac{1}{2}} \qquad 2\text{-}3$$

$$V_S = M_S\sqrt{\gamma R T_1} \qquad 2\text{-}4$$

Region II properties can now be calculated. The equation for the velocity in region II is developed in John (1984), and temperature is calculated using the normal shock relationships.

$$V_2 = \frac{2}{\gamma+1}\left(V_S + \frac{a_1^2}{V_S}\right) \qquad 2\text{-}5$$

$$P_2 = \frac{P_2}{P_1}P_1 \qquad 2\text{-}6$$

$$T_2 = T_1\frac{P_2}{P_1}\left[\frac{2+(\gamma-1)M_S^2}{(\gamma+1)M_S^2}\right] \qquad 2\text{-}7$$

$$a_2 = \sqrt{\gamma R T_2} \qquad 2\text{-}8$$

Following the normal shock wave down the tube is a contact surface, a temperature discontinuity separating the air compressed by the shock from those cooled by the expansion. The air in regions II and III move with the same velocity and are at the same pressure, yet there is a density and temperature difference distinguishing these two regions. The temperature and density for region III is calculated using the isentropic relationships that exist between region IV (known values) and region III.

$$\begin{aligned} V_3 &= V_2 \\ P_3 &= P_2 \\ T_3 &= T_4\left(\frac{P_3}{P_4}\right)^{\frac{\gamma-1}{\gamma}} \\ a_3 &= \sqrt{\gamma R T_3} \end{aligned} \qquad \text{2-9}$$

An initial pressure ratio (P4/P1) at constant temperature (T4 and T1) was iterated to find the required pressure ratio that would achieve Mach = 0.8 in either regions II or III. For a Mach of 0.8 in region II, a pressure ratio of 15.5 is required. For region III, a pressure ratio of 6.9 is required. This establishes the steady flow properties and the lower boundaries for regions II and III. Establishing the upper boundaries for these two regions is the next step.

The expansion wave proceeds toward the high-pressure open end. When the leading edge of the expansion wave reaches the open end of the tube, it reflects as a compression wave and interacts with the remainder of the trailing expansion wave. The initial wave reaching the open high-pressure side of the tube has the flow properties of region IV. This is necessary to satisfy the boundary condition that the pressure at the exit is P_4. The reflected compression wave will have an initial slope of $\frac{1}{a_4}$. This

compression wave interacts with the remainder of the trailing expansion wave ultimately forming the upper boundary of region III.

The Method of Characteristics (MOC) for one-dimensional unsteady flow (Hoffman and Zucrow, 1976) is used to calculate the flow properties on the reflected compression wave as it interacts with the trailing expansion wave. This establishes the series of points where the reflected compression wave interacts with the trailing edge of the initial expansion wave.

The shock wave that was created when the diaphragm was ruptured heads towards the low-pressure side and reaches the low-pressure open end of the tube. There are three possible outcomes when the shock wave reaches the open end of the tube. Depending on the boundary conditions at the low-pressure end of the tube, if the Mach in region II is subsonic, the shock wave will reflect either as a full expansion wave or only a portion will reflect and there will be sonic conditions at the exit. The third possibility is if the Mach in region II is greater than 1.0, there will be no reflection. (Rudinger, 1955, and Hoffman and Zucrow, 1976) If there is a reflected expansion wave, it will form a part of the boundary for region II. If the Mach in region II is less than 1, an expansion wave reflects from the open end. The leading edge of the wave has a slope of $1 / (V_2 - a_2)$. The flow properties along this characteristic will be the values from region II.

At this time, a reflected compression wave is coming from the high-pressure side, a reflected expansion wave is coming from the low-pressure side, and a contact surface is still moving towards the low-pressure end of the tube. There are two possibilities that may occur that will finalize the boundaries of regions II and III.

First, the reflected expansion wave from the low-pressure side will interact with the contact surface first and meet the oncoming compression wave. In this case, the boundaries for region II will be the shock wave, the contact surface, and the reflected expansion wave from the low-pressure side. The boundaries for region III will be composed of the contact surface, the trailing edge of the initial expansion wave, the reflected compression wave and the reflected expansion wave after it interacts with the contact surface. This possibility is depicted in Figure 2-2.

A second possibility is the reflected compression wave from the high-pressure side will interact with the contact surface and meet the oncoming reflected expansion wave. In this case, the boundary for region II will be composed of the shock wave, the contact surface, the reflected expansion wave form the low pressure side and the reflected compression wave from the high pressure side after it interacts with the contact surface. The boundaries for region III will be made up of the contact surface, the trailing edge of the initial expansion wave the reflected compression wave from the high-pressure side.

Which reflected wave interacts with the contact surface first needs to be determined. The time and position the reflected expansion wave from the low-pressure side interacts with the contact surface without interference from any other waves is calculated. The time and location the reflected compression wave from the high-pressure side interacts with the contact surface without interference from any other wave is calculated. Whichever time is smaller, that is the wave that interacts with the contact surface first. The slope of the appropriate wave after it interacts with the contact surface completes the calculations.

These calculations establish the boundaries for regions II and III on the x-t diagram. Where and when steady flow conditions exist in the shock tube are known. The last step is to calculate the useable time the free stream conditions are available in the test section.

The useable time must be large enough to allow the flow diagnostics equipment to record the required information when steady flow conditions exist in the test section without the presence of any type of waves. These waves include the initial shock wave, the contact surface, the trailing edge of the initial expansion wave, the reflected compression wave, and the reflected expansion wave. Useable time is defined as the difference between the start time when initially there are no waves in the test section and the end time when waves again appear in the test section. For the purpose of this analysis, a test section of 0.3175 meters in length is assumed.

Region II start time is after the initial shock passes the downstream edge of the test section but before the contact surface reaches the upstream edge. If the contact surface reaches the test section prior to the shock wave exiting the test section, by definition, there is no start time and therefore no useable time. The end time occurs when the contact surface reaches the upstream edge of the test section or the reflected expansion wave from the low-pressure side reaches the downstream edge, whichever occurs first. The difference between the start time and end time is the maximum useable time.

Region III start time is after the contact surface passes the downstream edge of the test section but before the trailing edge of the initial expansion wave reaches the upstream edge. If the trailing edge of the initial expansion wave reaches the test section prior to the

contact surface exiting the test section, by definition, there is no start time and therefore no useable time. The end time occurs when the trailing edge of the expansion wave or the reflected compression wave from the high pressure side reaches the upstream edge of the test section or the reflected expansion wave from the low-pressure side reaches the downstream edge, whichever occurs first. The difference between the start time and end time is the maximum useable time.

This establishes the methodology to calculate the free stream properties in a shock tube within region II and III with associated useable time based on a known initial pressure ratio (P_4/P_1), temperatures T_4 and T_1, and diaphragm location. That methodology will now be used to calculate the performance of the proposed shock tube. For this analysis, the tube length is assumed to be 3.048 meters. It is also assumed that the test section is 0.3175 meters in length. The exact placement of the test section along the length of the tube will be determined based on maximum useable time.

The pressure and temperature on the high-pressure side of the diaphragm are the pressure and temperature in the room where the shock tube is located. The 5.66 m^3 tank pressure and temperature are set so as to provide the initial pressure ratio and temperature. The tank is rated to 1 mm of mercury (0.133 KPa) of internal pressure. When the room is at atmospheric conditions of 101 KPa pressure and 294 ^oK temperature, a pressure ratio of up to 760 can be achieved. This maximum pressure ratio provides a maximum Mach of 1.37 in region II and 4.19 in region III. Figure 2-3 is a plot of the Mach in regions II and III as a function of the initial pressure ratio with the temperature T_4 and T_1 equal to 294 ^oK. Both regions II and III can meet the Mach requirement for the investigation.

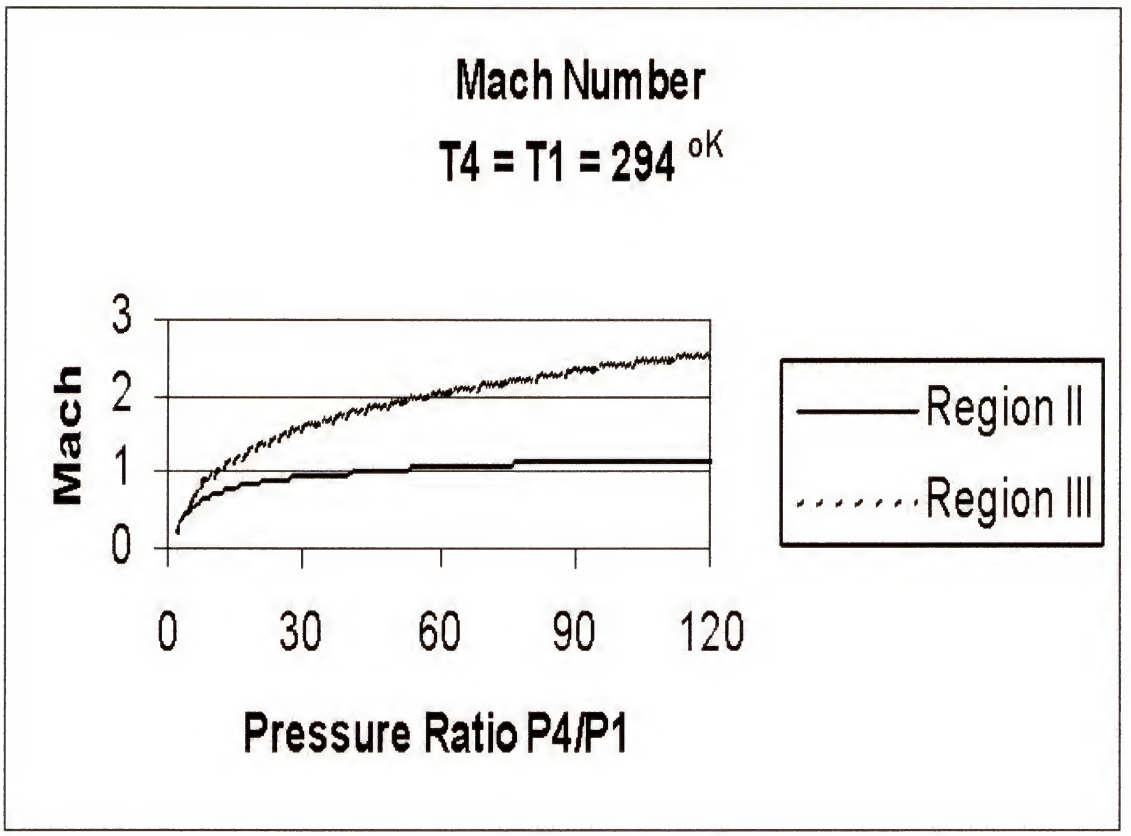

Figure 2-3 Shock Tube Mach Number

Equally important is the Reynolds number. In the shock tube, the Reynolds number is directly related to the Mach number. Mach number and Reynolds number can not be altered independently. Figure 2-4 shows the range of Reynolds number available as a function of Mach. Region III provides a range of Reynolds number on the order of the Reynolds numbers from previous experimental investigations. Region II provides a considerably lower Reynolds number.

Useable times were calculated using the previously described methodology. Of importance in calculating the useable times are the location of the diaphragm and the location of the test section with respect to the diaphragm. For this analysis, the diaphragm was located at three places; at a quarter, half and three-quarters of the length of the tube from the open high-pressure end. The center of the test section was

considered to be midway between the diaphragm and the open low-pressure tank. Figure 2-5 shows the available time when the test section is in region II as a function of Mach for three different diaphragm locations. Figure 2-6 shows the same thing for region III.

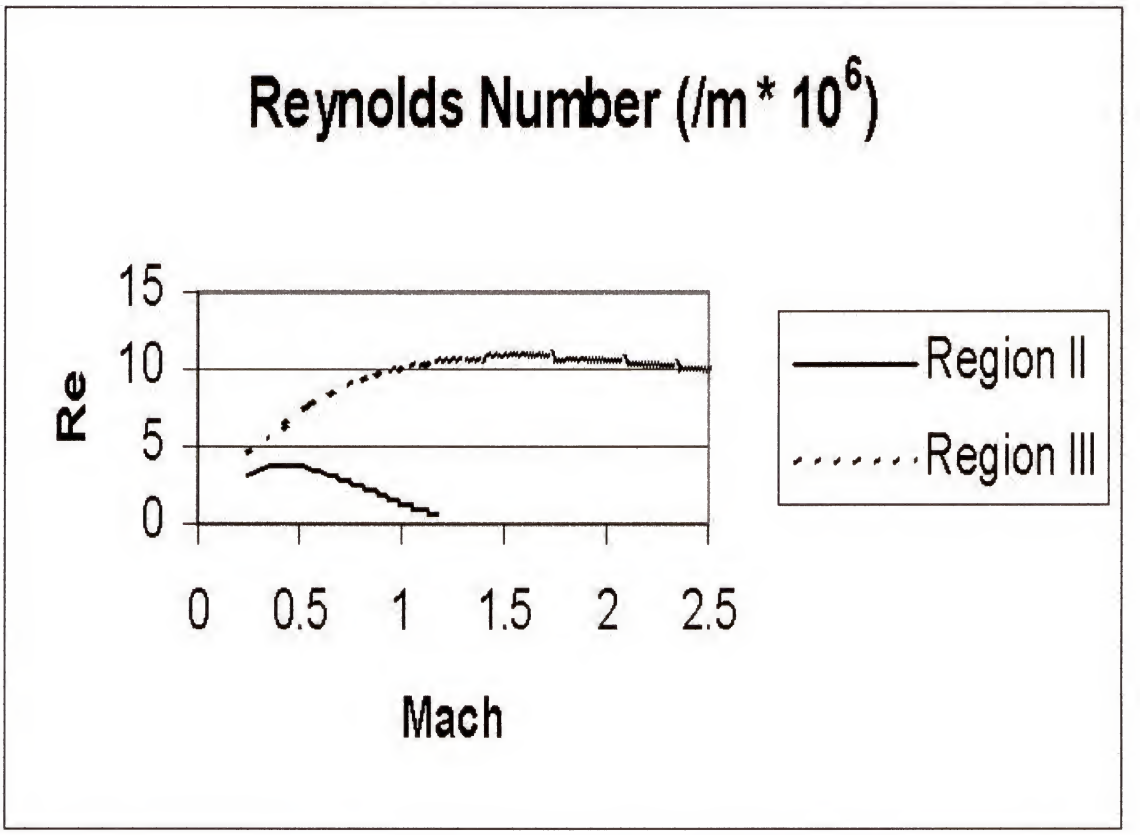

Figure 2-4 Shock Tube Reynolds Number

From Figure 2-5, maximum useable time for Mach 0.8 in region II is obtained when the diaphragm is placed a quarter of the way from the open high-pressure end. Figure 2-6 dictates that the diaphragm be placed midway along the tube to achieve Mach 0.8 in region III. Figure 2-7 shows the useable time for region II. The pressure ratio required for Mach = 0.8 in region II is 15.5. Figure 2-8 shows the useable time for the test section in region III. The pressure ratio required for Mach = 0.8 in region III is 6.9.

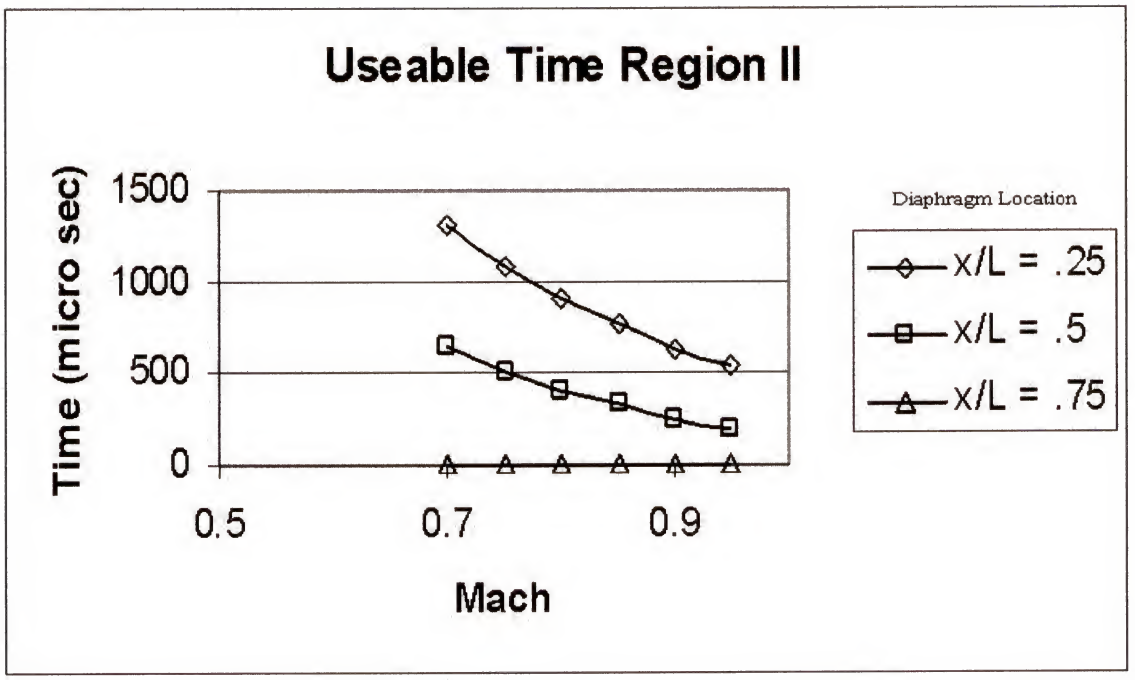

Figure 2-5 Region II Useable Time

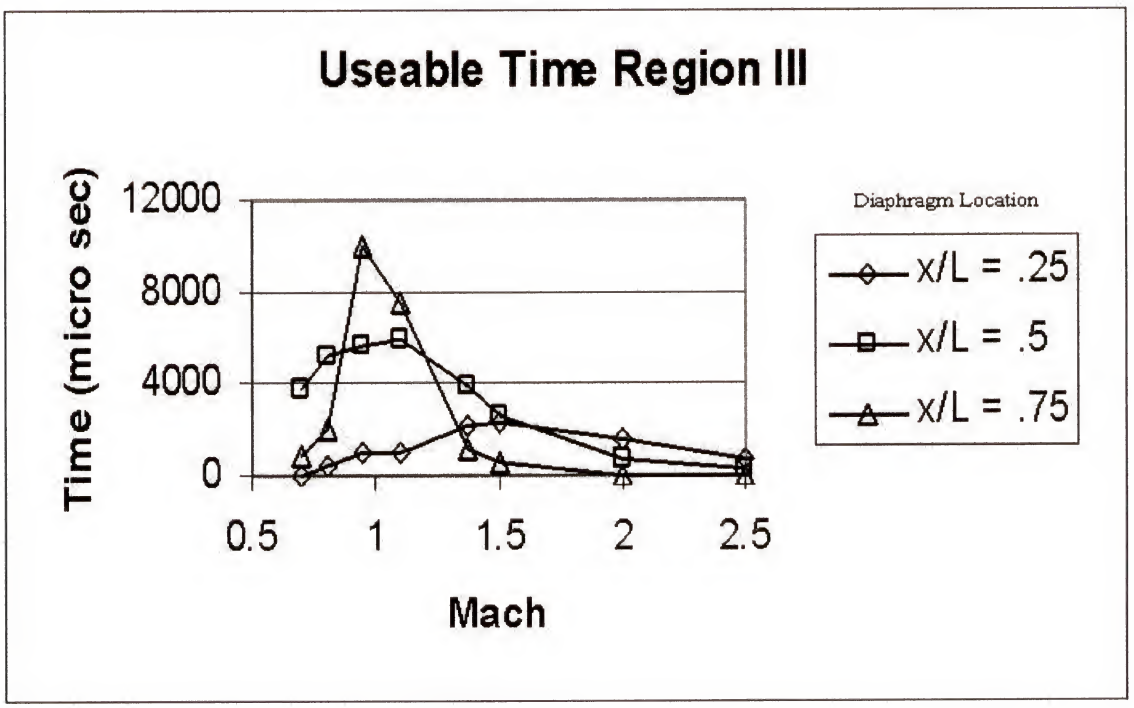

Figure 2-6 Region III Useable Time

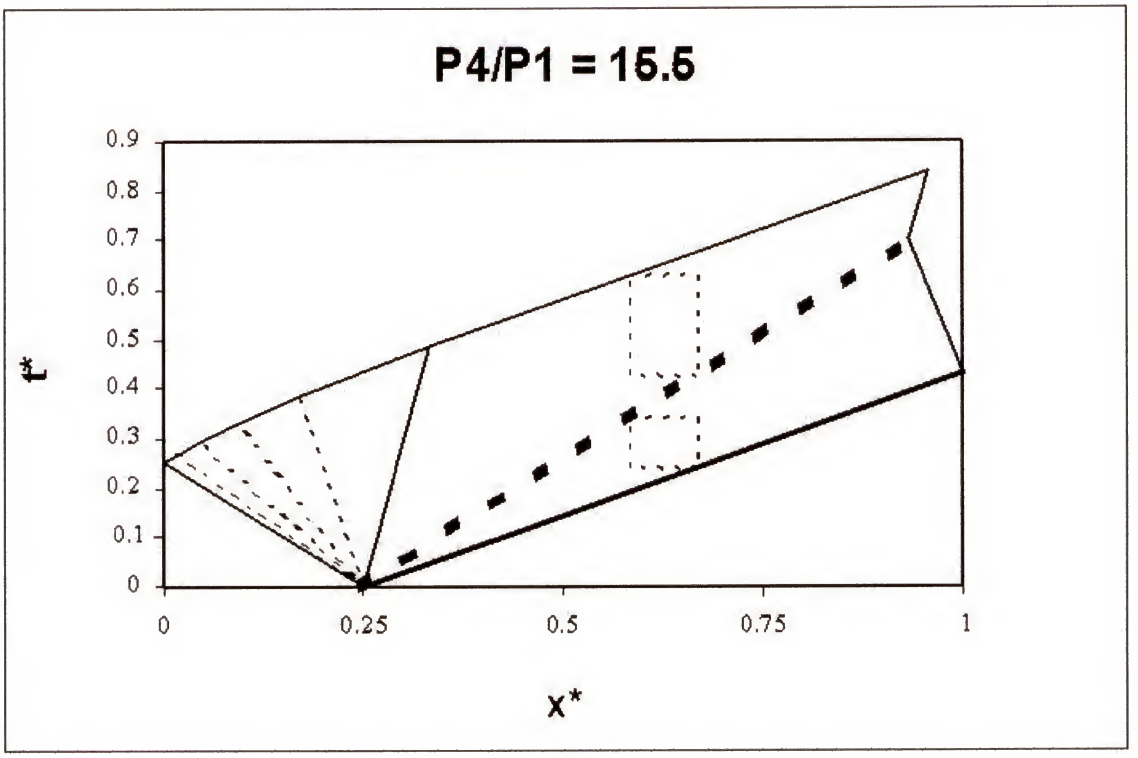

Figure 2-7 Region II x-t Diagram

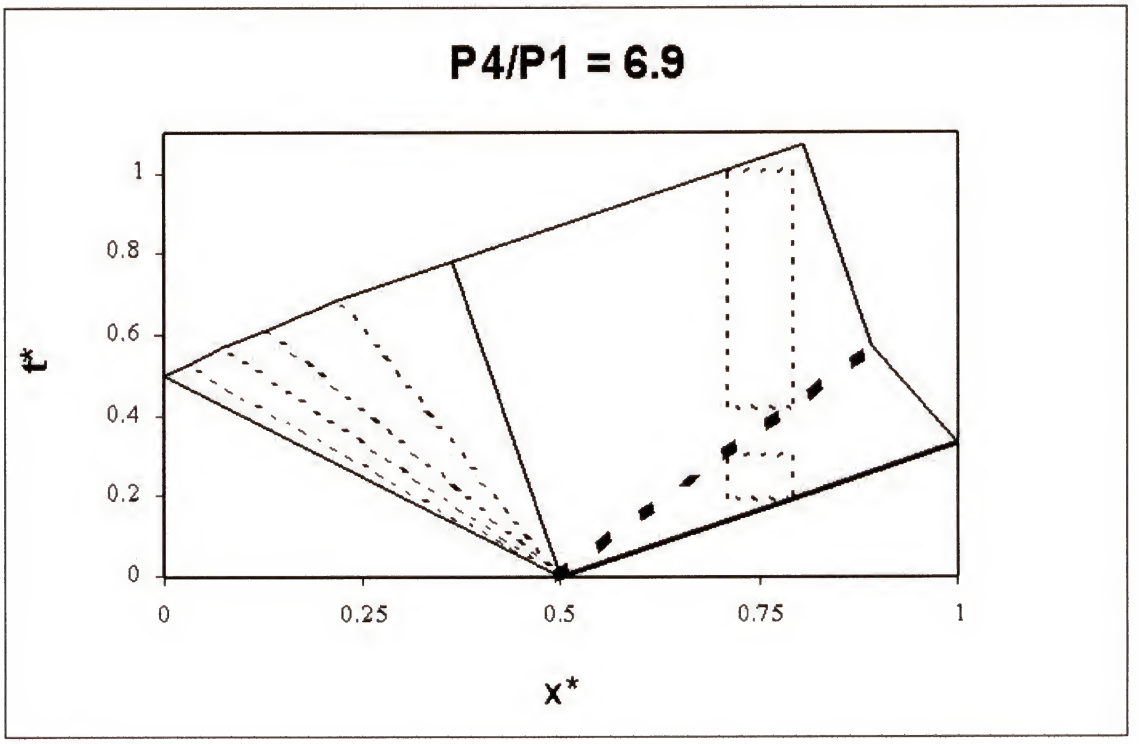

Figure 2-8 Region III x-t Diagram

Steady flow conditions can be reached in either region II or III. Region II gives the desire Mach of 0.8 and a useable time of 905 microseconds. However, because of the high temperature in region II, the available Reynolds number is only $2.42 * 10^6$ /m. On the other hand, region III produces the desired Mach of 0.8 for a much longer useable time of 5184 microseconds. The Reynolds number meets the requirements but the low temperature may not allow the use of this region since the test section may be obscured by fog. Therefore, a look at the flow properties in the tunnel when set up in an in-draft configuration is performed.

2.2.2 Choked Flow with Friction

An alternative to using a shock tube is to use the tank and constant area duct as an in-draft tunnel with a quick actuating butterfly valve for flow start up. An initial pressure ratio large enough to establish choked flow at the entrance to the tank can be set by reducing the pressure in the tank. As previously stated, this can be as low as 1 mm providing an initial pressure ratio of 760. Assuming a friction factor of 0.015, a minimum pressure ratio of 2.43 is required to establish choked flow in the tunnel. Increasing the ratio past this number still provides choked flow but for a longer period of time. The analysis was completed using a pressure ratio of 760 and a friction factor of 0.015. The butterfly valve is closed, the pressure in the tank is reduced establishing the initial pressure ratio, and the butterfly valve is opened to allow the air to flow into the tank. After a period of time, choked conditions will exist in the tunnel.

Using flow in a constant area duct with friction commonly referred to as Fanno flow the Mach number and the Reynolds number can be determined along the length of tunnel (Owczarek, 1964 and John, 1984). Figure 2-9 shows the Mach number along the

length of the tunnel. Figure 2-10 shows the Reynolds number available at these Mach numbers. At the maximum pressure ratio of 760, the useable time until the tube unchokes is 6.86 seconds. The Mach is achievable and the Reynolds number meets the requirement.

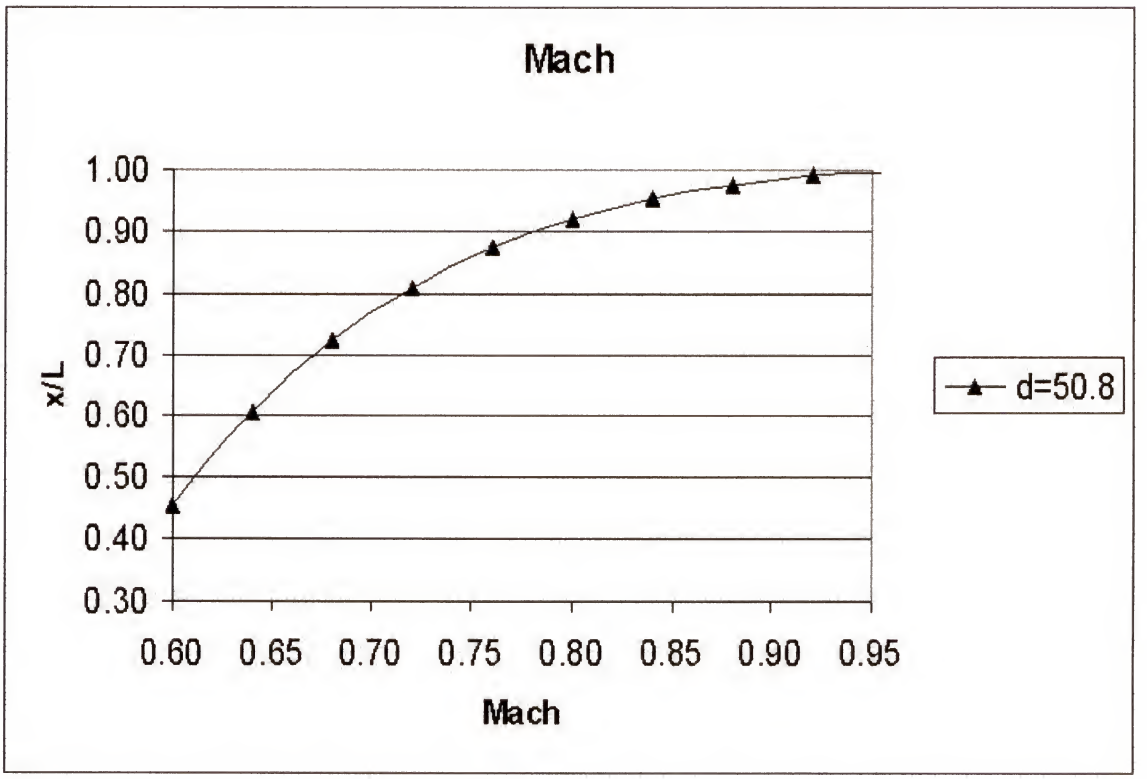

Figure 2-9 Mach Number Choked Flow

A comparison between regions II and II and the in-draft tunnel is shown in Table 2-1. Mach 0.8 can be achieved either by a shock tube for region II and III or by an in-draft configuration. Region II has the least amount of useable time and does not meet the Reynolds number requirement. Region III has two orders of magnitude more useable time and meets the Reynolds number requirement. The in-draft tunnel meets both the Mach and Reynolds number requirement plus it has the largest useable time for testing. In addition, it is much simpler to build and use a butterfly valve system as opposed to a

diaphragm system for airflow start up. Therefore, the in-draft tunnel option was selected as the testing apparatus.

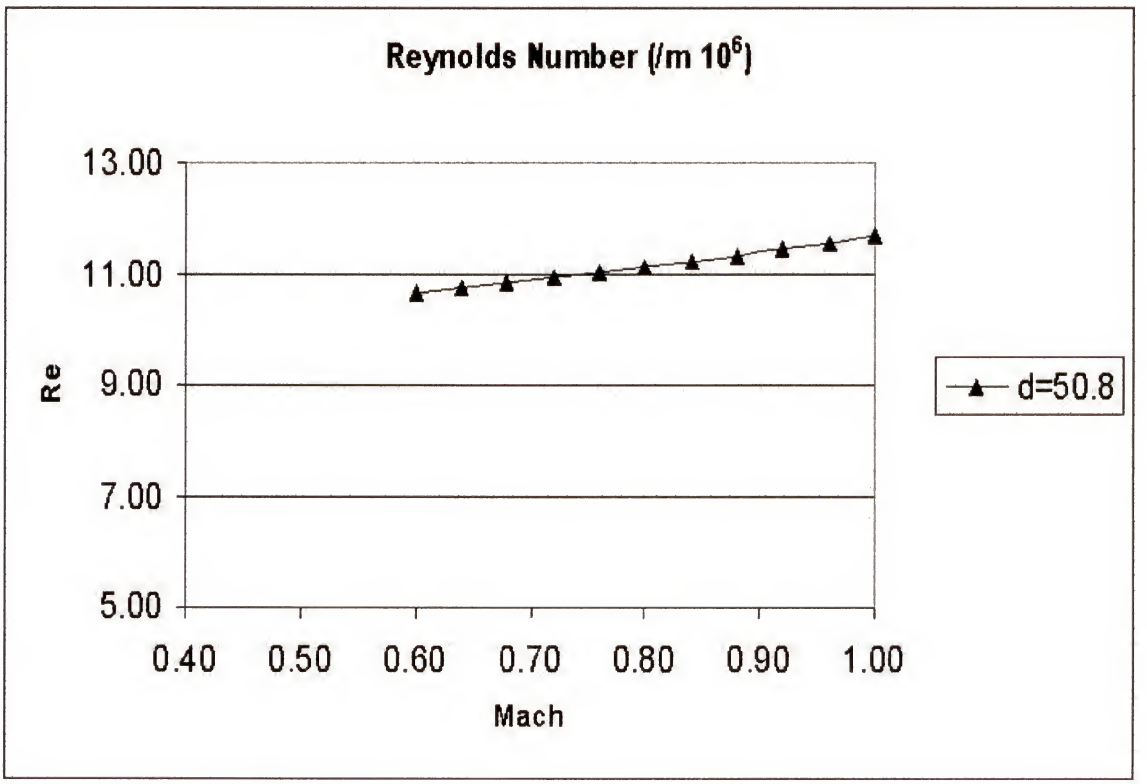

Figure 2-10 Reynolds Number Choked Flow

Table 2-1 Regions II and III Comparison with In-draft Tunnel

Initial Conditions	Region II	Region III	In-draft Tunnel	
P4	101	101	101	KPa
T4	294	294	294	°K
P1	6.52	14.63	0.133	KPa
T1	294	294	294	°K
P4/P1	15.5	6.9	760	-
Test Section				
P	22.06	35.8	52.95	KPa
T	456	235	260	°K
M	0.8	0.8	0.8	-
Re	2.42	9.5	11.0	$/m * 10^6$
Useable Time	0.905	5.184	6860	msec

2-3 Wind Tunnel Design

The in-draft tunnel was selected for design and construction to provide a free stream flow at a high transonic Mach (M = 0.8) over a rectangular two-dimensional cavity. A 50.8-mm square tube, 3.048 meters long was attached to a 5.66 cubic meter tank with a 203.2-mm butterfly valve at the entrance to the tank. The thickness of the tunnel wall is 6.35 mm. A test section is located 2.62 meters from the entrance to the tube and has an overall length of 0.32 meters. The butterfly valve is electrically actuated and hydraulically operated. Once a signal is sent to the valve, it takes less than 0.25 seconds for the valve to fully open. (Figure 2-11)

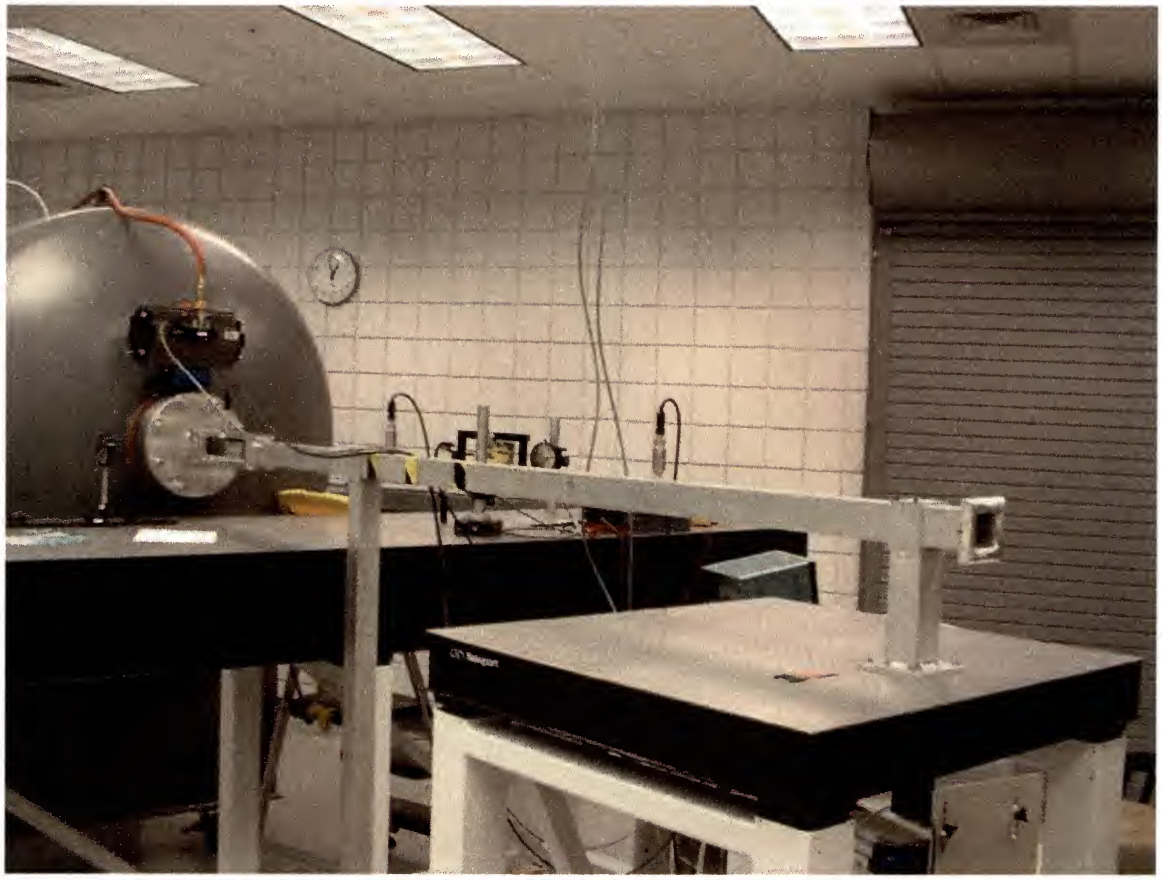

Figure 2-11 In-draft Tunnel

Cavity models span the width of the test section and are located with the leading edge of the cavity 2.77 meters from the entrance of the tunnel. Removal of a portion of the lower tunnel wall allows the insertion of various depth (D) cavity models all having the same length (L = 25.4 mm). Three inserts were made to fill the gap created by removal of the tunnel wall. One of the inserts when installed returns the tunnel to a square, constant area cross section. The other two inserts each produce a cavity model with different depths but the same length spanning the width of the tunnel. The inserts create cavity models with dimensions of L/D/W = 25.4/6.35/50.8-mm and L/D/W = 25.4/3.1275/50.8-mm. (Figure 2-12)

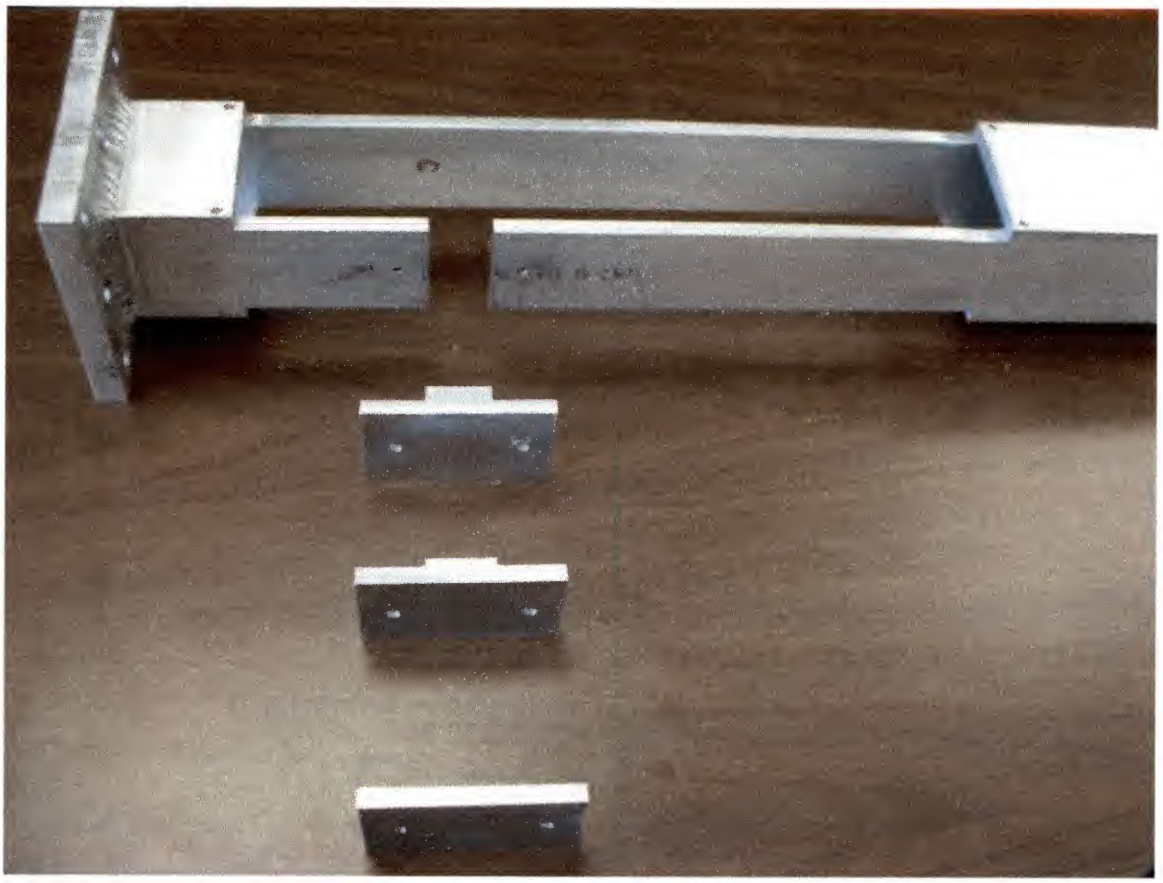

Figure 2-12 Cavity Models

The room acts as a tunnel reservoir with constant total temperature and pressure. Pressure was recorded using a Pace Scientific P300-0-30-A pressure sensor with a combined linearity, hysteresis, and repeatability of ±0.5% maximum range (30 PSI). Temperature was recorded using a J-type thermocouple with a range of 200 to 385 °K with accuracy of ±2.2 °K . The same temperature and pressure probes were used in the tank. Three static pressure sensors were placed along the length of the tunnel to record pressure along the tunnel length. The sensors are PCB Piezotronics static pressure sensors, model number 1501A21FJ30PSIA with a pressure range of 0 to 30 PSI and a quoted accuracy of better than ±0.5% of full scale. Room, tank and tunnel parameters were recorded using LabVIEW hardware (PCI-603E I/O board, SCB-100 connector block and SH100100 cable assembly) and software (version 5.1).

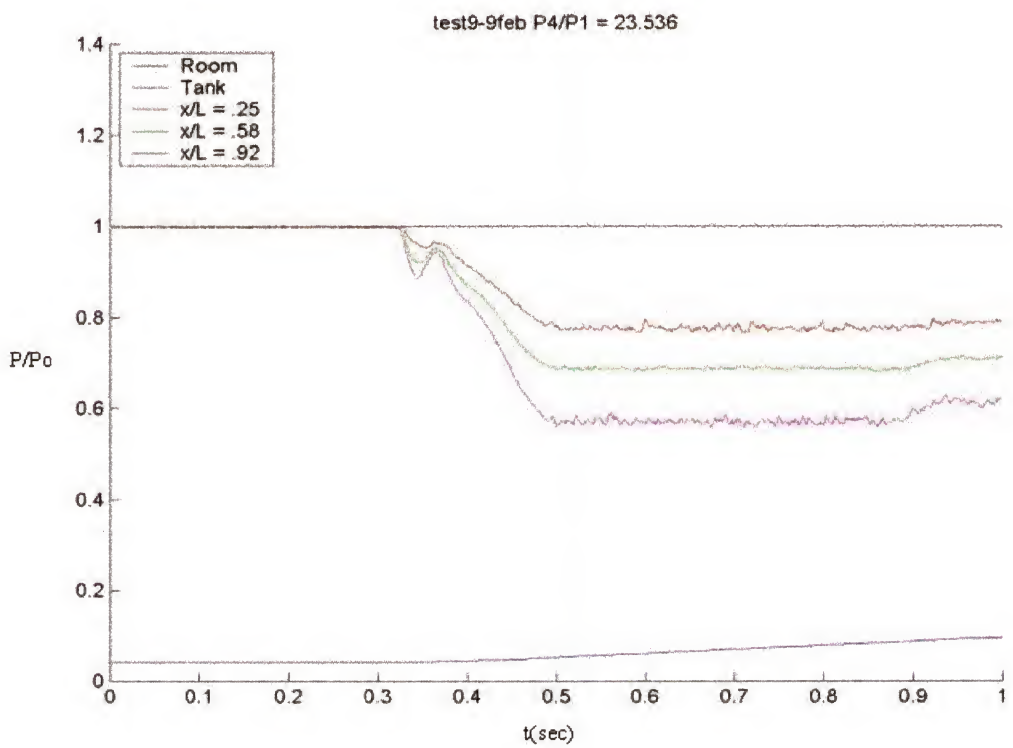

Figure 2-13 In-draft Tunnel Pressure Time History

2-4 Tunnel Performance

A total of seven tests were run with an average starting pressure ratio (room to tank) of 22. Figure 2-13 is a typical time history of the pressure in the room, the tank, and the three static pressure locations after an electrical signal was sent to open the butterfly valve. Comparisons of the seven tests indicate that the pressure traces shown in Figure 2-13 are repeatable.

As the valve opens, an expansion wave is created and propagates upstream towards the open end of the tunnel. This expansion wave reflects at the open end and starts its return trip as a compression wave. This compression wave arrives at the entrance to the tank and reflects starting back towards the open end of the tunnel as an expansion wave. Shortly after this last reflection, viscosity effects start to dominate and stabilize the flow in the tunnel to flow with friction in a constant area duct. Choked flow occurs at approximately .5 seconds after a signal is sent to the valve. While the flow is choked, the flow in the tunnel is steady in that it is not changing at a given location as indicated by the steady reading of static pressure from the three static pressure sensors. The average measured pressures at the three locations normalized to the room stagnation pressure (P/Po) for the seven tests were 0.767, 0.673, and 0.534. In order to find the remaining flow parameters in the tunnel, it was assumed that the flow in the tube approximated flow through a constant area duct with friction commonly referred to as Fanno flow. Solving the Fanno flow equations with a friction factor equal to 0.014 gives calculated pressure ratios at the three locations of 0.768, 0.686, and 0.534. These calculated values compare well with the measured values from the tunnel. Using a friction factor of .014, the stagnation pressure and temperature in the room and the Fanno

equations yields the following free stream conditions 2.77 meters downstream from the opening of the tunnel which corresponds to the leading edge of the cavity model.

Mach	=	0.80
P_∞	=	53570 Pa
T_∞	=	263 ^oK
U_∞	=	260 m/s
ρ_∞	=	0.71 kg/m^3
Re	=	11.0×10^6 /m

CHAPTER 3
FLOW MEASUREMENT SYSTEM

This chapter details the optical measurement system used in this research. The goal of the optics system is to provide information about the flow in and above a cavity using non-obtrusive techniques. Unlike probes (e.g. pressure or temperature) which interrupt the flow of interest, optical systems can provide information on the unsteady flow field around a cavity. In addition, time resolved data can provide additional information on how the flow evolves. This feature is essential to determine the development flow structures such as vortices and shear layers. Additionally, the time accurate flow measurement system allows examination of events that occur at microsecond intervals. Recording the events using a digital camera provides the ability to store the data for later analysis.

3.1 Objective

In order to experimentally investigate the flow in and above cavities, a means of measuring the flow parameters or some property of the environment about the flow from which the flow parameters can be derived is required. The measurement method cannot disrupt the flow, which implies some type of optical system. In addition, in order to be of any use, the measurement technique must provide quantitative results that are both spatially and time resolved and sensitive to any change in the flow field environment. The objective then is to identify a measurement method that addresses the five

characteristics of non-intrusive, time-resolved (<10 μsec), spatially resolved (<1.0 mm), high sensitivity, and direct & quantitative.

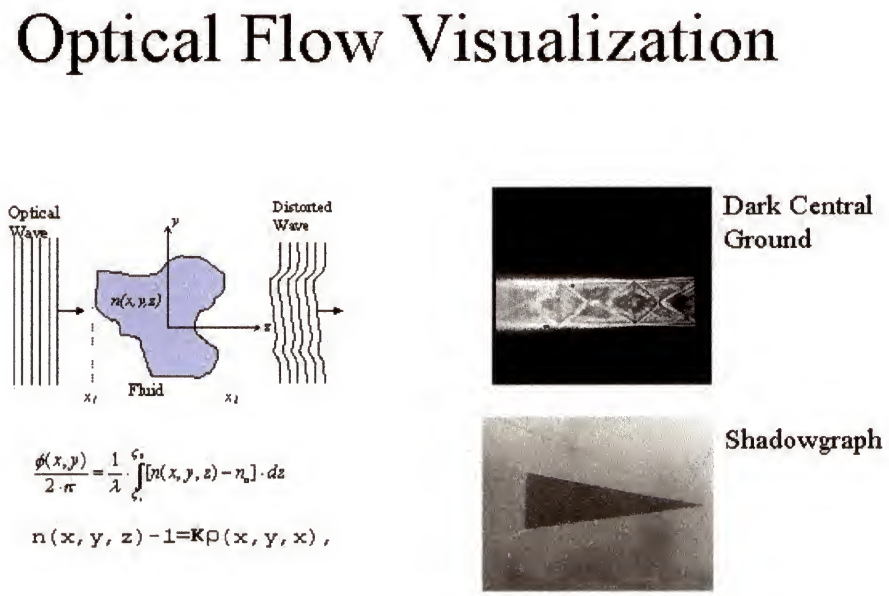

Figure 3-1 Optical Flow Visualization

3.2 Measurement Options

As stated in paragraph 3.1, the measurement method cannot disrupt the flow, which implies some type of optical system. Optical systems rely on an optical wave front being disrupted (refracted) as it passes through a varying density field. Upon passage of the optical wave front, some type of optical recording device such as a camera records the optical wave front either as a photograph or digitally. Typical optical measurement techniques consist of Shadowgraph, Schlieren, Dark Central Ground (a version of

Schlieren), Interferometry, and a Shack Hartman sensor. Figure 3-1 shows the concept of the wave front passing through a changing density field and becoming deformed after it has passed through this field. An example of a Dark Central Ground and Shadowgraph is shown. The phenomenon of interest within a flow field usually involves changes to the fluid's density (ρ), which according to equation 3.1, is directly related to the refractive index given as (Fuller, 1997)

$$n - 1 = k\rho \tag{3.1}$$

Here, n is the index of refraction and k is known as the Gladstone-Dale constant, which is a function of the particular fluid medium.

The optical effects brought about by local changes in density can be made visible by three general methods:

- Shadowgraph method in which the optical response is related to the rate of change of density gradient along a distance x ($d^2\rho / dx^2$).
- Schlieren method in which the optical response is related to the density gradient ($d\rho / dx$)
- Interferometry in which the optical response is related to a uniform change in density (ρ)
- Shack Hartman Sensor in which the optical response is related to the density gradient ($d\rho / dx$)

3.2.1 Shadowgraph

According to Fuller (1997), Shadowgraphs are the least demanding form of flow visualization in terms of apparatus and complexity. Shadowgraphs can be taken with only a short duration light source and a sheet of film or equivalent and give excellent results. Figure 3-2 illustrates a divergent Shadowgraph system. For a Shadowgraph, in regions where the density gradient is increasing (i.e., $d^2\rho / dx^2$ is positive) the light rays

will diverge and the illumination on the film will decrease. For the requirements of this research, it meets the non-intrusive requirement. It could also meet the time resolution if coupled with a high-speed camera. However, it does not provide spatial resolution, quantitative information about the flow field parameters, nor is it sensitive to small changes in the density gradient.

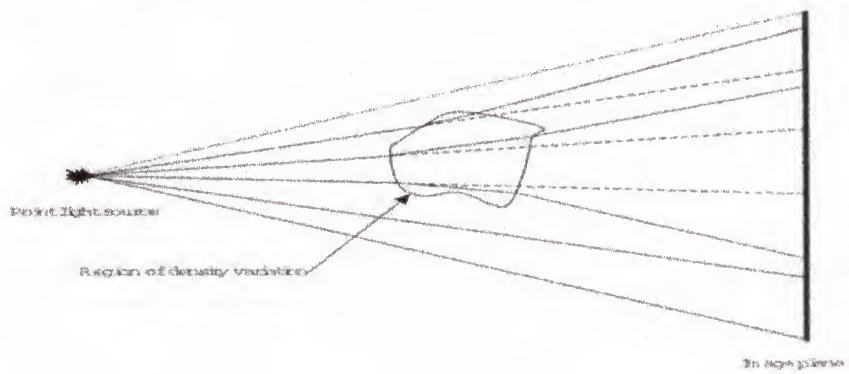

Figure 3-2 Diagram of Operation of a Basic Shadowgraph System

3.2.2 Schlieren

A basic Schlieren system is shown in Figure 3-3. Light from the slit is focused onto a plane by the lens. A knife-edge is placed in the plane and positioned to cut off a portion of the slit image. A screen or camera is placed to receive the plane image. If a medium of constant refractive index is placed in the test area (the region of the aerodynamic disturbance), the camera film will be evenly illuminated. If a refractive index change occurs in the test area, a light ray previously cut off by the knife-edge may be deflected enough to now reach the camera and produce a light image. Thus, the image

plane will show regions of darkness where the incident beam was "blocked" by the presence of the knife-edge and will show regions of brightness where the incident beam was not blocked.

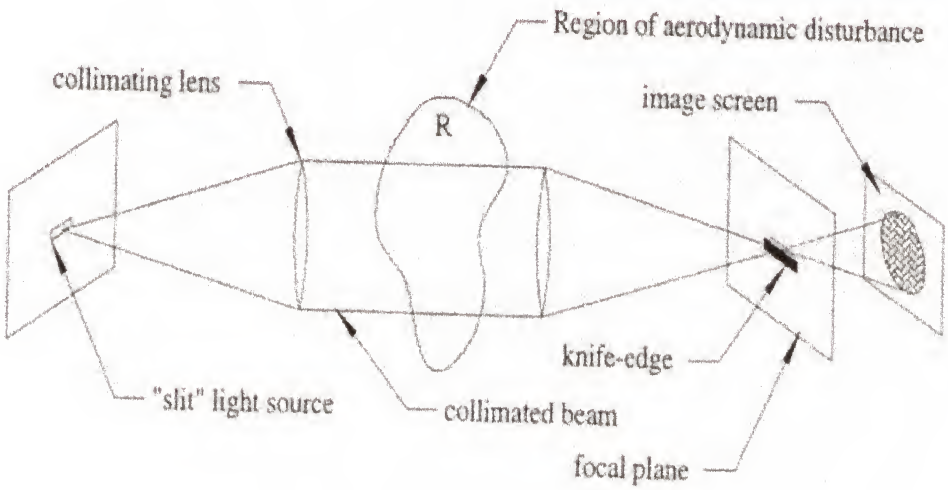

Figure 3-3 Schematic of Schlieren System with Knife Edge Filter

For the requirements of this research, it meets the non-intrusive requirement. It could also meet the time resolution if coupled with a high-speed camera. However, it does not provide spatial resolution, quantitative information about the flow field parameters, nor is it sensitive to small changes in the density gradient. Another disadvantage of such a system is its directional dependence. That is, only those changes in density that refract the light normal to the knife edge will be seen at the image plane.

3.2.3 Dark Central Ground (DCG)

Another technique that relies on the refraction of light is DCG. DCG is a simple improvement to the knife-edge Schlieren system. This system is shown in Figure 3-4. Here the slit source is replaced with a point source and the corresponding filter at the

image plane is an opaque "spot." The advantage of this system is that density gradients in any direction will be observed on the image plane. An experimental investigation of this technique was performed to assess the applicability of its use to meet the five characteristics listed in paragraph 3.1.

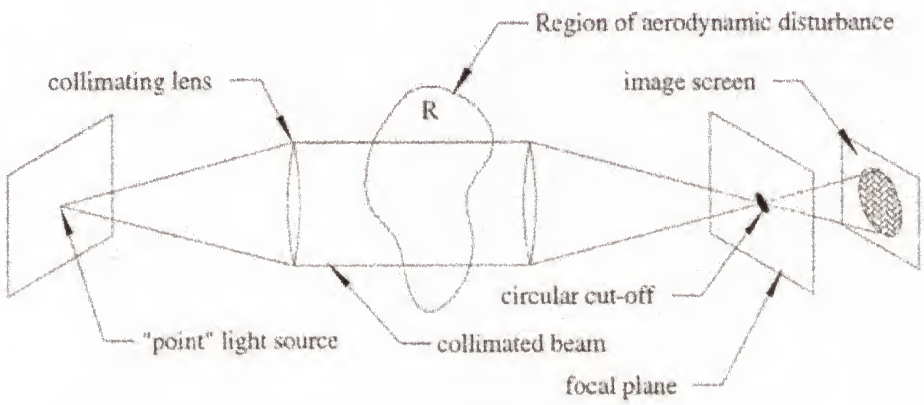

Figure 3-4 Schematic of Dark Central Ground with Circular Spot

DCG uses a point source of light, collimated prior to passage through the test region, focused to a point (circular spot) after passage through the test region and then recorded by a camera. A schematic of the test set up used to assess DCG's applicability for this research is shown in Figure 3-5. Without flow in the test region, the light is focused to the circular spot. As long as there is no flow or disturbance between the light source and the central spot, light will not pass beyond this spot. When a disturbance occurs in the test region (i.e. unsteady flow around a cavity), the refraction index of the air will be changed so that light will bend and no longer be focused on the circular spot.

Light now passes on to the camera. The camera records the presence of density gradients as indicated by bright regions.

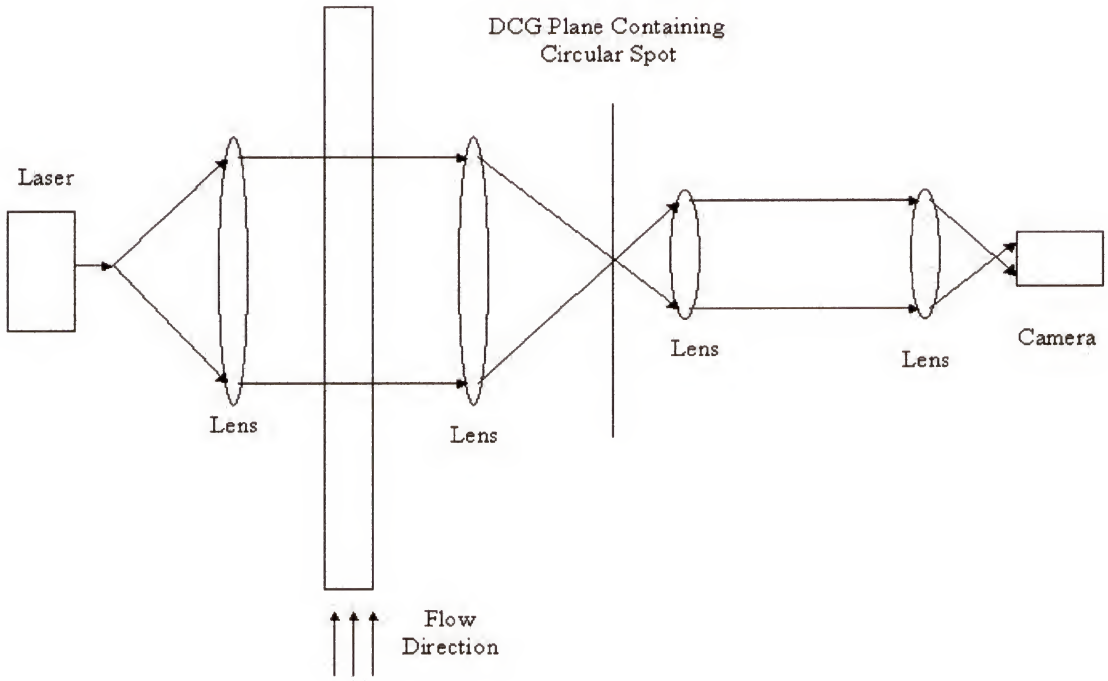

Figure 3-5 Schematic of DCG Test Set Up

Tests were conducted using DCG consisting of flow exiting from a constant area duct and immediately flowing over the cavity. The dimensions of the cavity were 50.8 mm long, 25.4 mm deep, and 12.7 mm wide providing an L/D ratio of 2 and W/D ratio of 0.5. A tank at a stagnation pressure of 618.4 KPa gage pressure and stagnation temperature of 294 ^{o}K was connected to a 558.8-mm long, constant area square duct. A valve was opened and the air was allowed to escape from the tank through the duct. As the air exited the duct, it immediately flowed over the cavity. The laboratory test set up is shown in Figure 3-6.

A Hadland 468 camera took a sequence of eight pictures at various integration times and spacing times between frames. The Hadland 468 framing camera has eight individual image intensifiers and CCD detectors to allow the capture of eight time-resolved images. The camera supports interframe times of 30 nanoseconds. After the event is complete, the images are sent via fiber-optic link to a computer where they can be image enhanced or viewed in a time-sequenced movie format.

Figure 3-6 Laboratory DCG Test Set Up

Exit flow properties from the constant area duct were calculated for two exit conditions. One was choked flow with exit Mach equal to 1.0. The other condition was for unchoked flow with exit Mach equal to 0.86. At a gage stagnation pressure of 412.2 KPa, the exit flow conditions were choked. Flow properties at the exit were

Mach = 1.0

P_∞ = 141 KPa

T_∞ = 245 °K

U_∞ = 314 m/s

ρ_∞ = 2.01 kg/m^3

Re = 40.0 x 10^6 /m

For unchoked flow, the gage stagnation pressure reading for the tank was 206 KPa. Flow properties at the exit were

Mach = 0.86

P_∞ = 101 KPa

T_∞ = 256 °K

U_∞ = 276 m/s

ρ_∞ = 1.38 kg/m^3

Re = 23.2 x 10^6 /m

Figure 3-7 shows the DCG files for choked flow over the cavity. The flow is from left to right with the cavity at the top of each frame. Timing of the data recording consisted of 1 μsec integration with 15 μsec spacing between pulses for a total elapse time of 105 μsec. Shock and/or expansion waves are evident in the jet from the constant area duct where large density gradients (light areas) are observable. However, there are no clues as to the type of wave since the direction of the gradient is not known. From the known exit conditions from the constant area duct and the known conditions in the room, the flow is under-expanded. Therefore the first wave is an expansion wave.

A flow structure, possibly a vortex, appears to be located in the shear layer just above the cavity at mid length in frame 1. This structure appears in the shear layer as a protrusion into the cavity. The position of this protrusion moves toward the aft cavity wall and appears to reach it by frame 7. An estimate of the velocity of this structure is 212 m/s (first frame to seventh frame moves approximately 19 mm in 90 μsec). Some type of flow activity in the corner of the forward wall and floor of the cavity seems evident in all the frames. No other flow structures are observable in the cavity

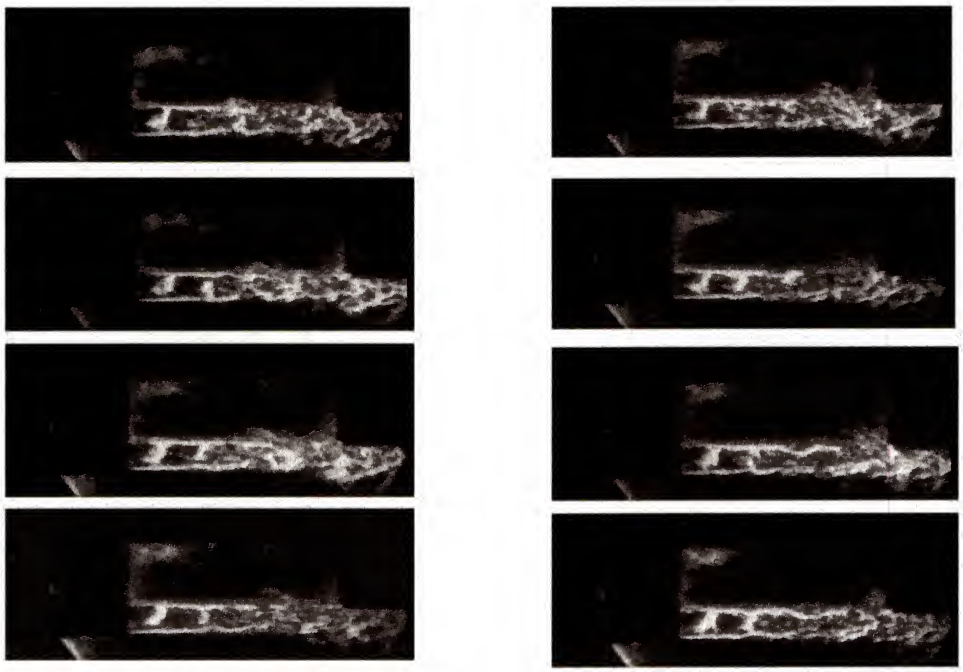

Figure 3-7 DCG Choked Flow

The shear layer forms at the exit from the duct and stays straight half way across the cavity. The shear layer also thickens from the exit to halfway across the cavity. Interaction with flow in the cavity seems to disrupt the shear layer over the aft half of the cavity. What the shear layer is doing in the aft half of the cavity is difficult to determine

from DCG. Not knowing the direction of the gradient and the requirement that the gradient be large so as to show up as a light area makes it difficult to even qualitatively assess the shear layer movement over the aft half of the cavity.

Figure 3-8 shows the DCG files for unchoked flow over the cavity. The flow is from left to right with the cavity at the top of each frame. Timing of the data recording consisted of 1 μsec integration with 15 μsec spacing between pulses for a total elapse time of 105 μsec. Since the exit flow is subsonic, no shocks and/or expansions waves are expected and none are evident from the eight frames of data.

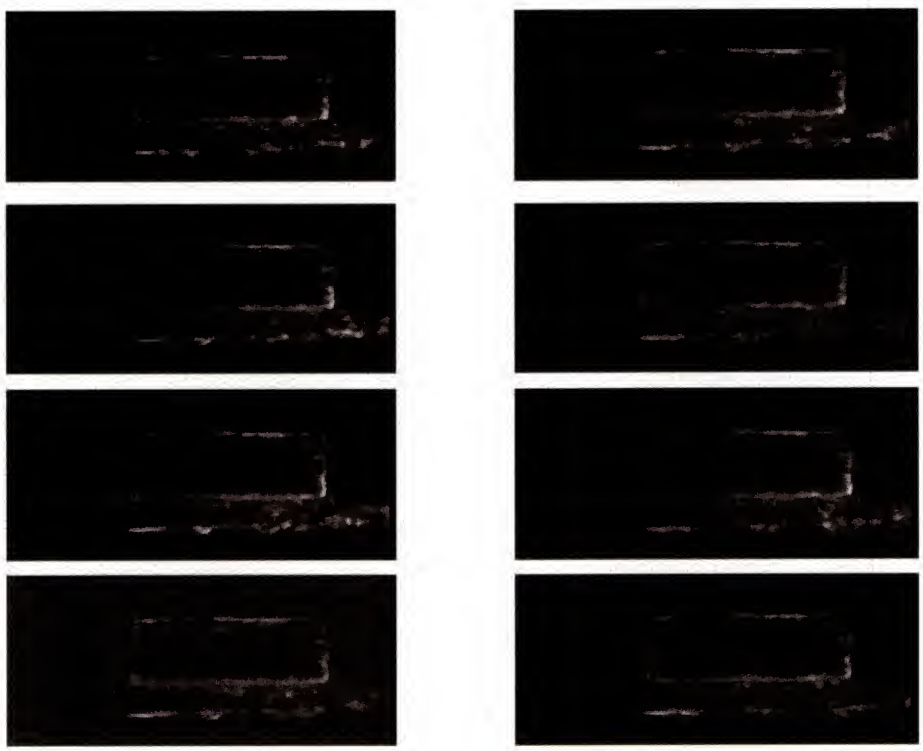

Figure 3-8 DCG Unchoked Flow

There appears to be an unsymmetrical vortex in the forward portion of cavity. The vortex does not appear to change over the measured time period. This "vortex" was not present in other tests and may be a result of a smudge on the glass. There is no indication

of any activity in the corner of the forward wall and floor of cavity. Little to no activity can be seen in the cavity.

A shear layer is present at the exit from duct. The shear layer appears to remain straight up to half way across the cavity and it also gets thicker. Interaction with flow in the cavity over the aft half of the cavity causes slight changes in the shear layer as evident by protrusions into the cavity from the shear layer. The types of structures these protrusions represent are not readily identifiable from the DCG images.

In general, DCG provides a qualitative method of capturing the flow field physics in and above a cavity provided the density gradients are large enough to be recorded. Where large density gradients were present, flow structures such as shear layers, shocks, and expansion waves were easily identifiable from the DCG files. Identification of vortices using DCG files was a much more difficult task, being almost an art form. A vortex is defined as a location where the density is decreasing down to a minimum value at a point. Another way of defining a vortex is if you stand at the center, the density gradient would be increasing as you moved away from the center. Since DCG shows where gradients exist but no information on the direction of the gradient, identification of vortices strictly from a DCG frame is impossible. Some other information would be required to identify vortices such as the existence of a rearward-facing step. The lack of large gradients inside the cavity prevented any type of analysis of the flow in this region. This occurred at both the choked and unchoked condition.

A quantitative assessment is not feasible because the position of the flow structures is impossible to establish. Only a crude estimate can be made as to the position of the protrusions in the shear layer from frame to frame. Therefore, only a crude

estimate can be made about the velocity and acceleration. Also, the distribution of flow variables such as pressure, temperature or density is not available from this technique. For the requirements of this research, DCG meets the non-intrusive requirement. Coupled with the Hadland 468 camera, it also meets the time resolution requirement. However, it does not provide spatial resolution, quantitative information about the flow field parameters, nor is it sensitive to small changes in the gradient.

3.2.4 Interferometry

While both the Shadowgraph and Schlieren methods make use of light deflection in a compressible fluid media, the associated phase alteration is the basic effect for visualization with an interferometer. The most common interferometer for the photographic observation of flow fields in wind tunnels is the Mach-Zehnder. In a classical Mach-Zehnder system, the phase of an undisturbed light ray is compared with that of a ray that has passed through a compressible media. The subsequent interference of the reference and disturbance beams is recorded for flow field visualization. This arrangement gives sensitivity directly related to the density. A basic arrangement for an interferometric system is given in figure 3-9. Usually, the reference and disturbed beam originate from the same light source and traverse the same optical path length. The main drawback of this system is the optical complexity required for visualization and the sensitivity of the components to vibration. Zhang and Edwards (1990) used holographic interferometry to observe the supersonic flow field in and above various L/D cavities and to make density measurements. Both absolute and differential holographic interferograms were taken. Figure 1.3 showed some of the results published in 1990. Absolute interferograms were able to show shocks, vortices and shear layer. Differential

interferograms showed the vortical structures in the shear layer. However, a time history was not presented. Only single event recordings were presented. Zhang and Edwards (1992) used the same method when investigating the flow over cavities in tandem. The same types of results were reported.

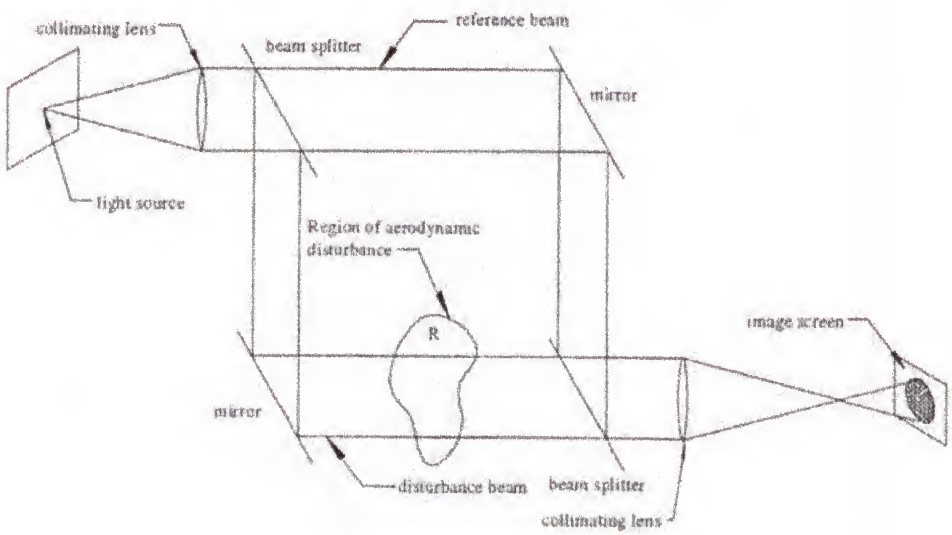

Figure 3-9 Schematic of an Interferogram System

For the requirements of this research, use of Interferometry would meet the non-intrusive requirement and spatial resolution. It does not appear that time resolved data is available from this technique. Only single exposures that are compared to a reference frame when there is no flow (absolute interferograms) and single exposures compared to frames taken microseconds prior (differential interferograms) are available from this technique. It is unclear how this technique could be coupled with a high-speed camera to address the time resolution requirement. This technique also does not provide any quantitative information about the flow field density either in absolute terms or in terms

of the gradient direction. Because the tests were run at supersonic Mach numbers, density gradients were large enough to be recorded. It is unclear if this technique would be sensitive enough to measure subsonic flow in and above a cavity. It is anticipated that the results would be similar to the use of DCG. Interferometry meets the non-intrusive and spatial requirement. Time resolution, high sensitivity, and direct & quantitative are not addressed.

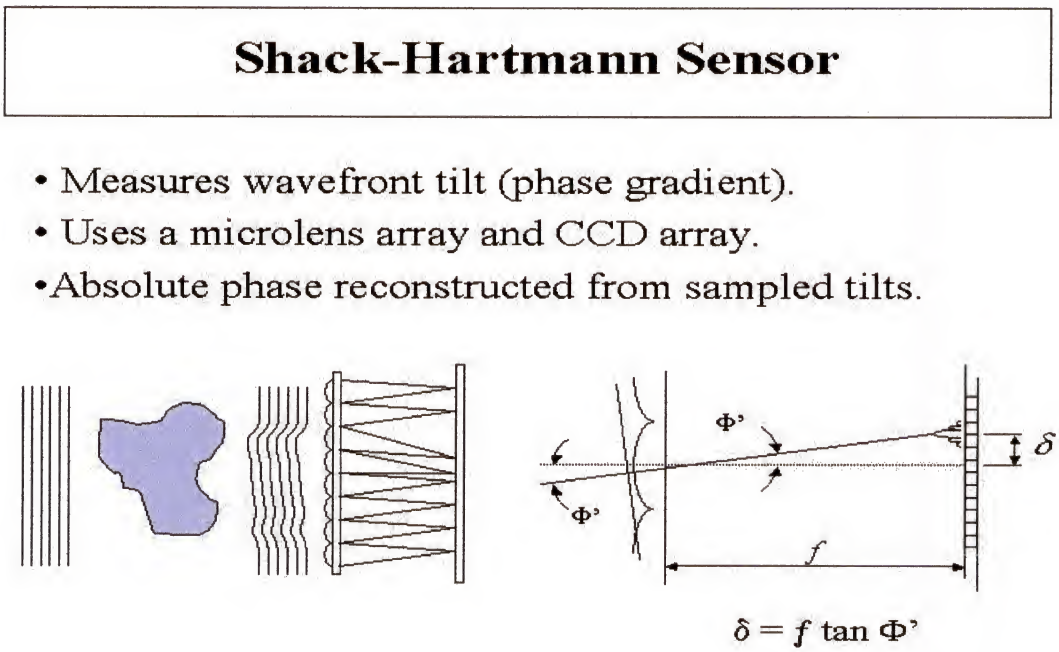

Figure 3-10 Shack Hartman Sensor

3.2.5 Shack Hartman Sensor

A Shack Harman sensor relies on the same refractive property of a changing density field, as do Shadowgraph and Schlieren. However, the Shack Hartman sensor introduces an array of lenslets after the optical wave front has passed through the test section. Each lenslet focuses a portion of the optical wave front to a spot a focal length away from the lenslet. A digital camera, focused to this plane, records the location of the spot for each lenslet (Figure 3-10). Absolute phase angle can be reconstructed from the

known wave front tilt if the location of the spot were known for the wave front passing through a vacuum. This is not readily available. Therefore, comparing spot locations for a variable density field (test frame) and a known uniform density field (reference frame) is used to implement this technique. What the Shack Hartman sensor measures is the location of the spots for a reference and test frame. The difference between the spot locations in the reference frame and test frame is the change in slope of the optical wave front, $\Delta\Phi'$.

Numerous methods are available to calculate the change in phase from a known change in phase front slope. One method to calculate this change in phase angle from a known change in the slope of the optical wave front was demonstrated by Gunia (1999). Use of this technique was also demonstrated for flow exiting from a converging/diverging nozzle (Land 2000). The same method used by Gunia (1999) and Land (2000) is used in this research. The software developed by Gunia (1999) and refined by Land (2000) to calculate the change in phase is used. The change in phase angle calculated from the known change in optical wave front slope is directly related to the density of the medium that the light passes through.

$$\Delta\Phi = \frac{2\pi}{\lambda}\int_0^w (k\rho - k\rho_b)dw \qquad 3.2$$

$\Delta\Phi$ is the change in the phase angle, λ is the wavelength of the laser, k is the Gladstone-Dale constant equal to 0.2332 cm^3/g for air, ρ is the density of the air when the flow is on, ρ_b is the reference density with the flow off, and w is the width along which the integration is done. Assuming that the gradients of density along the length and depth are much greater than the gradients across the width, the gradients across the width can be

ignored. This makes the density a function of the length, depth, and time only. Carrying out the integration and solving for the density yields the following expression.

$$\rho = \rho_b + \frac{\lambda}{360kw}\Delta\Phi \quad \Delta\Phi \text{ In degrees} \qquad 3.3$$

The tests conducted for the DCG were repeated to verify the capability of the Shack Hartman sensor. The same test set up as shown in Figure 3-5 was used with the exception that the circular spot was removed and a lenslet array was inserted. Test conditions were as previously stated for the DCG.

3.2.5.1 Single exposure

The initial set of tests used a single exposure to verify the software that calculates the change in slope and change in phase angle. The cavity model was the same as that used for the DCG tests. Figure 3-11 is the result for choked flow. The orientation of the flow is from right to left. The cavity location and constant area duct are superimposed on the respective plots. Exit conditions from the constant area duct are such that the flow is under expanded. As the flow exits from the constant area duct, it will go through a series of expansion and shock waves beginning with an expansion wave trying to equalize the pressure to the back plane pressure.

From Figure 3-11, it can be seen that immediately exiting the constant area duct, the density decreases indicating that the flow is being expanded. The density continues to decrease followed by a sharp rise in density indicating the flow is passing through a shock. This flow pattern is usually depicted using Schlieren flow visualization techniques as a series of diamonds at the exit of high-speed nozzles (DCG example in Figure 3-1). The Shack Hartman technique shows the actual density distribution as the flow goes through the series of expansion and shock waves. From the density distribution, the

direction of the density gradients can be seen. Figure 3-12 shows the same results for unchoked flow over the same cavity. Missing from the exit are the expansion and shock waves since the flow is already at the back plane pressure. Flow is again from right to left. In addition to the density and gradients of density at the exit of the constant area duct being visible, the density and density gradients in the cavity are also available.

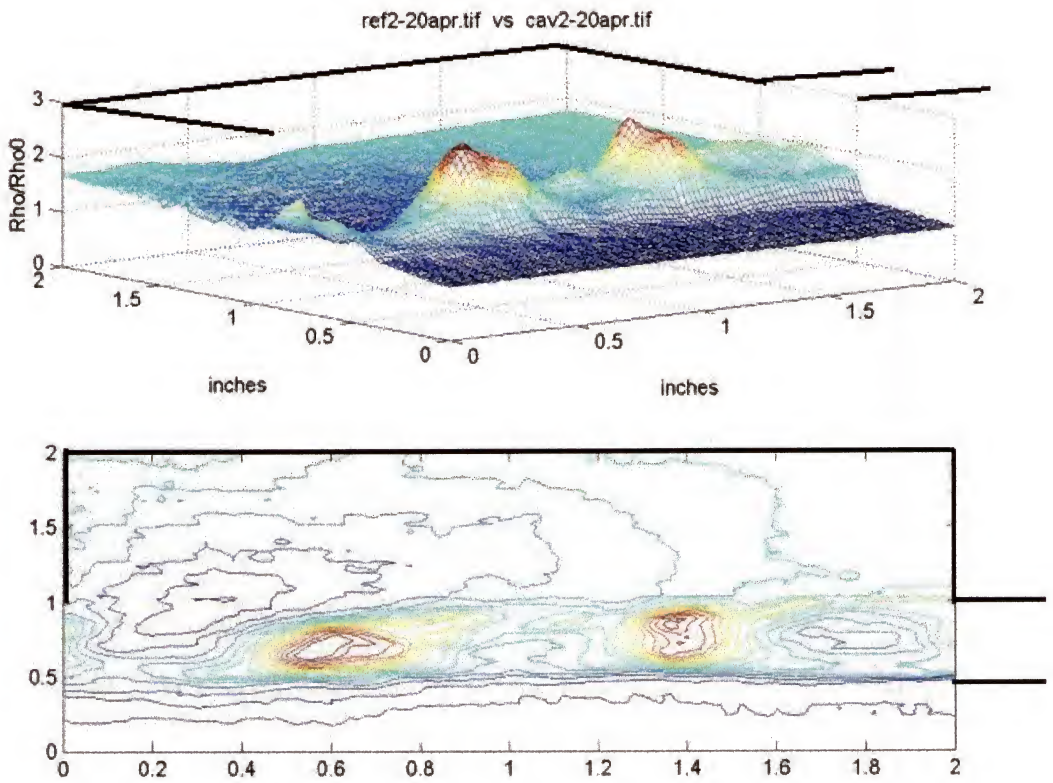

Figure 3-11 Shack Hartman Sensor Choked Flow, Single Exposure

The entire density field is measurable using a Shack Hartman sensor. A Shack Hartman sensor meets the non-intrusive, spatially resolved, high sensitivity, and direct & quantitative requirements. Time resolution needs to be addressed next. It is known from previous experiments that the flow in and above the cavity is unsteady. To correctly

assess what is happening, the ability to continuously measure the change in optical wave front slope is required.

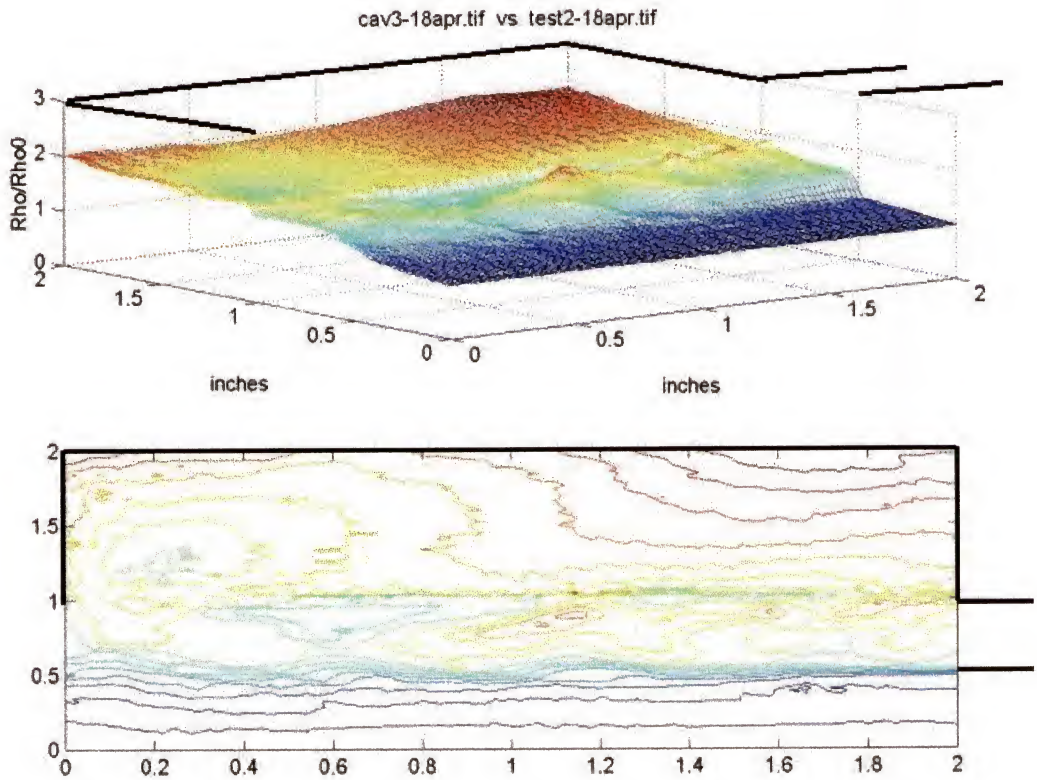

Figure 3-12 Shack Hartman Sensor Unchoked Flow, Single Exposure

3.2.5.2 Multiple exposure

A method was developed to multiple expose one CCD array with four individual lasers sequentially pulsed. This provided successive test frames closely spaced in time as opposed to only a single test frame. The Shack Hartman sensor design previously used and demonstrated by Land (2000) has been expanded to include 4 lasers physically separated at the point source. Figure 3-13 shows the lasers mounted on a board located at the point source of the flow visualization set up.

Land's design separated the spots created by the Shack Hartman lenslet array by an average of 9 pixels on the CCD array. That design is still incorporated for each laser. However, due to the fact that the lasers are physically separated at the point source, an individual laser's spots are offset from the other laser's spots by a distance proportional to the physical separation at the point source. This equates to 3 to 4 pixels in the horizontal and vertical direction on the CCD array. Figure 3-14 shows an entire CCD array that has been multiple exposed. If you look carefully, you can distinguish groups of 4 spots. Figure 3-15 is a blow-up of such a cluster of 4 spots.

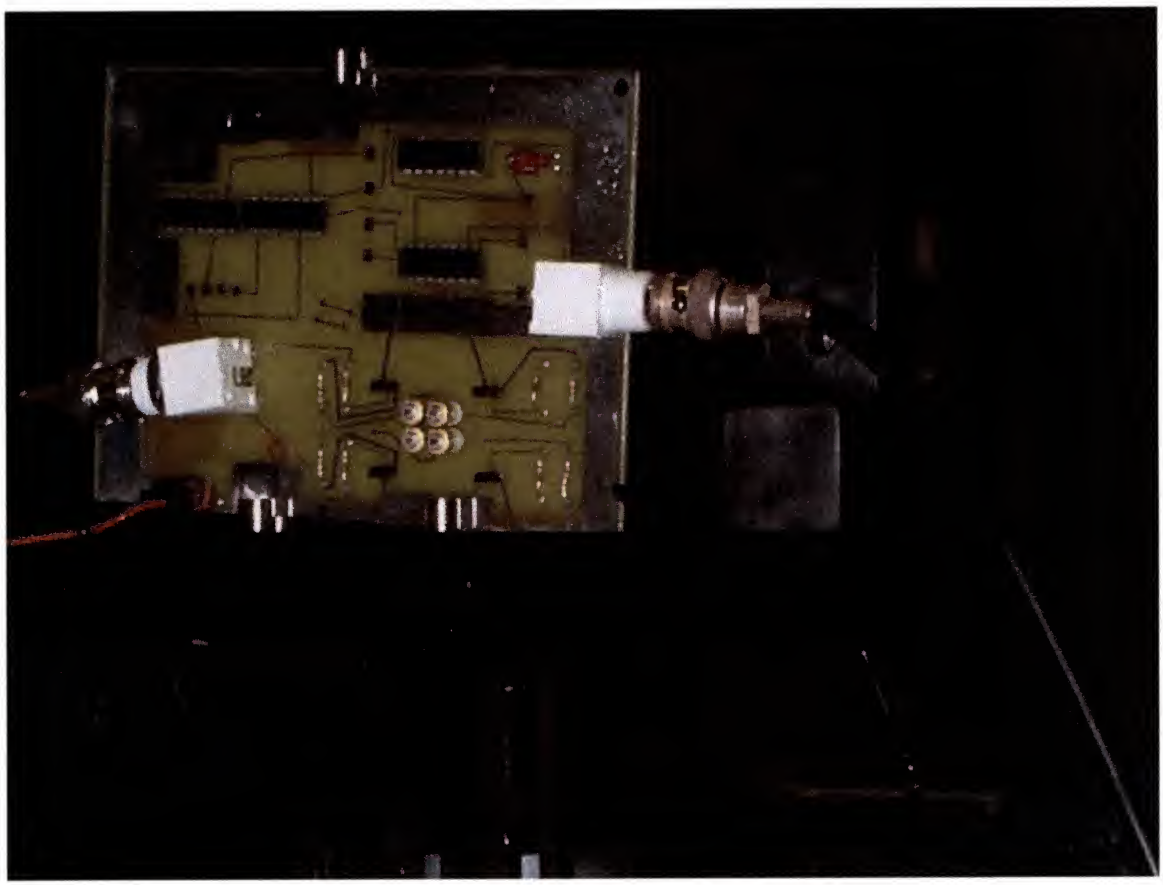

Figure 3-13 Four-Laser Point Source

The four spots shown in Figure 3-15 correspond to the slope of the optical wave front passing through the same location in the test section at four successive times. The

lasers are pulsed in the same sequence each time a test frame or reference frame is taken. A test frame coupled with a reference frame allows the calculation of the change in slope of the optical wave front for four successive times.

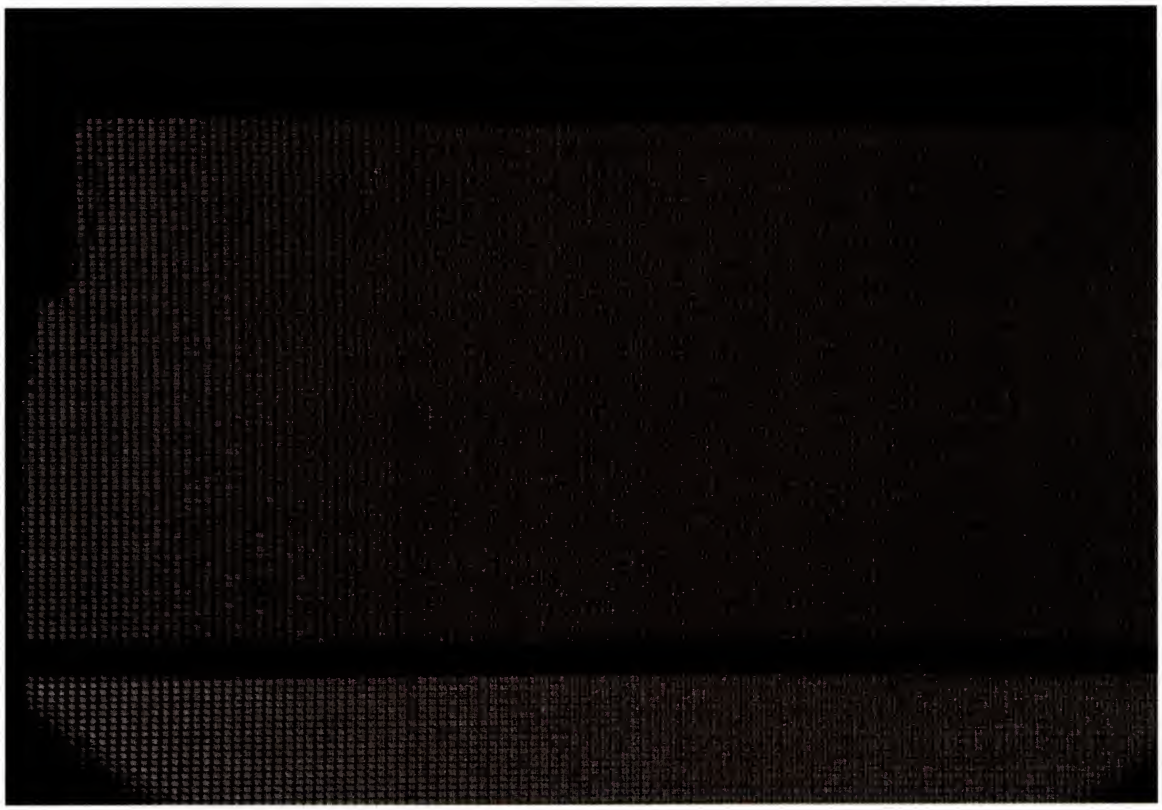

Figure 3-14 Multiple Expose CCD Array

The same techniques employed by Land (2000) to compare the spot locations to a reference frame are employed to calculate the change in slope of the optical wave front. Gunia's method for calculating the change in phase is used for each set of spots at each successive time. The location of each spot within the 9X9-pixel array was the only software modification required. This multiple exposure of a Shack Hartman sensor provides a time resolved recording of the density in and above the cavity. Time accurate information for the behavior of a flow parameter (density) in and above the cavity is now available.

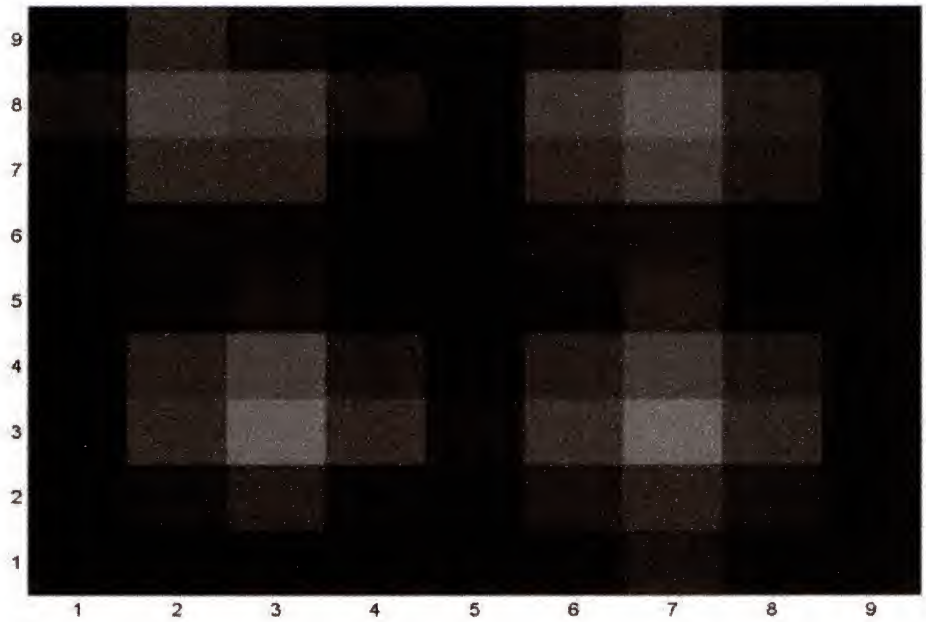

Figure 3-15 9X9 4 Spot Cluster

A series of tests were performed to test the multiple exposed Shack Hartman sensor design. Because of the physical separation of the lasers at the point source, some field of view was lost in the test area. Therefore, the two-dimensional cavity model previously used for the DCG and the single exposure Shack Hartman tests had to be redesigned. The original model had a L/D ratio of 2. Because of the reduction in field of view, either a shallower cavity or shorter cavity had to be used.

A 12.7 mm plug was inserted into the existing cavity creating a shallower cavity. The length was maintained at 50.8 mm, the depth was cut in half to 12.7 mm giving a cavity model with an L/D ratio of 4. The original model had glass only on the sides of the cavity. The redesigned cavity includes glass on the sides of the cavity and extends above the cavity into the field of view of the laser beam. Figure 3-16 shows the geometry of the cavity model used in testing the multiple expose Shack Hartman sensor.

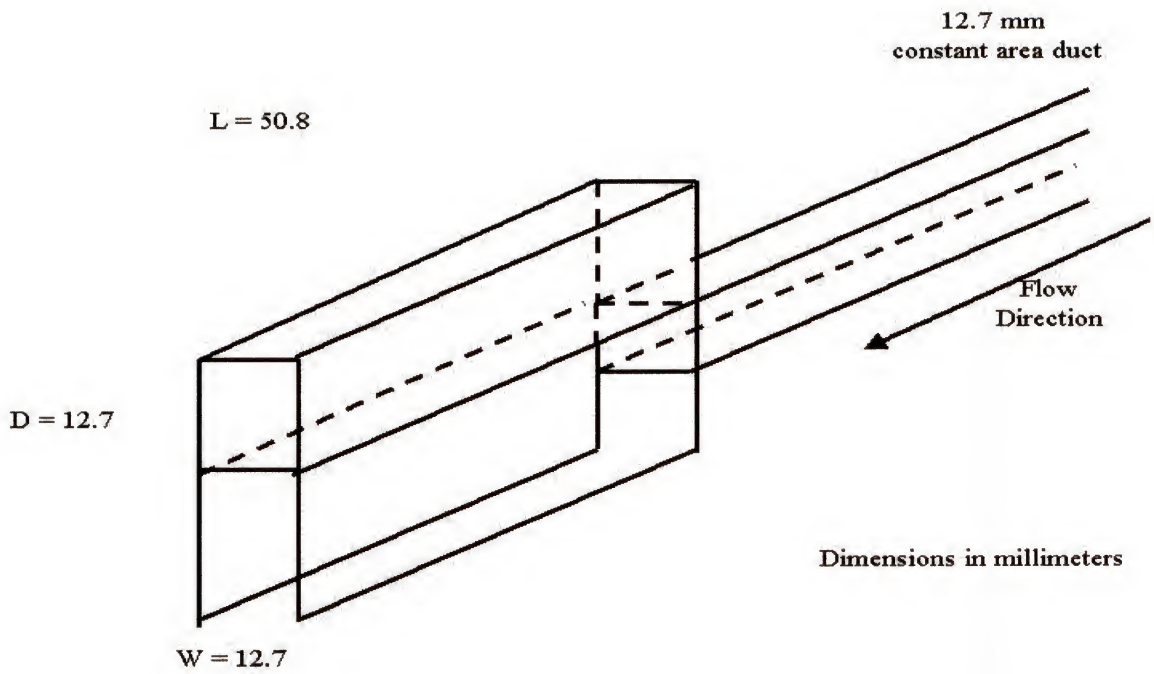

Figure 3-16 Cavity Geometry

A series of tests were run using the four-laser point source and the new 2-dimensional cavity. A reference frame of data was taken with no flow in the test area. The lasers were individually pulsed and the spots recorded by the camera to produce a reference frame. With the flow on, a test frame of data was taken by pulsing the individual lasers with a known delta time between pulses. The spots within the 9X9-pixel array were separated. The location of each spot was found and compared to its corresponding reference frame spot location. The change in the optical wave front slope and the change in phase angle were calculated for each set of spots. The 2-dimensional assumption is made and the density distribution in and above the cavity is calculated. When complete, a sequence of how the density behaves over time is obtained.

Figure 3-17 is the data available from a multiple expose Shack Hartman sensor. This information in its current format (density distribution) or after it has been

manipulated can provide information on the formation, movement, interaction and impact of cavity flow structures on the cavity surface pressure coefficient. The types of manipulation that can be done will be covered in the next chapter.

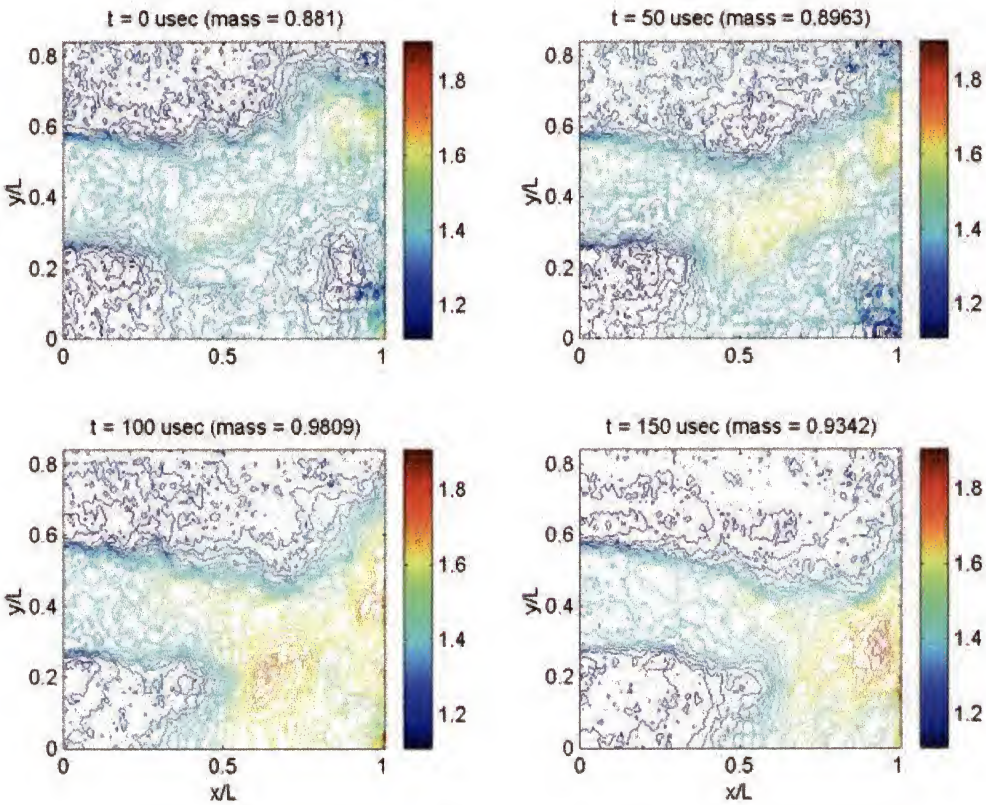

Figure 3-17 Density Distribution

The multiple exposed Shack Hartman technique is a viable method for measuring and analyzing the flow in and above cavities. The change in phase front slope passing through a changing density medium is what the Shack Hartman sensor measures. This allows the calculation of the density distribution in and above a cavity. The multiple exposures Shack Hartman sensor meets the five requirements of non-intrusive, time-resolved (<10 μsec), spatially resolved (<1.0 mm), high sensitivity, and direct & quantitative

3.3 Shack Hartman Sensor Performance

To validate the results obtained from the Shack Hartman sensor, a method to calculate a density distribution across the area of the duct by some accepted classical method or access to experimental data is required. This data is then used for comparison to the measured density from the Shack Hartman sensor. This section will describe how a density distribution is obtained from fully developed turbulent flow in constant area ducts and pipes. The results are then compared to the Shack Hartman measured data for both the small constant area duct described in this chapter and the larger constant area duct described in the previous chapter.

3.3.1 Density Distribution, Constant Area Duct

The Shack Hartman sensor experiment described in this chapter used flow exiting from a constant area duct and immediately flowing over a two dimensional cavity (preliminary tunnel). This flow had an exit Reynolds number based on the hydraulic diameter of the duct of 296000. For flow in the larger constant area duct described in the previous chapter (in-draft tunnel), the Reynolds number based on the hydraulic diameter is 560000.

Flow in a constant area duct is laminar up to a Re of 2300. At this value, the flow starts to transition from laminar to turbulent and is normally considered fully turbulent when the Reynolds number exceeds 3000 (Wilcox 1997). Fully developed flow occurs at $\frac{l_e}{D_h} = 4.4R_e^{1/6}$ where l_e is the length from the inlet of the constant area duct and D_h is the hydraulic diameter (the diameter for a circular pipe or the length of the side for a square pipe) (Wilcox 1997). For the preliminary tunnel with a Reynolds number of 296000, the flow will be fully developed 35 diameters downstream from the inlet of the constant area

duct. The exit of the constant area duct for the preliminary tunnel is 44 diameters downstream from the inlet. For the in-draft tunnel with a Reynolds number of 560000, the flow will be fully developed 40 diameters downstream from the inlet. The leading edge of the cavity in the in-draft tunnel is located 54 diameters downstream from the inlet. Therefore, both the preliminary and in-draft tunnels will have flow over the cavity that is both turbulent and fully developed.

Applying the perfect gas law, the density at any given point along the cross section is equal to the pressure divided by the gas constant and the temperature. Steady, two-dimensional, compressible boundary layer viscous-flow equations of motion simplify in the same manner as for incompressible flow. The momentum equation normal to the surface simplifies to $\partial P/\partial y = 0$ so that the pressure is a function only of distance along the surface (Wilcox 1997). The density across the cross section can be calculated if the temperature across the cross section is known.

$$\rho(y) = \frac{P}{R_g T(y)} \qquad 3.4$$

To find the density distribution, a temperature distribution is needed. A duct with a constant circular cross section containing fully developed turbulent flow can be assumed to be a two-dimensional flow. The two dimensions are the radius r and the length along the duct. An approximation for the square cross section can be made using the results from the round cross section calculations. This is done via the hydraulic diameter D_h which for a square cross section is the length of the side of the duct. "In the case of two-dimensional flow, and irrespective of the shape of the body, there exists a remarkably simple relation between the fields of velocity and temperature. A. Busemann first used the corresponding proposition when he calculated the compressible boundary

layer on a plate. It can be stated simply by asserting that irrespective of the form of the viscosity function μ(T), the temperature T depends solely on the velocity component u taken parallel to the wall, i.e. T = T(u). Thus curves of constant velocity (u = constant) are identical with the isotherms (T = constant)." (Schlichting 1979) For an adiabatic wall, this simple relation between the field of velocity and temperature takes the form

$$T = T_w - r\frac{\gamma - 1}{2\gamma R_g}u^2 \qquad 3.5$$

Where T_w is the temperature at the wall, r is a recovery factor equal to .90 for turbulent flow, γ is the ratio of specific heats, R_g is the gas constant and u is the velocity. This gives us one equation but it contains 2 unknowns, the wall temperature T_w and the velocity u. However, the average temperature over the cross section $\overline{T}$ can be calculated from flow with friction in a constant area duct (Fanno Flow). Integrating the expression for temperature over the cross section and dividing by the cross sectional area, an expression for $\overline{T}$ is found.

$$\overline{T} = \frac{\int T dA}{A} \qquad 3.6$$

Substituting the expression for temperature from equation 3.5 into equation 3.6 leads to.

$$\overline{T} = T_w - \frac{r(\gamma - 1)}{2\gamma R_g}\frac{\int u^2 dA}{A} \qquad 3.7$$

To calculate the temperature distribution in the tunnel, it is necessary to choose a shape for the velocity profile. Lacking extensive experimental data in compressible channel flows, the usual custom is to employ the empirically determined power law for incompressible flow (Shapiro 1953). Experimental observations for boundary layers in external flows and for flows in pipes and channels show a common structure. Often as an

approximation, turbulent boundary layer profiles are represented by a power law relationship (Wilcox 1997).

Incompressible **Compressible**

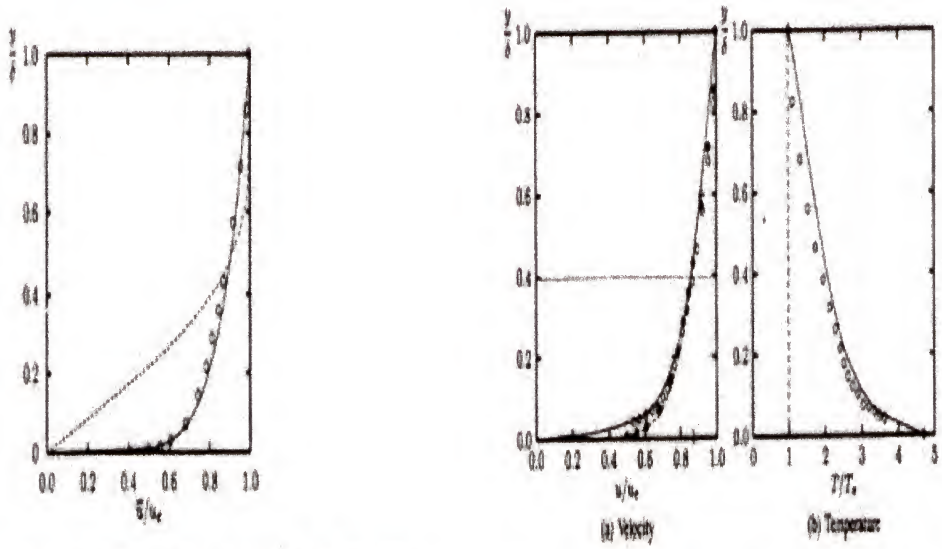

Figure 14.28: *Power-law velocity profile:* — $\bar{u}/u_e = (y/\delta)^{1/7}$; ○ *Wieghardt data at* $Re_x = 1.09 \cdot 10^7$ *[Coles and Hirst (1969)];* · · · *Blasius (laminar).*

Figure 15.23: *Turbulent velocity and temperature profiles for a constant-pressure, adiabatic-wall boundary layer. Measured:* • $M = 0.1$ *Wieghardt [Coles and Hirst (1969)],* ○ $M = 4.5$ *Coles [Fernholz and Finley (1981)]. Computed:* · · · $M = 0.1$; — $M = 4.5$.

Figure 3-18 Incompressible and Compressible Velocity Profile Comparison

Figure 3-18 shows a comparison between a measured incompressible and compressible boundary layer velocity profile with a computed power law velocity profile (Wilcox 1997). Both computed power law profiles show good agreement with experimental data. For this investigation, the power law velocity distribution is used in equations 3.5 and 3.7. The velocity power law takes the form:

$$\frac{u}{V_c} = \left(\frac{y}{R}\right)^{1/n} \quad \text{Power Law} \qquad 3.8$$

where u is the velocity, V_c is the maximum velocity along the centerline of the pipe, R is the radius of the pipe, and n is a constant whose value depends on the Reynolds number using the hydraulic diameter as the reference length. The value n ranges from n = 4 for $Re_d = 4 * 10^3$ to n = 10 for $Re_d = 3.2 * 10^6$ (Benedict 1980). For the preliminary tunnel, n = 7 and for the in-draft tunnel, n = 8 was used.

Since the velocity in the center of the duct is seldom known, an expression using the average velocity across the cross section is needed. Numerous texts were available that related the average velocity distribution for fully developed, turbulent flow in a constant area duct with a circular cross section to the radius of the cross section (Daugherty and Franzini 1965, Morris 1963, Benedict 1980, and Schlichting 1979). This expression is

$$\frac{u}{V} = \left[\frac{(2n+1)(n+1)}{2n^2}\right]\left(\frac{y}{R}\right)^{1/n} \qquad 3.9$$

Just as the average temperature can be found using flow with friction in a constant area duct, the average velocity V can also be found. Using this value V in equation 3.9 gives a velocity distribution as a function of only one variable, y. The references quoted above (Daugherty and Franzini 1965, Morris 1963, Benedict 1980, and Schlichting 1979) also present the result of comparing this law to numerous experimental investigations and show very good agreement.

Substituting equation 3.9 into equation 3.7 and integrating over the cross sectional area results in the following expression for the average temperature in terms of the wall temperature and the average velocity.

$$\overline{T} = T_w - \frac{r(\gamma-1)}{2\gamma R_g}\left[\frac{(2n+1)(n+1)}{2n^2}\right]^2 \frac{n^2}{(n+1)(n+2)} V^2 \qquad 3.10$$

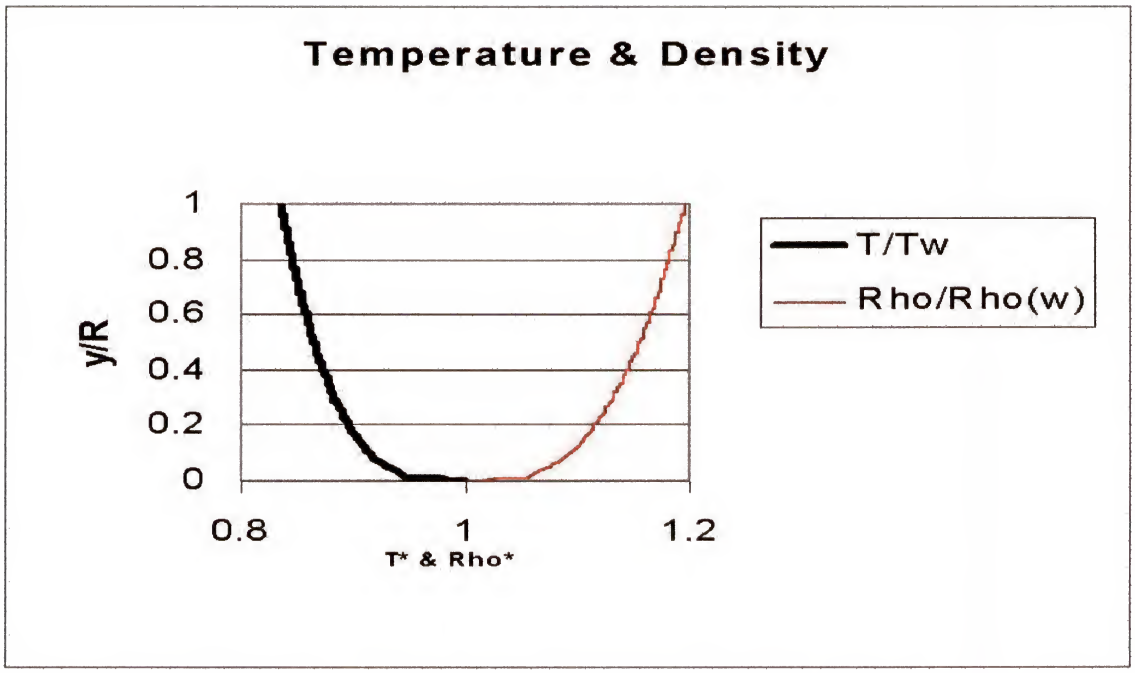

Figure 3-19 Temperature and Density Distribution, Preliminary Tunnel

The average velocity and average temperature are found using the Fanno Flow equations. Equation 3.10 is solved for the wall temperature, T_w. The average velocity (V) and temperature at the wall (T_w) are now known. Equation 3.5 can now be solved for the temperature distribution by substituting the value for T_w and equation 3.9 for the velocity. With the assumption that the pressure is constant over the cross section, the density distribution is found using the result from solving 3.5 and plugging the result into equation 3.4. Figure 3-19 shows the results of solving equations 3.4 and 3.5 with the assumption that the pressure gradient in the vertical direction is zero. The results shown are for the unchoked flow conditions with the preliminary tunnel. Similar results were obtained for both the choked conditions in the preliminary tunnel and for flow in the in-draft tunnel.

3.3.2 Theoretical Density Compared to Measured Results

A comparison of the theoretical distribution of density from the surface to centerline for the preliminary tunnel is shown in Figure 3-21. The results shown are for the unchoked flow condition. The calculated theoretical density distribution is plotted as the solid black line. The measured density distributions from the Shack Hartman sensor at the exit of the small tunnel for the four different time frames (t1 to t4) are plotted using the indicated symbols. An average of the four Shack Hartman measured density values is calculated and plotted on as the solid red line. A ± 1.5% error band is also plotted indicating where the measured density value falls compared to the calculated theoretical values. As can be seen, the mean value of the measured density from the Shack Hartman sensor falls to within a 1.5% error band. This error can be attributed to the fact that the flow is turbulent and the noise in the measurement system. Similar results are shown for the in-draft tunnel in Figure 3-22.

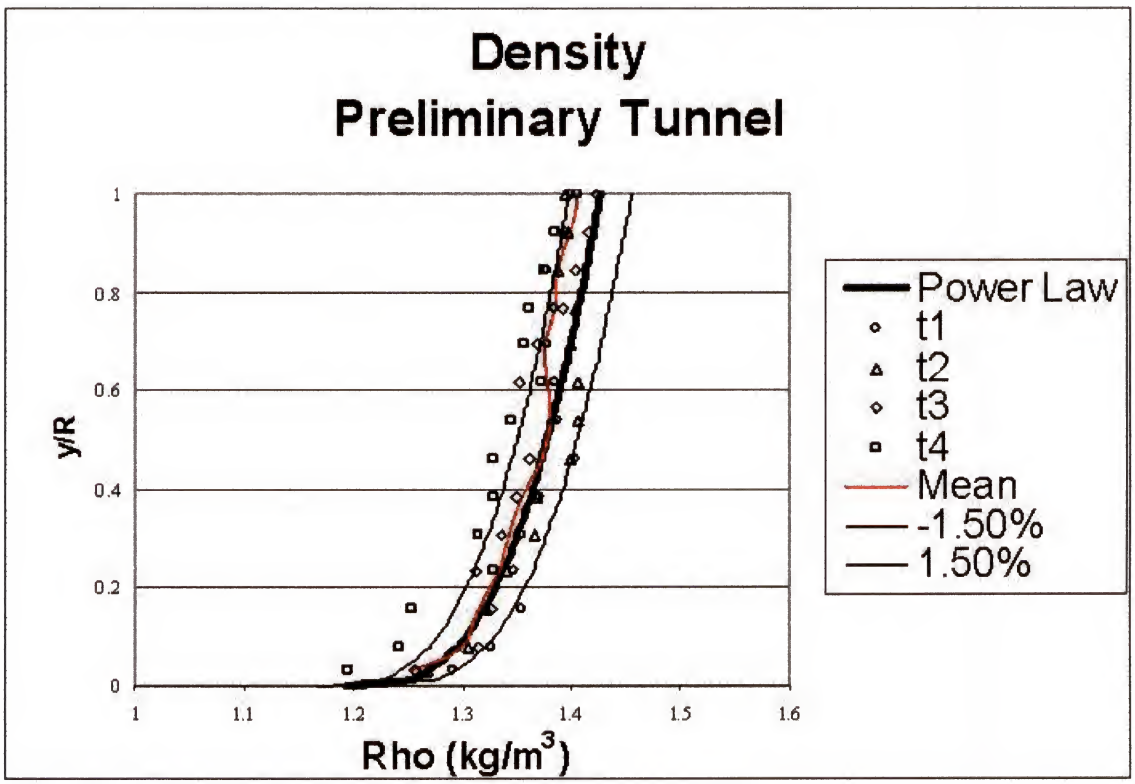

Figure 3-20 Shack Hartman Density, Preliminary Tunnel

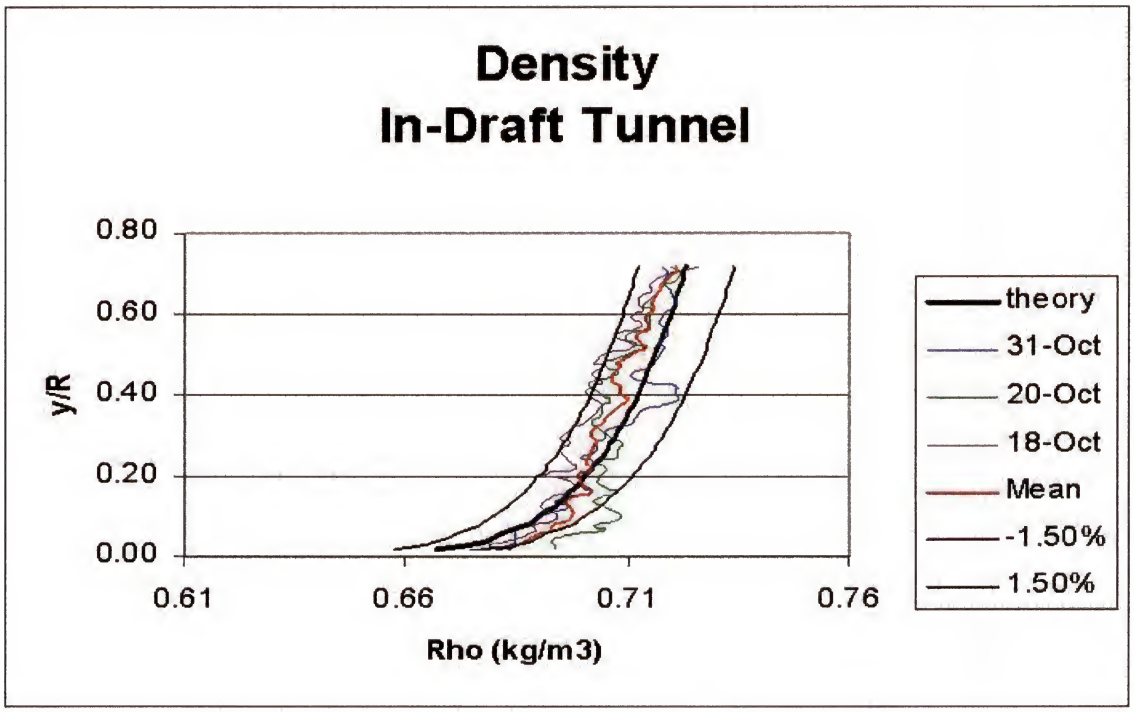

Figure 3-21 Shack Hartman Density, In-draft Tunnel

CHAPTER 4
EXPERIMENTAL DATA

This chapter describes the information that can be obtained about the flow over a two-dimensional cavity when coupling a Shack Hartman multiple exposed sensor with the in-draft tunnel design described in chapter 2.

4.1 Laser Timing options

There are two timing lengths that need to be addressed when using a Shack Hartman sensor. These are the spacing between the laser pulses and the integration time (the time the laser pulse is on). Spacing between laser pulses is a function of the cycle time of the cavity if a cycle exists. Integration time is a function of the time scales at which events occur in the flow for the given free stream conditions and geometry of the cavity. The time scale can be as small as the time scale of turbulence or the time it takes a particle to traverse the length of the cavity. With the spatial resolution well above the turbulent length scale, the integration time will be based on the time it takes a particle to traverse the spacing between spots recorded by the Shack Hartman sensor.

4.1.1 Laser Pulse Spacing.

A method to determine the spacing between laser pulses is to first identify the existence of a cycle if a cycle exists. This is done using the modified Rossiter equation (Rossiter 1964, Dix and Bauer 1993) given by:

$$f = \frac{U_\infty (m - \alpha)}{L\left(M_\infty \frac{a_\infty}{a_o} + \frac{1}{\Phi_D} \right)} \qquad 4.1$$

Here f is the frequency, U_∞ is the free stream velocity, m is an acoustic mode number, α is a phase constant (taken to be .25), L is the cavity length, M_∞ is the free stream Mach number, a_∞ is the speed of sound in the free stream, a_o is the speed of sound in the free stream at the stagnation temperature and Φ_D is the ratio of the mean velocity of the vortices separating from the leading edge of the cavity to the free stream velocity. For the first three modes, the expected frequencies are 3060, 7140, and 11220 Hz respectively. This corresponds to three possible times over which a cycle may take place (330, 140, and 90 microseconds). To ensure that the Shack Hartman sensor captures the results for the smallest cycle time, the four laser pulses have to be spaced so that four frames of data are taken over a minimum of 90 microseconds.

For the given Shack Hartman sensor, the minimum spacing that can be set is 10 microseconds. This is low enough that a third of a cycle can be captured even if the cavity is cycling at the third mode. With a spacing of 30 microseconds, a mode three cavity can be captured. A mode 2 cavity would require spacing on the order of 50 microseconds and a mode 1 cavity would require spacing on the order of 100 microseconds. For the series of tests, spacing was set at 10, 20, 30, 50 and 100 microseconds. Data were taken for all laser pulse spacing for both cavity geometries. An additional 3 tests were run at 50 microseconds spacing for the L/D = 4 and 2 additional tests were run at 20 microseconds for the L/D = 8. This resulted in 15 tests with 60 frames of data for the L/D = 4 cavity and 14 tests with 56 frames of data for the L/D = 8 cavity.

4.1.2 Laser Pulse Integration

The minimum integration time (the time the laser is on and data is being recorded on the camera CCD) was determined based on the velocity of a particle. The time for a particle to traverse the length of the cavity is approximately 100 microseconds found from the free stream velocity of 260 m/s and length of the cavity of .0254 m. There are 29 spots spanning the length of the cavity. Each spot is separated by 27 pixels for a total of 783 pixels over a 25.4-mm length. This equates to 0.0324 mm/pixel. The objective is to start integrating the light onto the CCD and be complete prior to a particle from the upstream spot traversing half the length between spots. This should prevent the spot from smearing. The time for a particle to travel half the distance between spots is found by taking the distance (13.5 pixels) times the length of a pixel (0.0324-mm/pixel) divided by the free stream velocity (0.260 mm/microsecond). This results in a maximum integration time of 1.71 microseconds. The laser pulse for these tests was integrated for 0.6 microseconds. The distance a particle would travel in 0.6 microseconds is roughly 5 pixels, which is less than a fifth of the distance between spots.

4.2 Shack Hartman Sensor Data

Various plots of the data obtained from the Shack Hartman sensor will be shown. All data was obtained for the same field of view. This field of view comprised the length of the cavity (25.4 mm) and a height of 25.4 mm above the floor of the cavity. Figure 4-1 shows pictorially the field of view. The flow is from left to right. The height of the tunnel is 50.8 mm. The L/D = 4 cavity model is shown. When the L/D = 8 model was used, the field of view extended nearer to the centerline of the tunnel, but still below the center line of the tunnel.

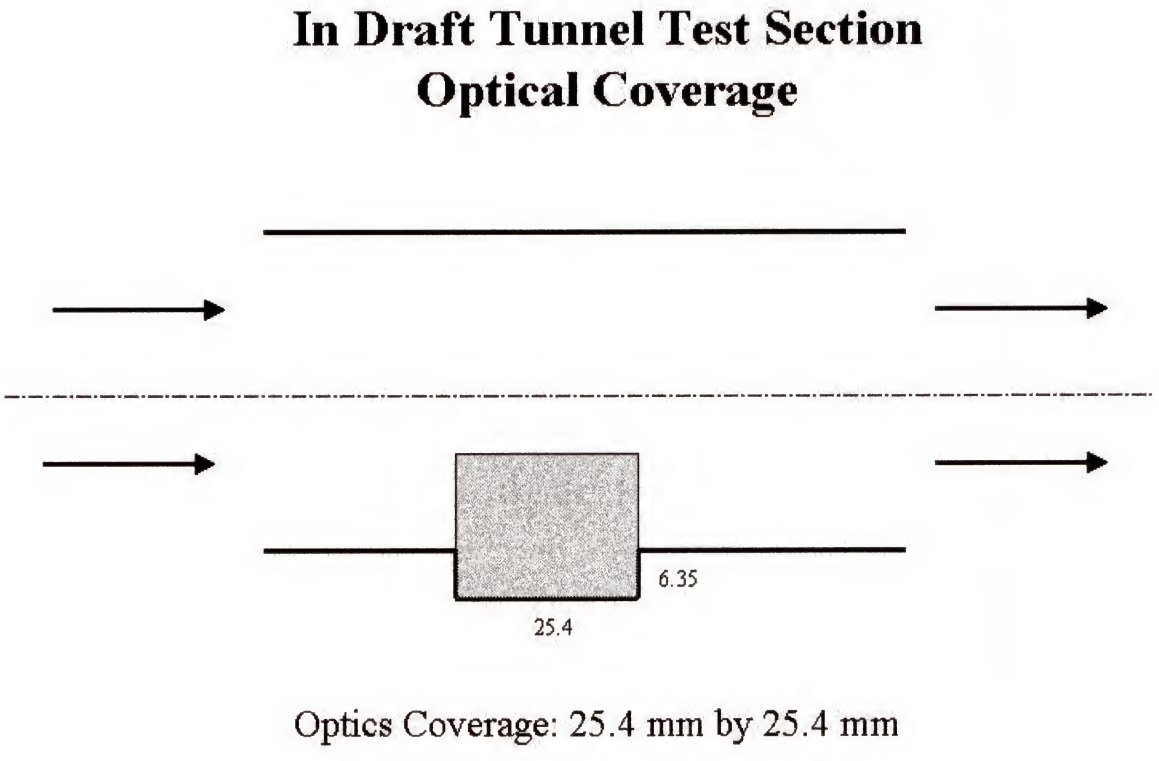

Figure 4-1 In-Draft Tunnel Test Section Optical Coverage

4.2.1 Shack Hartman Density Measurement

The Shack Hartman sensor measures the change in slope of a phase front as it passes through a varying density field. This change in slope is with respect to the zero slope of a phase front passing through a vacuum. The absolute phase is found by integrating the slope resulting in the following expression.

$$\Phi = \frac{2\pi}{\lambda}\int_0^w (k\rho + 1)dz \qquad 4.2$$

Where Φ is the phase angle, λ is the wavelength of the laser, k is the Gladstone-Dale constant equal to 0.2332 cm^3/g for air, ρ is the density distribution, and w is the width along which the integration is done. In implementing the Shack Hartman sensor, a

change in slope of the phase front is found by taking the difference between a reference frame at a known density distribution and a test frame where the density distribution is unknown. Each frame of data is integrated to find the absolute phase per equation 4.2. The difference between the absolute phase angle of the test frame and the reference frame is found by subtracting the reference frame absolute phase from the test frame absolute phase. This results in the following expression

$$\Delta\Phi = \frac{2\pi}{\lambda}\int_0^w k(\rho - \rho_b)dz \qquad 4.3$$

This expression is similar to the previous one except it now contains the additional term ρ_b, which is the known reference density when the flow is off. Gunia (1999) demonstrated a method to calculate the change in phase angle ($\Delta\Phi$) from the known change in slope of the phase front ($\Delta\Phi'$) using Single Value Decomposition (SVD). Land (2000) used this same technique to calculate the phase angle distribution for flow exiting from a converging/diverging nozzle. The same method used by Gunia (1999) and Land (2000) is used in this experimental investigation. The Shack Hartman sensor measures the change in slope of the phase front. The change in phase is found using Gunia's SVD method. The next step is to extract the density based on the change of phase angle, $\Delta\Phi$.

The flow over the cavity in the in-draft tunnel is assumed to be two-dimensional. The cavity spans the entire width of the tunnel. It is assumed that the gradients in the direction of integration are small compared to the gradients in the longitudinal and transverse direction. From equation 4.3, the Gladstone-Dale constant and density can be taken outside of the integral and the integration completed. The density when the flow is on is solved for and results in the following expression

$$\rho = \rho_b + \frac{\lambda}{360kw}\Delta\Phi \qquad \Delta\Phi \text{ in degrees} \qquad 4.4$$

The density distribution in and above the cavity is now available at a time resolution of less than 10 microseconds. The spatial resolution for the tests in the in-draft tunnel was less than 1 mm (approximately .88 mm). Figure 4-2 shows a typical density distribution plot for a L/D = 4 cavity. The scale shows that the sensor is sensitive enough to capture a change in density over a range of 0.1 Kg/m^3.

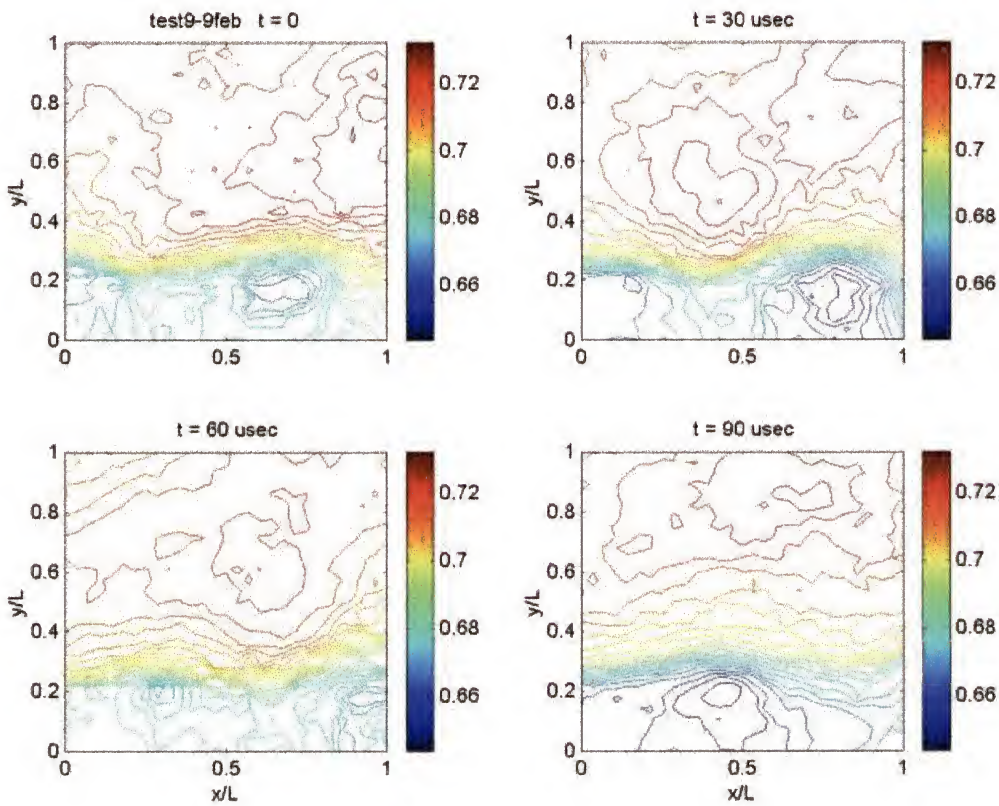

Figure 4-2 Shack Hartman Density Distributions

4.2.2 Two-Dimensional Assumption

Chung (2000 and 2001) investigated the three-dimensional effects on rectangular cavities for various L/W ratios over a wide range of L/D ratios. The test model consisted of a flat plate and an interchangeable instrumentation plate with a rectangular cavity. The

test model was 150 mm wide and 600 mm long with a single foot support mounted on the bottom wall of the test section. The front face of the cavity was located 500 mm from the leading edge of the flat plate. Figure 4-3 is a schematic of the test apparatus that was placed in the tunnel. Free stream conditions were set at Mach = 1.28 with a Reynolds number of $30.0 * 10^6$/m.

The three-dimensional effect is caused by flow entering the cavity over the sides along the length. The length to width ratio (L/W) is generally referred to as the three-dimensional parameter of a cavity flow. Chung (2000 and 2001) found that the effect of L/W is significant only at the aft half of the cavity as well as downstream of the cavity indicated by a change in the mean pressure downstream of the cavity and an increase in the magnitude in pressure fluctuations in the aft half of the cavity. For $L/W \leq 1.0$, little change was noted in the mean pressure distribution and fluctuation of the pressure. When the L/W ratio was set at 2.0, the mean pressure distribution on the floor of the cavity showed little change. However, the three dimensional effect at L/W = 2.0 was identified via a decrease in the mean pressure downstream of the cavity along with an increase in the pressure fluctuation on the floor of the cavity. Chung (2000 and 2001) also found that the three-dimensional effect on the pressure distribution is much greater for closed and transitional cavity flows than for open cavity flow. Stallings and Wilcox (1987) reported similar results.

As can be seen from Figure 4.3, the cavity in this test did not span the width of the tunnel. Flow was allowed to flow into the cavity along the length of the cavity. For the present investigation, the cavity spans the width of the tunnel. In addition, the L/W ratio for the present investigation is 0.5 (L = 25.4 mm, W = 50.8 mm). There should not be

any three-dimensional effects. However, there could be an impact from the flow along the wall. From pipe flow, it is known that the density gradient near the wall is large. This could impact the ability of the Shack Hartman sensor to record the change in slope of the phase front as the phase front passes through the disturb density field in and above the cavity. The set up for this investigation is similar to the one used by Zhang and Edwards (1990 and 1992) and Murray and Elliott (2001).

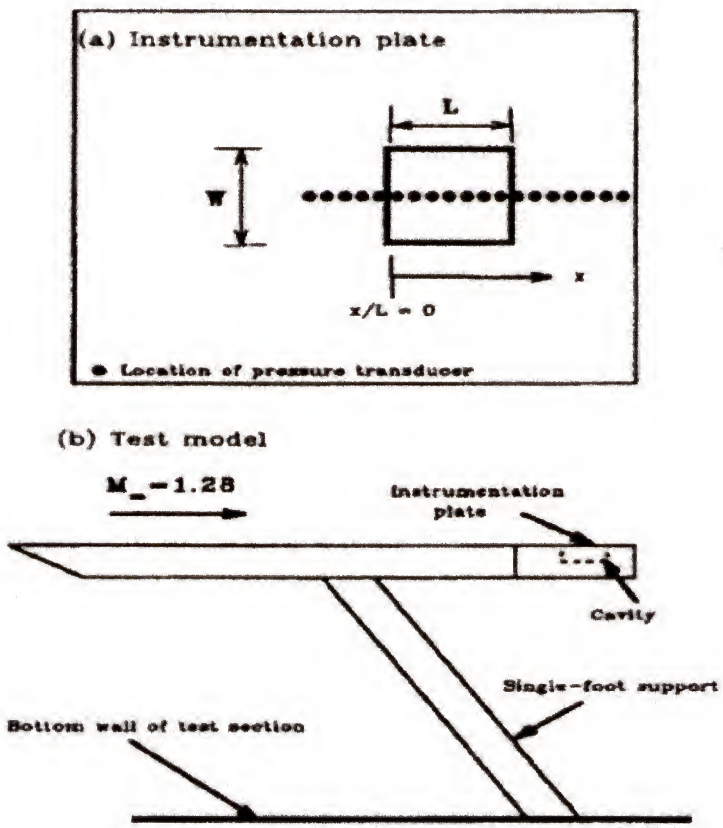

Figure 4-3 Three Dimensional Effect Test Configuration

Zhang and Edwards (1990 and 1992) cavity model had a constant depth (15mm) and constant width (114mm), which spanned the width of the tunnel. Length was varied to capture data for L/D = 1, 3, 5, 7, and 9 with corresponding L/W = 0.13, 0.39, 0.66, 0.92, and 1.18. Mach number was 1.5 and 2.5 with a Reynolds number of 30.0 * 10^6 per

meter. Oil flow visualization at Mach = 1.5 for L/D = 3.0 (L/W = 0.39) reported by Zhang and Edwards (1990) is shown in Figure 4-4. As can be seen, the flow is not uniform across the width of the cavity. There are large gradients in the vicinity of the wall. However, a case can be made that it is nearly symmetrical about the longitudinal centerline of the cavity.

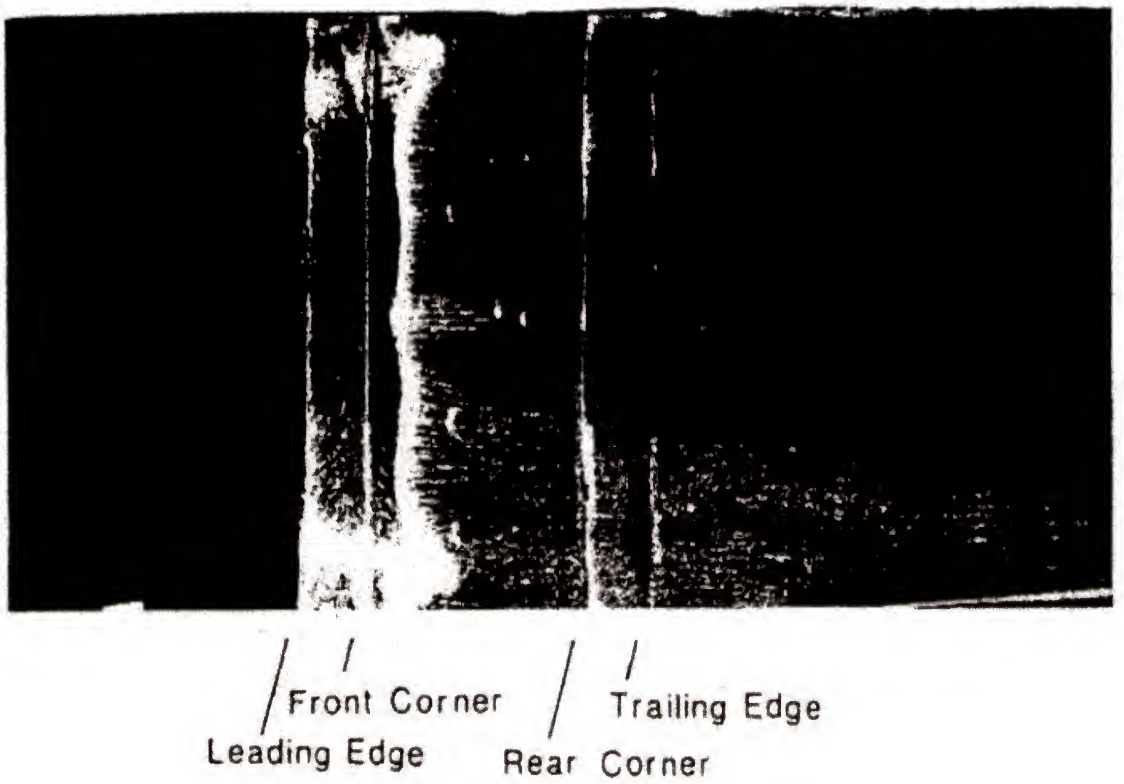

Figure 4-4 Oil Flow Visualization at Mach 1.5 for L/D = 3

Murray and Elliott (2001) cavity model had a depth of 12.7mm, width of 101.6mm, and length of 38.1mm. The width of the cavity spanned the width of the tunnel like Zhang and Edwards (1990 and 1992) and the experimental set up for the present investigation. L/D was 3.0 and L/W was 0.375. Mach number was 1.8, 2.1, 2.8, and 3.5. Reynolds number varied from 36.7 to 73.5 * 10^6 per meter. Per Murray and

Elliot (2001), "Plan views of the flow field were taken for each free stream Mach number and are shown in Figure 4-5. These plan view images give insight into the three dimensionality of the flow. For the lower two Mach numbers, dark bands are seen running from the top to the bottom of each frame (span wise in the tunnel). These bands indicate the entertainment of warmer fluid from the cavity into the shear layer in a highly two-dimensional fashion, spanning the full width of the cavity."

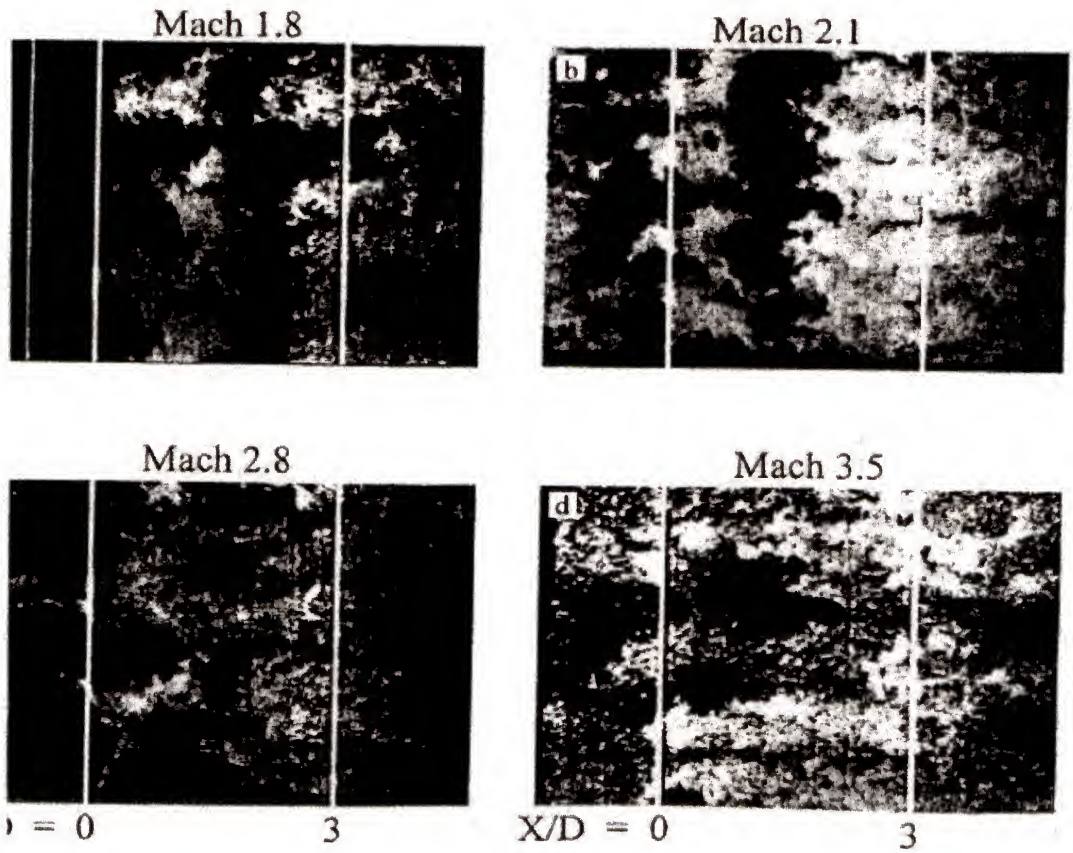

Figure 4-5 Schlieren Plan Views of Flow Over Cavities

Flows over cavities that span the width of the tunnel are not strictly speaking two-dimensional. However, an examination of Figures 4-4 and 4-5 does reveal that the flow is nearly symmetrical about the longitudinal centerline of the cavity for the lower Mach numbers investigated (1.28, 1.8, and 2.1). For this investigation, the test set up is similar

to that of Zhang and Edwards (1990 and 1992) and Murray and Elliott (2001) in that the cavity model spans the width of the tunnel. The Mach is subsonic near the transonic range but at the lower end of the transonic range (0.8 to 1.2). Flow should be symmetrical about the centerline of the tunnel. Wall effects will have a tendency to retard the flow at or near the wall. Moving away from the wall, the flow will increase in velocity. A corresponding increase in density will occur as predicted by pipe flow. With this symmetrical change in density in the span wise direction, the slope of the wave front will initially bend in one direction up to the centerline of the tunnel and will bend back to its original slope over the second half of the tunnel. Differentiating equation 4.2 with respect to the span wise coordinate results in

$$\Phi' = \frac{2\pi}{\lambda}(k\rho + 1) \qquad 4.5$$

The density (ρ) is a function of the distance along the path of the light through the varying density medium. At the beginning of the width of the tunnel, the slope will take on a certain value. This value will continue to increase as the density increases up to the centerline of the tunnel. At the centerline, the density will start to decrease and continue to decrease until it reaches the wall value at the other side of the tunnel/cavity. The slope of the phase front passing through a symmetrical varying density field will have a net no change. When a portion of the phase front after passing through this symmetrical density field is focused to a spot via a Shack Hartman sensor, the change in position of the spot will be the result of a change from the reference no flow density. The change in slope of the phase front passing through a symmetrical density field will be the result of the change in density in the longitudinal and transverse direction.

In summary, for the present investigation, the three-dimensional effect should not be a problem since the L/W ratio is less than 1.0 and the cavity spans the width of the tunnel, which prevents flow into the cavity along the length of the cavity. In addition, the cavities being investigated are classified as open. Three-dimensional effects are more dominant for closed and transitional cavities. Wall effects do cause a change in density along the span wise direction. But since this change is symmetrical, the change in slope that will be measured by the Shack Hartman sensor will be a net zero. The two-dimensional assumption appears to be a valid assumption for this investigation.

4.3 Direct Results

The density distribution is directly measurable using a Shack Hartman sensor. Since time and spatially resolved data is available, an estimate of the local time derivative and the gradient of density distribution can be calculated. This provides additional information about the flow.

4.3.1 Density Gradient in y Direction

Figure 4-6 is the gradient of the density in the y direction. The gradient was calculated using the gradient function in MATLAB and the Shack Hartman density like the one shown in Figure 4-2. MATLAB uses a forward or backward first order difference scheme for values on the boundary. For internal points, it uses a second order, central difference scheme. Although the shear/mixing layer is readily observable in the instantaneous density distribution, a method was needed to show the position of the shear layer on various plots that can be derived from the density distribution. The gradient in the y direction was used to estimate the position of the shear layer. The maximum value of the instantaneous density gradient in the y direction in the vicinity of the top of the

cavity was found. The location of this maximum is called the center of the shear/mixing layer. A fifth order polynomial was fitted through these points. This fifth order polynomial is plotted on the charts. Figure 4-6 not only shows the gradient of density in the y direction but also shows the position of the shear layer.

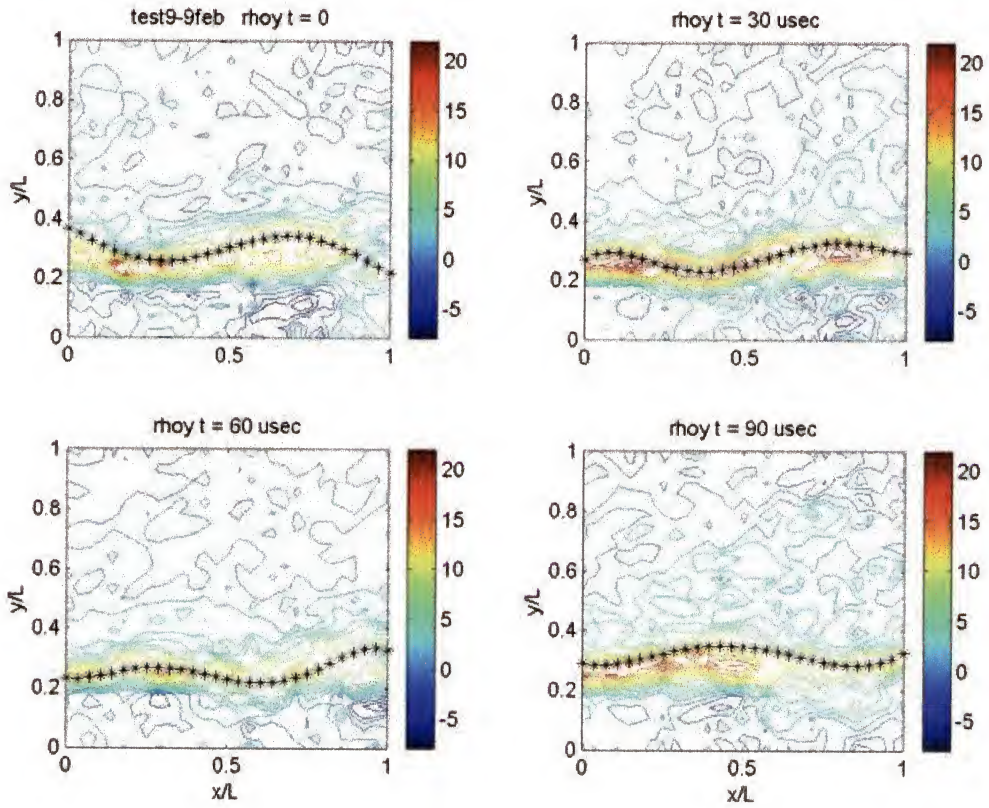

Figure 4-6 Density Gradient in Y direction

4.3.2 Density Gradient in x Direction

The gradient of density in the x direction was obtained using the same procedures as for the gradient in the y direction. An example of the gradient in the x direction is shown in Figure 4-7. An examination of the plot shows peak and valley density gradients in the vicinity of the shear layer. It is possible that this is what Rossiter (1964) saw from his Schlieren visualizations. From these peaks and valleys of density gradients in the x

direction, Rossiter would have been able to derive his edge tone frequency equation. Murray and Elliott (2001) were able to use Schlieren coupled with a high-speed camera and measure the position and velocity of these structures. Forestier et al. (1999) also reported using Schlieren coupled to high-speed camera and showed the existence of flow structures in the vicinity of the shear layer. With these structures visible using traditional flow visualization techniques, the empirical constant of the ratio of the vortices velocity to the free stream velocity has been shown to be over a range of .35 to .65 compared to a value of .57 as first suggested by Rossiter (1964).

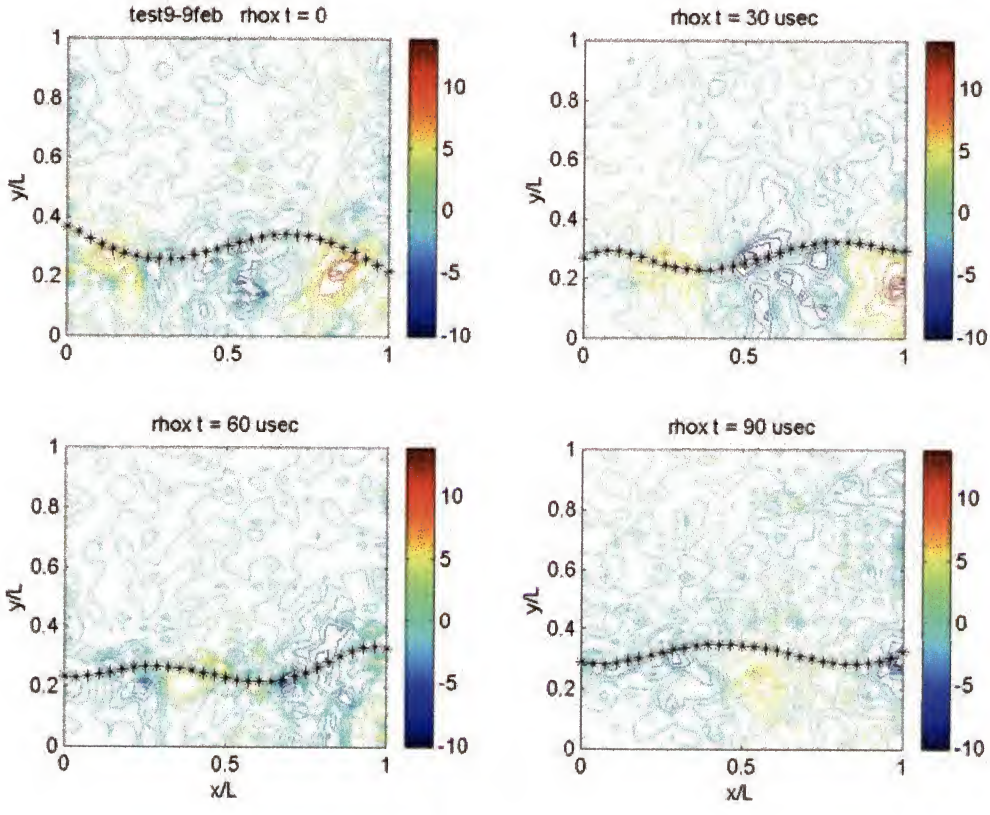

Figure 4-7 Density Gradient in X direction

4.3.3 Local Time Derivative of Density

Figure 4-8 is a plot of the local time derivative of density. The local time derivative was calculated using a first order, backward difference approximation. That is why you see only three plots. A first order, forward difference could be done for the initial pulse but it would look exactly like the backward difference at t = 30. It was felt that including it would only confuse the issue.

From the continuity equation, $\rho_t + \nabla \bullet \rho U = 0$, when ρ_t is negative, the quantity $\nabla \bullet \rho U$ is positive. The dot product of two vectors is defined as the product of the magnitudes of the vectors times the cosine of the angle between them. The result of the dot product is positive only when the angle between the vectors falls within the range of plus or minus 90 degrees. Now the direction of the gradient is 45 degrees to the horizontal axis. For the quantity $\nabla \bullet \rho U$ to be positive, the vector ρU must make an angle with the horizontal axis in the range of –45 degrees to +135 degrees. If the sign of ρ_t is known, a general idea of the direction of the flow and where the cavity is filling and emptying along the length of the cavity can be determined. From Figure 4-8, where the contours are negative (blue), the quantity $\nabla \bullet \rho U$ is positive. This suggests that the flow is headed up and to the right or exiting the cavity. Red regions would then suggest that the cavity is filling in these areas. The time sequence of the frames also suggests that the location along the length of the cavity where filling and emptying occur is not constant. The shear layer dips into the cavity when the filling of the cavity occurs. These sequences of ρ_t suggest that the shear layer dips into the cavity at other places besides the aft wall.

The local time derivative plots provide the same type of information that was shown by Zhang and Edwards (1990) when they used holographic Interferometry in a differential mode. What they were able to see were the flow structures (peaks and valleys of changes in density) in the shear layer. Since they could record only one picture at a time, only the existence and position of the structures was identified. The velocity could not be obtained since they did not have time resolved data.

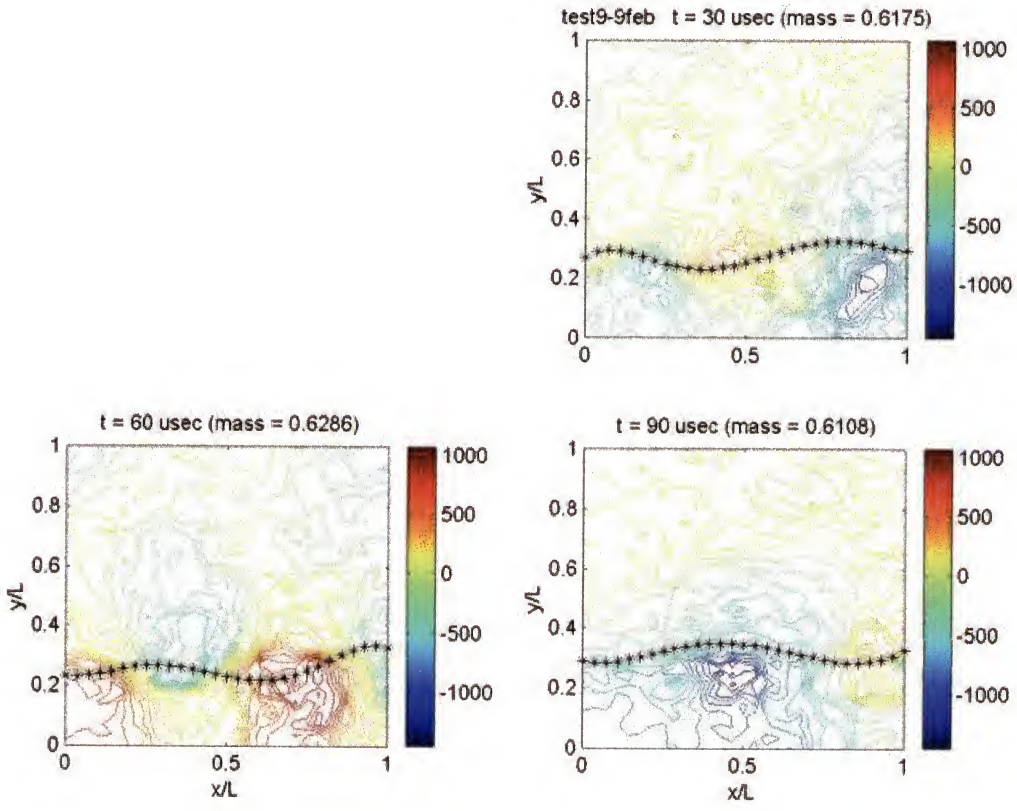

Figure 4-8 Local Time Derivative of Density

4.3.4 Digital Dark Central Ground (DCG)

Armed with the gradient in the x and y direction, a digital Dark Central Ground can be constructed by finding the magnitude of the gradient. This is done by taking the square root of the sum of the squares of the gradient in the x and y direction. Results are

shown in Figure 4-9. As can be seen, even though the gradient was derived from known values of the density, the large gradients in the vicinity of the shear layer overshadow the gradients in the cavity. Little information is provided about flow activity in the cavity. This was one of the short falls in using Schlieren and DCG to quantitatively analyze flow in a cavity that had subsonic free stream flow. Gradients were not large enough everywhere to allow one to identify all the structures that were present in the flow. The shear layer gradient overshadowed all other gradients. When analyzing choked flow where shocks and expansion waves were present, these gradients were much larger than the gradients in the cavity. Therefore, flow activity in the cavity could not be analyzed. Even when flow is unchoked and gradients are smaller in the vicinity of the shear layer, they are still much larger than those in the cavity and therefore are not visible. Even when a digital DCG image is made, the same problem occurs. This demonstrates that a Shack Hartman sensor is really needed to experimentally examine flow in and above a cavity with subsonic flow in the free stream.

Derived results can be estimated using the density distribution obtained from the Shack Hartman sensor along with some simplifying assumptions. Examples of derived results are the pressure coefficient distribution on the surface of the cavity, an ensemble average from which deviations from this ensemble average can be calculated, and a pressure distribution.

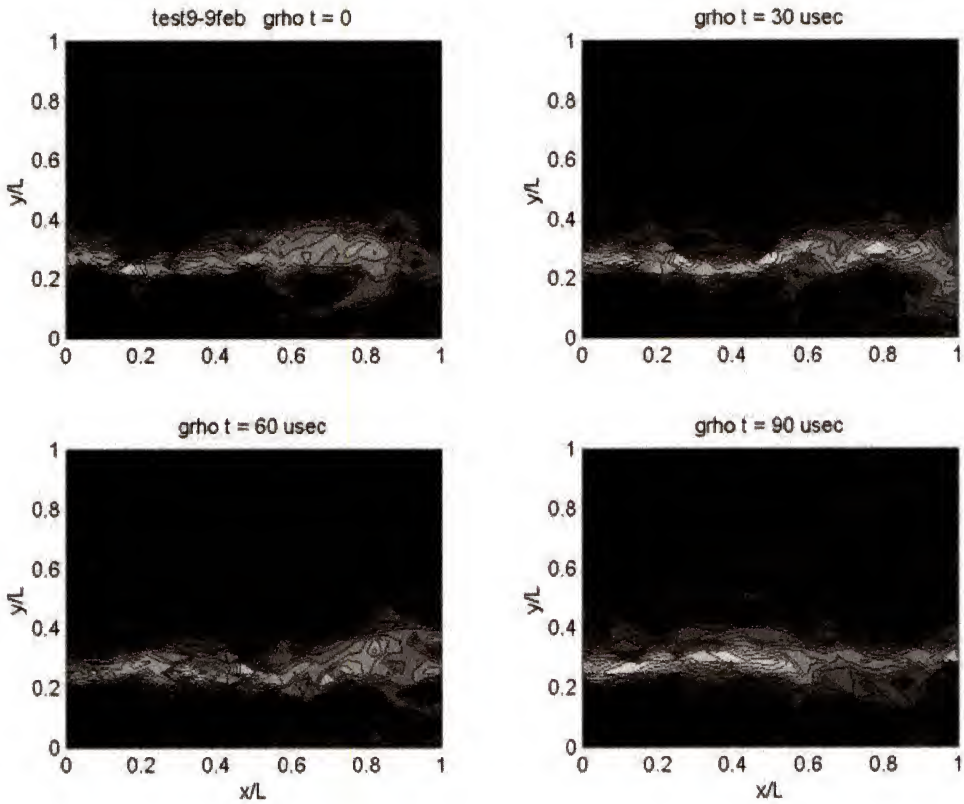

Figure 4-9 Gradient of Density (Digital Dark Central Ground)

4.4 Derived Results

4.4.1 Pressure Coefficient (Cp) Distribution

An estimate of the pressure coefficient on the surface of the cavity is calculated from the density. The equation for the pressure coefficient is defined as:

$$C_p = \frac{P - P_\infty}{\frac{1}{2}\rho_\infty U_\infty^2} \qquad 4.5$$

Starting with this equation, using the perfect gas law, defining star quantities as the ratio of the local value to the free stream value, and substituting into the pressure coefficient equation yields

$$C_p = \frac{\rho^* T^* - 1}{\frac{\gamma}{2} M_\infty^2} \qquad 4.6$$

T* is the ratio of the wall temperature to the free stream temperature. Heller et al. (1970) modified the Rossiter equation to take into account the temperature in the cavity being different from the free stream temperature. In their experiment, they determined that the cavity temperature was related to the free stream by the following expression

$$\frac{T}{T_\infty} = 1 + r\frac{\gamma - 1}{2} M_\infty^2 \qquad 4.7$$

Where r is a recovery factor. From their experiments, the recovery factor was determined to be in the range of 0.8 to 1.0. For this investigation, a value of 0.9 was used.

The ratio of the local density to the free stream density is ρ*. The Shack Hartman sensor measures the local density. The free stream density is known from the tunnel conditions.

Substituting for T* and ρ* gives the pressure coefficient on the surface of the cavity as a function of the density distribution.

$$C_p = \frac{\frac{\rho}{\rho_\infty}\left(1 + r\frac{\gamma - 1}{2} M_\infty^2\right) - 1}{\frac{\gamma}{2} M_\infty^2} \qquad 4.8$$

This equation provides the exact pressure coefficient on the surface of the cavity provided one has the density on the surface of the cavity. It can only be estimated from these tests since the density is not known on the surface. However, the density very near the surface (< 0.88-mm) is known and this is the value used. Figure 4-10 and 4-11 are

the mean pressure coefficient distributions on the surface of the cavities for the two respective cavity geometries.

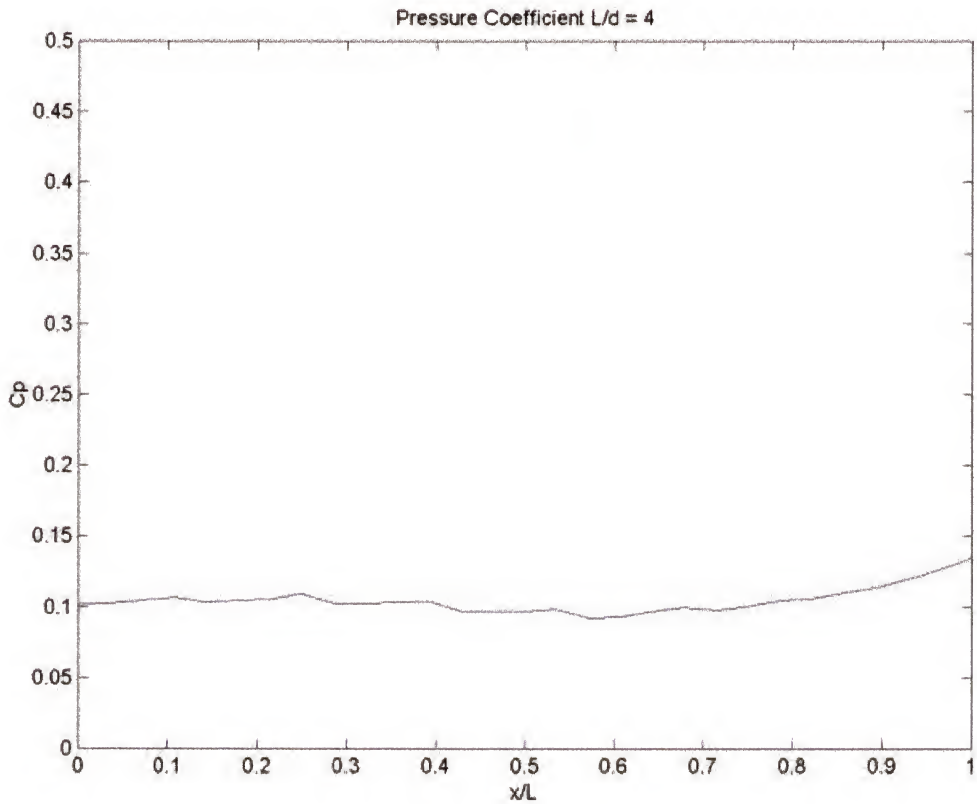

Figure 4-10 Mean Pressure Coefficient Distribution, L/D = 4

In general, cavities are classified as open for L/D < 8, transitional for 8 < L/D < 12 and closed for L/D > 12. Deep cavities are classified as L/D < 1 (Dix and Dobson 1990 and Plentovich et al. 1993). This classification is based on the mean pressure coefficient distribution on the floor of the cavity. According to these classifications, the L/D = 4 should behave as an open cavity. The L/D = 8 cavity can be either open or transitional based on these classifications. As can be seen from Figure 4-10, the L/D = 4 cavity acts more as a deep cavity (L/D < 1) as indicated by a fairly flat pressure coefficient distribution. Past experimental investigations have shown that at transonic

Mach numbers, a given L/D cavity may change its classification to a less shallow cavity when the depth is reduced from 2.4 inches to 1.2 inches while keeping the L/D ratio constant (Plentovich 1990, Plentovich et al. 1991, and Plentovich et al. 1993). The depth for the L/D = 4 cavity in the present tests is an order of magnitude smaller, 0.25 inches. It appears that the L/D = 4 cavity for this investigation follows this trend. From Figure 4-11, the L/D = 8 behaves as an open cavity but shows signs of being transitional as indicated by a slight concave-down shape to the Cp distribution over the last half of the cavity. This particular cavity classification agrees with past attempts at cavity classification.

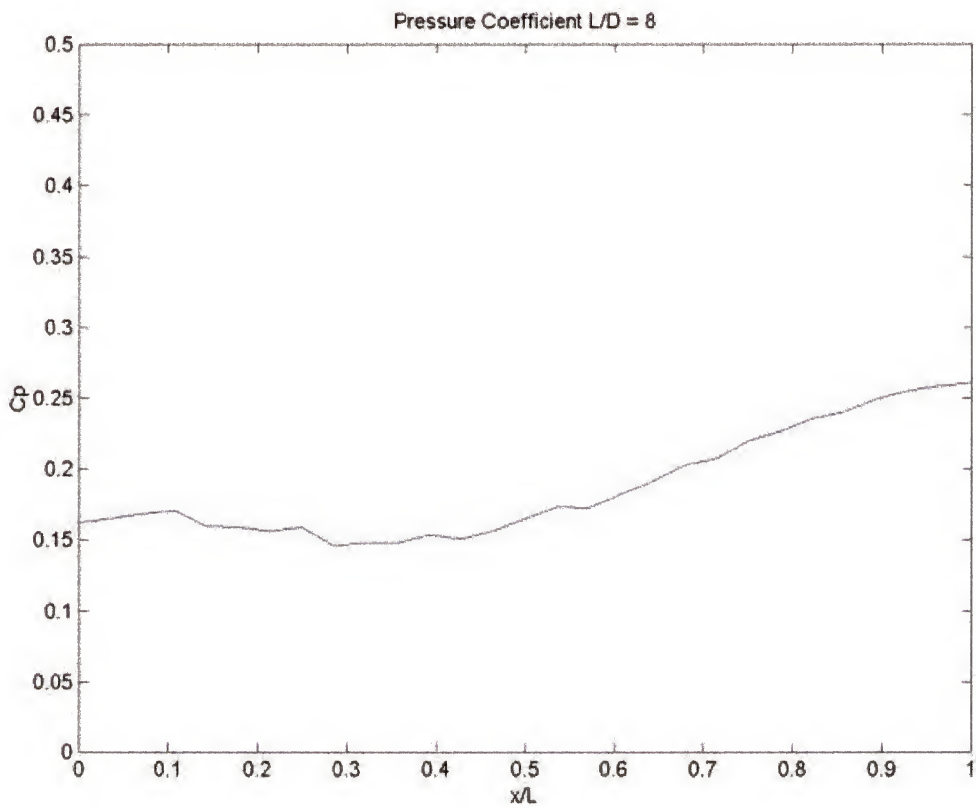

Figure 4-11 Mean Pressure Coefficient Distribution, L/D = 8

4.4.2 Ensemble Average ($\overline{\rho}$)

Ensemble averages were computed for each cavity geometry. The results are shown in Figures 4-12 and 4-13. The ensemble average was calculated by sequentially averaging each frame of density for each cavity geometry. There were a total of 15 tests with 4 frames of data per test for a total of 60 frames for the L/D = 4. There were 56 frames of data for the L/D = 8 cavity. The ensemble average converged after sequentially averaging 20 frames of data. Also shown in Figures 4-12 and 4-13 is the convergence history for the ensemble average. The ensemble average is used to find a density variation by subtracting the ensemble average from the instantaneous density for each frame of data taken.

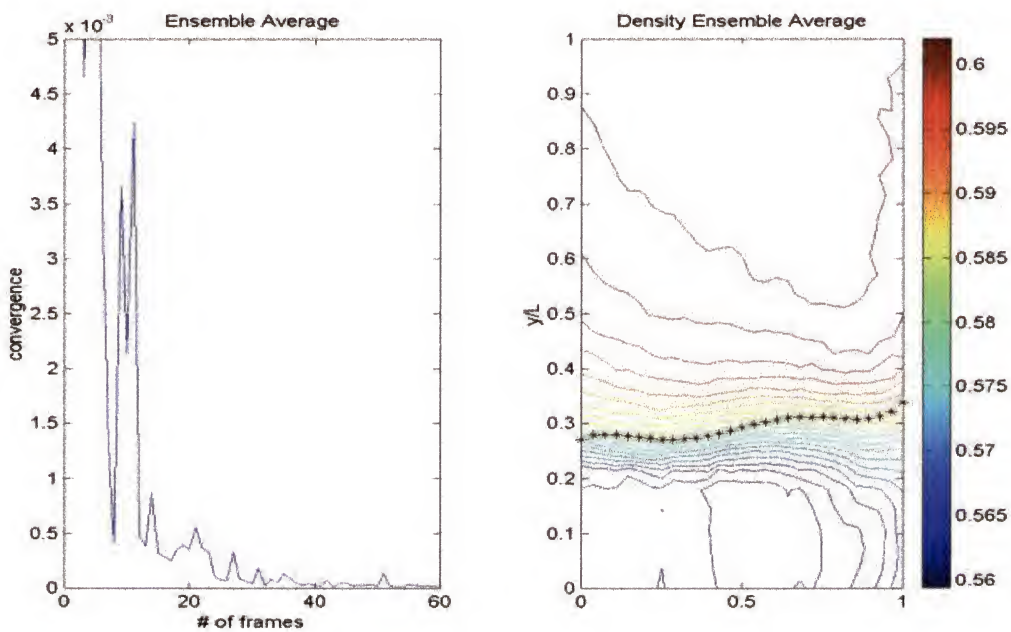

Figure 4-12 Density Ensemble Average, L/D = 4

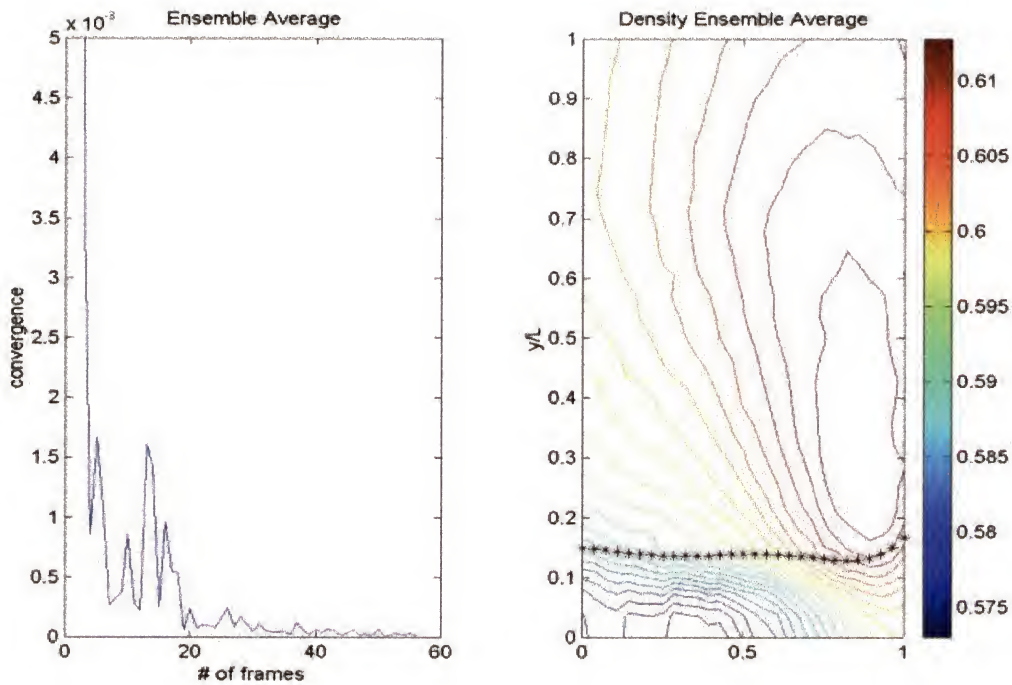

Figure 4-13 Density Ensemble Average, L/D = 8

4.4.3 Density Deviation (ρ')

Large-scale structures in the shear layer can be located by calculating the deviation of density using the ensemble average and the instantaneous density measurements. The density is composed of an average and a deviation from that average. This deviation from the average is used to locate the large-scale structures within the shear layer. The density deviation is found by subtracting the ensemble average from the instantaneous values of density.

$$\rho' = \rho - \overline{\rho} \qquad 4.9$$

Figure 4-14 shows the results of computing the deviation of density by subtracting the ensemble average shown in Figure 4-12 from the instantaneous density distributions shown in Figure 4-2. Readily identifiable are peaks and valleys of density deviation from the ensemble average in the shear layer. These peaks and valleys are readily identifiable

and appear to move downstream as the position of these peaks and valleys changes as a function of time. Since the position of the structures can be located, the velocity of the structures can also be calculated.

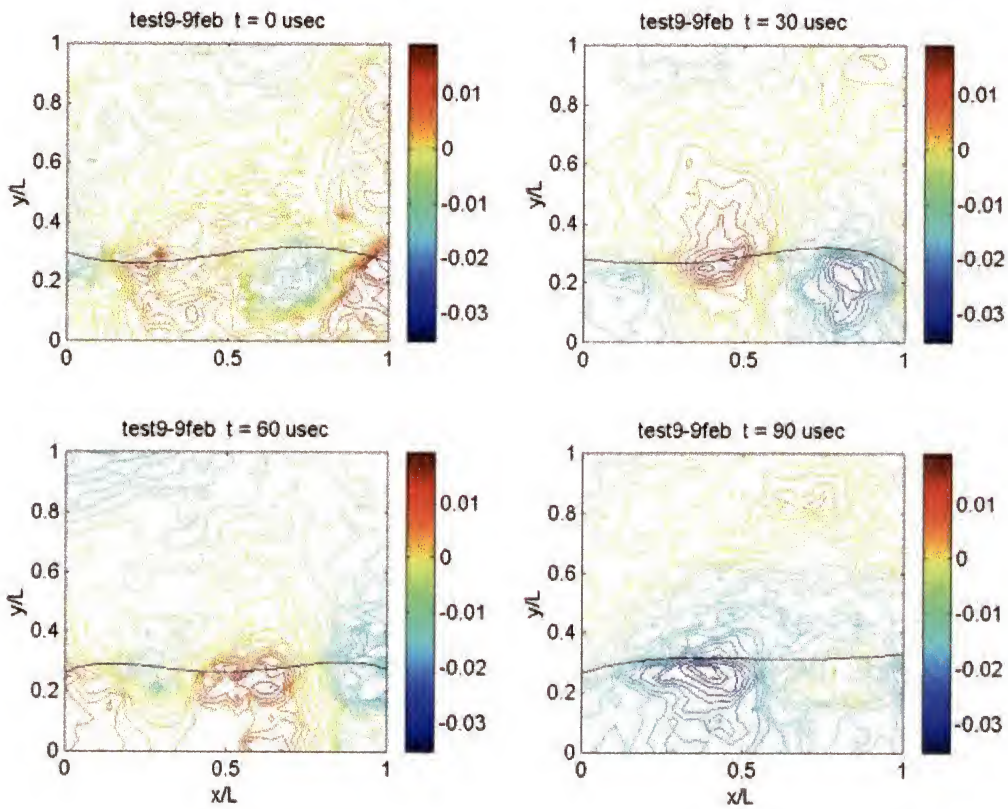

Figure 4-14 Density Deviation

A comparison of the density deviation with the gradient in the x direction and the local time derivative is shown in Figure 4-15. An estimate of the position of the shear layer large-scale structures and their velocity can be found from either the deviation of density, the gradient of density in the x direction or the local time derivative of density plots. Any of these plots can be used to find the empirical constant in the modified Rossiter equation, Φ_d.

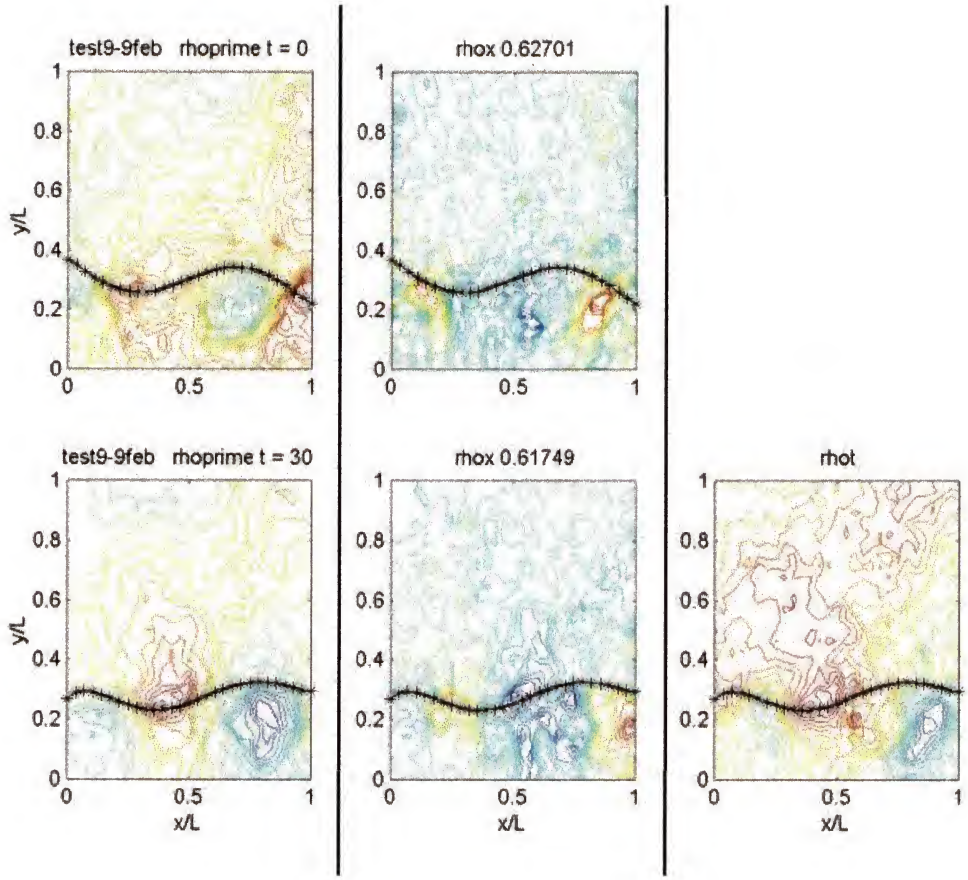

Figure 4-15 Comparison of Density Deviation, X Gradient, Time Derivative

4.4.4 Pressure Distribution (P(x,y))

The temperature in the cavity up to the start of the shear/mixing layer is assumed to be constant. Heller et al. (1970) modified the Rossiter equation to take into account that the temperature in the cavity will be different from the free stream temperature. In the experiment, they concluded that the cavity temperature was related to the free stream by the following expression

$$\frac{T}{T_\infty} = 1 + r\frac{\gamma - 1}{2}M_\infty^2 \qquad 4.10$$

Where r is a recovery factor. For turbulent flows, r is the cube root of the Pandtl number and equal to approximately 0.9. Since the free stream temperature is known from the known tunnel conditions, an estimate for the cavity temperature can be calculated.

It is assumed that this temperature is constant up to the beginning of the shear/mixing layer. For the flow conditions of this test, the velocity of the large-scale structures in the cavity normalized to the free stream velocity is 0.40. With a free stream Mach number of 0.8, the Mach number in the cavity is approximately 0.3. The flow over the cavity is adiabatic. There is no change in total temperature. Free stream conditions are obtained via flow through a constant area duct with friction. For a Mach number of 0.3, the ratio of To/T = 1.018. By making the assumption that the temperature in the cavity is constant causes less than a 2% error.

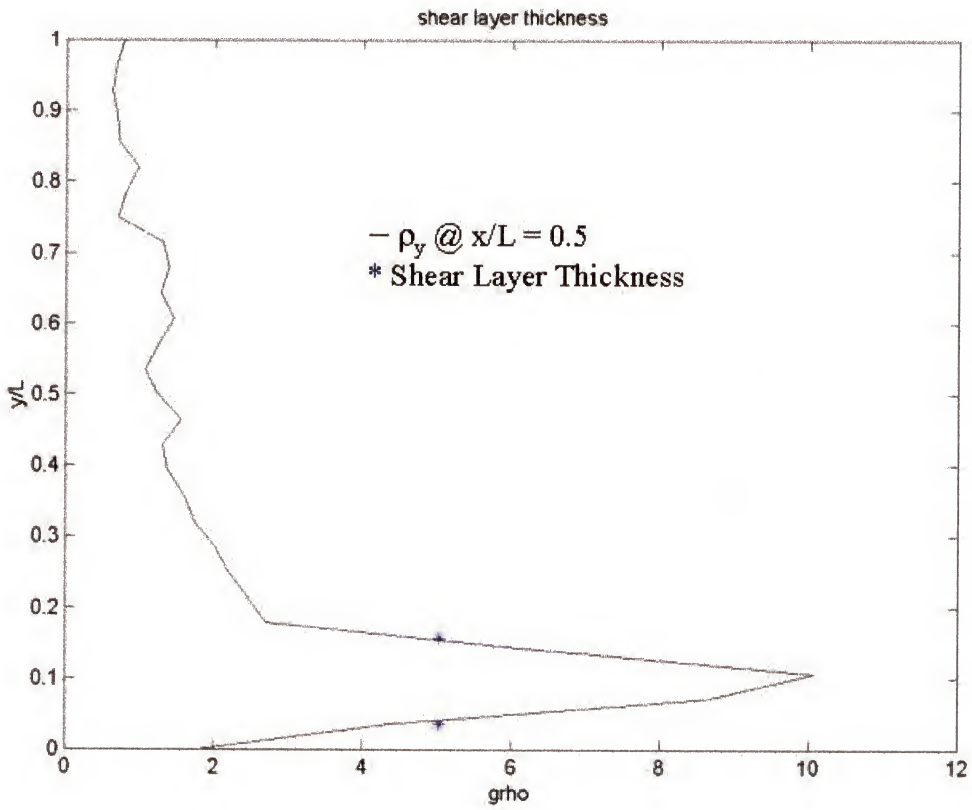

Figure 4-16 Shear Layer Thickness

The next step in estimating the temperature distribution is to determine where the bottom of the shear layer begins. Figure 4-16 shows a vertical cut of the gradient of

density in the y direction at location x/L = 0.5. The center of the shear layer is established as the largest value of the gradient in the y direction. The start of the shear layer is assumed to start at a value half the maximum value of the gradient in the y direction. This point is plotted as a blue star in the Figure 4-16. Half the value was selected based on the way the beam width of a radar beam is determined. The width is normally determined 3dB down from the maximum power value. 3dB is half the max value. I used the same method to determine the start of the shear layer in the cavity.

After passing the maximum gradient value that establishes the center of the shear layer, a constant decrease in the gradient at a decreasing rate occurs until reaching y/L = 1.0. This suggests that the top "half" of the shear layer is larger than the bottom "half" of the shear layer. In order to find the temperature, the thickness of the bottom and the top of the shear layer must be taken into account.

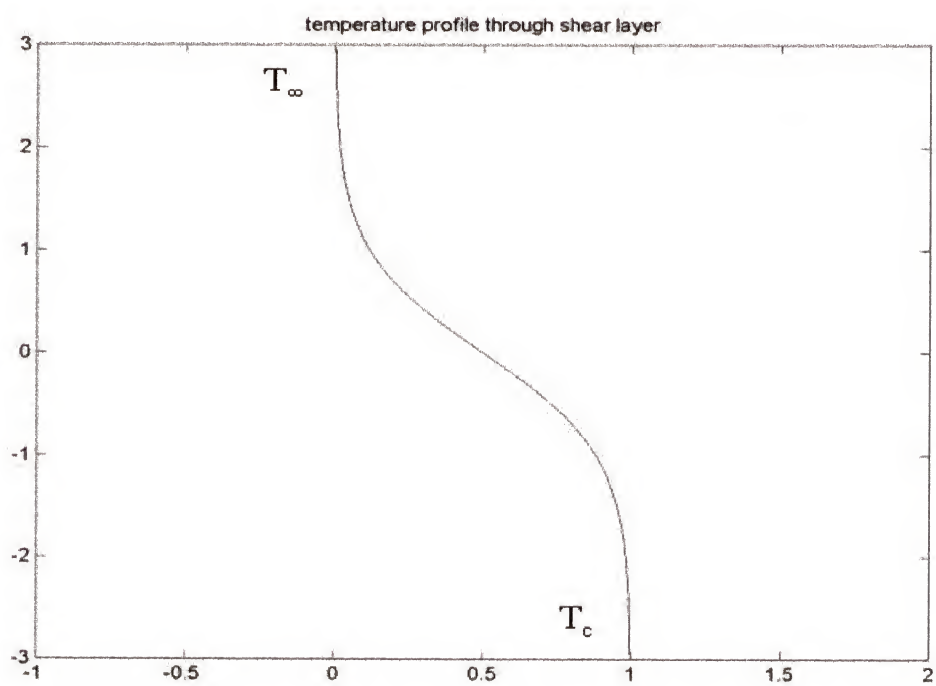

Figure 4-17 Theoretical Shear Layer Temperature Profile

At the beginning of the shear layer, the temperature will start to decrease as the velocity increases to the free stream velocity. Per John (1984), a temperature distribution in a compressible-flow shear layer is given as shown in Figure 4-17. This temperature distribution can be approximated using the hyperbolic tangent function.

The temperature in and above the cavity is calculated in three steps. The first step is from near the surface to the beginning of the shear/mixing layer. This is assumed constant and is calculated using equation 4.10. At the start of the shear layer to the center of the shear layer the temperature is calculated using the following expression

$$T = T_c + (T_\infty - T_c)\frac{1 + \tanh(-3y^*)}{2} \qquad 4.11$$

$$y^* = \frac{y - y_{mid}}{y_{mid} - y_{low}} \qquad 4.12$$

Where y_{mid} is the center of the shear layer and y_{low} is the start of the shear layer in the cavity. Form the center of the shear layer to the free stream the temperature is calculated using the same equation 4-11 but a different definition of y*. From the middle of the shear layer to the y/L=1.0, y* is defined as

$$y^* = \frac{y - y_{mid}}{y_{top} - y_{mid}} \qquad 4.13$$

Where y_{top} is the free stream and y_{mid} is the center of the shear layer.

Executing this method for calculating the temperature in the cavity for the example presented is shown in Figure 4-18. What is plotted is the calculated temperature normalized to the cavity temperature (T/Tc). Also shown on the plot is the measured density normalized to the surface density. The temperature has a shape suggested by

John (1984) for a compressible shear layer. The density distribution looks like a mirror image of the temperature distribution.

It is admitted that the temperature is not known exactly. This is an estimate. For this test, the flow in the tunnel is produced using only friction (adiabatic). An estimate of the starting or cavity temperature can be established. How the temperature behaves as the velocity increases through the compressible shear layer is known. An estimate of how the pressure behaves can be estimated using the assumed behavior of the temperature along with the measure density.

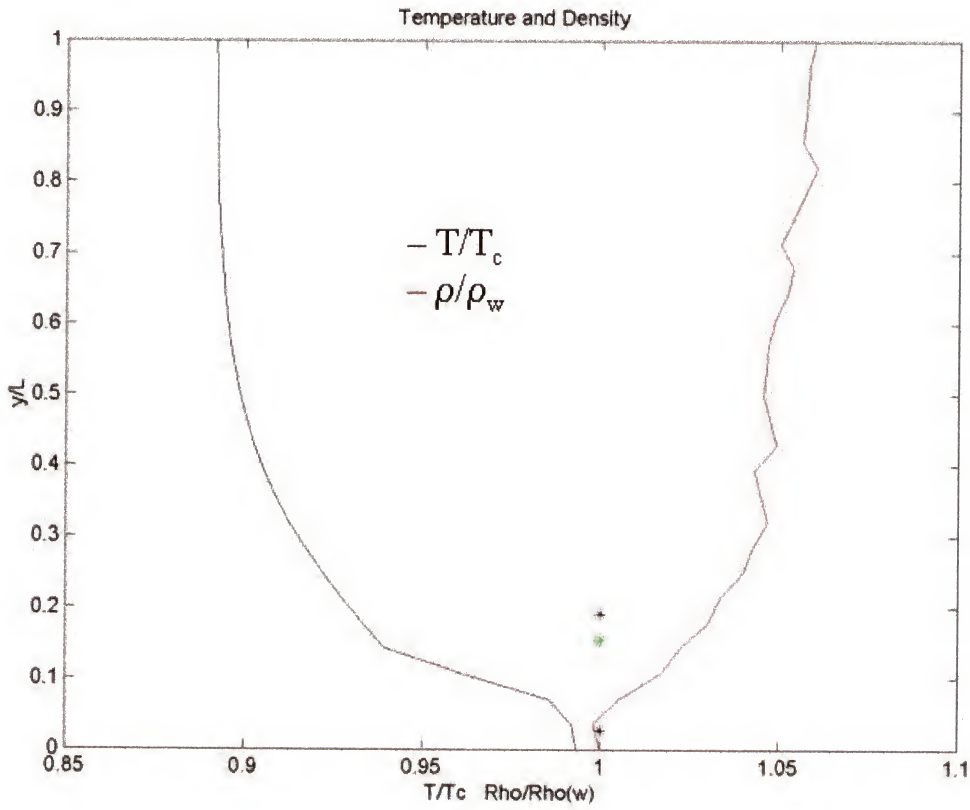

Figure 4-18 Estimated Shear Layer Temperature Profile

With these assumptions, the pressure distribution in and above the cavity is calculated and is shown in Figures 4-19 and 4-20. What is shown is the pressure

distribution calculated from the density ensemble average. The largest pressure values are at the aft wall where the shear layer large-scale structures interact with the aft wall as they move downstream and interact with the aft wall. Once past the shear layer, the change in temperature in the vertical direction along with the change in the density distribution show that the pressure changes are very small compared to the changes in the cavity and shear layer and also that the pressure is more stratified.

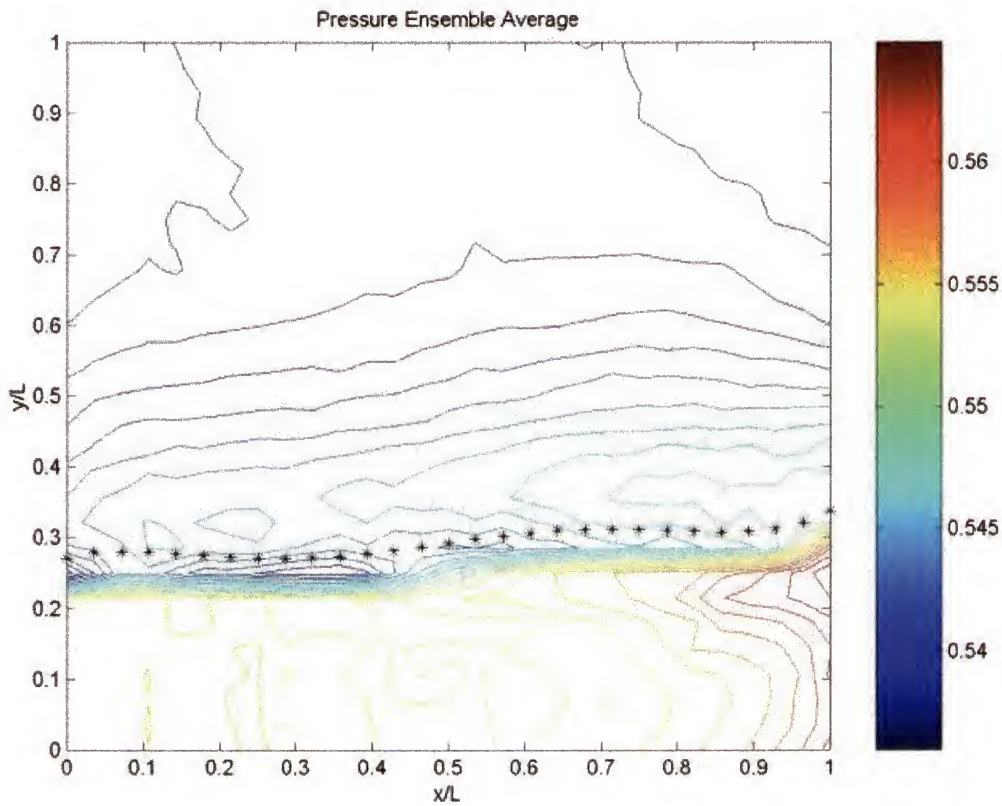

Figure 4-19 Pressure Distribution, L/D = 4

The pressure values above the L/D = 4 cavity suggest that the cavity is behaving as a deep cavity indicated by the pressure patterns above the cavity parallel to the longitudinal direction. The L/D = 8 cavity shows a source of pressure fluctuation on the

aft wall of the cavity as indicated by the pressure patterns emanating from the aft wall and pointed more upstream.

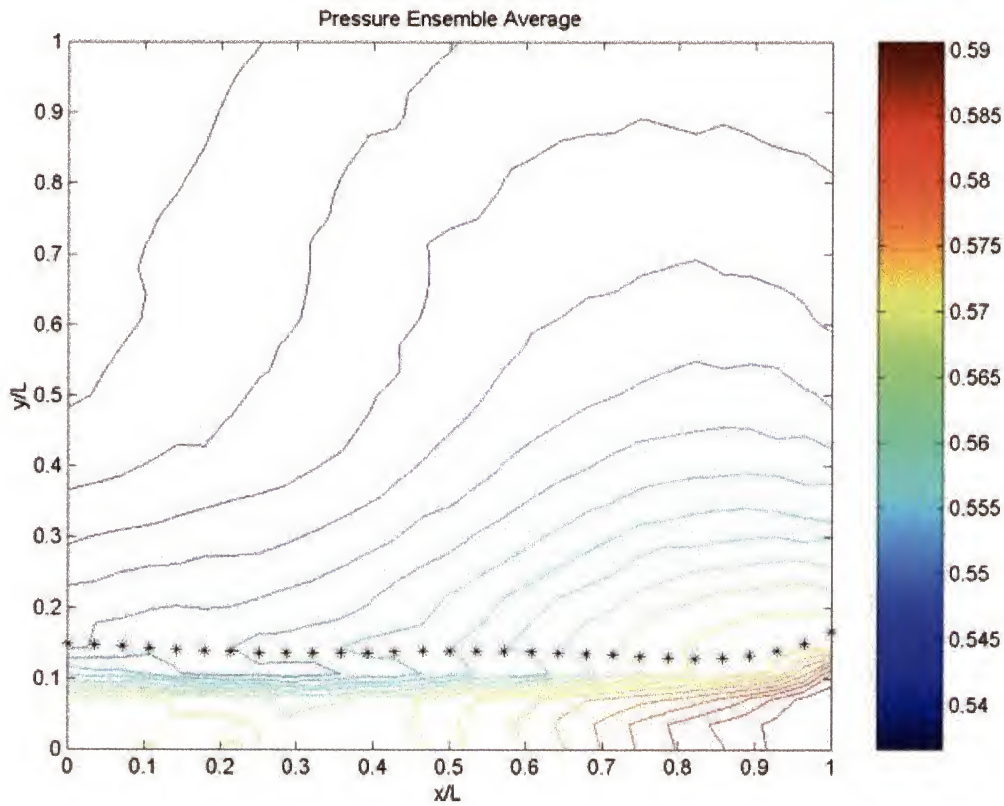

Figure 4-20 Pressure Distribution, L/D = 8

4.5 Flow Structure Position and Velocity

Since time accurate data is available, the position and velocity of the large-scale structures in the shear layer as well as the large scale structures within the cavity can be calculated. With the position and velocity of the flow structures in and above a cavity known, the temporal environment can now be analyzed experimentally. The impact of the movement and interaction of these structures on the surface pressure coefficient can now be determined.

4.5.1 Shear/Mixing Layer

The shear layer position is found from the gradient of density in the y direction. The maximum value of the gradient in the y direction is found in the vicinity of the top of the cavity. A fifth order polynomial is fitted through these points. This is then called the center of the shear layer. The position of the shear layer has appeared on all the distributions shown so far (instantaneous density, gradients, time derivatives, pressure, ensemble averages, etc.).

4.5.2 Shear Layer Large-Scale Structures

The deviation of density plot (ρ') is used to find the position and velocity of the shear layer large-scale structures. The x and y coordinate of the structures are located at each time frame. The time derivative is calculated using a first order, backward difference approximation. The position and the velocity vectors for the shear layer large-scale structures can be plotted separately or in conjunction with other direct or derived data.

4.5.3 Cavity Large-Scale Structures

The density plots are used to find the position and velocity of the cavity flow structures. Cavity flow structures are defined as regions of low density. The time derivative is calculated using a first order, backward difference approximation. The position and the velocity vectors of the cavity flow structures can be plotted separately or in conjunction with other direct or derived data.

4.5.4 Data Presentation Example

Figure 4-21 shows typical results for a L/D = 4 test. In the first column, the density deviation is plotted for successive time frames. These plots are used to establish

the position of the shear layer large-scale structures. At the first frame, the position of the shear layer and the shear layer peaks and valleys are established. The center of the shear layer peaks are shown as black stars and the center of the shear layer valleys are shown as red hexagonals. The shear layer position is shown as a solid black line. Also plotted in the individual plots in the first column is a black dashed line that establishes the top of the cavity. Flow orientation is from left to right. The cavity is in the bottom of the plot. The estimate of velocity for the structures is shown as an arrow super imposed on each flow structure. The direction of the arrow shows the direction the structure would have had to travel from the previous frame to arrive at its present location. The size of the arrow represents the magnitude of the velocity scaled to the largest value of flow structure velocity in that particular frame.

In the second column is plotted the corresponding instantaneous density which is used to establish the position of the cavity flow structures. At the first frame, the position of the cavity flow structure is established. The center of the cavity flow structure is shown as either a black circle or a black square. The shear layer position is shown as a solid black line. The estimate of velocity for the cavity structures is shown as an arrow super imposed on each flow structure. The direction of the arrow shows the direction the structure would have had to travel from the previous frame to arrive at its present location. The size of the arrow represents the magnitude of the velocity scaled to the largest value of flow structure velocity in that particular frame. At the top of each plot in the second column is the mass in the cavity. This is calculated by integrating the measured density over the volume of the cavity. It is then normalized using the no flow mass.

In the last column are plotted the corresponding pressure distribution in and above the cavity. The Cp distribution on the floor of the cavity is shown as a solid black line. The Cp distribution has been scaled in order to be able to show it on the same plots as the pressure distribution. The actual value of the Cp cannot be gotten from these plots. However, the change in Cp from frame to frame is consistent with the actual calculated values of Cp. Super imposed on the Cp distribution are arrows showing the direction the Cp changed from the previous frame. The size of the arrow represents the magnitude of the change scaled to the largest value of Cp change in that particular frame.

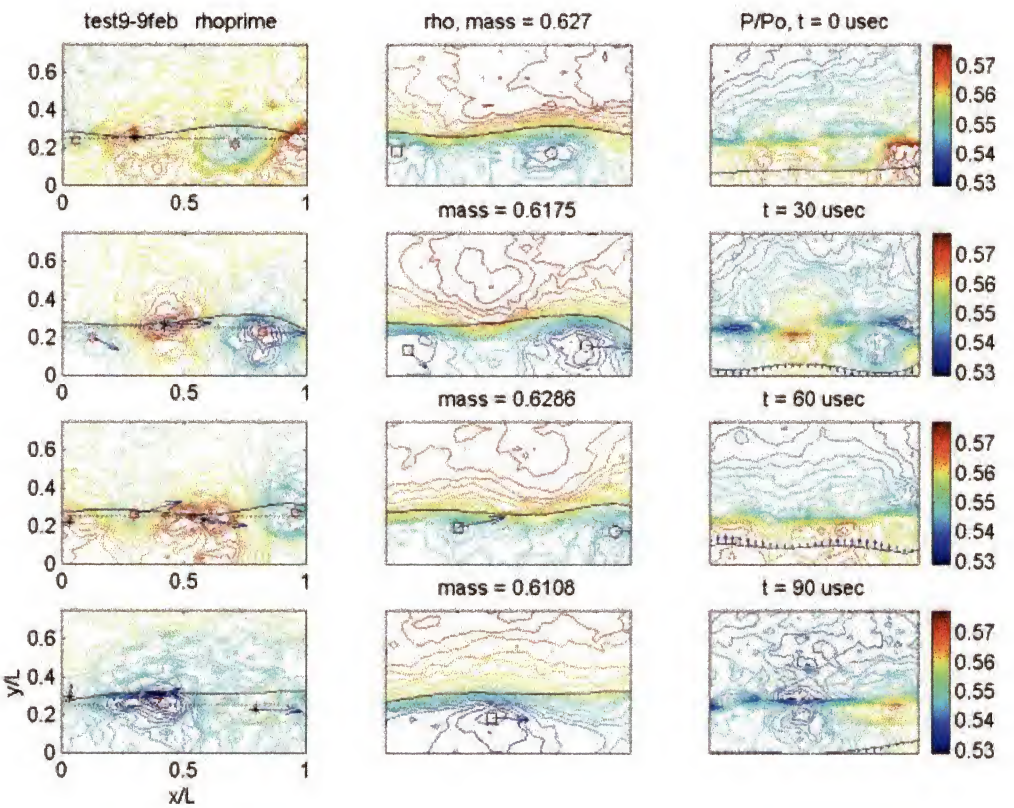

Figure 4-21 Temporal Environment, L/D = 4, test9-9feb

4.6 Comparison with Past Experimental Work

Results from the present experiment are considered representative of flow over a cavity with a free stream Mach number of 0.8. Past experimental work was completed over a large range of Reynolds number and cavity geometries. Reynolds number varied over two orders of magnitude (3.3 to 328 $*10^6$ per meter). Geometries as indicated by the length of the cavities also varied over two orders of magnitude (15 to 1067 mm). Table 4-1 summarizes the Reynolds number and cavity geometry of past experimental investigations and the current research. For like L/D ratios, cavities from past experimental investigations had like cavity classification based on the mean pressure distribution on the surface of the cavity. This classification agreed with the classification guides outlined by Plentovich et al. (1993) and Dix and Dobson (1990). Agreement with this classification was not only for past experimental work but also for the current research. As was shown in section 4.4, the classification of the cavities for this research is also in agreement with the cavity classification outlined by Plentovich et al. (1993) and Dix and Dobson (1990).

Table 4-1 Experimental Summaries versus Current Research

Experiment	Mach	Re(/m) *10⁶	L(mm)	W(mm)	D(mm)	L/D	W/D
1. Rossiter (1964)	.5 - 1.2	7.2	203	50.8	Varied	2 to 10	.25 to 2.5
2. Heller et al. (1970)	0.8 - 3.0	1.77 - 9.5	508	178	Varied	4 to 7	2.86
3. Heller and Bliss (1975)	0.8 - 2.0	13.1 - 16.4	508	178	Varied	2.3, 4.0, 5.5	
4. Shchukin et al. (1980)	4.5	7.0 - 34.7	144	2-D	Varied	1 to 5	1 to 5
5. Stallings and Wilcox (1987)	1.5-2.86	6.6	63.5-305	13-64	13-64	1 to 24	1 to 5
6. Plentovich (1990)	.3-.95	3.3 - 13.1	1067	244	Varied	4.4, 11.7	1, 2.67
7. Dix and Dobson (1990)	.6-5.0	6.2 - 9.8	457	102	51-102	4.5, 9, 14.4	1, 2, 3.33
8. Zhang and Edwards (1990)	1.5 2.5	30	15 - 135	144	15	1 to 9	7.6
9. Plentovich et al. (1991)	.2 - .9	6.6 - 328	286	64	Varied	4.4 to 20	.98 to 4.46
10. Zhang and Edwards (1992)	1.5 2.5	30	15 - 135	144	15	1 to 9	7.6
11. Plentovich et al. (1993)	.2-.95	7.2 - 15.4	1067	244	varied	1 to 17.5	1 to 10
12. Stallings et al. (1995)	.2 - .95	6.6 - 15.4	660-762	244	61-122	5.4 - 12.5	2, 4
13. Chung (2000)	1.28	29.5	N/R	N/R	1 to 10	2.43 to 43	.5, 1.0, 2.0
Current Research	**0.8**	**11**	**25.4**	**50.8**	**6.35, 3.18**	**4, 8**	**8, 16**

Strouhal numbers for past experiments when compared to the modified Rossiter equation also track from experiment to experiment even though there are significant differences in Reynolds number and cavity geometries. Table 4-2 is a subset of Table 4-1 containing only those past experimental investigations that reported frequencies and/or Strouhal numbers. Table 4-2 compares the Strouhal numbers for L/D ratios between 3 and 5. A plot of the Strouhal numbers and how they compare with predictions from the modified Rossiter equation is shown in Figure 4-22.

Table 4-2 Strouhal Number Comparisons

							S_t	
Experiment	**Mach**	**Re(/m) *10^6**	**L**	**D**	**L/D**	**mode1**	**mode 2**	**mode3**
Rossiter (1964)	0.8	7.2	203	51	4	0.30	0.68	1.05
Heller et al. (1970)	0.8	1.77 - 9.5	508	127	4		0.61	1.10
Zhang and Edwards (1990)	1.5	30	45	15	3	0.23	0.60	0.90
	1.5	30	75	15	5	0.23	0.60	1.00
	2.5	30	45	15	3	0.23	0.53	0.78
	2.5	30	75	15	5	-	0.50	0.90
Dix and Dobson (1990)	0.6	6.2 - 9.8	457	101.6	4.5	0.33	0.86	1.34
	0.95	6.2 - 9.8	457	101.6	4.5	0.29	0.72	1.13
Rossiter (1964)	0.8	7.2	203	51	4	0.30	0.68	1.05
Tracey et al. (1992)	0.8	19.8	292.1	66	4.4	0.31	0.72	-
	0.8	99.2	292	66	4.4	0.34	0.72	-
	0.8	330.7	292	66	4.4	0.34	0.72	-
Current Research	**0.8**	**11**	**25.4**	**6.35**	**4**	**-**	**.46-.62**	**-**

As can be seen, there is a good agreement between the Strouhal numbers reported from past experiments and the predictions using the modified Rossiter equation. The Strouhal number from the current research seems to be less than the predicted value and not in good agreement with past experimental work. This can be explained by the use of a generally accepted value for the ratio of the velocity of propagation of a vortex moving across the cavity opening to the velocity of the free stream, $\Phi_d = 0.57$. The lack of time-resolved data in previous investigations precluded reporting of the velocity of

propagation of a vortex and it was not known what the actual value should be. In comparing the Strouhal number, past experimental reports simply chose the value of 0.57. However, as reported by Dix and Dobson (1990) and Dix and Bauer (1993), Φ_d can take on a value between 0.35 and 0.65. For this current research, a value for Φ_d was calculated to be 0.40, the ratio of the horizontal velocity of the peaks and valleys with the free stream velocity. Figure 4-23 shows the results of comparing the Strouhal number from the current research with the predictions using the modified Rossiter equation. Agreement is very good for a mode 2 cavity, which is the mode of the cavities in the current research.

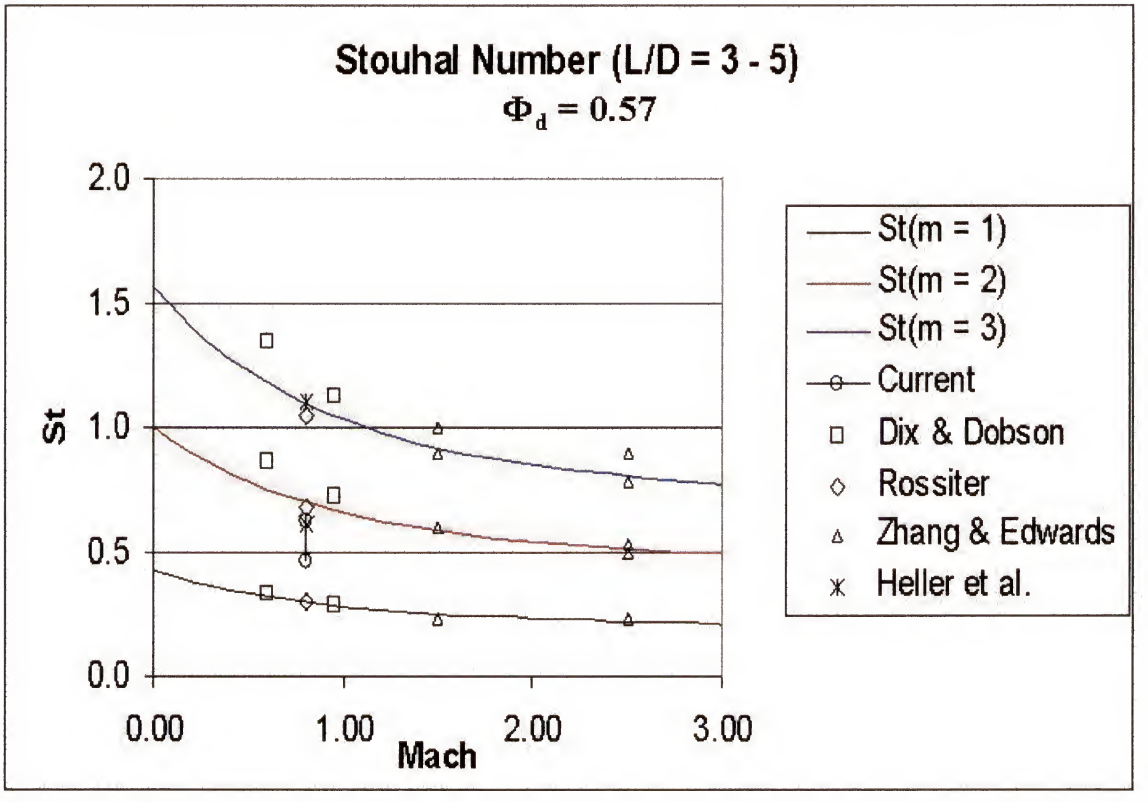

Figure 4-22 Strouhal Number $\Phi_d = 0.57$

Although the geometry and Reynolds number vary (two orders of magnitude in both length scales and Reynolds number), cavity classification and Strouhal numbers for

the current investigation are in agreement with past experimental results. This indicates that the current results are representative of flow over a cavity defined by the L/D ratios 4 and 8 with a free stream Mach number of 0.8.

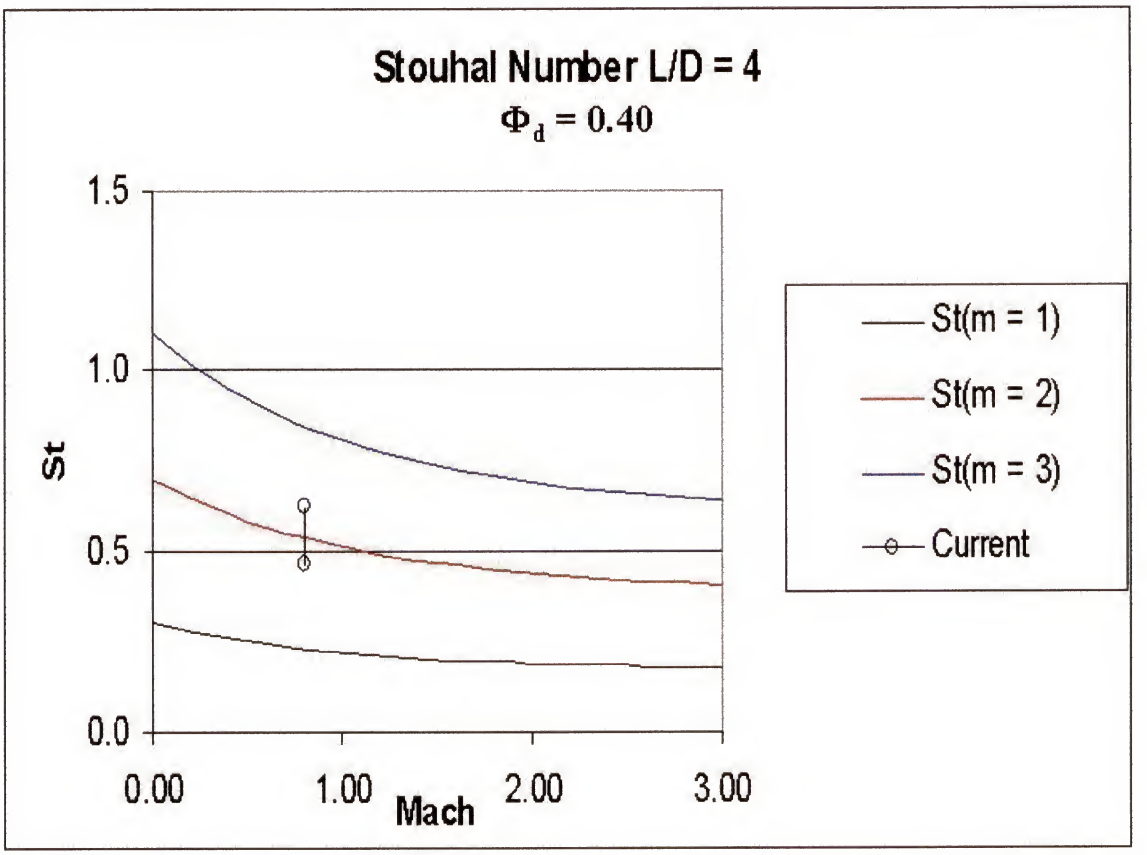

Figure 4-23 Strouhal Number $\Phi_d = 0.40$

4.7 Summary

Flow structures such as shock and expansion waves, shear/mixing layers and vortices are generated as a result of flow over cavities. When the free stream conditions are in the transonic range (Mach ≈ 0.8) only shear/mixing layers and vortices are present. The position and movement of these structures in and above cavities influence the pressure distribution on the surface of the cavity. In the past, pressure distributions have been measured experimentally on the surface of the cavity. In order to control this

pressure on the surface of the cavity, an understanding of where the flow structures are and their movement is required. The temporal environment in and above the cavity is analyzed in the next chapter. The primary method for analysis will be to use the data generated by the Shack Hartman sensor and presented as in Figure 4-21.

CHAPTER 5
RESULTS AND DISCUSSIONS

In this chapter, the data generated by the Shack Hartman sensor is used to analyze the flow in and above a two dimensional cavity. Of specific interest are the location, movement, and interaction of recognizable flow structures and the impact these have on the surface pressure and the pressure in and above the cavity. For the purpose of this analysis, these flow structures are the shear layer peaks and valleys, cavity structures indicated by areas of low relative density, and the shear layer itself. The impact of the position, movement, and interaction of these flow structures on the surface pressure of the floor of the cavity and the pressure in and above the cavity are analyzed. Two cavity geometries are analyzed at the same free steam conditions. The geometries are defined by the L/D ratios of L/D = 4 and L/D = 8. Both geometries have the same length (L). Only the depth (D) is varied. The free stream conditions are those listed at the end of the second chapter. The shear layer, the shear layer peaks and valleys, the cavity structures and the pressure on the floor of the cavity and in and above the cavity were found as described in the previous chapter.

For this chapter, the flow structures will be called valley, peak, and cavity structure. Valley and peak refer to the large-scale structures in the shear layer. Cavity structure refers to the flow structure in the cavity. The shear layer will be referred to as the shear layer, and the pressure coefficient will be referred to as Cp. The value for Cp is

not the value shown on the charts in this chapter. The Cp distribution was scaled to allow it to be plotted on the same plots with the peaks, valleys, cavity structure, and shear layer. The analysis concentrated on how the Cp changed as a result of the position and movement of the flow structures.

5.1 Cavity Flow Model

Subtracting the density ensemble average from the instantaneous measurements helps to identify large-scale structures in the shear layer. It will be shown that it is the position and movement of these large-scale structures in the shear layer that directly impact the pressure distribution not only on the surface of the cavity but also in and above the cavity.

These structures in the shear layer can be likened to balls that are created at the leading edge of the cavity and move downstream at a certain velocity in both the horizontal and vertical direction. Figure 5-1 shows how the flow structures in the shear layer from an actual frame of data are modeled. The top of the figure is a notional model of what is occurring in the bottom of the figure. The plot at the bottom of the figure represents an actual frame of data. The top of the figure has had all but the location of the large-scale structures in the shear layer and their associated velocity vectors deleted.

The red balls, referred to as peaks, represent a positive deviation from the density ensemble average while the blue balls, referred to as valleys, represent a negative deviation from the density ensemble average. When a peak is in close proximity to the surface or moving towards the surface, the density at that point will be larger than the average value i.e., increasing. With an assumption that the temperature at the surface is constant, the change in pressure will then follow the change in density. This results in an

increase in pressure when a peak moves towards the surface and a reduction in pressure when moving away. Since a valley represents a negative deviation in density, the pressure will decrease when the valley moves toward the surface and increase when the valley moves away from the surface. In addition to this independent movement of the peaks and valleys, they can also be within close proximity to each other resulting in either an increase or decrease in pressure on the surface of the cavity depending on the following conditions. For example, a peak may be moving faster towards the surface than the valley resulting in a net increase in density and a corresponding increase in pressure on the surface. Alternatively, a valley may be moving faster towards the surface than the peak resulting in a net decrease in density, thus decreasing the pressure on the surface. At or near the surface, the peaks and valleys apparently interact with the surface similar to bouncing balls, collide with each other, and interact or influence the movement of the shear layer. If the shear layer moves away from the cavity, the net effect is to reduce mass in the cavity, which reduces density, which reduces pressure. The reverse effect can also take place, i.e. the shear layer moves into the cavity allowing mass to accumulate at the aft end, increasing the density at the aft end, which will increase the pressure.

With this model, one can predict the change in the pressure distribution if one knows the position and movement of the large-scale structures (peaks and valleys) in the shear layer. A brief description of the behavior observed as a result of the motion of the peaks and valleys follows.

In Figure 5-2 is shown how the movement of the peaks and valleys change the density in the cavity, the effect this has on the pressure on the floor of the cavity, and how the

movement of the structures at the aft end impact the movement of the shear layer. Red circles represent peaks, blue circles represent valleys, a solid black line represents the shear layer, and a solid red line represents the pressure on the floor of the cavity. In Figure 5-3 is shown how the interaction of the structures with the floor, aft wall, and each other affects the shear layer movement. Red circles show the peaks, blue circles show the valleys. The initial position of the shear layer is shown as a solid black line. The position of the shear layer after the interaction of the peaks and valleys is shown as a dashed red line. The new position of the peaks and valleys after interacting uses the same color scheme but the balls are outlined in dashed lines.

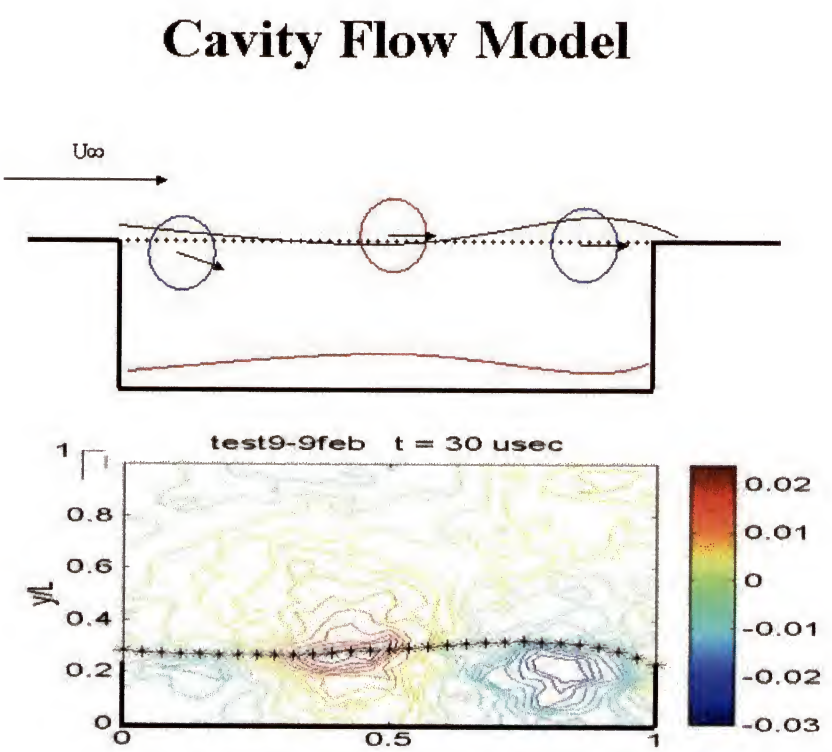

Figure 5-1 Cavity Flow Model

In the top model of Figure 5-2, the peaks have a net velocity out of the cavity and the valleys have a net velocity into the cavity. With the peaks headed out, the increase in

density is headed away from the floor of the cavity. With the valleys moving in, a decrease in density is moving into the cavity. With the density decreasing in the cavity, the Cp distribution on the floor of the cavity is fairly flat. However, for the same position of the peaks and valleys but with a reversed vertical movement for the peaks, the Cp distribution on the floor of the cavity will be a mirror image of the shape of the shear layer. Where the peak is headed into the cavity, there is an increase in density in the cavity below the peak. This is reflected by an increase in Cp directly below the peak. The valley, also with a velocity into the cavity, has the effect of reducing density and is reflected as a decrease in Cp directly below the valley. This result is shown in the middle model.

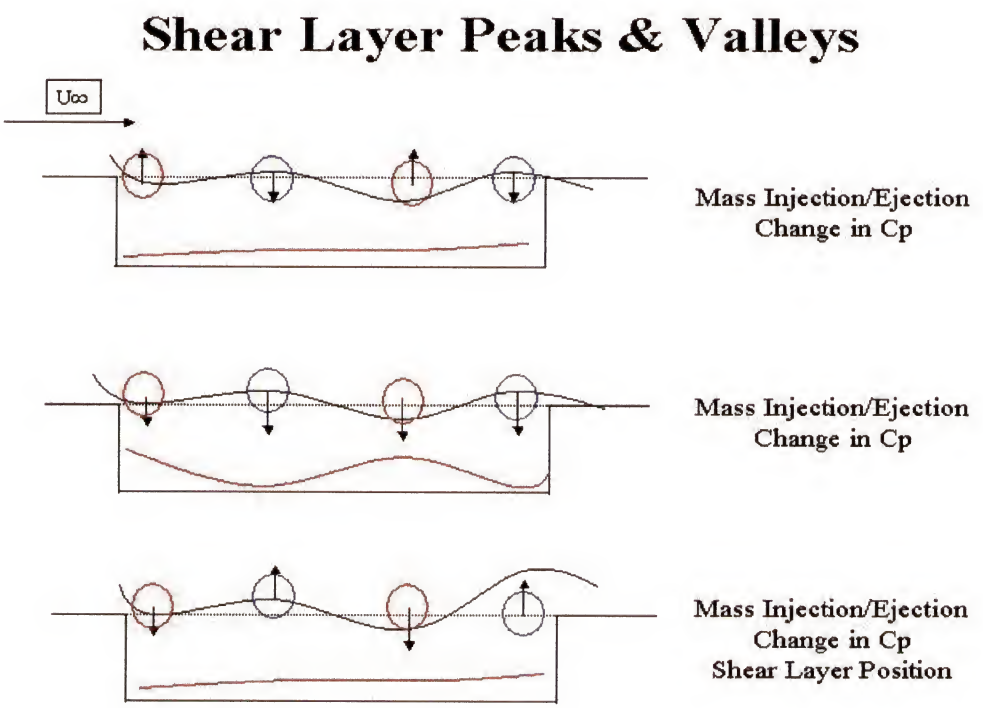

Figure 5-2 Shear Layer Peaks & Valleys, L/D = 4

Even though the peaks may have a velocity into the cavity and the valleys a velocity out of the cavity, which should result in an increase in density in the cavity and

an increase in pressure, this is not always the case. This is caused by the position of a valley at the aft end of the cavity above the lip of the cavity. When this occurs, the valley continues passed the cavity lip at the aft wall without interacting with the aft wall. It will appear that the shear layer has flapped up and away from the cavity allowing mass to be ejected, reducing the density in the cavity. With this decrease in density, the Cp on the surface will be flat and less than expected even though the peaks are headed in and the valleys are headed out. This case is shown in the bottom model of Figure 5-2.

In Figure 5-3 is shown the results when the peaks and valleys interact with the geometry of the cavity (aft wall and floor) and with each other. In the top model, a peak is at the aft wall with a velocity into and down the aft wall. Trailing this peak is a valley with a velocity downstream and away from the cavity. There are also a peak and a valley further upstream that have been created by the flow over the cavity. At a delta time later, the peak at the aft wall has bounced off the aft wall and with the floor of the cavity. The trailing valley has continued downstream and is now interacting with the peak. The end result is that both of these structures are now headed out of the cavity. The upstream peak has continued to move downstream and the valley that had been created at the leading edge of the cavity is now moving away from the cavity. The interaction of the peak and valley at the aft wall has resulted in moving the shear layer away from the cavity allowing mass to be expelled at the aft end.

In the middle model, a valley has bounced into the aft wall and moved upstream. A trailing peak that had a downstream velocity along with a velocity into the cavity has interacted with this valley moving upstream. The result of this interaction is the shear layer moves into the cavity over the aft portion of the cavity. Because the peak has

stalled, its trailing valley was forced away from the floor of the cavity and is now moving out of the cavity. The original peak and two valleys are still present but an additional peak is created at the front end of the cavity. Over this time sequence, the quantity of large-scale structures over the cavity increases from three to four. This is an example of the shear layer compressing like a spring hitting a stationary wall.

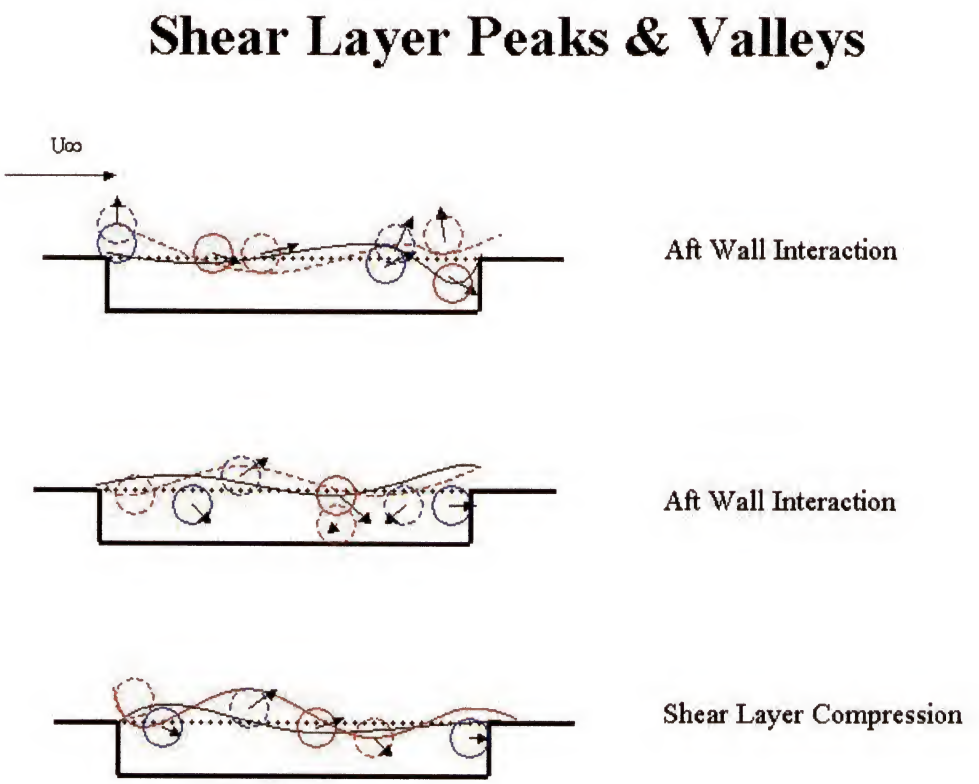

Figure 5-3 Shear Layer Peaks & Valleys, L/D = 8

In the bottom model of Figure 5-3 is shown how the shear layer can "compress" like a spring when a valley is interacting with the aft wall. Over a very small time frame (< 30 microseconds), the valley at the aft wall will appear to remain stationary. The upstream peaks and valleys will continue to move downstream with peaks moving into the cavity and valleys moving away from the cavity. As the upstream peaks and valleys

continue to move downstream, a peak or valley will be created at the leading edge of the cavity. Over a very small time frame, the number of large-scale structures in the shear layer will vary depending on the interaction of the structures at the aft wall.

This model was found to be consistent with all the data recorded while performing the tests. No violations of this model were observed. A correlation between the position of the large scale structures in the shear layer and the surface Cp distribution has been found. With this model, knowing the position and velocity of the peaks and valleys in the shear layer allows one to predict the impact on the surface pressure distribution. Results of tests follow where the correlation between the position and movement of the shear layer large-scale structures is shown to correlate with the pressure and change in pressure on the surface of the cavity.

5.2 L/D = 4 Cavity

As was shown in Chapter 4, the L/D = 4 cavity acts as a deep cavity as indicated by a fairly flat pressure coefficient distribution on the floor of the cavity. The ensemble average shown in Figure 4-12 shows the shear layer spans the length of the cavity. There is a small interaction of the fluid with the aft wall causing a slight concave out shape of the pressure coefficient distribution on the floor of the cavity at the aft end of the cavity. Also evident is the presence of only one cavity flow structure located about mid span of the cavity. The remainder of this section will concentrate on identifying what flow structures have the largest influence on the floor pressure distribution and the impact these structures have on the pressure in and above the cavity.

5.2.1 Individual Results, L/D = 4

5.2.1.1 Test6-9feb

Figure 5-4 shows the results for test6-9feb. Spacing between laser pulses was 10 microseconds. Initially, there are three structures in the shear layer, two peaks and one valley. The peak near the aft wall has a net velocity into the cavity and interacts with the aft wall over the test time period of 30 microseconds. It appears that the peak at the aft wall is almost stationary while the upstream structures continue their movement downstream. As a result, it appears that the shear layer is being compressed. The valley continually moves away from the cavity while the upstream peak continually moves into the cavity. At the last frame, a new valley is created at the leading edge of t he cavity. The impact this has on the surface Cp can be seen in the last column. At time t = 10 microseconds, the peaks are headed into the cavity and the valley is headed out. This should result in an increase in the Cp and this is in fact what happens. At the next frame, the peaks and valleys continue their movement into and out of the cavity respectively. The Cp continues to increase as seen at t = 20 microseconds. In the center column, the mass in the cavity continues to increase indicating that the pressure on the surface of the cavity is directly related to the amount of mass in the cavity. In the next frame, however, the mass in the cavity decreases even though the peaks and valleys continued their movement into and out of the cavity respectively. At the aft wall, the pressure increased, as it should since the peak at the aft end was moving into the cavity. The Cp however, decreased in the forward part of the cavity even though the peak was moving into the cavity. The shear layer compressing and the center valley moving out of the cavity, which has the effect of moving the shear layer away from the cavity at mid span, explain

this change in Cp. Even though mass is being ingested at the forward peak, more mass is being ejected at the center of the cavity resulting in a net outflow of mass. This results in a lowered Cp in the front half of the cavity.

For this test, the Cp follows the movement of the peaks and valleys. However, the cavity structure does not appear to have an impact on the Cp. In the second frame, an area of low density is moving further into the cavity. One would expect to see the Cp decrease but it fact it increased. At the next frame, the movement of the cavity structure appears to have an impact on the Cp in the correct direction but the movement of the peaks and valleys can also explain the impact. In the last frame, the cavity structure is moving downstream. One would expect to see an increase in Cp upstream of this structure. As has already been shown, the Cp decreased. It appears that the cavity structure has little to no impact on the Cp on the surface of the cavity. The same conclusion was also reached for the remaining tests. The cavity structures will not be addressed any further. The analysis will concentrate on the position and movement of the shear layer peaks and valleys and the shear layer itself.

The peak interacting with the aft wall appears to be causing a pressure disturbance into the cavity and above the cavity. The upstream peak also appears to be causing the same type of disturbance but at a lower magnitude. There does not appear to be any disturbance from the valley in the center of the cavity either into the cavity or above the cavity.

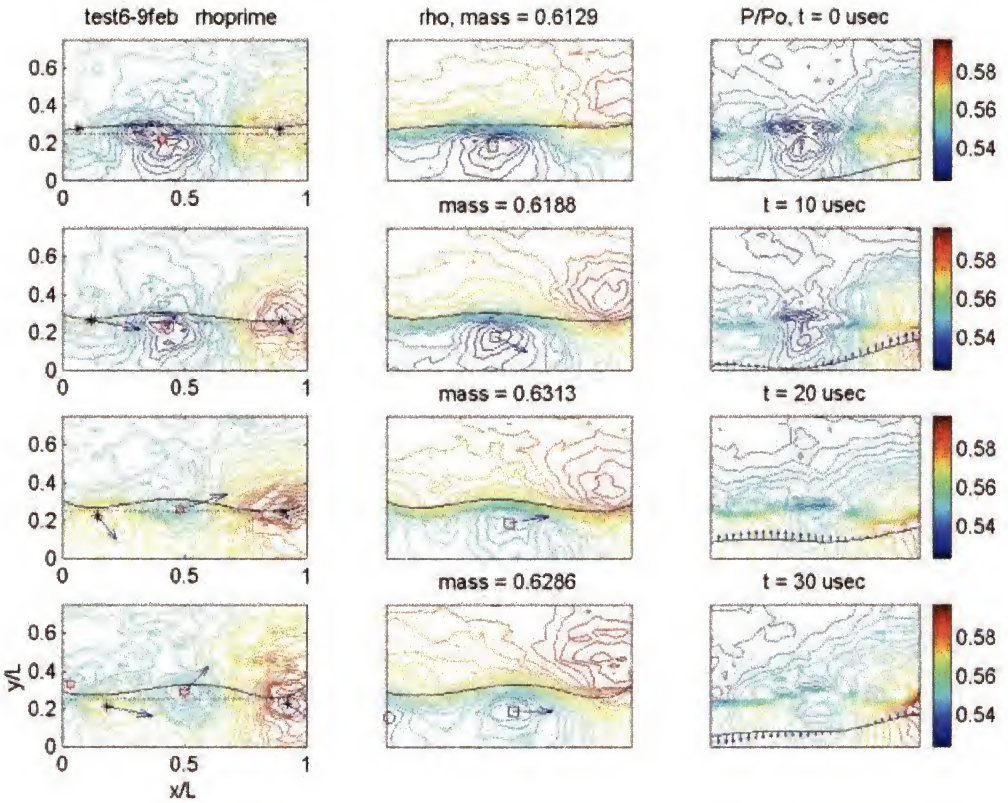

Figure 5-4 Test6-9feb, L/D = 4

5.2.1.2 Test7-9feb

Figure 5-5 shows the results for test7-9feb. Spacing between laser pulses was set to 10 microseconds. This test appears to have a similar sequence as that shown in Figure 5-4. The start of the sequence appears to have started slightly before that shown in Figure 5-4. The first frame shows two peaks and only one valley. Over the test time of 30 microseconds, no additional peaks and valleys appear indicating that during this sequence, the shear layer did not compress. A case could be made for just prior to the start of data being taken that the shear layer over the length of the cavity did contain four large-scale structures. This can be seen from the first frame where a case could be made

that a valley has just passed the trailing edge of the cavity. This could be the first frame where the shear layer became uncompressed.

In the second frame, the peaks are moving into the cavity and the valley is moving away from the cavity. The change on the surface Cp follows the direction of these structures. There is also a net increase in mass into the cavity although the shear layer at the aft end is pointing away from the cavity. Since mass is being ingested into the cavity and the shear layer is pointing away from the cavity, mass ingestion must be occurring upstream where the peaks are moving into the cavity. At the third frame, the peaks and valley continue their movement into and away from the cavity respectively. The Cp changes in the correct direction and mass is increased in the cavity. At the last frame, the peak at the aft wall has started to move away from the cavity allowing the trailing valley to move into the cavity. It also appears that the aft peak moving away from the cavity has had the effect of moving the shear layer away from the cavity allowing mass to exit at the aft end. The mass does decrease in the cavity but especially in the front half of the cavity. The peak at the aft end moves out of the cavity. A larger decrease in Cp should have occurred but did not. This means that mass had to be added to make up for the mass being expelled at the aft end. This occurs from the upstream peak moving downstream with no apparent vertical velocity component. Mass is being added by this peak but is immediately moving downstream resulting in a lower Cp on the floor of the cavity upstream. This sequence shows that the movement of the peaks and valleys has a direct impact on the Cp distribution and also has an impact on the shear layer movement, which can also cause a change in Cp on the surface. The peak at the aft end is above the lip of the cavity.

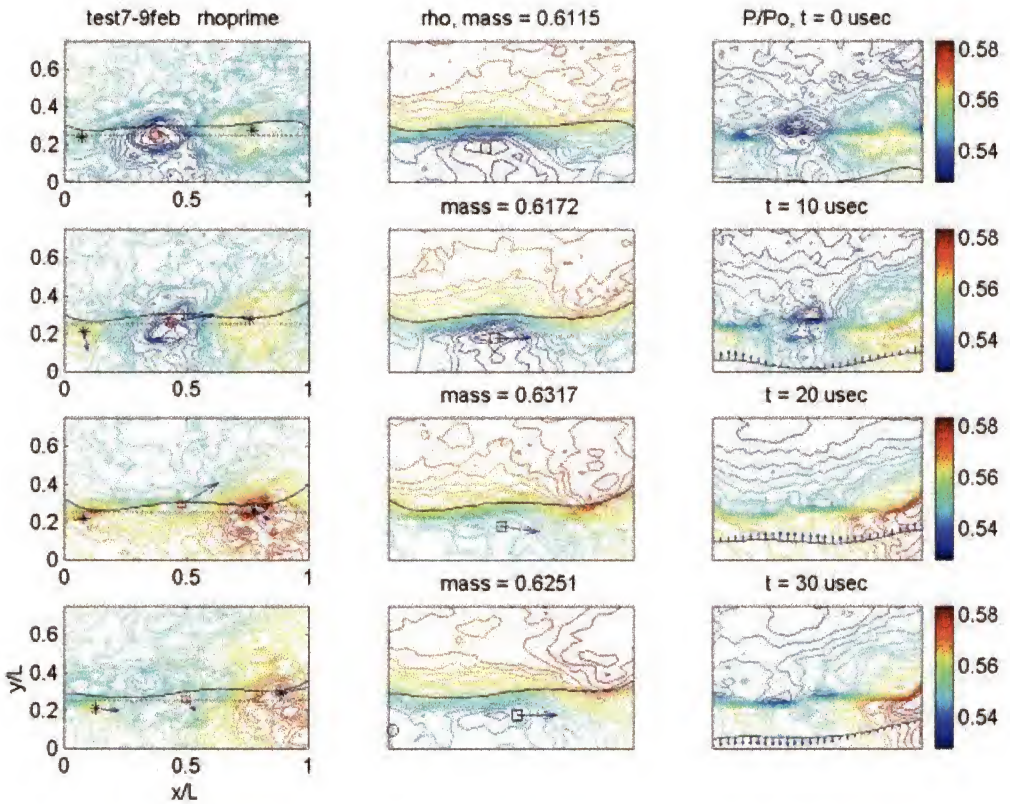

Figure 5-5 Test7-9feb, L/D = 4

The peaks also appear to be causing a disturbance in the pressure field not only into the cavity but also above the cavity. In the first frame where the peaks are just above the cavity, the disturbance is into and out of the cavity. For the last three frames, the peak at the aft end has started to interact with the aft wall and the magnitude of the disturbance has increased. The upstream peak does not appear to be large enough to cause a disturbance.

5.2.1.3 Test2-6feb

Figure 5-6 shows the results for test2-6feb. This test had spacing of 20 microseconds. The appearance of four structures in the shear layer indicates that the

shear layer has experienced compression. The peak at the aft end has started to move out of the cavity and will continue its movement downstream of the cavity. Over the next two frames, only three structures (two valleys and one peak) can be seen. However, at the last frame, it appears that the valley may have been interacting with the aft wall between the third and fourth frame causing some shear layer compression. However, the valley did not interact with the aft wall long enough to cause a readily identifiable compression of the shear layer as only three large-scale structures are seen in the last frame.

At the second frame, the two valleys are moving into the cavity and the peak has only a slight movement into the cavity. Where the valleys are moving into the cavity, the Cp decreases. The slight movement of the peak has prevented much change in the Cp directly below the peak. At the third frame, the valley has reached the aft wall. The peak is headed out of the cavity and the upstream valley is headed into the cavity. This should result in a decrease in Cp everywhere. This change in Cp does occur but at a much larger change than would be expected just from the shear layer structure movement. At the second frame, the shear layer is definitely positioned away from the cavity as can be seen in the center column. Mass is allowed to move out of the cavity from frame two to frame three. The movement of the valleys into the cavity coupled with the movement of the peak out of the cavity and the shear layer at the aft end allowing mass to exit all contribute to the large change in Cp over the floor of the cavity. However, as quickly as mass exited the cavity at the aft end, the mass enters again from the front in the last frame. The peak is moving into the cavity, the valley is moving out. Another peak is

being created at the leading edge of the cavity. This causes mass to enter the cavity along the front portion of the cavity and a corresponding increase in Cp.

The upstream peak does appear to be causing a disturbance above the cavity and into the cavity as it travels downstream. The other disturbance is being caused the valley interacting with the aft wall. This is not as big a disturbance as when a peak interacts with the aft wall but a disturbance all the same.

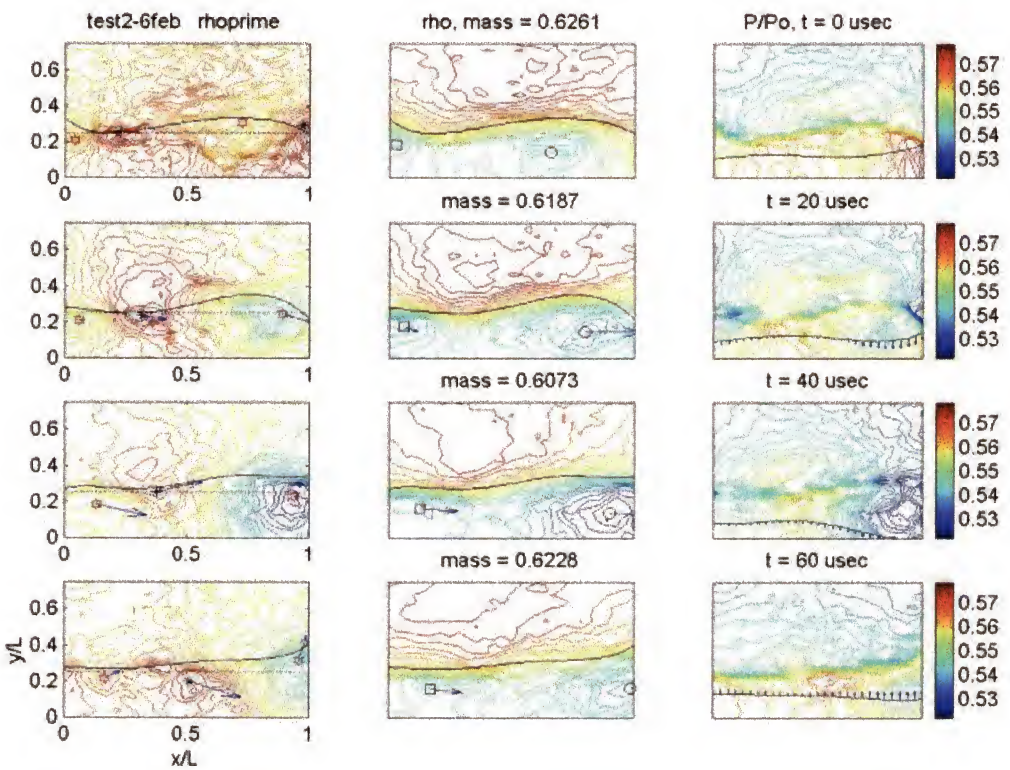

Figure 5-6 Test2-6feb, L/D = 4

5.2.1.4 Test8-9feb

Figure 5-7 shows the results of test8-9feb. Spacing between laser pulses was set to 30 microseconds. No apparent compression of the shear layer seems to have taken place. However, from previous test cases already covered, compression of the shear layer can occur over 30 to 40 microseconds. Therefore, compression may have occurred

between the second and third frame. For this particular test, only three structures in the shear layer are visible. The effect of movement of the peaks and valleys in the second and third frames on the floor Cp are consistent with what has already been presented. At the last frame, all structures are headed out of the cavity. The peak moving away is expected to cause a decrease in Cp. This in fact occurs. A moving away of a valley however is expected to increase the Cp. This does not occur. However, the movement of the downstream valley is causing the shear layer to a position away from the cavity allowing mass to exit the cavity at the aft end. The mass in the cavity does decrease from the third to the fourth frame. This is occurring not only at the aft end but also where the peak is moving out of the cavity. The end result is the shape of the Cp distribution remaining flat but decreasing along the entire length of the cavity.

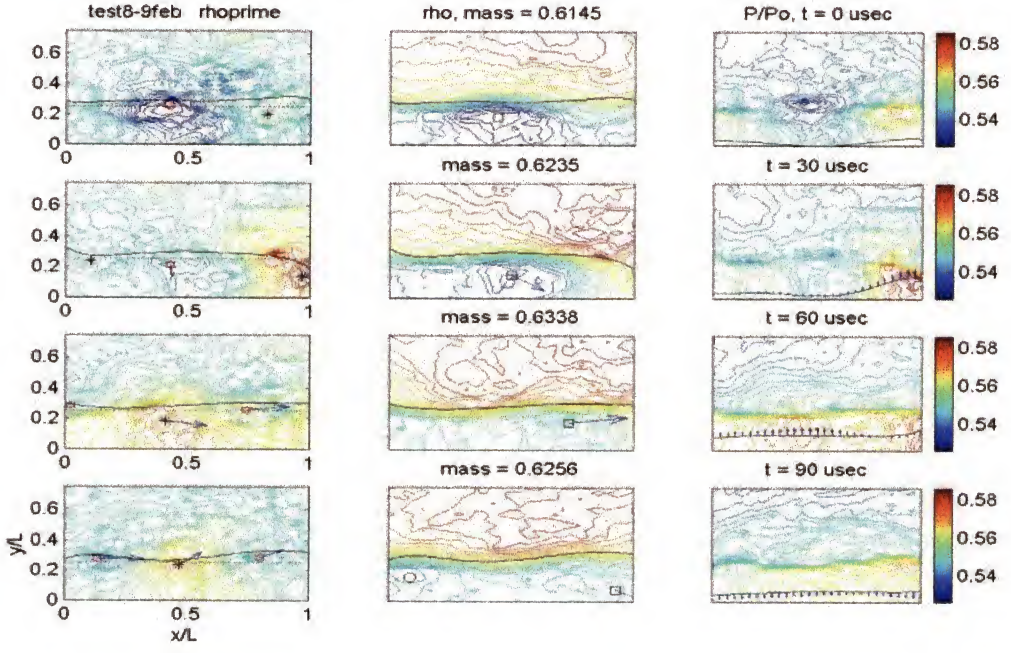

Figure 5-7 Test8-9feb, L/D = 4

The peaks in the shear layer also cause pressure disturbances as shown in the previous test cases. These pressure disturbances are both into and away from the cavity.

The magnitude of the disturbance is largest at the aft end when the peak interacts with the aft wall.

5.2.1.5 Test9-9feb

Figure 5-8 shows the result of test9-9feb. Spacing between laser pulses was set to 30 microseconds. Frame one seems to be at or just prior to frame four from test8-9feb. Also, frame four seems to be at or just prior to frame one from test8-9feb. It would appear that one test is the continuation of the other test or one test precedes the other test. Therefore, with a total of 90 microseconds for each test, a potential cycle of 180 microseconds seems to exist. Using Rossiter's modified equation, the ratio of the shear layer peaks and valleys velocity to the free stream velocity can be estimated. Solving for Φ_D from the modified equation yields

$$\Phi_D = \frac{1}{\frac{U_\infty}{L}\frac{1}{f}(m-\alpha) - M\frac{a_\infty}{a_0}} \qquad 5\text{-}1$$

Where m is the mode of cavity frequency. Citing Tracey and Plentovich (1992), the mode can be obtained by looking at the shape of the pressure distribution on the surface of the cavity. With the assumption that the temperature is constant near the surface, the shape of the distribution of the density near the floor of the cavity should also provide the mode of the cavity. Figure 5-9 indicates that the mode of this cavity is 2. Plugging all known values into the above equation yields a value for Φ_D equal to 0.40. The value for Φ_D for the L/D = 4 cavity tests was calculated to be 0.36. Plugging this value into the modified Rossiter equation yields a cycle time of roughly 200 microseconds. A possible cycle time for this cavity on the order of 180 to 200 microseconds is possible. This will be explored in a later paragraph.

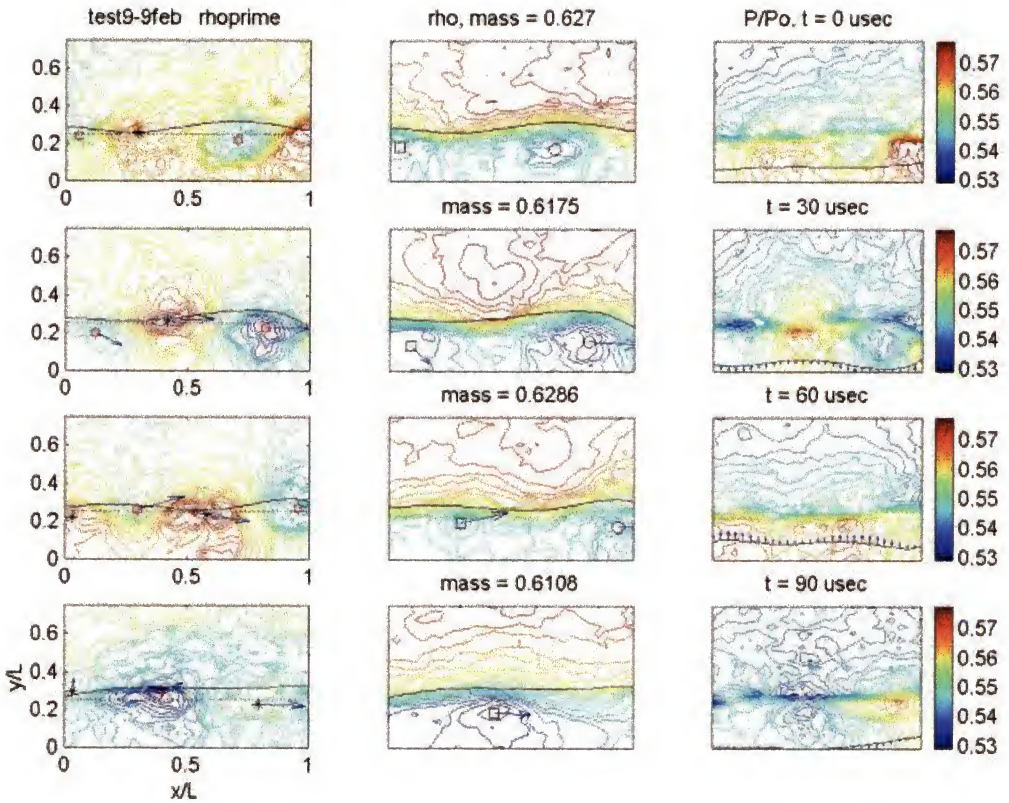

Figure 5-8 Test9-9feb, L/D = 4

Compression of the shear layer appears to have taken place between the second and third frames. In between these two frames, the downstream valley interacts with the aft wall causing the shear layer to compress. This is indicated by the appearance of a peak at the upstream edge of the cavity in the third frame. The behavior of the peaks and valleys and their impact on the Cp is as previously discussed.

Pressure disturbances in and above the cavity can again be traced to the movement of the shear layer peak with the larger disturbance occurring when the peak interacts with the aft wall.

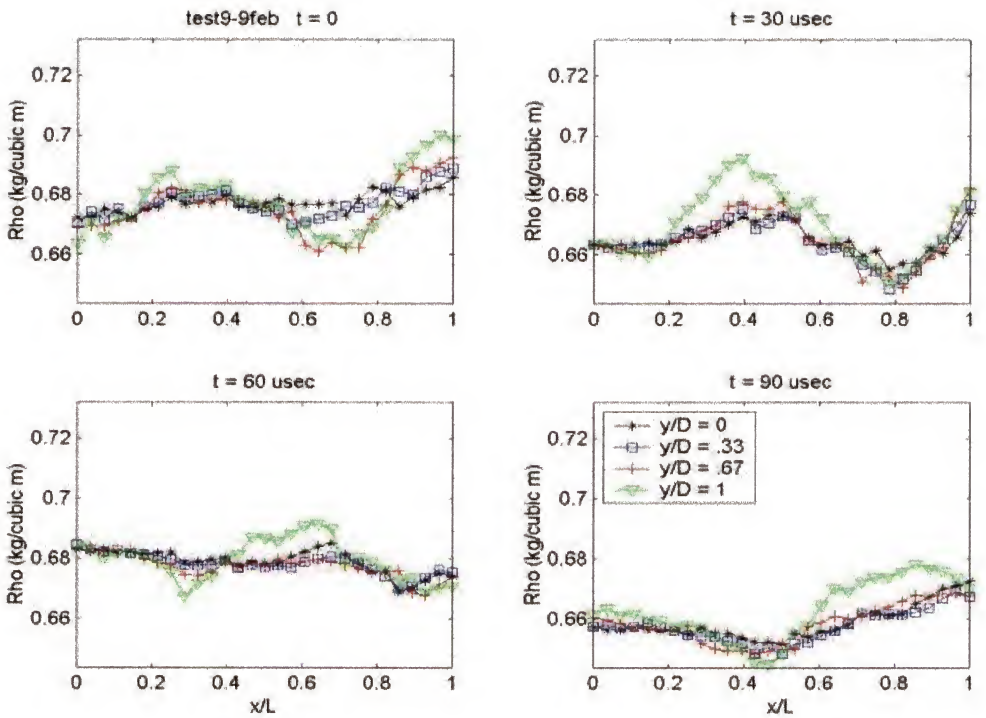

Figure 5-9 Density Distribution, test9-9feb, L/D = 4

5.2.1.6 Test1-10feb

Figure 5-10 shows the results for test1-10feb. Spacing between laser pulses was set to 30 microseconds. If a cycle exists for this cavity, frames from this test should be able to be inserted in the sequence suggested by test8-9feb and test9-9feb. Comparing results of this test with test8-9feb, the first frame would seem to occur after the first frame of test8-9feb. This conclusion is reached because the downstream peak in test1-10feb is nearer the aft end of the cavity than in test8-9feb. Since the spacing is the same for each test, the last frame would have to be very near the last frame as test8-9feb. A comparison indicates that this is the case. The last frame for this test is very similar in structure position and movement as that shown in the last frame of test8-9feb. Test9-9feb could precede the test results for this test. The last frame in test9-9feb appears to occur only slightly ahead of the first frame for test1-10feb. If a cycle exists as previously

indicated, the last frame of test should be very close to the same description as test9-9feb. It appears that the last frame for test1-10feb could occur after the first frame in test9-9feb. Again, this points to a possible cycle for this cavity, which is occurring at a time that is predictable from the Rossiter's modified equation.

It also can be intermingled with the results of test2-6feb. The third frame can be placed at or very near the same time as the second frame in test2-6feb. This implies that the last frame from test1-10feb occurs between the third and fourth frame from test2-6feb. The position and movement of the shear layer, the shear layer peaks and valleys and the cavity structures suggests that this is possible. This further indicates that the cavity does have a cycle over which the structure movement occurs. Three test results from three different days at different spacing can be made to mesh together showing the cycle of this cavity.

The movement of the structures is also consistent with the previous test results. At frame two, the peaks have a movement into the cavity resulting in an increase on the Cp. The upstream peak in frame three continues its movement into the cavity further increasing the Cp on the cavity. The movement of the downstream valley is parallel to the floor and therefore its movement has little impact on Cp. From frame three to frame four, the valley will move further downstream with its center above the aft wall. As the valley nears the aft wall, it will seem like the shear layer has flaps away from the cavity when in fact only the shape of the shear layer has moved downstream with the valley. This has the effect of allowing mass to exit the cavity. This is shown in the fourth frame. The valley is headed out and taking the shear layer with it. In addition, the trailing peak is also headed away from the cavity resulting in a large decrease in Cp along the entire

length of the cavity. Pressure disturbances in and above the cavity can again be traced to the position of the shear layer peaks with the larger disturbance at the aft wall.

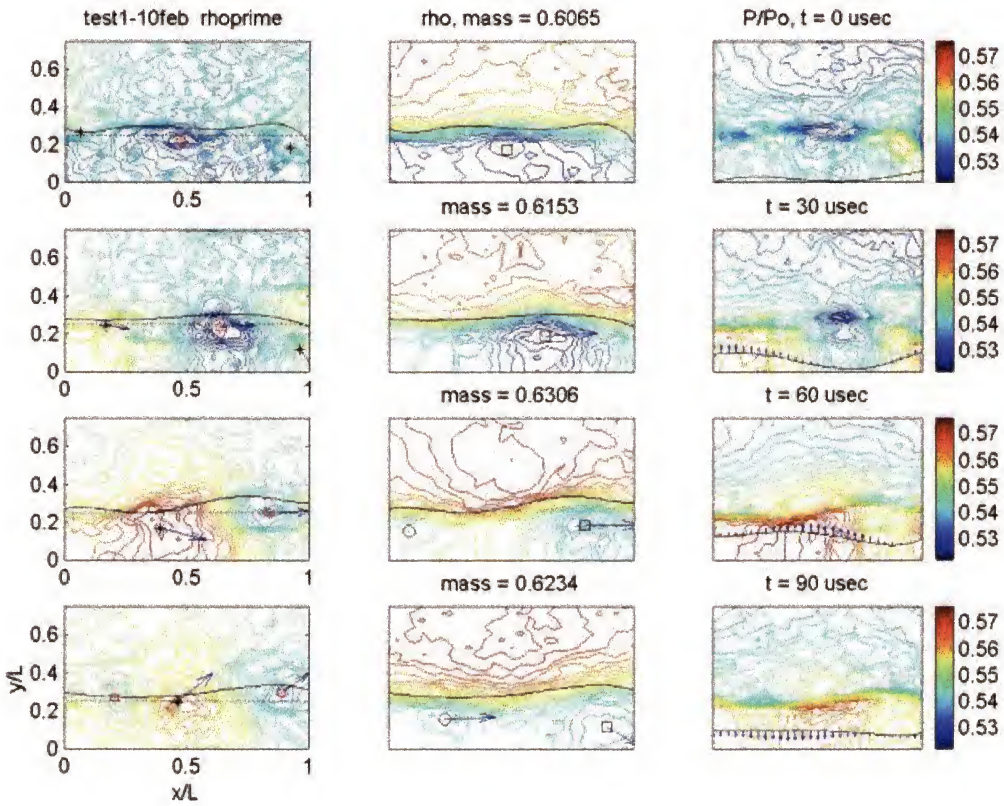

Figure 5-10 Test1-10feb, L/D = 4

5.2.2 Cavity Cycle, L/D = 4

The remaining tests that will be presented were taken with laser pulse spacing of 50 and 100 microseconds. The structure interaction and impact on the Cp is consistent with previous tests and will not be elaborated on. What will be presented is the fact that a cycle is identifiable for this cavity.

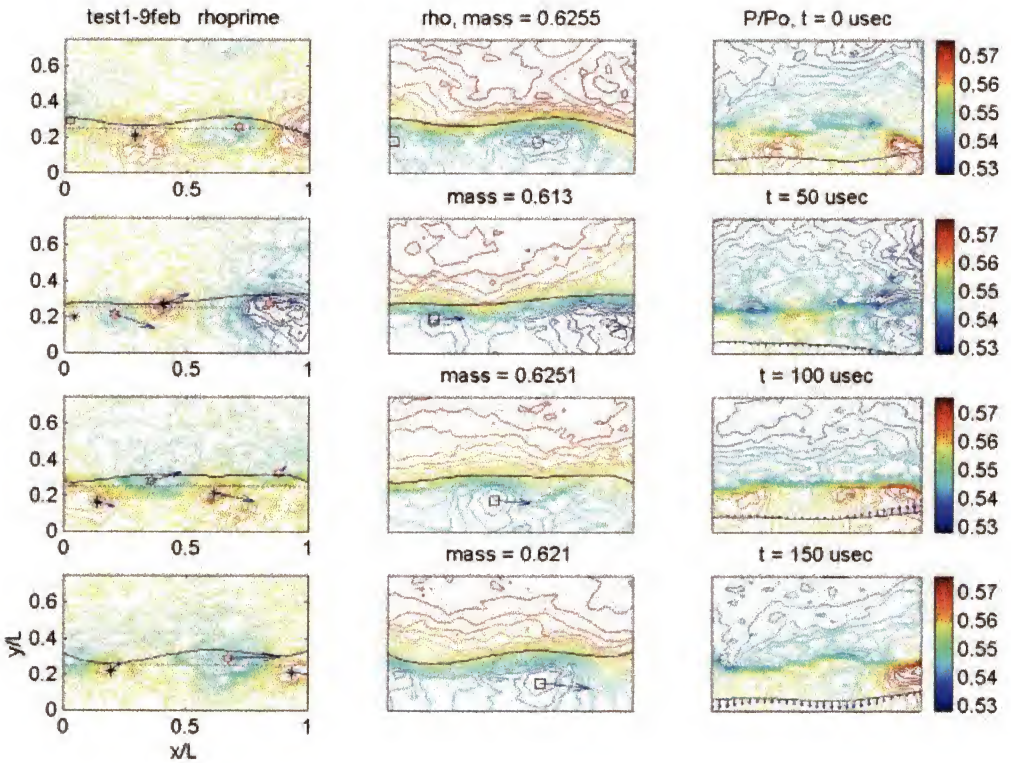

Figure 5-11 Test1-9feb, L/D = 4

Figure 5-11 shows the results for test1-9feb. Spacing between laser pulses was set to 50 microseconds. The total test time was 150 microseconds, which is less than the cycle time of 200 microseconds predicted using the modified Rossiter equation (Equation 4.1). If a cycle time of approximately 200 microseconds does exist, one should be able to extrapolate the position of the peaks, valleys, and cavity structures in the last frame to the position of these structures in the first frame. For the tests conducted, the velocity of these structures is estimated to be 0.0037 to 0.0041 non-dimensional length units (x/L) per microsecond. This was derived by using a value of 0.36 to 0.40 for the ratio of the average peak and valley velocity to the free stream velocity (Φ_D). Over 50 microseconds, the flow structures in the last frame should move downstream 0.185 to 0.205 x/L units. Extrapolating the structures to these new positions would place them past the expected

position for a 200 microseconds cycle time. The results from Figure 5-11 suggest that the cycle time for this test is less than the predicted 200 microseconds.

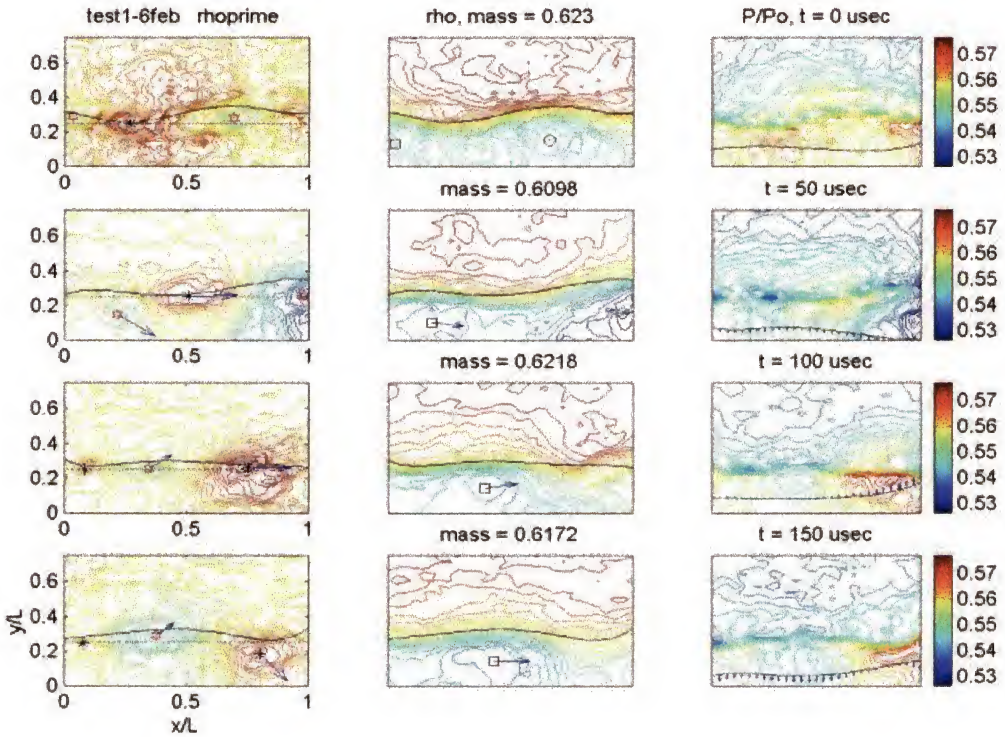

Figure 5-12 Test1-6feb, L/D = 4

Figure 5-12 shows the results for test1-6feb at the same laser pulse spacing of 50 microseconds. Figure 5-13 shows the results for test2-9feb at the same spacing. Extrapolating the position of the structures in the last frame forward 50 microseconds for these two tests would yield a picture similar to the first frame for each test. From the last two tests, a cycle on the order of 200 microseconds exists for this cavity. Coupled with results shown in Figure 5-11, the cycle time would appear to be between 150 to 200 microseconds.

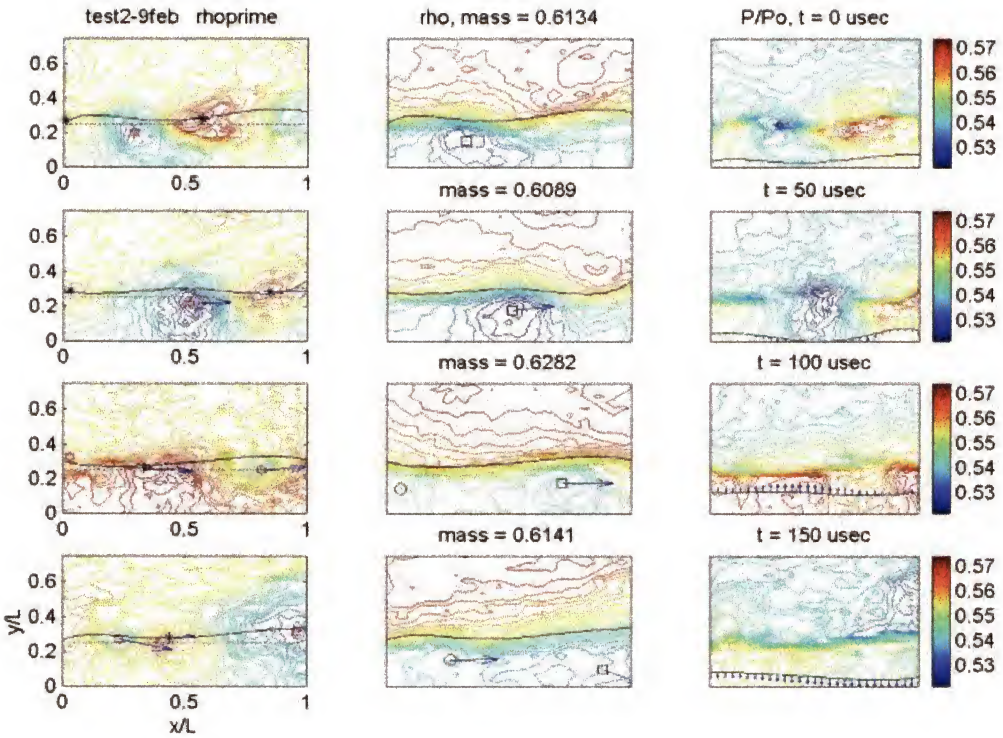

Figure 5-13 Test2-9feb, L/D = 4

Figure 5-14 shows the results for test2-10feb. Spacing for this test was 100 microseconds. The display of the shear layer peaks and valleys from the first frame would have to be reproduced between the second and third frame for a cycle time of 150 microseconds. If that did occur and a cycle time of 150 microseconds exists, the last frame would have to approximate the first frame. Comparing the first and last frames shows that this is the case. The peaks and valleys exist at approximately the same location, there are the same amounts of cavity structures and their location is approximately the same, and the shape of Cp on the floor of the cavity is nearly identical. For this test, it appears that the cavity went through two cycles of 150 microseconds duration. However, as extrapolated for Figures 5-12 and 5-13, the cycle time can also be in the neighborhood of 200 microseconds.

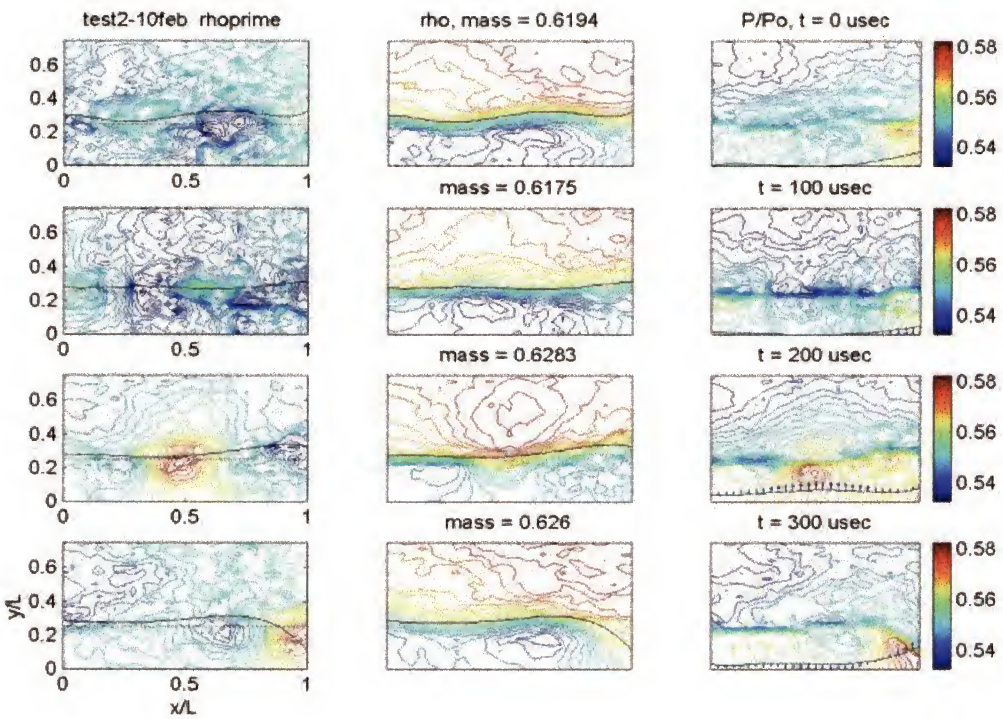

Figure 5-14 Test2-10feb, L/D = 4

Figure 5-15 shows the results for test3-6feb. Laser spacing was set to 100 microseconds. From this test, extrapolating the structures from the second frame 50 microseconds would approximate the position of the structures in the first frame indicating that a cycle time of 150 microseconds was experienced by this cavity during this test. However, the second and last frames are nearly identical indicating that the cycle time is 200 microseconds.

This cavity definitely goes through a cycle. The length of this cycle varies between 150 to 200 microseconds. There appears to be a correlation between the number of peaks and valleys to the cycle time. Test1-6feb, test2-9feb, and test 3-6feb contained three peaks and valleys and a cycle time on the order of 200 microseconds. Test1-9feb had four peaks and valleys with a cycle time of 150 microseconds. Test2-10feb also had four peaks and valleys and appeared to go through two 150 microseconds cycles. Cycle

time varies and is tied to the quantity of large-scale structures (peaks and valleys) in the shear layer.

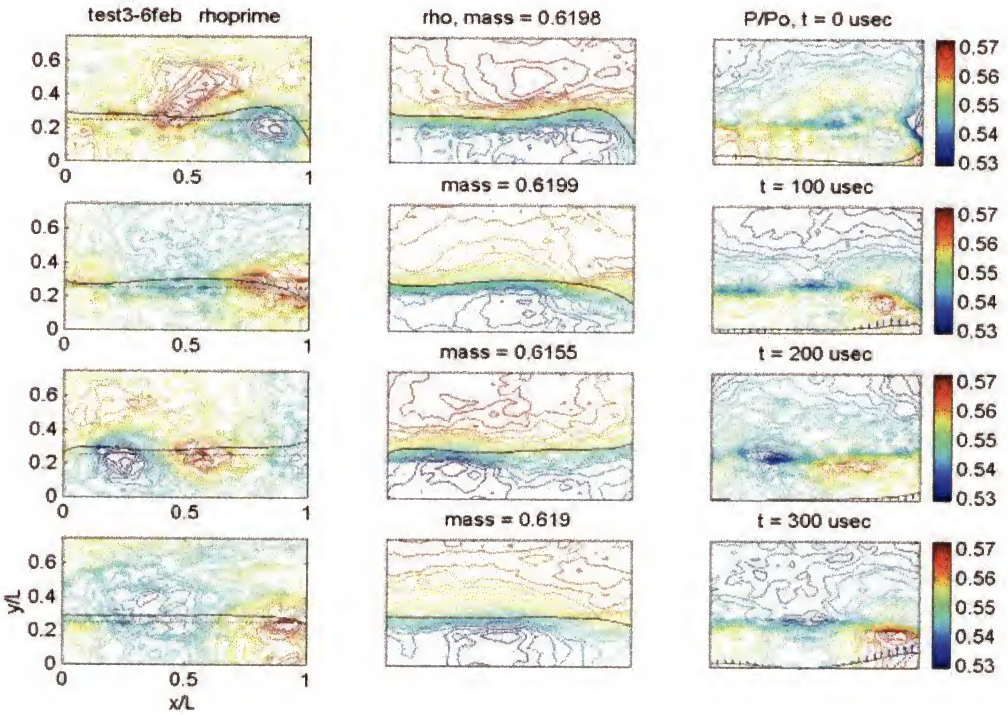

Figure 5-15 Test3-6feb, L/D = 4

5.2.3 Flow Structure Position and Movement, L/D = 4

Figure 5-16 shows the vertical position of the shear layer peaks and valleys and the cavity structures along the length of the cavity. In the top chart is plotted the actual data from the various tests conducted. The bottom chart is the result of fitting a line through the data from the tests. This was done in order to see if a trend in the vertical position of the structures was identifiable as function of the horizontal position along the length of the cavity.

The cavity structure is created at approximately y/L = 0.15. There is a slight rise in position by about mid length followed by a decrease in height over the aft half of the cavity. Ahead of this cavity structure is a shear layer peak interacting with the aft wall

causing the shear layer to move into the cavity. The shear layer bending into the cavity pushes the cavity structure into the cavity. When the valley, which is moving with the cavity structure, arrives at the end of the cavity, the shear layer shapes away from the cavity allowing the cavity structure to move out of the cavity. This movement is indicated over the last half of the cavity in Figure 5-16.

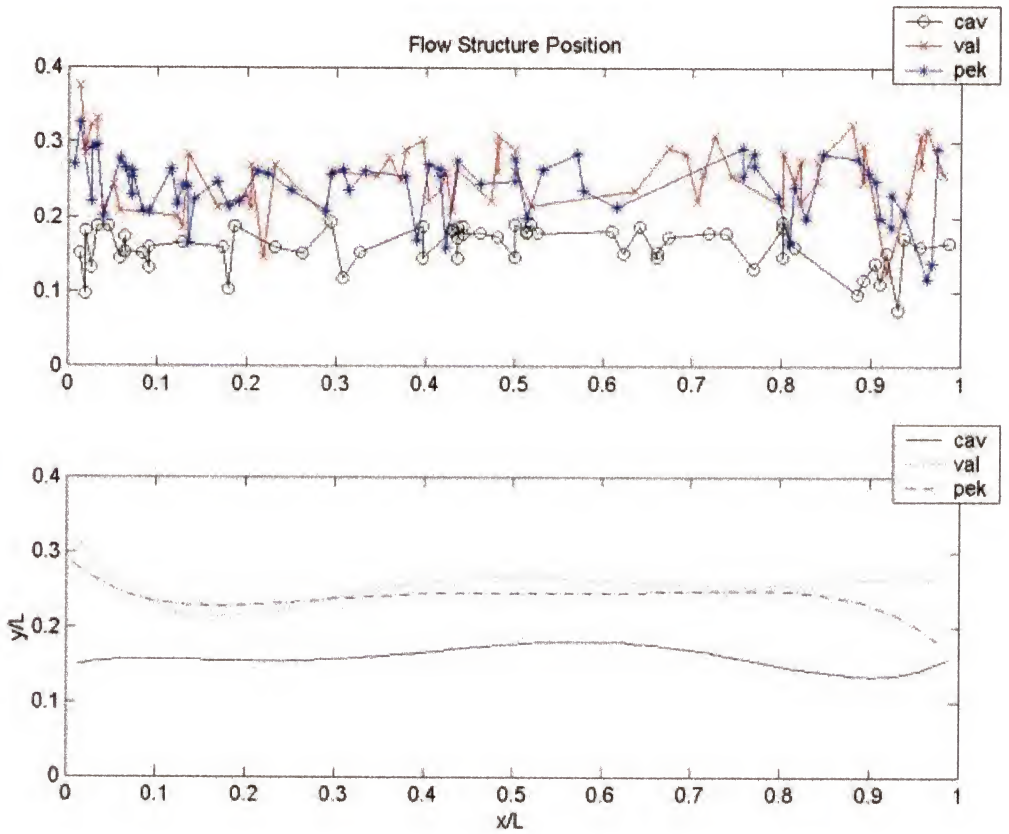

Figure 5-16 Flow Structure Position (y/L)

The peaks and valleys are initially created above the cavity. As they move downstream, the valley moves to just slightly above the top of the cavity and the peaks move to slightly below the top of the cavity. The average position remains relatively constant until approaching the aft end of the cavity. The valley continues its movement over the cavity and on the average does not interact with the aft wall. When the valley

arrives at the aft wall, the shear layer is shaped away from the cavity allowing fluid to escape from the cavity. This results in a reduction in Cp on the floor of the cavity.

In contrast, when the peak arrives at the aft wall, an interaction takes place since on the average the peak position is slightly below the top of the cavity. This interaction moves the peak into the cavity at the aft end. When the peak arrives at the aft end, the shear layer is shaped into the cavity allowing fluid to enter the cavity causing the Cp to increase on the aft wall. The movement of the peaks and valleys governs the Cp on the floor of the cavity. As their movement is relatively flat, the Cp on the floor should also be flat. This is in fact the case. The Cp distribution from the ensemble average most closely resembles a mirror image of the vertical peak movement.

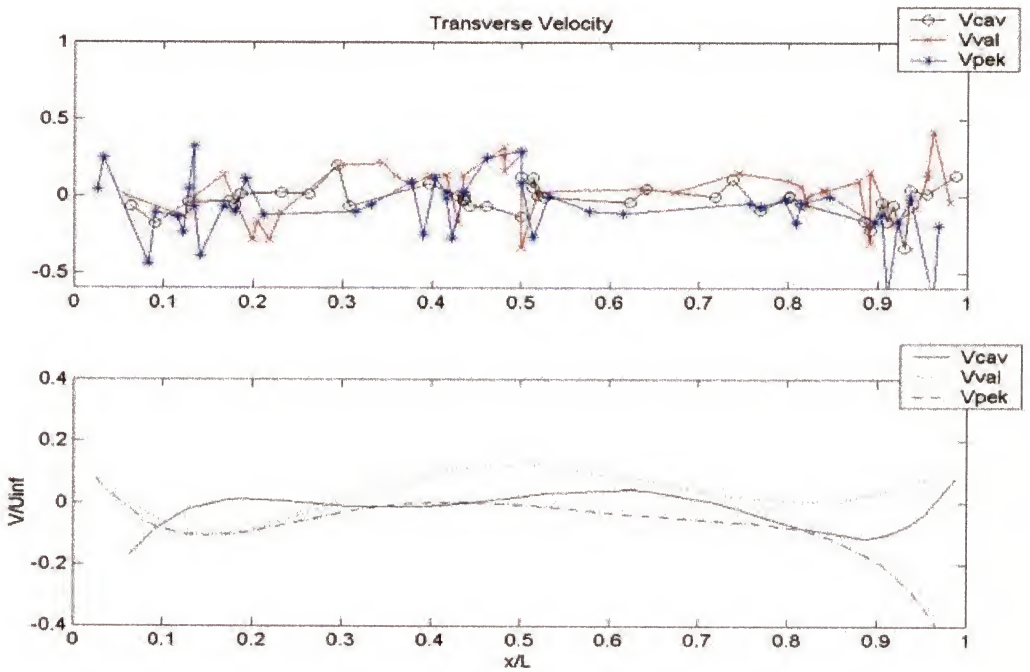

Figure 5-17 Transverse Velocity, L/D = 4

The position of the shear layer peaks and valleys is confirmed when looking at the vertical velocity component for these structures (Figure 5-17). At their creation at the

forward lip of the cavity, they have an initial positive component (away from the cavity). The velocity decreases, becomes negative, and the position of the peaks and valleys stabilizes. All along the length, the valley has a more positive velocity and is borne out by the statistics shown in Figure 5-18. The peak has an average negative vertical velocity and moves into the cavity at the aft end.

L / D = 4

Non-dimensional Flow Structure Velocity

	Ucav	Vcav	Uval	Vval	Upeak	Vpeak
Mean	0.404	-0.024	0.372	0.034	0.354	-0.072
Std Dev	0.168	0.101	0.219	0.172	0.218	0.212
Min	0.075	-0.337	0.063	-0.337	0.021	-0.678
Max	0.772	0.199	1.019	0.421	0.993	0.323

Non-dimensional Flow Structure Position (y/L),

	Ycav	Yval	Ypeak
Mean	0.158	0.254	0.233
Std Dev	0.029	0.044	0.041
Min	0.076	0.125	0.118
Max	0.193	0.324	0.297

Figure 5-18 Non-dimensional Flow Structure Statistics, L/D = 4

From Figure 5-18, the average position for the peak is within the cavity. Therefore, when arriving at the aft wall, the peak will interact with the aft wall and move further into the cavity. Because of the curvature of the shear layer behind the peak, the shear layer will appear to curve into the cavity. When the following valley arrives at the aft wall, the valley will continue on past the aft end of the cavity since its average distance is above the top of the cavity. When it passes the aft end, it will appear that the

shear layer has altered directions and has "flapped" away from the cavity. What appears to be a flapping of the shear layer is just an alternate movement of the peaks and valleys near the aft wall.

5.3 L/D = 8 Cavity

As was shown in the previous chapter in Figure 4-11, the L/D = 8 cavity behaves as an open cavity and very near the transitional classification. The open classification is indicated by an increase in the Cp over the aft half of the cavity. A hint that it may be near the transitional classification is the fact that the Cp distribution has a concave in shape over the aft half of the cavity. The ensemble average shown in Figure 4-13 shows the shear layer interacts with floor of the cavity prior to arriving at the aft wall. This would explain the increase in Cp over the aft half and also explain the concave in shape of the distribution. Also evident is the presence of only one cavity flow structure in the cavity located in the forward half of the cavity. The only difference between the geometry for the L/D = 8 cavity and L/D = 4 is the depth. The depth was cut in half to obtain the geometry for the L/D = 8 cavity.

5.3.1 Individual Results, L/D = 8

5.3.1.1 Test11-10feb

Figure 5-19 shows the results for test11-10feb. Spacing between laser pulses was set to 10 microseconds. Although this cavity is shallower than the L/D = 4 cavity, shear layer compression is also apparent. For the first two frames, there are only three recognizable peaks and valleys. However, there are four in the third and fourth frames. A peak interacting at the aft wall and apparently coming to a standstill causes this. The upstream peaks and valleys continue downstream eventually allowing the creation of

another peak or valley at the leading edge of the cavity. This shear layer compression causes the same movement of the peaks and valleys for a shallow cavity as it did for the deeper cavity: the valleys move away from the cavity, the peaks move further into the cavity. This movement of the shear layer peaks and valleys should cause an increase in the Cp all along the length of the cavity. This is occurring in the third frame. However, in the last frame, the Cp is decreasing. At the last frame, the peak at the aft wall is moving out of the cavity. A corresponding decrease in Cp at the aft end is noted. As can be seen from the last frame, the shear layer is still in the cavity. Contributing to the decrease in Cp is the horizontal movement of the trailing valley. Due to the close proximity of the valley to the floor of the cavity, the valley behaves as a sink removing mass and causing a decrease in Cp. The upstream peak has flattened out its movement resulting in essentially no change in Cp over the forward floor of the cavity.

The peak interacting at the aft wall causes a pressure disturbance similar to that caused in the deeper cavity. However, for this cavity, the disturbance seems to be pointing partially upstream. Like the deeper cavity, the disturbance is greater when the peak is interacting with the aft wall. Unlike the deeper cavity, both upstream peaks and valleys appear to cause disturbances. The direction of the disturbance appears to rely more on the vertical movement of the peaks and valleys. For instance, the upstream peak for this test does not seem to cause a disturbance in the pressure field above the cavity. Its position is below the top of the cavity and its vertical velocity is mainly into the cavity for the entire test. However, the furthest upstream valley in the last frame seems to cause a disturbance above the cavity. Its position is above the top of the cavity and its vertical movement is away from the cavity. This accounts for a pressure disturbance from a

valley. There were no identified pressure disturbances caused by valleys for the deeper cavity.

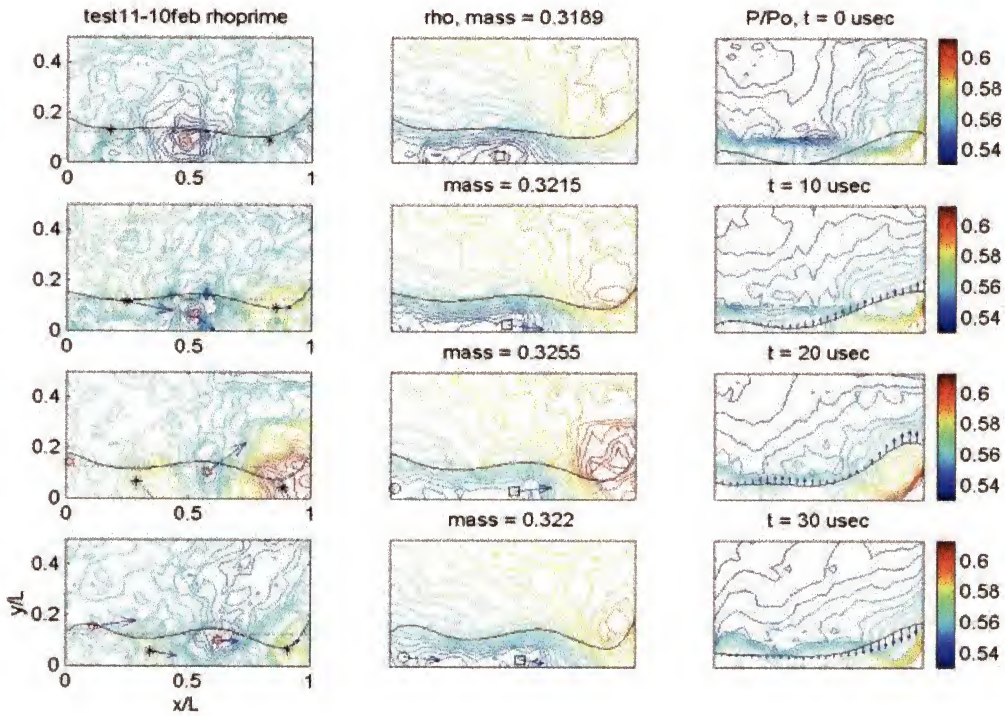

Figure 5-19 Test11-10feb, L/D = 8

5.3.1.2 Test10-10feb

Figure 5-20 shows the results for test10-10feb. Spacing between laser pulses was set to 20 microseconds. The same shear layer compression is depicted for this test but the primary cause for this test is a valley interacting with the aft wall. There are only two valleys and one peak in the first two frames. While the downstream valley interacts with the aft wall, the upstream peaks and valleys continue downstream and allow the creation of an additional peak at the upstream lip of the cavity as shown in the third frame. When the shear layer starts to compress between frame two and frame three, the movement of the peaks and valleys change their directions. Valleys change from into the cavity to out of the cavity and peaks change from out of the cavity to into the cavity. This causes a

drastic change in the Cp. In frame two, the Cp was decreasing following the movement of the peaks and valleys. Valleys were headed into the cavity and the lone peak was headed out. This resulted in a decrease in Cp from the first frame. Because of the compression of the shear layer and the change in direction of the peaks and valleys, there is a large change in Cp between the second and third frame. From the third to the fourth frame, the valley at the aft wall moves up into the free stream and continues its movement downstream of the cavity aft lip. This allows mass to exit the cavity as the shear layer will be above the lip of the cavity. Even with the trailing peak adding mass, mass is leaving faster than can be added by this trailing peak. This results in a decrease in Cp for the last frame. The quantity of mass as indicated in the center column follows the peaks, valleys, and shear layer movement.

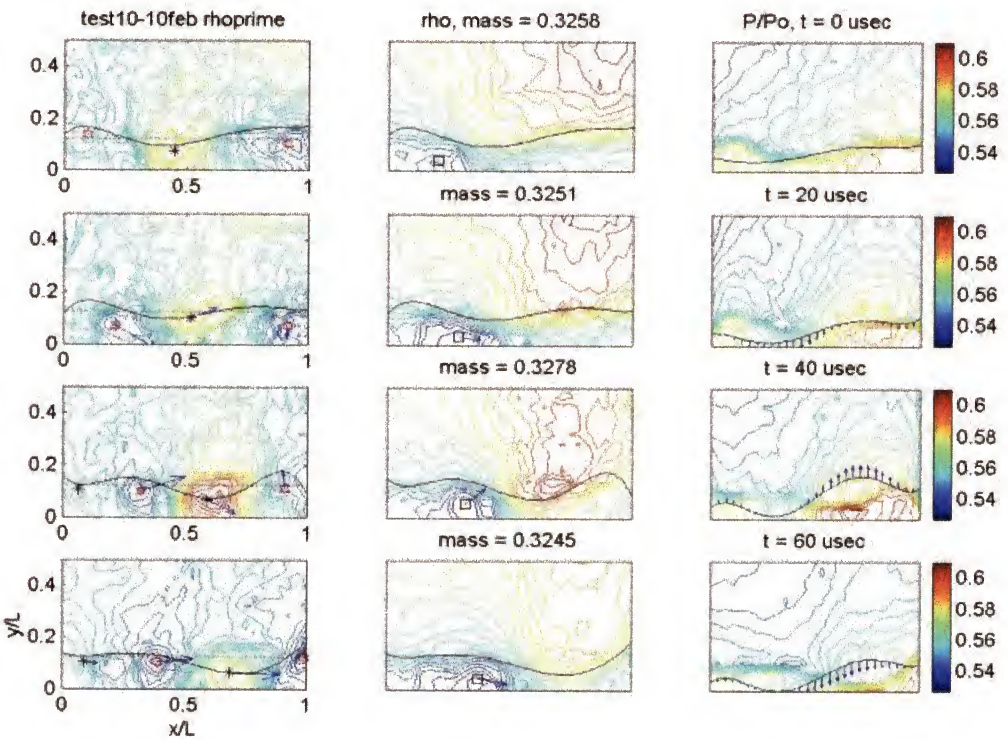

Figure 5-20 Test10-10feb, L/D = 8

A valley is interacting at the aft wall. This interaction is causing a pressure disturbance in and above the cavity. The disturbance not only has a vertical component but also a horizontal component and is heading back upstream. There does not appear to be any pressure disturbances caused by the upstream peaks and valleys. Notice that the position of the peaks and valleys are below the top of the cavity.

5.3.1.3 Test3-11feb

Figure 5-21 shows the results for test3-11feb. Spacing between laser pulses was set to 30 microseconds. This test is the first instance of the shear layer structures not only interacting with the aft wall and floor but also with each other and thereby impacting the movement of the shear layer. Again, there is indication of shear layer compression. The cause this time is a peak at the aft end of the cavity. Cp follows the movement of the peaks and valleys as previously described. At frame two, the downstream peak is headed into the cavity. One would expect to see a significant increase in Cp but this is not the case. In the first frame, the shear layer is above the lip of the cavity. This allows mass to exit the cavity. As shown in previous tests, the shear layer allowing mass to exit will sometimes overcome the addition of mass by a peak moving into the cavity resulting in a net decrease in mass and therefore a decrease in Cp. This appears to be the case here. Mass is added by the peak but it is allowed to escape due to the position of the shear layer. There is still a slight increase over the aft portion of the floor but the increase is minimal. With the trailing valley also moving downstream, the Cp decreases.

Notice that the total mass in the cavity remains constant for the third and fourth frame. Also notice that the change in Cp changes direction between these two frames. The amount of mass or the change in mass in a cavity is not a very good indication of the

change in Cp or change in pressure in and above the cavity. The position and movement of the shear layer structures is the best indicator of what happens in a cavity. At the third frame, there is a peak moving into the cavity at the aft end followed by a valley moving parallel to the floor of the cavity. Ahead of this valley is a peak moving into the cavity with a valley just created ahead of it. The position and movement of these structures and the effect they have on Cp is as previously described. At the last frame, the peak at the aft wall has headed back upstream and interacted with the trailing valley moving the entire shear layer up and allowing mass to escape from the cavity. There is a decrease in Cp at the aft of the cavity. Slightly upstream, an increase in Cp is indicated. This agrees with the movement of the valley out of the cavity. The upstream peak and valley has the effect on Cp as previously described. That is, when a peak moves away from the cavity, the Cp below it is decreased. When a valley moves away from the cavity, the Cp below it increases.

The downstream peak has not reached the aft wall in frame one. However, a pressure disturbance in and above the cavity is evident where the peak is located. This disturbance is both into and away from the cavity. Upon arriving at the aft wall, the disturbance starts to have a horizontal upstream component. There are not any indications of any disturbances upstream. Note again that all the upstream structures are below the top of the cavity.

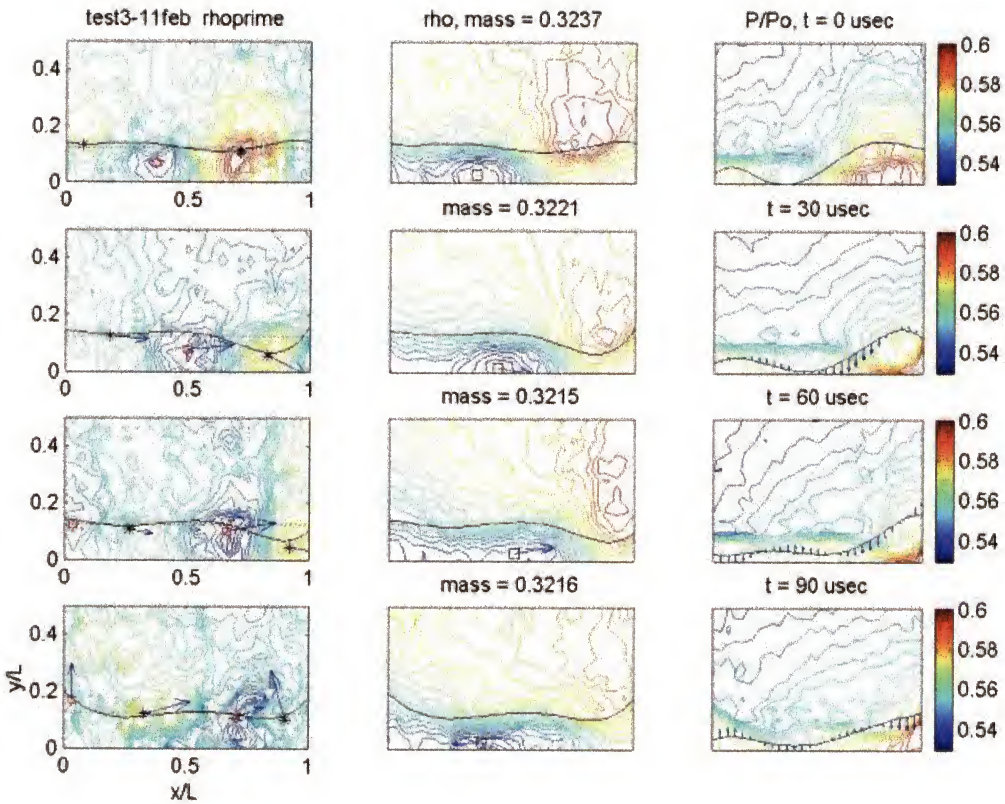

Figure 5-21 Test3-11feb, L/D = 8

5.3.1.4 Test4-11feb

Figure 5-22 shows the results for test4-11feb. Spacing between laser pulses was set to 30 microseconds. There is indication of shear layer compression from frame three to frame four. A valley is interacting with the aft wall below the lip of the cavity at frame three and has started upstream as shown in frame four. The upstream structures continue downstream and an additional valley is created at the upstream lip of the cavity. The valley that interacted at the aft wall has moved upstream at frame four essentially stopping the progress of the trailing peak. The trailing valley behind this peak had no place to go and therefore seems to bounce off the stalled peak and out into the free stream and away from the cavity.

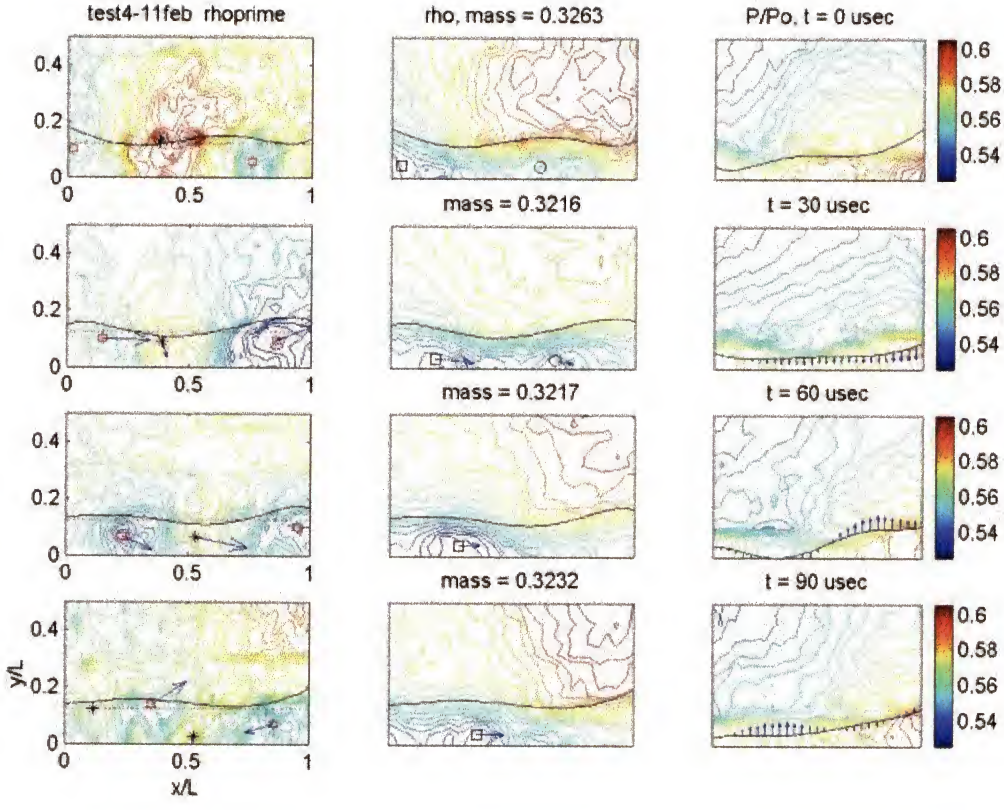

Figure 5-22 Test4-11feb, L/D = 8

The Cp on the surface again follows the position and movement of the shear layer peaks and valleys. At frame two, a valley has moved over the aft part of the cavity with a slight up curvature of the shear layer, which would allow mass to exit. The net result should be a lowering of the Cp on the aft cavity floor. This is observed. A peak is headed into the cavity at mid cavity but with the exit of mass due to the position of the shear layer, mass addition rate is lower than the mass ejection rate. At the aft end of the cavity, the net effect is the Cp decreases. A valley is also headed from the upstream wall, which should also cause a lowering of Cp on the floor of the cavity. At frame three, the over all mass in the cavity remains constant. One would be tempted to say that the Cp should not change. This is not the case. The movement of the downstream valley has gone from away from the cavity to parallel to the floor of the cavity and is interacting

with the aft wall. A peak also headed downstream and into the cavity follows the valley. The Cp over the aft half of the cavity consequently increases. Further upstream, a valley continues its movement downstream and into the cavity. The Cp over the front part of the cavity decreases. At the fourth frame, the valley at the aft wall has bounced off the aft wall and has started a movement upstream stalling the trailing peak and causing its trailing valley to move away from the cavity. Where the upstream valley moves into the cavity, the Cp decreases, where the valley moves out of the cavity, the Cp increases as expected. There is a net increase in mass at the fourth frame but this is in the front half of the cavity. This mass addition appears to be result of the two peaks moving into the cavity over the front half of the cavity.

A disturbance caused by the peak at x/L = 0.5 in the first frame is observable. This peak is above the top of the cavity. The last frame also shows the same result for the furthest upstream peak. All the other peaks are below the top of the cavity and have a movement into the cavity. Therefore, no disturbance is seen above the cavity. The valley interacting with the aft wall causes a disturbance that has an impact not only in the vertical direction but also in the horizontal direction upstream of the aft wall.

5.3.1.5 Test5-11feb

Figure 5-23 shows the results for test5-11feb. Spacing between laser pulses was set to 30 microseconds. The last two frames for test5-11feb are similar to those for test4-11feb. At frame three, there is a valley at the aft wall below the top of the cavity with a trailing peak and valley. At the last frame, the valley bounces of the aft wall and moves upstream inside the cavity. The trailing peak, since it was moving parallel to the surface as opposed to into the cavity, has bounced off the valley and has started to move out of

the cavity. This peak's trailing valley has tried to move downstream but has no place to go and therefore heads out of the cavity. The change in surface Cp is reflective of this movement. The valley that has bounced off the aft wall and moved upstream moving the trailing peak out of the cavity has caused a decrease in Cp along the floor. The peak moving out of the cavity causing its trailing valley to move out of the cavity has caused an increase in Cp below the valley. There is no indication of shear layer compression in this sequence. However, there may have been some following this sequence, as there is some indication of a peak beginning to form at the upstream lip of the cavity.

Pressure disturbances are identifiable in the first frame where a peak is interacting with the aft wall. The disturbance is both vertical and upstream. The peak upstream also shows some disturbance above the cavity. This peak is above the top of the cavity. At the next frame, the disturbance at the aft wall has greatly decreased. An examination of the peak movement indicates that it has started to move out of the cavity and its position is near the top of the cavity. Another disturbance occurs at frame three due to the interaction of a valley at the aft wall. At frame four, this disturbance has moved upstream as indicated by the valley moving upstream and interacting with the trailing peaks and valleys. Although some of these peaks and valleys are not above the top of the cavity, a disturbance is identifiable above the cavity relative to their position. Each of the these peaks and valleys has movement away from the cavity.

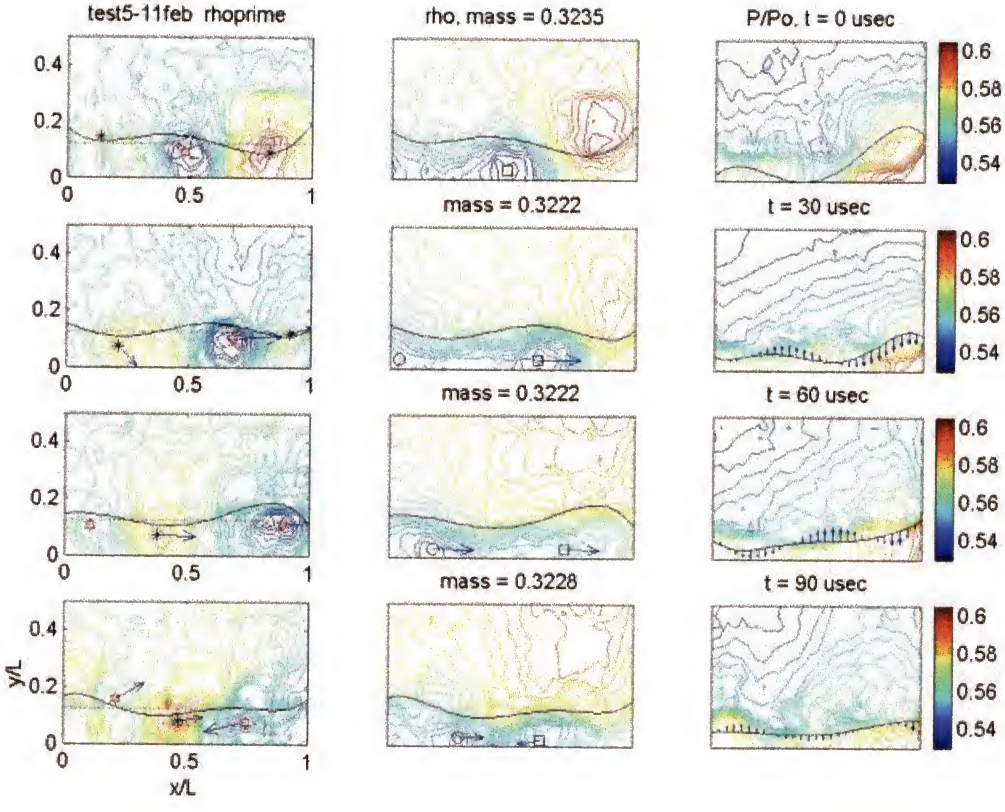

Figure 5-23 Test5-11feb, L/D = 8

5.3.2 Cavity Cycle, L/D = 8

The remaining results that will be presented were taken with laser pulse spacing of 50 and 100 microseconds. The structure interaction and impact on the Cp is consistent with previous tests and will not be elaborated on. What will be analyzed is to see if a cycle for the shallow cavity can be identified similar to that for the L/D = 4 cavity.

The modified Rossiter equation was used to predict the frequency at which the pressure is expected to oscillate (Equation 4.1) for the L/D = 4 cavity. A frequency of 5000 Hz was calculated when the cavity is a mode 2 cavity. Since the parameters in the Rossiter equation are the same for the shallower cavity (L/D = 8), the same frequency is expected. This translates into an expected cycle time of 200 microseconds for both

cavities. It was shown that the L/D = 4 cavity apparently had a cycle time on the order 150 to 200 microseconds depending on the quantity of peaks and valleys in the shear layer.

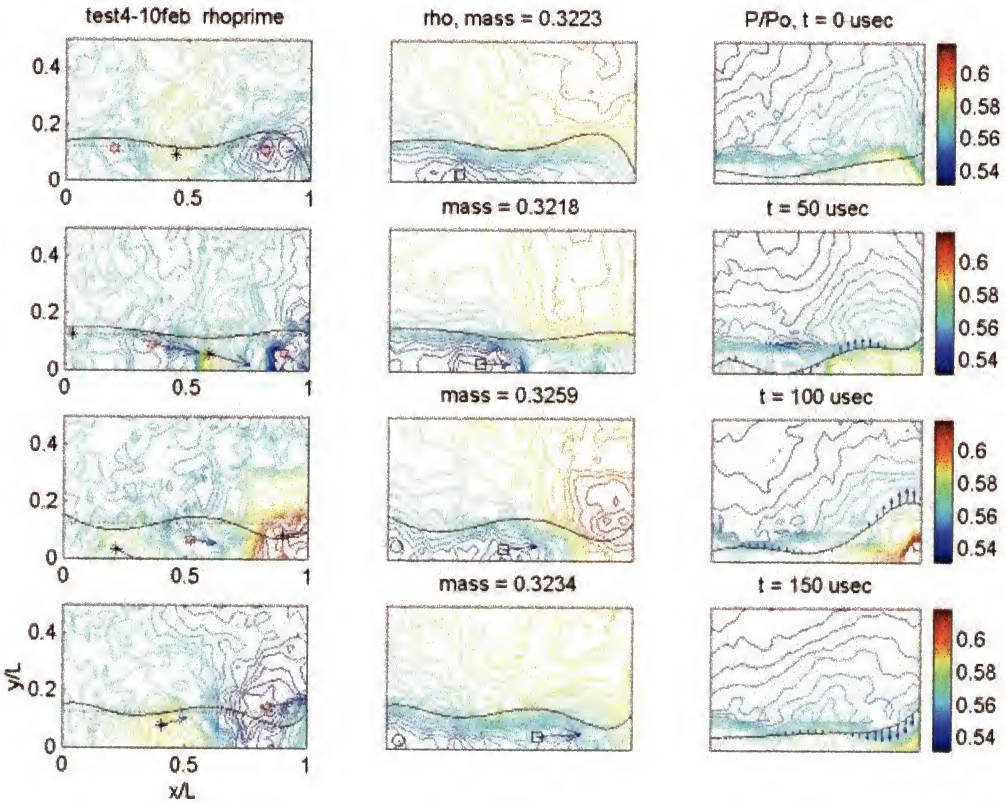

Figure 5-24 Test4-10feb, L/D = 8

An examination of Figure 5-24, test4-10feb, indicates a cycle time on the order of 150 microseconds. The first and last frames are very similar in the location of the shear layer peaks and valleys. There is only one cavity structure in the first frame while there are two in the last frame. The Cp distribution is also very similar between the first and last frame. Although not specifically identified in the third and fourth frame, there are four peaks and valleys in each of these frames. This particular L/D = 8 test seems to

agree with the results from the L/D = 4 tests. There are four peaks and valleys in the shear layer with an apparent cycle time of 150 microseconds.

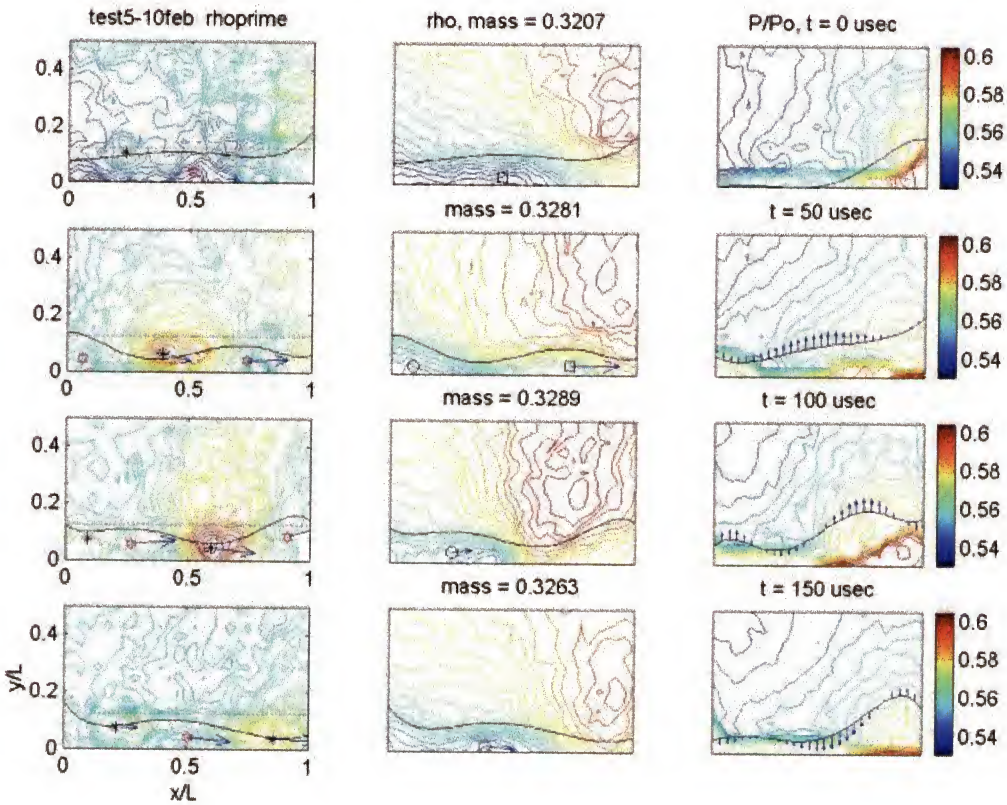

Figure 5-25 Test5-10feb, L/D = 8

In figure 5-25, test5-10, the cycle seems to be larger than the 150 microseconds shown in Figure 5-24 but less than the 200 microseconds suggested by the modified Rossiter equation. The last frame has a peak approaching the aft wall. In the first frame, the peak has already interacted with the aft wall and has started to move downstream past the aft lip of the cavity. Notice that for the second and third frame, there are four recognizable peaks and valleys indicating that the mode during this test was at least 2. However, in the first and last frame, there are only three peaks and valleys. This could account for the cycle time between 150 to 200 microseconds. Results from test6-10feb,

shown in Figure 5-26, are similar to those shown in Figure 5-25. A one to one comparison of the frames in figure 5-26 to those in figure 5-25 show that they are almost identical. Although these two tests are nearly identical, they were run one hour apart. Recall that the timing for the start of taking data was set to 0.6 seconds after a signal was sent to open the valve. This ensured that the flow conditions in the tunnel would be at steady state. The fact that the same test results were obtained is also a strong indication that a cycle exists for the shallow cavity. Both of these last two tests also suggest that the cycle time is dependent on the amount of peaks and valleys in the shear layer.

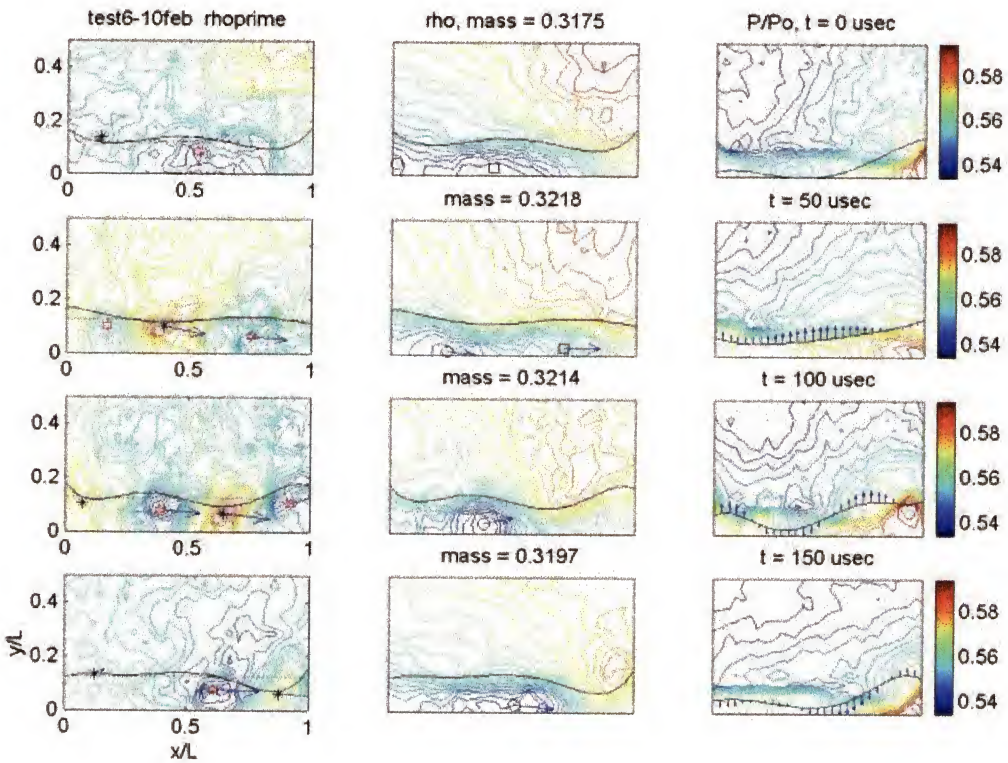

Figure 5-26 Test6-10feb, L/D = 8

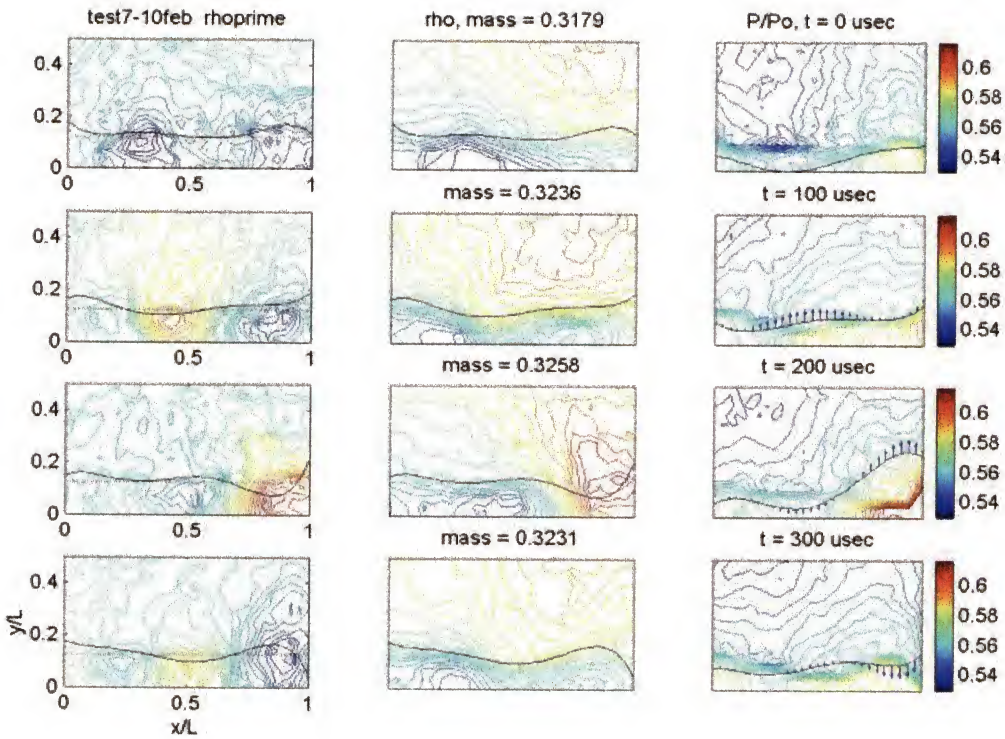

Figure 5-27 Test7-10feb, L/D = 8

Tests were also run with 100 microseconds spacing. Figure 5-27 shows the results for test7-10feb. In the first frame, there are four structures in the shear layer, two peaks and two valleys with a valley near the aft wall. In the next frame, the upstream valley has moved to just ahead of the aft wall. If the shear layer compression occurs as in previous test, it should happen between the second and third frames. If this occurs, then the first frame location of peaks and valleys will occur between the second and third frame. This would be a cycle time on the order of 150 microseconds caused by the addition of a valley at the upstream end of the cavity when the shear layer compressed. Again, it follows previous observations, the more large-scale structures in the shear layer, the shorter the cycle time. Frame four seems to be the same image as in frame two. There are three peaks and valleys in the shear layer; two cavity structures in the cavity, and the Cp curves have similar shape. The cycle time indicated is on the order of 200

microseconds, which is consistent with previous finds with only three peaks and valleys in the shear layer.

Figure 5-28 shows the results for test8-10feb. Similar conclusions as for test7-10feb can be reached. For this test, comparing the flow structure positions and Cp distribution on the floor of the cavity between frame one and three indicates a cycle time slightly less than 200 microseconds. There are three structures in the first two frames with a fourth added in the third frame. The less structures in the shear layer, the longer the cycle time. With the addition of a fourth structure somewhere between the second and third frame, the cycle time was decreased from 200 microseconds. This also appears to be the case for the second and fourth frame. The cycle time here is again slightly less than the 200 microseconds caused by the addition of a fourth structure in the shear layer.

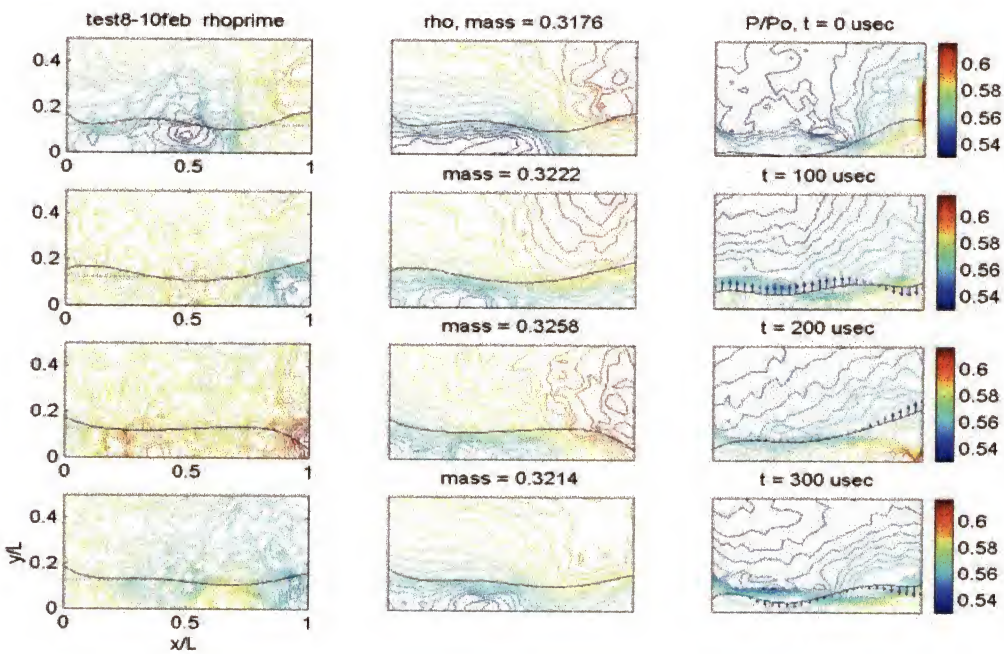

Figure 5-28 Test8-10feb, L/D = 8

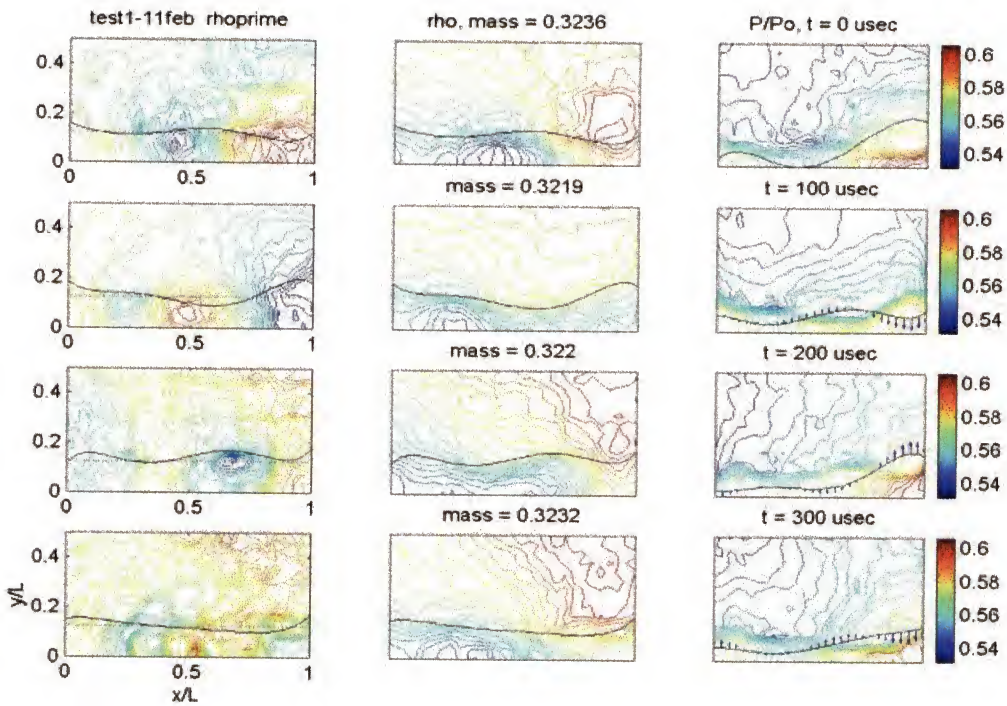

Figure 5-29 Test1-11feb, L/D = 8

Figure 5-29 shows the results for test 1-11feb. This test was taken the day after the previous test but the spacing between frames was maintained at 100 microseconds. The same conclusions reached for the previous test apply for this test also.

The shallower cavity goes through a cycle as the deep cavity. The shape of the Cp on the floor of the cavity is different but the cycle time is the same. The length of this cycle time varies between 150 to 200 microseconds like the deeper cavity. There is again a correlation between the number of peaks and valleys to the cycle time. When there are three peaks and valleys in the shear layer, the cycle time is largest at 200 microseconds. When there are four peaks and valleys, the cycle time is 150 microseconds. As the number varies between three and four peaks and valleys, the cycle time will be somewhere in between. The same conclusion is reached as for the deeper cavity. Cycle

time varies and is a function of the quantity of large-scale structures (peaks and valleys) in the shear layer.

5.3.3 Flow Structure Position and Movement, L/D = 8

Figure 5-30 shows the vertical position of the shear layer peaks and valleys and the cavity structures along the length of the cavity. As with the L/D = 4 cavity, the top plot contains the actual data from the various tests conducted. The bottom chart is the result of fitting a line through the data from the tests. This is again done in order to see if a trend in the vertical position of the structures is identifiable as function of the horizontal position along the length of the cavity.

The cavity structure is created at approximately y/L = 0.04. The position of the cavity structure remains relatively constant as it moves downstream. For the test performed, there is no indication of a cavity structure past x/L = .75. This is the result of the shear layer structures interacting with floor of the cavity and preventing the movement of the cavity structure past this position.

The shear layer peaks and valleys are created at the top edge of the cavity. Their initial movement is into the cavity and continues into the cavity until x/L = 0.65. At this point both the peak and valley interact with the floor and appear to bounce away from the cavity. For the valley, the bounce is far enough that it passes past the aft lip and moves downstream. For the peak, the bounce is not as large and returns back into the cavity as it approaches the aft wall. When the peak arrives at the aft wall, its position moves further into the cavity.

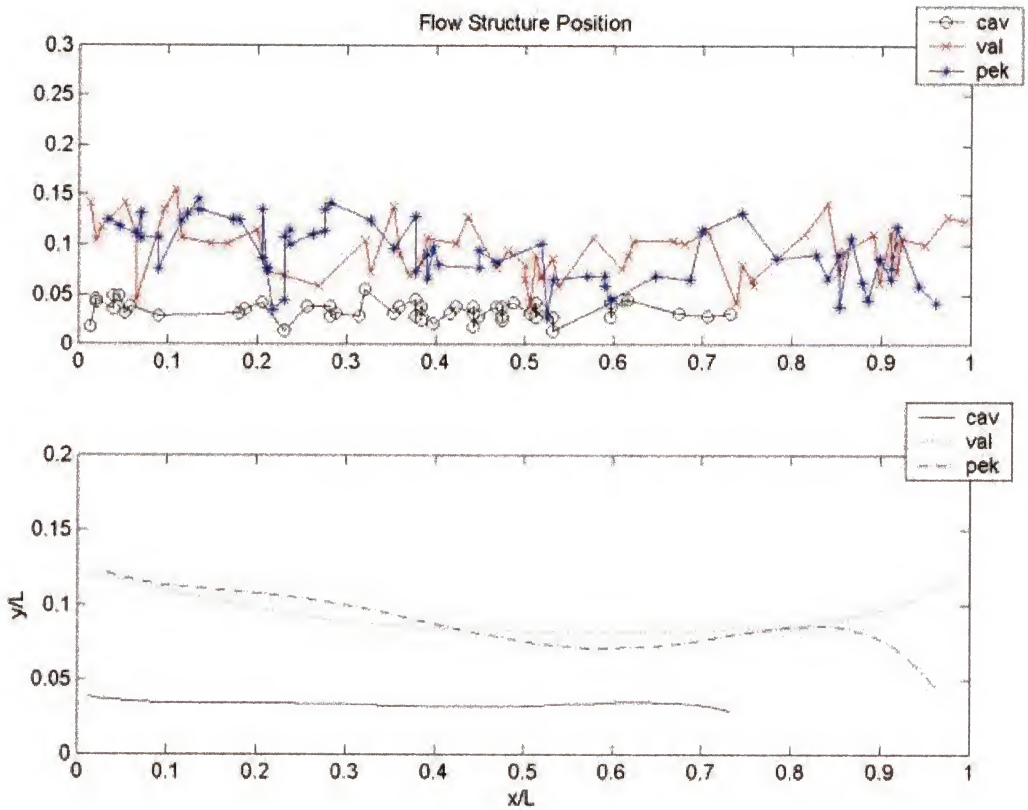

Figure 5-30 Flow Structure Position (y/L) (L/D = 8)

The position of the cavity structure and shear layer peaks and valleys is confirmed when looking at the vertical velocity component for these structures (Figure 5-31). The cavity structure vertical velocity is maintained at or very near zero along the entire length of the cavity over which it exists. On the average, there is very little vertical movement of the cavity structure. This is confirmed when looking at the statistics shown in Figure 5-32. The mean vertical velocity for the cavity structures is 0.000 and a standard deviation of 0.053. The shear layer peaks and valleys have a similar movement. There vertical velocity is initially away from the cavity but by x/L = 0.1, vertical movement relative to the floor of the cavity is constant until x/L = 0.7. At this point, it appears that both the valley and peak move away from the floor of the cavity. The valley continues to

move away and past the aft lip of the cavity. The peak, however, after initially moving away from the cavity, changes its direction and starts to move back into the cavity. When it reaches or approaches the aft wall, it vertical velocity increases more into the cavity. From Figure 5-32, the mean velocity of the valley is away from the cavity while that of the peak is negative and into the cavity.

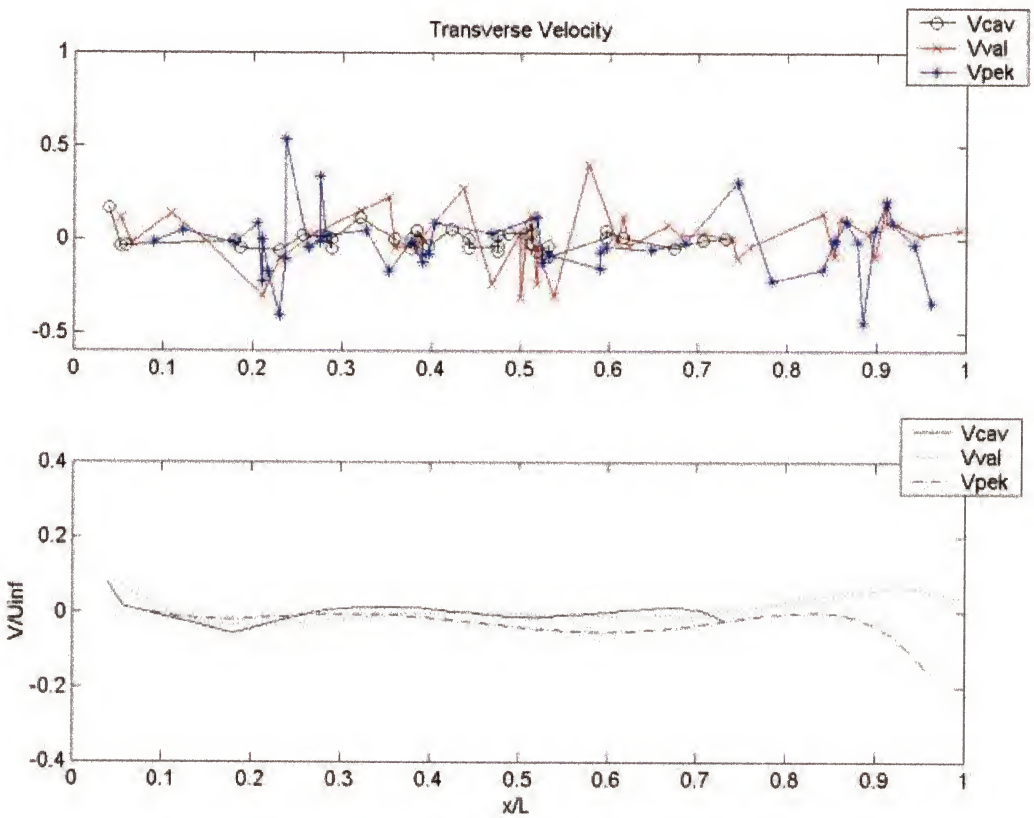

Figure 5-31 Transverse Velocity, L/D = 8

From Figure 5-32, the average position for the peak and the valley is within the cavity. Due to the close proximity of the structures to the floor of the cavity, not only the vertical movement of these structures but also the horizontal movement impact the Cp on the surface. These results were shown in the individual results of the L/D = 8 tests and seem to be confirmed by the statistics. The horizontal velocity of the peaks and valleys

are similar to those for the L/D = 4 cavity. The ratio of the horizontal velocity of the peaks and valleys to the free stream velocity is Φ_d, which is used in the modified Rossiter equation to predict the pressure oscillation frequency. It has been shown that both the deep and shallow cavities have similar cycle times. Therefore, it would be expected that this ratio would be the same for both cavities.

L/D = 8

Non-dimensional Flow Structure Velocity

	Ucav	Vcav	Uval	Vval	Upeak	Vpeak
Mean	0.285	0.000	0.355	0.010	0.362	-0.027
Std Dev	0.191	0.053	0.260	0.150	0.188	0.177
Min	-0.418	-0.091	-0.480	-0.308	-0.021	-0.444
Max	0.564	0.168	0.939	0.400	0.845	0.536

Non-dimensional Flow Structure Position (y/L)

	Ycav	Yval	Ypeak
Mean	0.033	0.093	0.092
Std Dev	0.009	0.027	0.030
Min	0.014	0.038	0.028
Max	0.055	0.155	0.146

Figure 5-32 Non-dimensional Flow Structure Statistics, L/D = 8

The cavity structure horizontal velocity is much lower that that for the deeper cavity. This is an indication that the cavity structures and the shear layer peaks and valleys are distinct from each other.

5.4 Summary

The results of the tests for both the L/D = 4 and L/D = 8 cavity have been shown to support the model described at the beginning of the chapter. That is, the structures in the shear layer can be likened to balls that are created periodically at the leading edge of the cavity and move downstream at a certain velocity in both the horizontal and vertical direction ultimately affecting the pressure on the surface of the cavity. These structures not only have a direct correlation with the pressure and change in pressure on the surface of the cavity but also have an indirect impact when interacting with each other and the cavity geometry. This was shown when peaks and valleys interacted with the aft wall and floor allowing the trailing valley or peak to interact with the leading peak or valley and move the shear layer in or out of the cavity. This shear layer movement allowed mass to be ingested or ejected thereby affecting the pressure and change in pressure on the surface of the cavity. Knowing the position and movement of these peaks and valleys with respect to the geometry of the cavity allows the prediction of the pressure and change in pressure on the surface as well as in and above the cavity. Using control volume techniques and calculating the momentum flux across the control volume boundaries might permit further refinement of this model.

5.4.1 Mass Injection/Ejection

From the series of tests conducted for both the deep (L/D = 4) and shallow (L/D = 8) cavities, it is concluded that mass injection and ejection occurs all along the length of the cavity, not just at the aft wall where it appears that the shear layer flaps up and down allowing fluid to enter or exit the cavity. The mass injection and ejection upstream of the aft wall is related to the upstream position and movement of the shear layer peaks and

valleys. Mass enters the cavity when the peaks move into the cavity and mass exits the cavity when the peaks move away from the cavity. The peak can be likened to a bouncing ball that behaves as a positive change in density or an increase in mass. By themselves, peaks increase density when moving into the cavity and decrease density when moving away from the cavity. However, peaks do not exist alone. A valley exists in front as well as behind each peak. Valleys also act as bouncing balls but negative changes in density or decreases in mass. When valleys move into the cavity, density decreases in the cavity and increases when the valley moves away from the cavity.

When the peaks and valleys are in close proximity to each other, the increase in density may be larger when the change in peak density deviation is larger than can be offset by the negative density deviation from the nearby valley. This peak and valley interaction usually occurs over the aft half of the cavity after either a peak or valley has interacted with the aft wall or after a peak or valley has interacted with the floor of the cavity. The peak and valley interaction with the floor of the cavity was observed for the shallow cavity but was not observed for the deep cavity. This peak and valley interaction at the aft end of the cavity resulted in the shear layer moving in or out of the cavity. This tends to support the model of Heller and Bliss (1975), which states that mass addition and removal occurs at the aft end of the cavity.

5.4.2 Shear Layer Movement

The shear layer can compress from containing three large-scale structures to four large-scale structures. This occurred when a peak was near the aft wall for the deep cavity and when either a valley or a peak was near the aft wall for the shallow cavity. The position and movement of the peak or valley just prior to arriving at the aft wall

determined if the shear layer compressed or not. For the deep cavity, the peak was normally below the top of the cavity and the valley was above when arriving at the aft wall. Therefore, the peak interacting at the aft wall caused compression of the shear layer for the deep cavity. However, even if the peak is below the lip of the aft wall prior to arriving at the aft wall, shear layer compression will not take place if the peak has a vertical velocity component away from the cavity. The shallow cavity, on the other hand, could have either a peak or valley below the top of the cavity when arriving at the aft wall. In addition to the vertical velocity of the peak or valley, how the peak or valley interacted with the floor prior to the aft wall affected how the peak or valley interacted with the aft wall. Depending on this interaction with the floor immediately prior to the aft wall, the peak or valley may bounce past the aft wall, just barely touch it, or hit it full force and bounce back upstream causing compression of the shear layer.

Another observation was the apparent non-flapping of the shear layer at the aft wall for the deep cavity. When a valley was headed towards the aft end of the cavity and the valleys position was slightly above the top of the cavity, the valley would continue downstream without interacting with the aft wall. The curvature of the shear layer would move with the valley and it would appear that the shear layer flapped open at the aft end and allowed fluid to escape. In reality, the shape of the shear layer, which looks like a wave, was passing over the aft lip of the cavity without interacting with the aft wall. The same phenomenon occurs when a peak arrives at the aft wall. Its vertical position relative to the top of the cavity was below the lip. Consequently, as it arrived at the aft wall, it appeared that the shear layer flapped into the cavity.

For the shallow cavity, there were some instances where the peak and valley interacting with the aft wall appeared to stall or started to move upstream within the cavity. When this occurred, the trailing peak or valley would come nearer the peak or valley at the aft wall and interact as bouncing balls. Depending on the bounce, the shear layer would be moved either away from the cavity or into the cavity.

The movement of the peaks and valleys controls the movement and shape of the shear layer. The position and movement of the peaks and valleys with respect to the geometry of the cavity determine how they will interact. How the peaks and valleys interact with the geometry impacts how they will interact with each other. This brings us back to the start where the position and movement of the peaks and valleys controls the movement of the shear layer. Peaks and valleys exist when flow passes over a cavity. They are the cause of the pressure disturbance in and above the cavity as well as Cp on the floor.

5.4.3 Floor Cp Distribution

The average Cp distribution on the floor of the cavity has been used to classify cavities as deep, open, transitional, and closed. The relationship of the position and movement of the flow structures with the surface pressure distribution was a major research item for this dissertation. It was found that the most important structures that impact Cp are the position and movement of the peaks and valleys in the shear layer. The position and movement of the peaks and valleys and the movement of the shear layer caused by the interaction of the peaks and valleys exert the greatest influence on the floor Cp. This is in agreement with Plumblee et al. (1962) who stated that the shear layer spanning the free boundary of the cavity provides it with a broadband noise source from

which the cavity picks up certain frequencies to amplify. These findings also support Rossiter (1964) who stated that the driving mechanism of the cavity flow oscillation is a property of the flow over the cavity. How the density in the cavity behaves is directly related to how the peaks, valleys and shear layer behave. When density increases in the cavity, the pressure on the surface increases. When density decreases, pressure decreases.

For the deep/open cavity, not only the position of the peaks and valleys but their vertical movement affects the floor Cp. As explained in the model in section 5.1, there are a multitude of combinations of position, movement and interaction that impact the surface Cp. A model of bouncing balls that act as positive density (peaks) or negative density (valleys) changes was used to illustrate this effect on surface Cp. For the shallower cavity, not only the position and vertical movement were important for determining the impact on the floor Cp but also the horizontal movement. This is due to the fact that the peaks and valleys are nearer to the floor for the shallower cavity. Test results for the deep and shallow cavity were shown to agree with this model.

5.4.4 Pressure Disturbance Sources

When the peaks and valleys interact with the aft wall, a disturbance is created that radiates not only into the cavity but also above the cavity. When the cavity is deep, the disturbance tends to be more vertical or into and out of the cavity. When the cavity is shallower and the peaks and valleys interact with the aft wall more head on, the disturbance tends to have an upstream component as well as a vertical component. This disturbance source is not just restricted to when the peaks and valleys interact with the aft wall. For the deep cavity, the movement of the peaks and valleys downstream after they

are created cause a disturbance all along the length of the cavity. When they arrive at the aft wall, the intensity of the disturbance is increased if there is any interaction with the aft wall but the disturbance is still mainly in the vertical direction. The interaction with the aft wall happened mainly for the peaks in the deep cavity. The vertical velocity direction for the peaks and valley for the deep cavity did not appear to have an impact on whether a disturbance was created or not. Just the fact that they existed was enough to cause a disturbance in and above the cavity.

For the shallow cavity, not only the position of the peak with respect to the top of the cavity but also its vertical velocity component determined if a disturbance would be noticeable upstream of the aft wall. When the position of the peak was below the top of the cavity or if the peak had a negative vertical velocity component (into the cavity), a disturbance was not readily observable above the cavity. When the peak was above the top of the cavity or had a vertical velocity out of the cavity, there was evidence that the peak acted as a source of a disturbance. Valleys also seem to cause disturbance for the shallower cavity. The position and vertical movement similar to the peaks also governed the disturbances created by the valleys.

5.5 Conclusions

Shear layer peaks and valleys are the primary influence on the flow in and above a cavity. They are the primary influence on the pressure distribution not only on the floor of the cavity, which is used to classify the cavity but also the pressure distribution in and above the cavity. The existence and position of the peaks and valleys alone do not cause a unique pressure distribution on the surface. For the deep cavity, the vertical movement of the peaks and valleys is also important. When a peak moves in and out of a cavity, the

effect is to increase and decrease the density in the cavity respectively. This increase and decrease of density are directly related to the increase and decrease of the Cp on the floor of the cavity. In the case of the shallower cavity, the horizontal movement of the peaks and valleys is also important. This is due to the fact that the peaks and valleys are nearer to the floor of the shallow cavity compared to the deep cavity.

The peaks and valleys also have an impact on the cycle of a cavity. A frequency of between 5000 to 7000 HZ was observed. Non-dimensionalizing this frequency using the length (L = 0.0254 m) and free stream velocity (U_∞ = 260 m/s), a Strouhal number of 0.46 to 0.62 is obtained. From the modified Rossiter equation, a Strouhal number of 0.7 is calculated using the generally accepted value of $\Phi_d = 0.57$ (the ratio of the vortices velocity to the free stream velocity). The modified Rossiter equation predicts a higher Strouhal number than is calculated from the observed cycle time of the two cavity geometries. However, if one sets $\Phi_d = 0.4$ which is the average ratio of the peaks and valleys velocity to the free stream velocity calculated for all the tests, the Strouhal number predicted by the modified Rossiter equation is 0.54, which falls within the observed range of the experiment. For a particular test, an individual Strouhal number is found and this Strouhal number is related to the quantity of peaks and valleys visible in the shear layer. When there are three peak and valleys in the shear layer, the Strouhal number is 0.62. When there are four peaks and valleys in the shear layer, the Strouhal number is 0.46.

5.6 Future Work

This research showed the correlation between the position and movement of the large-scale structures in the shear layer and the change in the surface pressure

distribution. Given the position and movement of these large-scale structures, a model was proposed that can be use to predict the change in Cp on the surface of the cavity. However, still unknown is the cause of the number of large-scale structures in the shear layer and the magnitude of change in the Cp on the surface caused by the position and movement of these large-scale structures.

Future research should look into finding a correlation between the free stream and cavity geometry and the number of large-scale structures in the shear layer. The modified Rossiter equation is useful in predicting the fluctuating pressure frequency but does not provide any insight into which mode will dominate. The mode at which a cavity resonates is directly related to the quantity of large-scale structures in the shear layer. A parametric study should be undertaken using the Shack Hartman sensor to investigate which flow or geometry parameter affects the number of large-scale structures in the shear layer.

The structures in the shear layer have physical size associated with them. A magnitude of the deviation of density from the ensemble average is also associated with each large-scale structure. At the Mach number, Reynolds number and cavity length for this current research, the size of the structures and the deviation from the density ensemble average appeared to remain the same for both L/D = 4 and L/D = 8. A parametric study should be undertaken to investigate the effect of the free stream and cavity geometry on the size of these structures and the magnitude of the deviation of the density from the ensemble average.

Two major assumptions were made in the completion of this work; the two dimensionality of the flow over the cavity and the temperature distribution in and above

the cavity. The two dimensionality of the flow was assumed, which if true, would make the slope of a wave front passing through a constant density field constant. It is known that the flow in the in-draft tunnel does have gradients in density along the direction of the light travel especially near the wall. The two dimensional assumption was justified by using flow visualization from prior research to show that the flow is at least symmetrical with respect to the longitudinal center line of the cavity. Although the slope of the wave front will change as it passes through the span wise direction, the fact that it is symmetrical will result in a net zero change in the slope. Future work using the Shack Hartman sensor should measure the flow normal to the floor of the cavity to confirm that the flow in the tunnel is symmetrical.

A temperature distribution was assumed for the cavity, through the shear layer and above the cavity. Although it was based on prior theoretical work and known behavior of the temperature through shear layers, the exact temperature is not known. The ability to analyze the pressure in and above a cavity would benefit in the future through research in the temperature in and above a cavity. The temperature coupled with the measured density will provide the pressure, which for many engineering applications is necessary for the design of equipment that has to withstand the environment of flow over a cavity.

In addition to the temperature, a method for combining the Shack Hartman sensor with flow field velocity measurement techniques should be explored. Along with the temperature, this would provide everything needed to confirm the fluid flow equations experimentally. In conjunction with the velocity, a method to expand the amount of frames available from the Shack Hartman sensor should also be explored. This would

provide more time-resolved information, which would allow a more complete analysis of the cycle time and how the large-scale structures in the shear layer impact this cycle time.

REFERENCES

Ahuja KK, Mendoza J (1995) Effects of Cavity Dimensions, Boundary Layer, and Temperature on Cavity Noise with Emphasis on Benchmark Data to Validate Computational Aeroacoustic Codes, NASA Contract Report 4653, 1995

Anderson JD (1991) Fundamentals of Aerodynamics, McGraw-Hill, Inc., New York

Ashcroft G, Zhang X (2001) A Computational Investigation of the Noise Radiated by Flow-Induced Cavity Oscillations, AIAA 2001-0512

Baysal O, Stallings RL (1987) Computational and Experimental Investigation of Cavity Flow Fields, AIAA 87-0114

Benedict RP (1980) Fundamentals of Pipe Flow, Wiley-Inter Science Publication, Wiley & Sons, New York

Chung KM (2000) Characteristics of Transonic Rectangular Cavity Flows, Journal of Aircraft Vol. 37, No. 3, pages 463-468

Chung KM (2001) Three-Dimensional Effect On Transonic Rectangular Cavity Flows, Experiments in Fluids 30, pages 531-536

Daugherty RL, Franzini JB ((1965) Fluid Mechanics With Engineering Applications, McGraw Hill Book Company, New York

Dix RE, Dobson TW (1990) Database for Internal Store Carriage and Jettison, AEDC-TR-90-23, Vol. I

Dix RE, Bauer RC (1993) Engineering Model predictions of Aeroacoustic amplitudes in a weapons cavity, AIAA 93-0858

Forestier N, Geffroy P, Jacquin L (1999) Flow Over Cavities In Transonic Regime: A Test Case For Numerical Simulations, 1st International Symposium on Turbulence Shear Flow Phenomena, (1999, September)

Fuglsang DF, Cane AB (1992) Evaluation of Shear Layer Cavity Resonance Mechanism By Numerical Simulation, AIAA 92-0555

Fuller PWW (1997) Flow Visualization In: Ray S (ed) High-Speed Photography And Photonics, Focal Press, Oxford, UK, pages 254-280

Gunia MA (1999) Shack Hartman Reconstruction Algorithms for Flow Field Diagnostics, Master's Thesis

Hankey WL, Shang JS (1979) The Numerical Solution to Pressure Oscillations in an Open Cavity, AIAA 79-0136, 17th Aerospace Sciences Meeting

Heller HH, Holmes G, Covert EE (1970) Flow Induced Pressure Oscillations In Shallow Cavities, AFFDL-TR-70-104

Heller HH, Bliss DB (1975) The Physical Mechanism of Flow Induced Pressure Fluctuations In Cavities And Concepts For Their Suppression, AIAA 75-491

Hoffman JD, Zucrow MJ (1976) Gas Dynamics, Volume I and II, John Wiley & Sons, New York

John JEA (1984) Gas Dynamics, Allyn and Bacon, Inc., Newton, Massachusetts

Komerath NM, Ahuja KK, Chambers FW (1987) Prediction and Measurement of Flows over Cavities - A Survey, AIAA 87-0166

Krishnamurty K (1955) Acoustic Radiation From Two-Dimensional Rectangular Cutouts in Aerodynamic Surfaces, NACA Technical Note 3487

Land JE (2000) Shack Hartman Wave Front Sensor for Tomographic Reconstruction of Aerodynamic Flow Density Measurements, PhD Dissertation

Lillberg E, Fureby C (2000) Large Eddy Simulations of Supersonic Cavity Flow, AIAA 2000-2411

Morris HM (1963) Applied Hydraulics in Engineering, The Ronald Press Company, New York

Murray RC, Elliott GS (2001) Characteristics Of The Compressible Shear Layer Over A Cavity, AIAA Journal, Vol. 39, No. 5, (2001, May), pages 846-856

Owczarek JA (1964) Fundamentals of Gas Dynamics, International Textbook Company, Scranton, Pennsylvania

Plentovich EB (1990) Three Dimensional Cavity Flow Fields at Subsonic and Transonic Speeds, NASA Technical Memorandum 4209

Plentovich EB, Chu J, Tracy MB (1991) Effects of Yaw Angle and Reynolds Number on Rectangular Box Cavities at Subsonic and Transonic Speeds, NASA Technical Paper 3099

Plentovich EB, Stallings RL, Tracy MB (1993) Experimental Cavity Pressure Measurements at Subsonic and Transonic Speeds, NASA Technical Paper 3358.

Plumblee HE, Gibson JS, Lassiter IW (1962) A Theoretical And Experimental Investigation Of The Acoustic Response Of Cavities In An Aerodynamic Flow, WADD-TR-61-75

Rizzetta DP (1988) Numerical Simulation of Supersonic Flow Over a three-dimensional Cavity, AIAA Journal, Vol. 26, No. 7, pages 799-807

Rockwell D, Naudascher E (1978) Review - Self-Sustaining Oscillations of Flow Past Cavities, Journal of Fluids Engineering, Vol. 100, (1978, June), pages 152-165

Rona A, Dieudonne W (2000) Open Cavity Instability Models in Laminar Flow Using Uniform and Non-Uniform computational Grids, Proceedings of ASME FEDSM'00, ASME 2000 Fluids Engineering Division Summer Meeting, June 11-15, 2000

Rossiter JE (1964) Wind Tunnel Experiments On the Flow Over Rectangular Cavities At Subsonic And Transonic Speeds, R. & M. No. 3438, British Aeronautical Research Council

Rudinger G (1955) Wave Diagrams for Nonsteady Flow in Ducts, D. Van Nostrand Company, Inc., New York

Schlichting H (1979) Boundary Layer Theory, McGraw Hill Publishing Company, New York

Shchukin VK, Gortyshov YF, Varflolomeev IM, Nadyro NA (1980) Influence of Relative Depth and Reynolds Number on Heat Transfer in Cavities in Compressible Gas Flow, Soviet Aeronaut, Vol. 23, No. 3, pages 83-86

Shapiro AH (1953), The Dynamics and Thermodynamics of Compressible Fluid Flow, Volume I and II, John Wiley & Sons, New York

Shieh M, Morris PJ (2001) Comparison of Two and Three Dimensional Turbulent Cavity Flows, AIAA 2001-0511

Sinha N, York BJ, Cavallo PA (1997) Aircraft Weapon Bay Turbulent Flow Simulation Model, Phase I SBIR Final Technical Report, CRAFT Inc., Report No.: CRAFTR-9/97.011

Stallings RL, Wilcox FJ (1987) Experimental Cavity Pressure Distributions at Supersonic Speeds, NASA Technical Paper 2683

Stallings RL, Plentovich EB, Tracy MB, Hemsch MJ (1995) Measurements Of Store Forces And Moments And Cavity Pressures For A Generic Store In And Near A Box Cavity At Subsonic And Transonic Speeds, NASA Technical Memorandum 4611

Takakura Y, Higashino F, Yoshizawa T (1996) Numerical Study of Unsteady Supersonic Cavity Flows, AIAA 96-2092

Tracey MB, Plentovich EB (1992) Measurements of Fluctuating Pressure In a Rectangular Cavity In Transonic Flow At High Reynolds Numbers, NASA Technical Memorandum 4363

Vakili AD, Gauthier C (1991) Control of Cavity Flow by Upstream Mass Injection, AIAA-91-1645

Wilcox DC (1997) Basic Fluid Mechanics, DCW Industries, Inc., La Canada, California

Zhang X, Edwards JA (1990) An Investigation of Supersonic Oscillatory Cavity Flows Driven by Thick Shear Layers, Aeronautical Journal, (1990, December), pages 355-364

Zhang X, Edwards JA (1992) Experimental Investigation of Supersonic Flow Over Two Cavities In Tandem, AIAA Journal, Vol. 30, No. 5, pages 1182-1190

Zhang X (1995) Compressible Cavity Flow Oscillation Due to Shear Layer Instabilities and Pressure Feedback, AIAA Journal, Vol. 33, No. 8, (1995, August), pages 1404-1411

Zhang X, Rona A, Lilley GM (1995) Far-field Noise Radiation From an Unsteady Supersonic Cavity Flow, Joint CEAS/AIAA Aeroacoustics Conference, June 1995

Zhang X, Edwards JA (1996) Analysis of Unsteady Supersonic Cavity flow Employing an Adaptive Meshing Algorithm, Computers and Fluids Vol. 25, No. 4, (1996, May), pages 373-393

Zhang X, Rona A, Edwards JA (1998a) The Effect of Trailing Edge Geometry on Cavity Flow Oscillation Driven by a Supersonic Shear Layer, Aeronautical Journal, (1998, March), pages 129-136

Zhang X, Rona A, Edwards JA (1998b) An Observation of Pressure Waves Around a Shallow Cavity, Journal of Sound and Vibration (1998) 214(4), pages 771-778

Zhang X, Rona A, Edwards JA (1999) Attenuation of Cavity Flow Oscillation Trough Leading Edge Flow Control, Journal of Sound and Vibration, 221(1), pages 23-47

Zhang X, Edwards JA (1999) Pressure over a Dual-Cavity Cascade at Supersonic Speeds, Aeronautical Journal, (1999,January), pages 45-54

BIOGRAPHICAL SKETCH

John was born August 7, 1948, in Lewiston, Maine. John grew up in Lewiston, Maine, until he was 6 years old. His family moved to Elkins, West Virginia, where they stayed until John reached the age of 13. His family then moved to St. Louis, Missouri, where John attended both high school and college. He graduated from St. Louis University High School in May of 1966. He attended Parks College of Aeronautical Technology, graduating with a BS degree in aeronautical engineering in 1969. He entered the Air Force, attended pilot training and served on active duty until 1977. While on active duty, John earned an MBA from the University of Wyoming. He separated from the active forces but remained active in the Air Force Reserves. Eglin Air Force Base, Florida, hired him as an engineer in 1981. Since that time, he has been actively involved in the Air Force Air-to-Air missile programs in all phases from development to test. John earned an MS degree in aerospace engineering from the University of Florida through the Graduate Engineering Research Center in 1995. John is married to the former Deborah Susan Swann of Moultrie, Georgia. John and Debbie have five children: Michelle, Kristi, Dominique, Charles, and Jacquelyn. They also have two grandchildren: Jacob and Haley.

I certify that I have read this study and that in my opinion it conforms to acceptable standards of scholarly presentation and is fully adequate, in scope and quality, as a dissertation for the degree of Doctor of Philosophy.

Pasquale M. Sforza, Chairman
Professor of Aerospace Engineering,
Mechanics, and Engineering Science

I certify that I have read this study and that in my opinion it conforms to acceptable standards of scholarly presentation and is fully adequate, in scope and quality, as a dissertation for the degree of Doctor of Philosophy.

Chris S. Anderson, Cochairman
Assistant Professor of Electrical and
Computer Engineering

I certify that I have read this study and that in my opinion it conforms to acceptable standards of scholarly presentation and is fully adequate, in scope and quality, as a dissertation for the degree of Doctor of Philosophy.

Wei Shyy
Professor of Aerospace Engineering,
Mechanics, and Engineering Science

I certify that I have read this study and that in my opinion it conforms to acceptable standards of scholarly presentation and is fully adequate, in scope and quality, as a dissertation for the degree of Doctor of Philosophy.

Ulrich H. Kurzweg
Professor of Aerospace Engineering,
Mechanics, and Engineering Science

I certify that I have read this study and that in my opinion it conforms to acceptable standards of scholarly presentation and is fully adequate, in scope and quality, as a dissertation for the degree of Doctor of Philosophy.

David W. Mikolaitis
Associate Professor of Aerospace Engineering, Mechanics, and Engineering Science

I certify that I have read this study and that in my opinion it conforms to acceptable standards of scholarly presentation and is fully adequate, in scope and quality, as a dissertation for the degree of Doctor of Philosophy.

Henry Zmuda
Associate Professor of Electrical and Computer Engineering

This dissertation was submitted to the Graduate Faculty of the College of Engineering and to the Graduate School and was accepted as partial fulfillment for the requirements of the degree of Doctor of Philosophy

December 2001

Pramod Khargonekar
Dean, College of Engineering

Winfred M. Phillips
Dean, Graduate School